**TECHNICAL REPORT**

# Fundamental Reactive Characterization of Novel Nano-Scale Assembled Fuel/Oxidizers Using a New Mass-Spectrometry T-Jump Approach

March 2014

Michael R. Zachariah

Prepared by:
Department of Mechanical
Engineering
2181 Glenn L. Martin Hall
University of Maryland
College Park, MD 20742

# REPORT DOCUMENTATION PAGE

| 1. REPORT DATE *(DD-MM-YYYY)* | 2. REPORT TYPE | 3. DATES COVERED *(From - To)* |
|---|---|---|

**4. TITLE AND SUBTITLE**

**5a. CONTRACT NUMBER**

**5b. GRANT NUMBER**

**5c. PROGRAM ELEMENT NUMBER**

**6. AUTHOR(S)**

**5d. PROJECT NUMBER**

**5e. TASK NUMBER**

**5f. WORK UNIT NUMBER**

**7. PERFORMING ORGANIZATION NAME(S) AND ADDRESS(ES)**

**8. PERFORMING ORGANIZATION REPORT NUMBER**

**9. SPONSORING / MONITORING AGENCY NAME(S) AND ADDRESS(ES)**

**10. SPONSOR/MONITOR'S ACRONYM(S)**

**11. SPONSOR/MONITOR'S REPORT NUMBER(S)**

**12. DISTRIBUTION / AVAILABILITY STATEMENT**

**13. SUPPLEMENTARY NOTES**

**14. ABSTRACT**

**15. SUBJECT TERMS**

| 16. SECURITY CLASSIFICATION OF: | | | 17. LIMITATION OF ABSTRACT | 18. NUMBER OF PAGES | 19a. NAME OF RESPONSIBLE PERSON |
|---|---|---|---|---|---|
| a. REPORT | b. ABSTRACT | c. THIS PAGE | | | 19b. TELEPHONE NUMBER *(include area code)* |

**OBJECTIVE:**
The basic objective of this program is to explore new architectures for energetic materials, and to use novel diagnostic tools that probe the underlying nature of reactivity of this class of materials.

The specific objective of this program are two fold. **A.** Development of novel architectures for reactive metals. **B.** Characterization of nanoparticle reactivity, and development of scaling laws from novel measurements of reactivity using a new concept in mass spectrometry ( T-Jump Mass Spectrometry; TJMS).

**PART A: New materials for creating a more intimate fuel/oxidizer**
The greater the proximity between the fuel and oxidizer the greater should be the expected energy release rate. Our objective is to develop new architectures to enhance proximity between fuel and oxidizer using aerosol processing.
1. Develop an aerosol based process for the formation of passivated aluminum nanoparticles with primary focus on the coating with polymers and other metals.

**PART B: New Diagnostics**
As part of this work we will also develop new approaches to study thermite type reactions. Most import of these is a new type of mass spectrometry (TJMS) being develop in our laboratory, which will enable the study of fast solid-state reactions. One of the unique features of this work will be the ability to create samples which have an extremely narrow particle size distribution through on-the-fly gas-phase electrophoretic separation of particles.

The combination of new architectures, with the new TJMS characterization will afford the opportunity to explore new types of structures that may point the direction on how best to assemble fuel/and oxidizers at the nanoscale to optimize energy release. The new diagnostic approach presents an opportunity to develop a tool to study from a microscopic point of view, reactions between solids. In the latter case the new tool should be of utility to a wide variety of problems in energetic materials well beyond those of thermite chemistry.

**Part A: New materials**

We have begun by exploring in collaboration with Dr. Jason Jouet of Naval Surface Warfare Center, Indian Head a potential generation method for aluminum nanoparticles, which can be passivated, or coated with other metals or reactants. Our first goal is to create a pristine source of nanoaluminum. Furthermore, one additional constraint was the desire to explore a method that could have the potential to be scaled up to the industrial level. We have chosen to pursue the formation of nanoaluminum from vapor-phase thermal cracking of aluminum based metal organic precursors. There are many metalorganic precursors that can be used to produce aluminum, such as trimethylaluminum, triethylaluminum, and triisobutylaluminum. After researching their properties , we chose triethylaluminum (TEA). It was believed that TEA would crack at lower temperatures and reduce the possibility that we would produce solid carbon. If we did manage to crack the ethyl groups we could possibly produce an Al/AlC nanoparticle, something we do not want. With this in mind an 100 gram stainless steel bubbler was used to create a saturated vapor stream of the TEA in an Ar carrier gas.

TEA is high pyrophoric meaning it spontaneously combusts in air, and must be handled in an inert glove box. Once loaded in the bubbler, and installed into the rest of the system, the bubbler and tubing was wrapped in heating tape and insulation. Both the bubbler and the tubing are on separate controllable heating elements, allowing for varying thermal gradients through reactor. The bubbler is heated to increase the vapor pressure of the TEA, and thus the increase the amount of TEA in the Ar flow. The tubing between furnace and bubbler is heated to a temperature higher than the bubbler to ensure that the TEA/Ar aerosol does not condense in the line.

Temperature is monitored at two locations (see pictures) with k-type thermocouples. The bubbler has a 'Thermawell', which allows us to put a thermocouple down the center to the base of the bubbler. This provides an accurate measure of the TEA's temperature after the system is allowed to equilibrate. A second thermocouple if fitted to track the temperature of the aerosol flow after the bubbler.

Pressure is measured upstream of the bubbler in order to keep the TEA from degrading this sensor. We primary monitor the pressure to keep the system at less than ~6 psi over atmosphere.

A picture of our nanoparticle reactor is seen below:
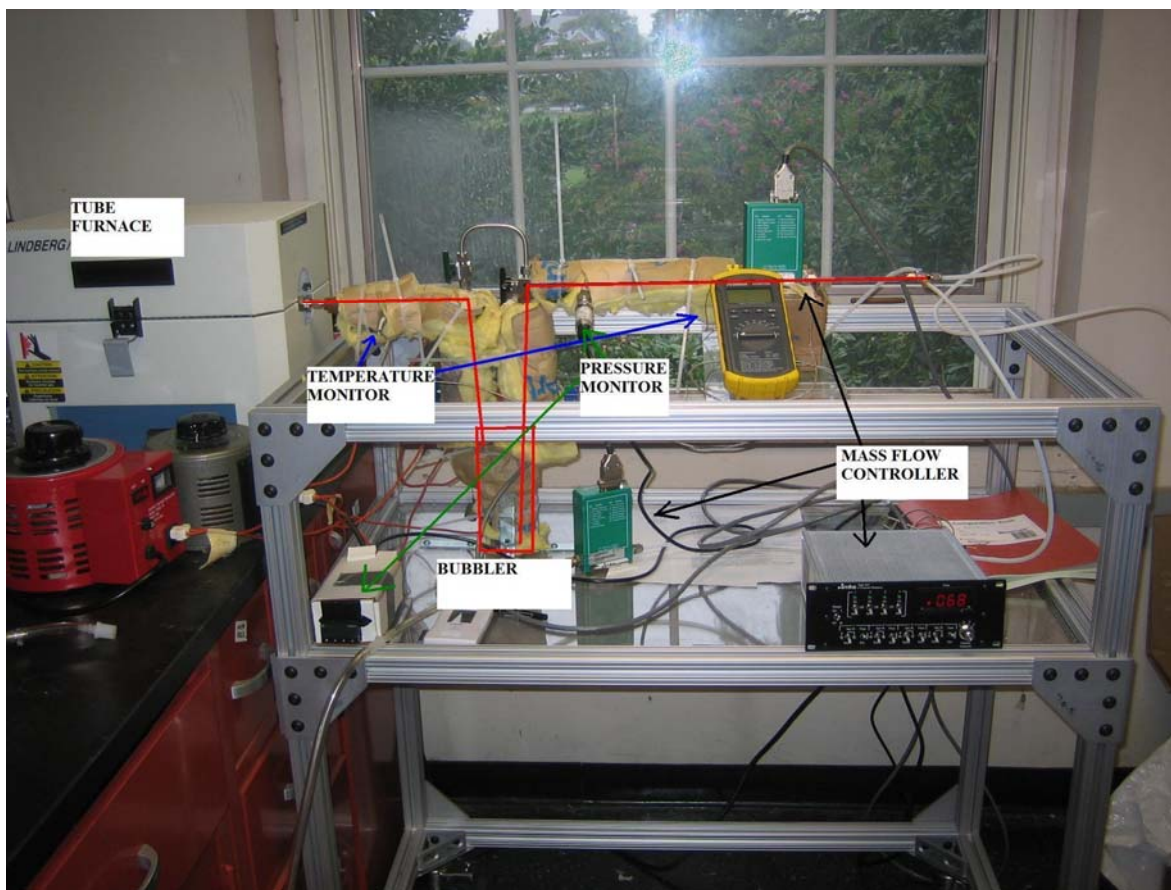
Below we provide an estimate of how much aluminum one could produce with our system. As previously mentioned we can control our production rates by varying the temperature of the bubbler and the argon flow rate. Normal operation of the bubbler is in the range of 40-70ºC, but we have the ability to run at higher temperatures. A table of TEA's vapor pressure, bubbler temperature and resultant theoretical production rate in grams per hour of aluminum is shown below.

| Temperature of Bubbler | Vapor Pressure of TEA | 1 Liter Per Minute | .5 Liter Per Minute |
|---|---|---|---|
| 30ºC | .0425 torr | 3.641E-3 g Al/hour | 1.821E-3 g Al/hour |
| 80ºC | 3.1 torr | 0.228 g Al/hour | 0.114 g Al/hour |
| 100ºC | 11.7 torr | 0.814 g Al/hour | 0.407 g Al/hour |

Particles generated are collected on 0.4 micron Millipore HDPE filter using a 47mm stainless steel Gelman/Pall filter housing. This provides an effective way to collect samples for analysis, but due to losses (through and around the filter) accurate experimental production rates can not currently be calculated this way.

Our first trials generated white particles with a furnace temperature of 300ºC, and flow rate of 1LPM. We believe at these settings our reactor is producing aluminum particles that are so small they are completely oxidized. When testing these white (same

color as aluminum oxide) particles in a flame, they proved to be a dead material (evidence of the complete oxidation of Al particles).          To deal with this problem we focused on making larger particles by increasing the residence time, and increasing the temperature to promote sintering. The first test, at 450ºC, yielded blackish-grey nanoparticles consistent with Al/Al$_2$O$_3$. These particles were then tested in a flame. They were observed to spark and burn, a sign of an energetic material. During one trial, we were collecting a sizable sample, the filter housing was opened (exposing contents to air) and the sample began to self combust.  This result is consistent with the production of nanoaluminum with minimal carbon contamination.

We have   recently completed collecting particle samples for various furnace temperatures, ranging from 450ºC to 900ºC in increments of 150ºC. At higher temperatures we should create larger particles, but risk carbon contamination. TEM analysis will be conducted to learn more about the particles structure (core-shell) and primary particle size.

Currently we are putting together a system to coat our aluminum particles with nickel. The system has just been assembled, a diagram of which is presented here:
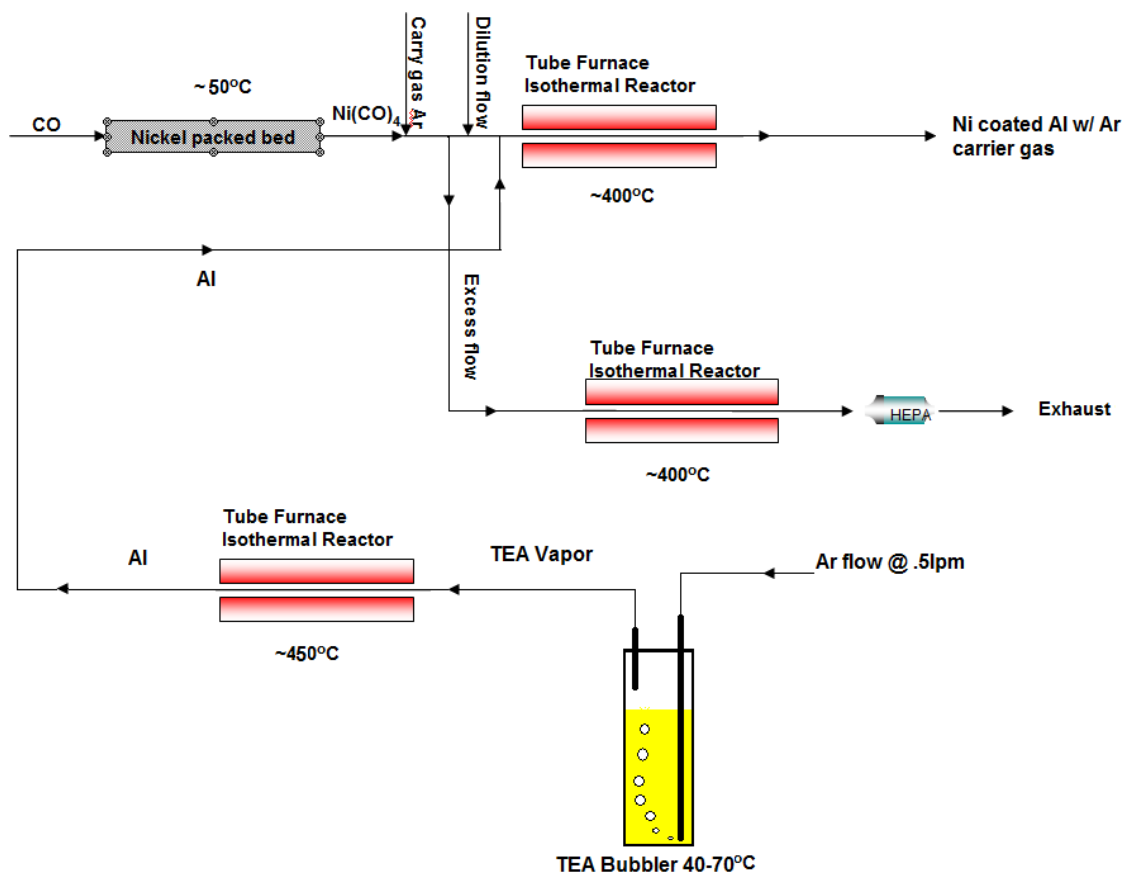


**Figure 1:**  *Schematic of nanoaluminum synthesis system and proposed Ni coating process.*

**Future work for coming year**:
1. Characterize by TEM, EDS and ion-mobility analysis the morphology, size and purity of nanoaluminum as a function of process parameters, ( temperauture, concentration, etc).

2. Explore surface treatment strategies including formation of a Ni coating and carbon based coatings.

3. Explore reactivity of these materials using pressure cell tests and TJMS.

**Part B: New Diagnostics: <u>TJMS: A New Mass Spectrometry Approach</u>**

The goal of this part of the project is to implement new diagnostic tools to augment our current capabilities for studying particle reactivity. In particular to develop what we term "T-Jump Mass spectrometry" (TJMS) to characterize thermite reactions.

*Our basic idea is to insert a fine platinum wire probe coated with the reactive material into the extraction region of the mass-spectrometer. This method will enable rapid, controlled heating of samples on a Pt ribbon filament at a rate up to 10E5K/s to a known temperature in the range of 200-1400K. The heated filament will result in reaction of the thermite mixture and the gaseous products will be analyzed.*

To capture the reaction process we employ a cross-beam electron gun for ionization. However, since this is a time-of-flight instrument we can gate and get spectra as a function of time by releasing the ions by pulsing the extraction and acceleration plates. In this way we can track in one experiment, the whole sequence of the chemistry as a function of time.
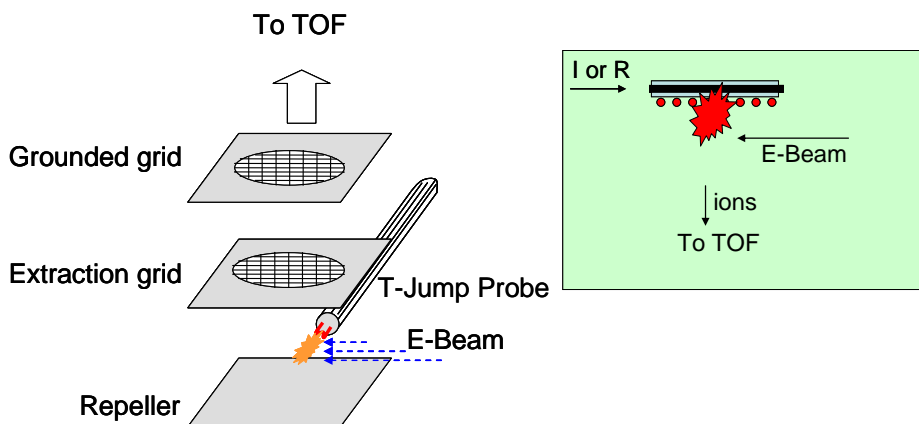


**Figure 2** *.Conceptual figure of T-Jump Mass Spectrometer.*

In parallel to the development of the mass-spectrometer instrument is the development of the T-Jump instrument itself. A by-product of the development is that during ignition the thermite coated wire will generate a strong optical signal, which can captured and analyzed as a parallel effort. As a result we have decided to build a separate optical system that can help characterize the operation of the T-jump, as well as provide an additional diagnostic tool. Below we describe the optical characterization system.

**Basic Concept**

A platinum wire is electrically heated to achieve ignition under rapid heating ($10^4$-$10^5$ Ks$^{-1}$) conditions. As ignition occurs, chemical energy is released and excited molecules emit light. Photomultipliers (PMT's) are used to identify the time of ignition (seen as sharp spikes in the PMT signal). The current (I) and voltage (V) of the wire is also monitored in real time to determine the resistance(R) of the wire. Resistance of a platinum wire is strongly correlated to the temperature by the Callendar-Van-Dusen equation discussed in details in the section on Temperature Calculation. Knowing the resistance at any instant would allow the temperature of the wire to be calculated.

**Sample preparation**

For instrument development purposes we use readily obtainable particles for preparation of a thermite mixture. An Al/CuO nanocomposite was prepared by mixing weighed amounts of ALEX and CuO in a solution of hexane. The weights of the fuel and oxidizers are varied to change the stoichiometry of the mixture. A small amount of the solution is taken in a dropper, and put on the wire in the presence of a small current through the wire, that serves to heat the wire and evaporate the hexane.

**Experimental setup**

A schematic of the experimental setup is shown below in Figure 3. The function of the pulse generator is to produce a square voltage pulse of adjustable height and width to vary the heating rate. The pulse is passed through a very thin platinum wire (diameter ~ 0.003 inch) and about 1-2 cm long coated with Al/CuO nanocomposite. Platinum is used because of its superior material properties, and chemical inertness at high temperature (~1500 C) and well known resistance-temperature correlation. A current probe was connected through a current amplifier (amplification = 500 when the oscilloscope is set at 10 mV/div) to the oscilloscope to monitor the current. With this system we can currently achieve heating rates of $10^4$-$10^5$ Ks$^{-1}$.

Light emission resulting from both black-body emission from the wire and thermite reaction is monitored with a photomultiplier tube (PMT). The square pulse, the current through the thin wire and the signal output from the photomultiplier tube is measured in real time using a 500 MHz oscilloscope. The wire is placed within a stainless steel cross so that the system can be evacuated, or an inert gas environment can be used.

The entire setup is mounted on a movable stage to facilitate imaging various parts of the wire. An aperture is used just before the PMT to enable the imaging of only the central portion of the T-jump wire.
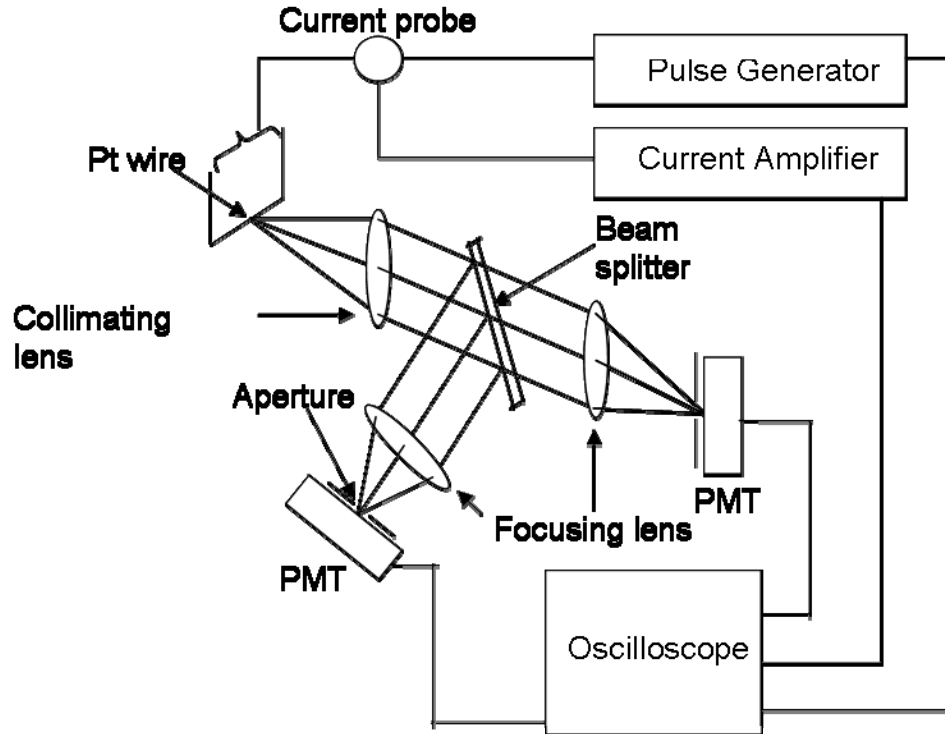
**Figure 3:** *Schematic of T-Jump optical system.*

A photographs of the system is shown in Figure 4.

**Calculation of Ignition Temperatue**

From the recorded voltage and current history, the resistance of the wire at any time is calculated. Resistance of a Pt. wire is very well correlated with temperature given by the Callendar-Van Dusen equation.

$$R(T) = R_0 [ 1 + \alpha T + \beta T^2]$$

where $R(T)$ : resistance of the wire at temperature T

$R_0$ : Resistance at 0 $^oC$ = $\rho L/\pi r^2$

$\rho$ : Resistivity at 0 $^oC$ = 1.06 x $10^{-7}$ ohm m.

L, r : Length and radius of the wire

$\alpha$ : 0.003908 $^oC^{-1}$

$\beta$ : - 5.78 x $10^{-7}$ $^oC^{-2}$

Knowing the resistance, the temperature can thus be back calculated at any given instant of time.
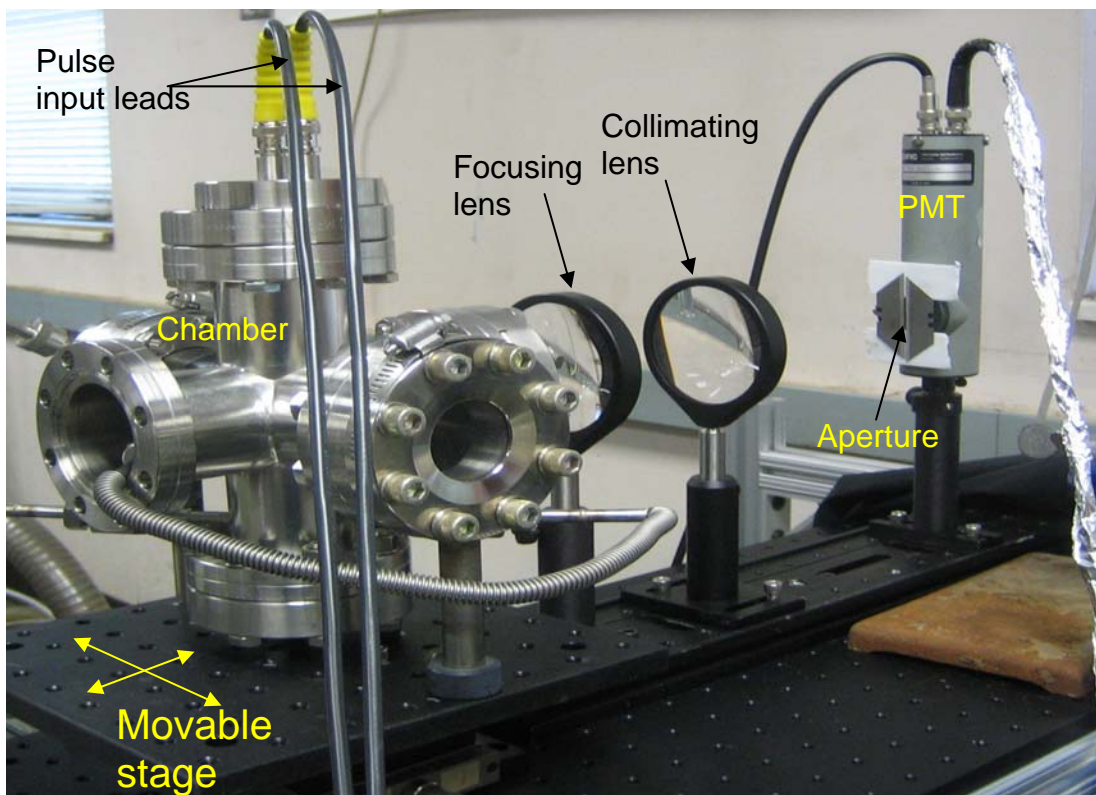
**Figure 4.** *Photograph of the T-Jump optical system.*

## Results

Al/CuO nanocomposites of 3 different stoichiometries are ignited using the T-jump system. Below we show SEM images of coated and reacted wires. The results show that the wire is indistinguishable after reaction indicating that reaction is primarily limited to the solid state.
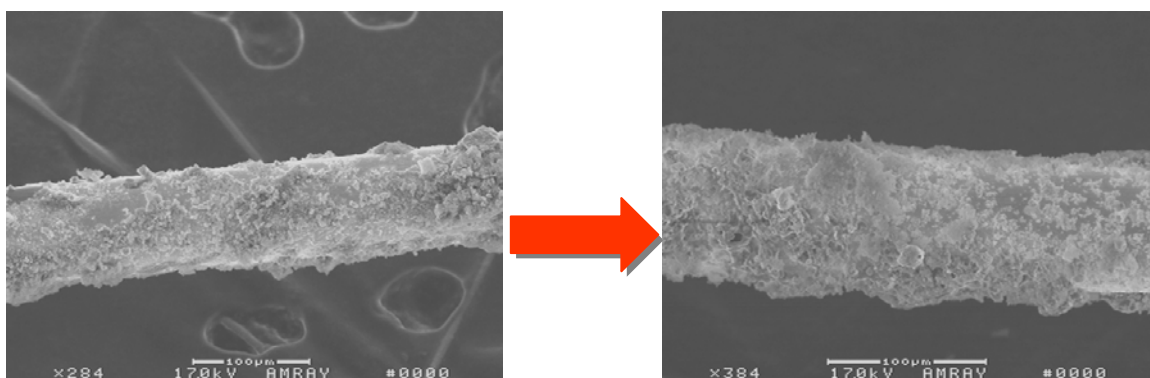


**Figure 5:** *SEM images of 0.001" diameter Pt wire coated with Al/CuO thermite. Before and after reaction.*

Heating the coated platinum wire causes an increase in resistance and a corresponding decrease in current. At high enough temperature, the wire starts to glow giving off light. To eliminate the effect of light emitted by the bare wire, the PMT signal with and without the coating is recorded, to remove the background from signal. Figures 6(a)-(d) shows the voltage pulse, the current, and the PMT signal with and without coating on the wire.
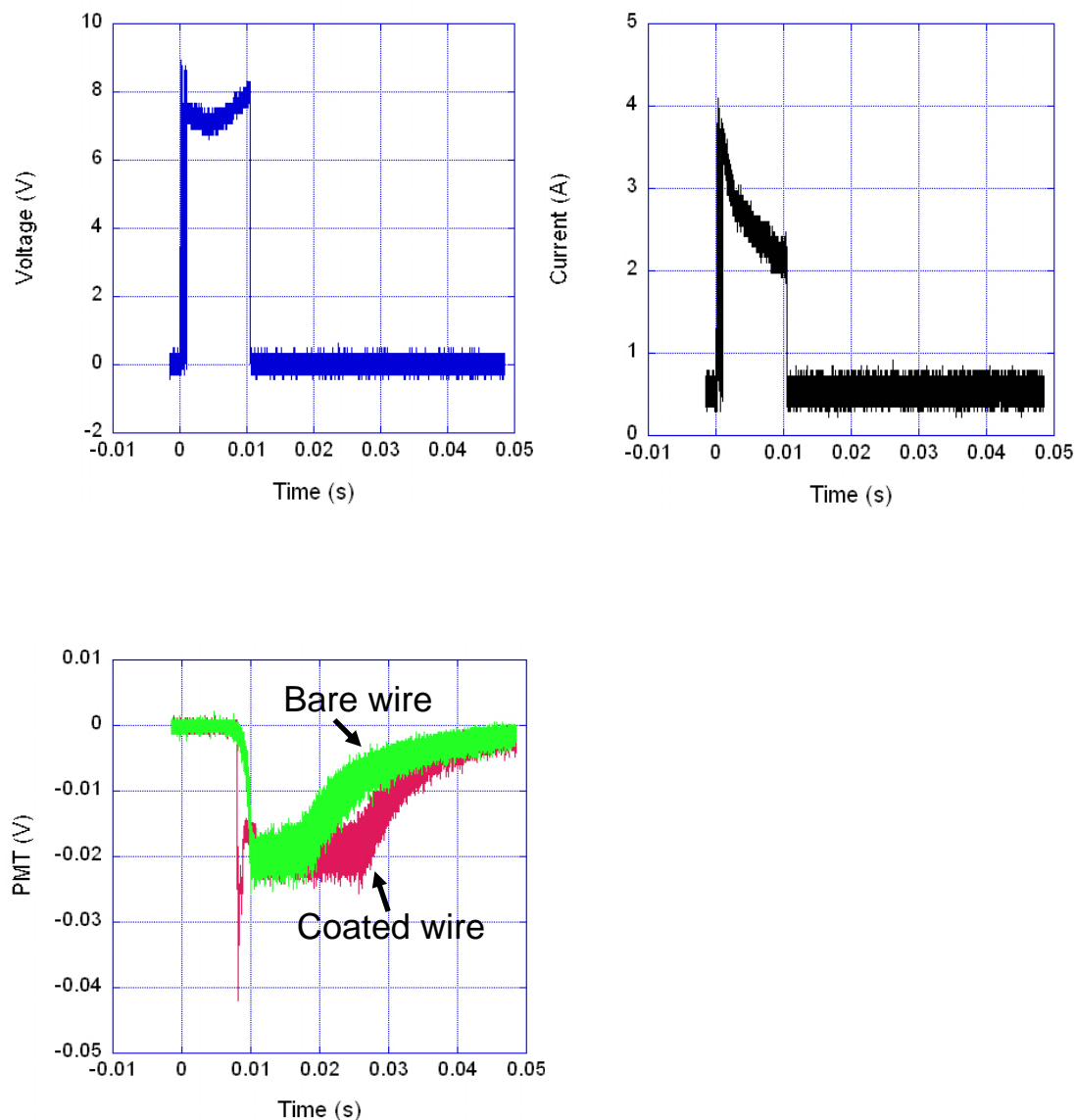


**Figure 6a-d:** *Temporal voltage, current, and PMT signal.*

The very sharp spike in the coated material corresponds to the thermite reaction. In Figure 7 we show an expanded view of the temporal emission signal from a rich mixture indicating that there is plenty of spectral structure in the emission signal . We have as yet not spectrally resolved the signal, but we are planning on doing so in the near future by

11

adding optical band pass filters.  If we look at the width of the optical signature corresponding to the thermite signal we can see that it is about ~ 1 ms wide indicating the width of the reaction time, at least as measured optically.
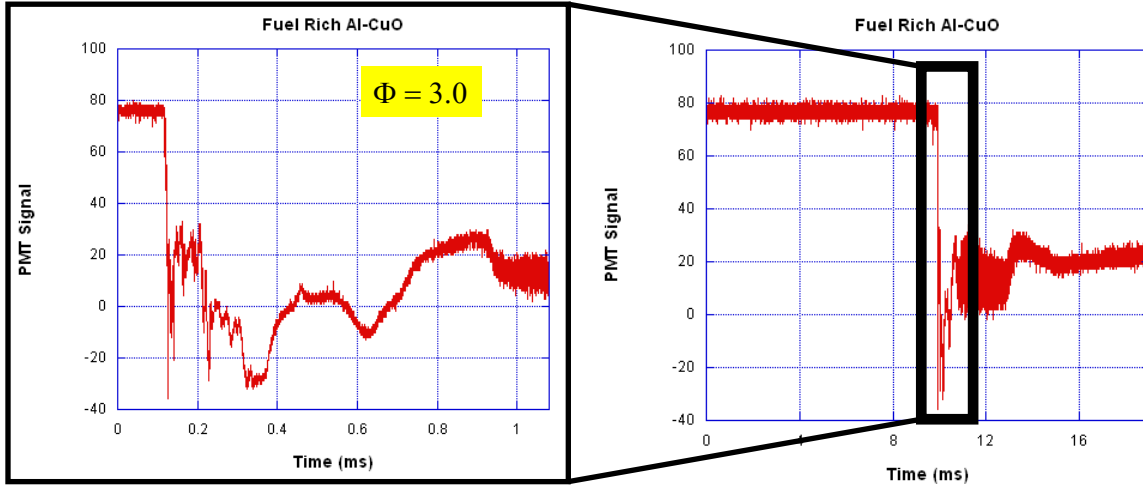


**Figure 7 :** *Expanded temporal view of thermite emission in T-Jump*

In principle these results should be correlated with temperature through the resistance measurement, however at this time we believe our resistance thermometry method is not accurate enough, and we have chosen not to present these results until we have that issue under control. We are currently implementing a pyrometry approach to calibrate the wire resistance measurement.  By conducting measurements at different mixture stoichiometry and by measuring the width of the optical emission we can make an estimate of reaction (Burn) time as a function of equivalence ratio. Such a plot is presented in Figure 8, which shows that as expected the reaction time is minimum at an equivalence ratio of unity. The results also show that reaction times can be shorter than 0.5 ms.
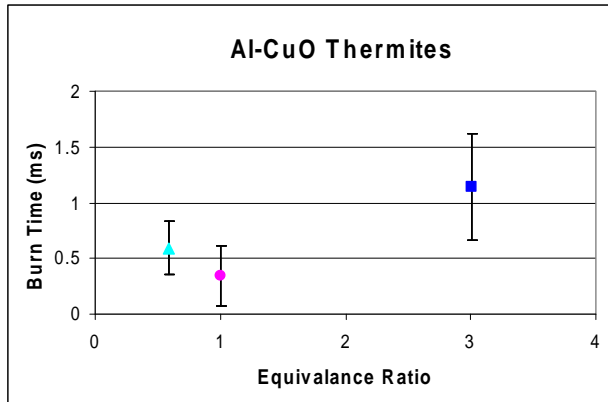


**Figure 8:** *Burn time vs. Equivalence ratio.*

As we have discussed the primary goal is to develop a T-Jump Mass spectrometer system. The T-Jump optical system experiments enabled us to understand how to operate the T-Jump so that it could be implemented within the mass-spectrometer environment. Our first task was to enable insertion of the wire system into a vacuum environment.

To aid in the efficient loading of the T-Jump system a feedthrough was developed that enables rapid insertion of the probe into the high vacuum system. and the input of power and the measurement of current.
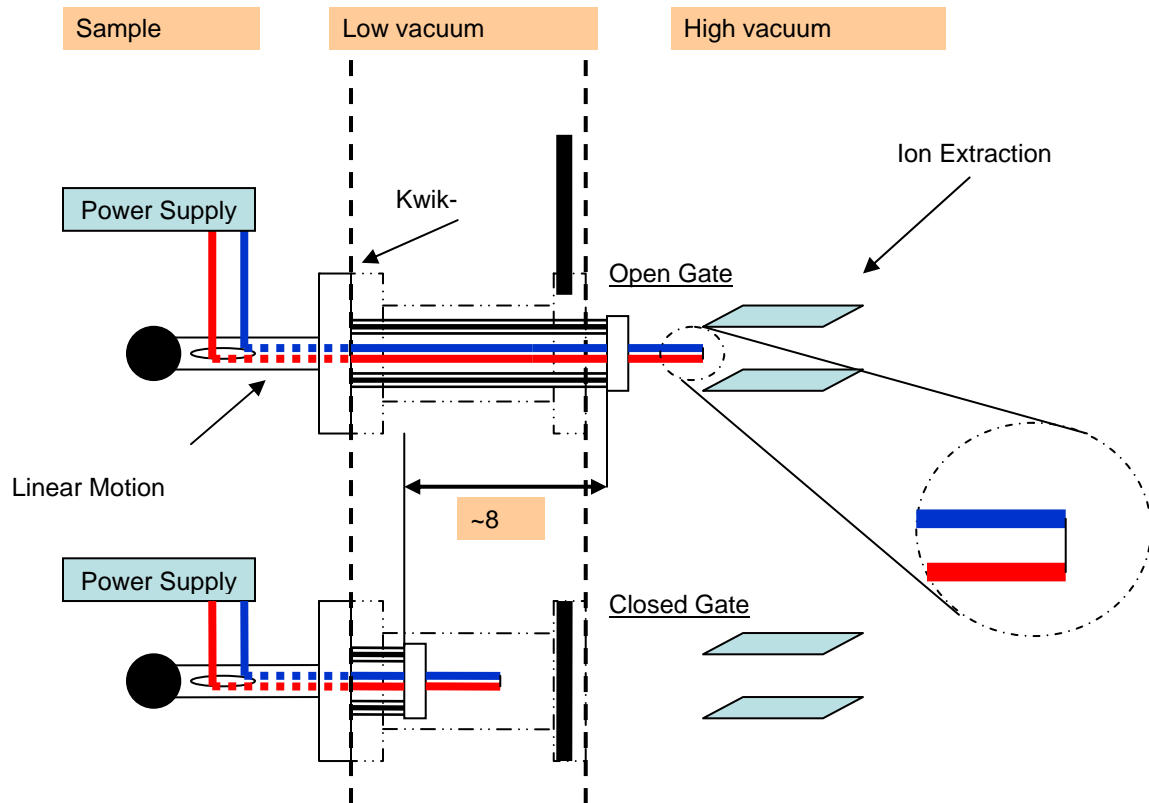


**Figure 9:** *T-Jump probe manipulator*

A photograph of the T-Jump mass spectrometer is shown in Figure 10 below.
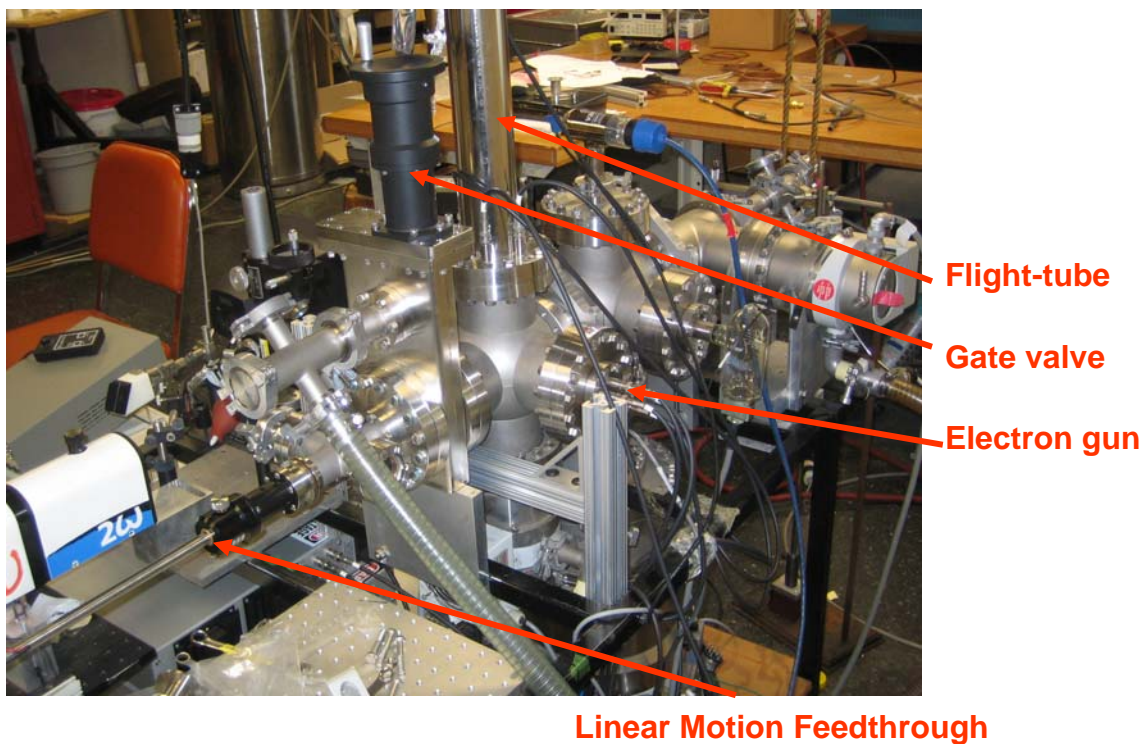
**Figure 10:** *Photograph of T-Jump Mass Spectrometer.*

Because of our desire to monitor the whole transient event of a thermite reaction we have developed a timing sequence that allows us to obtain repeated mass spectra.
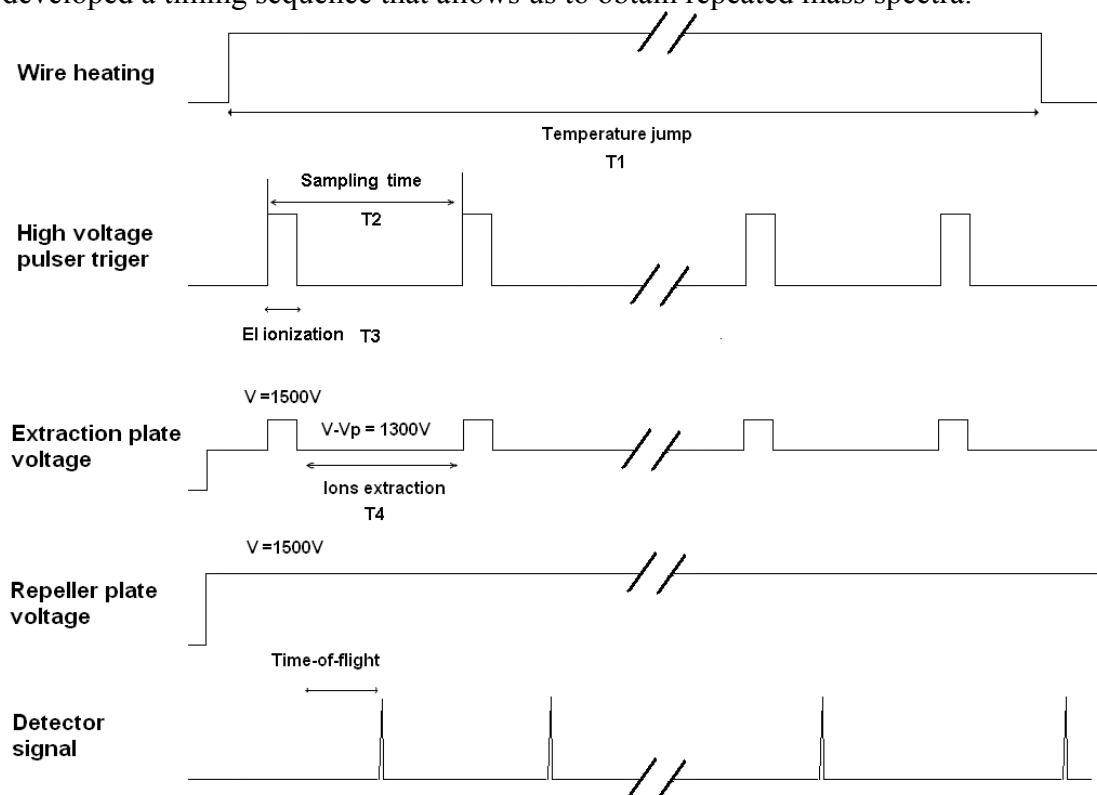
Some characteristics of the timing sequence are listed below:

- *Temperature Jump T1 ~15 ms (5 ms ~ 100 ms adjustable)*
- *Cycle Time T2 ~1 ms (down to 5 us)*
- *EI Ionization Time T3 ~5 us (50 ns to 12 us adjustable)*
- *Rise and Fall time ~10 ns*

In Figure 11, we show an example of a time series of spectra taken for the Al/CuO stoichiometric mixture.
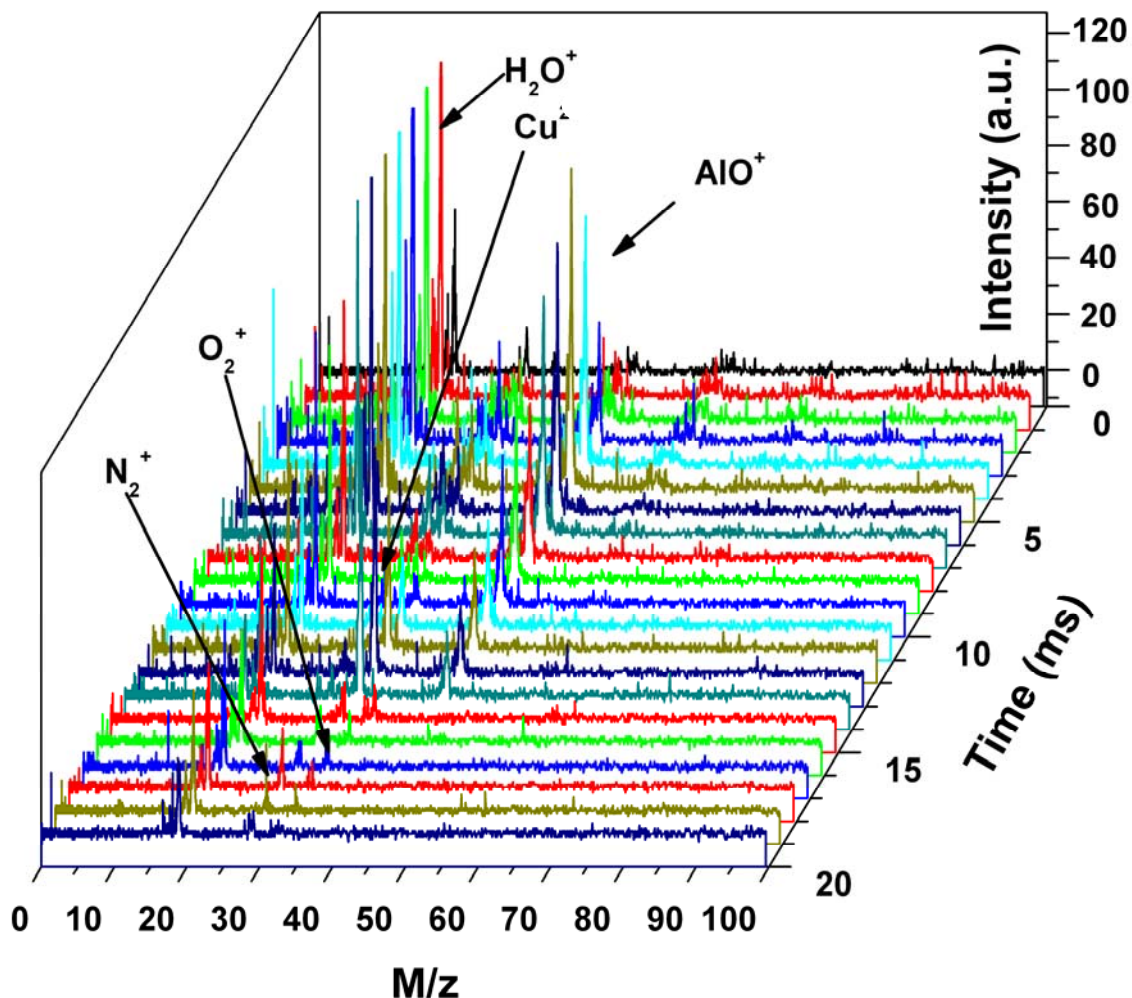


**Figure 11:** *Temporally resolved mass spectrum of thermite reaction.*

To the best of our knowledge this is the first time resolved mass spectrum of a thermite reaction. By plotting the peak heights of the major peaks we can track the time-evolution of species. In these figure we can see at T=0 when the wire is turned on with a heating rate of 80,000 K/sec that water signal saturates the detector. In addition, we observe the appearance of AlO, Cu and O atoms. Interestingly we see no elemental aluminum. We are in the process of analyzing these results.
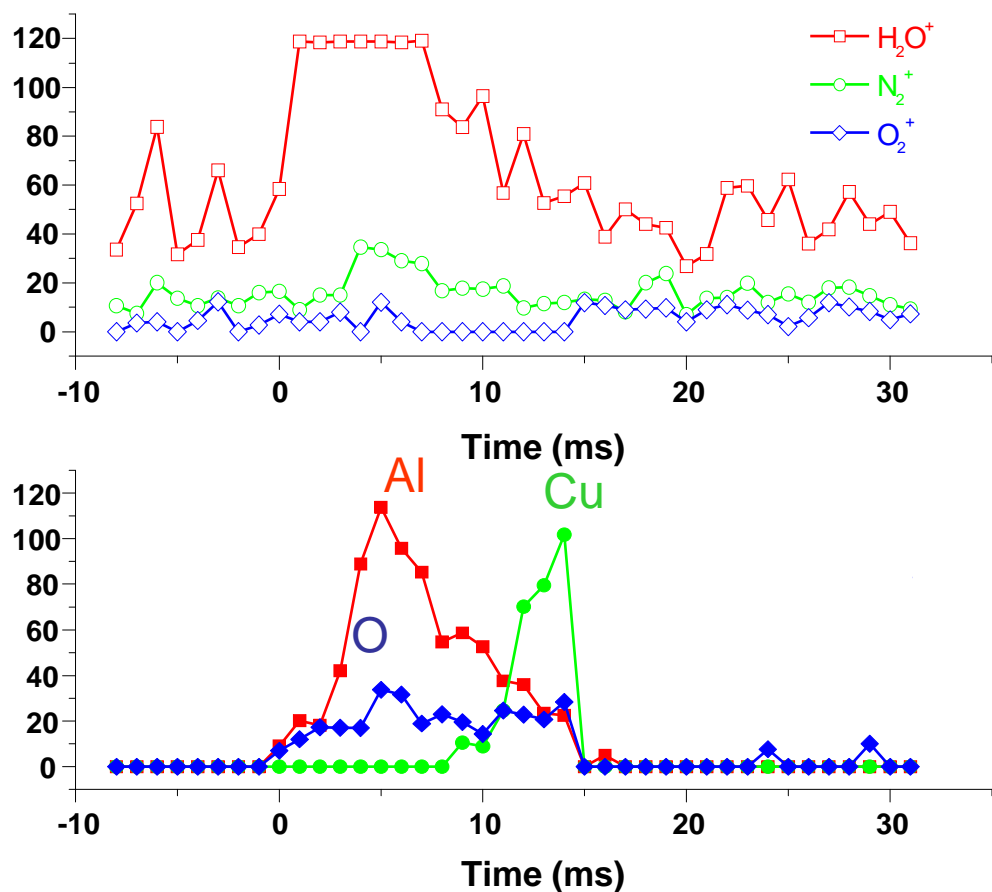
**Figure 12:** *Major species measured as a function of time during T-Jump*

One of the interesting points to note is that the mass-spec reaction time is considerable longer than the optical reaction times shown in Figure 8. In part this is expected since the optical signature is coming from excited state species with a shorted life time than ground state species. While the TJMS is probing all species independent of electronic state. This result is preliminary and will require significant further study.

**Future work for coming year:**

1. Characterize and calibrate temperature-time response of T-jump wire.
2. Development of systematic method to coat wires.
3. Characterize optical signal with thermite mixtures.
4. Characterize capabilities of T-Jump Mass-Spec system.
5. Study a series of thermite systems.

16

**OBJECTIVE:**
The basic objective of this program is to explore new architectures for energetic materials, and to use novel diagnostic tools that probe the underlying nature of reactivity of this class of materials.

The specific objective of this program are two fold. **A.** Development of novel architectures for reactive metals. **B.** Characterization of nanoparticle reactivity, and development of scaling laws from novel measurements of reactivity using a new concept in mass spectrometry ( T-Jump Mass Spectrometry; TJMS).

**PART A: New materials for creating a more intimate fuel/oxidizer**
The greater the proximity between the fuel and oxidizer the greater should be the expected energy release rate. Our objective is to develop new architectures to enhance proximity between fuel and oxidizer using aerosol processing.
2. Develop an aerosol based process for the formation of passivated aluminum nanoparticles with primary focus on the coating with polymers and other metals.

**PART B: New Diagnostics**
As part of this work we will also develop new approaches to study thermite type reactions. Most import of these is a new type of mass spectrometry (TJMS) being develop in our laboratory, which will enable the study of fast solid-state reactions. One of the unique features of this work will be the ability to create samples which have an extremely narrow particle size distribution through on-the-fly gas-phase electrophoretic separation of particles.

The combination of new architectures, with the new TJMS characterization will afford the opportunity to explore new types of structures that may point the direction on how best to assemble fuel/and oxidizers at the nanoscale to optimize energy release. The new diagnostic approach presents an opportunity to develop a tool to study from a microscopic point of view, reactions between solids. In the latter case the new tool should be of utility to a wide variety of problems in energetic materials well beyond those of thermite chemistry.

iii. **Status of Effort**

This year we have spend considerable time improving the T-Jump system. In particular at the beginning of the year we were able to demonstrate the abilty to obtain highly time resolved mass spectra or organic based energetic systems ( RDX, Nitrocellulose, etc). However we were unable to obtain spectra from nanothermites. We discovered that this was due to the large electrical current generated by the reaction which disrupted the electric fields in the instrument. Once we realized the problem we were able to make several design changes in the manner in which ions were extracted from the reaction which enabled us to obtain spectra. *As a result this year we have demonstrated the first instrument to obtain a time resolved mass spectrum of a thermite reaction.* With this new capability we have been able to obtain ignition temperature of thermites as a function of mixture composition and correlate them to species observed in the mass spectrometer. The instrument gives the most direct measure of the reaction time.

iv. **Accomplishments**
1. Completed construction of T-Jump Mass Spectrometer with real-time thermometry
2. Studied organic energetic materials including RDX, NC, and " high nitrogen compounds"
3. Demonstrated for the first time ever the time resolved mass spectrum of a thermite event.

v. **Personnel Supported**

Faculty: M.R. Zachariah
Graduate students:  D. Pines ( part time), S. Chowdhury, Zhou Lei ( part time)
Undergraduate: A. Peters ( part time)

vi. **Publications**

**a.** L. Zhou; N.Piekiel; M. R. Zachariah,, T-Jump Mass Spectrometry to probe Heterogeneous Combustion JANAFF  Propulsion Conference, March **2008**.

b. L. Zhou; N.Piekiel; S. Chowdhury; M. R. Zachariah, " *T-Jump/Time-of-Flight Mass Spectrometry for Time Resolved Analysis of Energetic Materials*" Rapid Comm. Mass. Spectrometry  **2008** in press.

**vii. Interactions**

    a. Paper presented at Army sponsored Nanoenergetics Workshop, Rutgers University, February 28, 2008

    b. Paper presented at JANNAF meeting in March 2008

    c. DARPA workshop at Microthermal Initiator and Nanoenergetics Device Workshop, Beltsville, MD, May 22 2008

    d. Discussion leader at Gordon Conference on Energetic Materials, June 2008

    e. Paper presented at Workshop on Energetic Materials, Univ. Southern California, July 28, 2008

# DETAILED DESCRIPTION OF T-Jump/Time-of-Flight Mass Spectrometry

**INTRODUCTION**

Here we report on a new Time-of-Flight mass spectrometer (TOFMS) electron ionization (EI) source that can obtain time resolved mass-spectra during the ignition of energetic materials. The unique feature of this apparatus is a) implementation of TOFMS/EI with a Temperature Jump (T-Jump) technique to monitor highly reactive condensed state-samples at high heating and decomposition rates, and 2) measurement of the chemistry in a bi-molecular gas-phase-free kinetic environment. Due to its low detection limits and fast time response, the instrument developed here allows for a time resolved characterization of the decomposition, ignition, and combustion of solid energetic materials

Quantitative measurement of the condensed phase reaction kinetics are usually performed using conventional thermal analysis techniques[1] such as TGA (Thermogravimetric Analysis) and DSC (Differential Scanning Calorimetry). However, those methods fail in the measurement of fast chemistry processes such as rapid thermal decomposition, ignition and combustion of energetic materials where high heating rates are involved. It is well established that the high heating rates in those processes are critical and must be attained in order to study rapid condensed phase reactions.[2-4] In recent years, many experimental diagnostic methods have been developed to characterize rapid reaction processes.[1, 5-12] In particular, T-Jump (Temperature Jump)/FTIR (Fourier Transform Infrared Spectroscopy) was developed for studying reaction kinetics of condensed-phase propellants.[2, 13] In the T-Jump/FTIR the sample is placed on a Pt filament and rapidly heated to a chosen temperature and the gaseous species are detected and quantified using FTIR spectroscopy. The thermal decomposition behavior of numerous energetic materials under isothermal conditions have been studied using this technique.[14-16] However, for rapid condensed phase reactions especially those associated with an ignition event, the relevant time scale can be on the order of milliseconds or less. The nominally low IR spectra scanning rate greatly limits the application of the T-Jump/FTIR spectroscopy in characterizing ignition, and combustion.

Mass Spectrometry (MS) is widely used to study condensed phase reactions.[11, 17] For decades, the use of MS alone or in conjunction with other techniques has become a powerful tool for thermal analysis.[9, 18-23] Blais and co-workers developed a TOFMS/EI apparatus capable of measuring the intermediates and products of chemical reactions from detonation of explosives.[9, 24] The decomposition of thermite based aluminum/iron (III) oxide energetic material was also studied using the Matrix-Assisted Laser Desorption/Ionization (MALDI)-TOFMS technique, and the products of laser initiated thermite reactions were identified.[25, 26] Time resolved measurements for condensed phase reactions have also been conducted using MS techniques. Dauerman and co-workers developed a scanning sector mass spectrometer which directly attaches to a low pressure strand burner to study the thermal decomposition and combustion of nitrocellulose.[8, 21] The sample is heated by exposure to the radiation of an arc image furnace and the gaseous species as well as the surface temperature are continuously analyzed by a mass spectrometer and thermocouple as a function of time. Behrens developed a thermogravimetric modulated beam mass spectrometer that combine thermogravimetric

analysis, differential thermal analysis, and modulated beam mass spectroscopy. This instrument is capable of quantitative measurement, and has been used to study thermal decomposition mechanisms and kinetics of many compounds.[27-29]Korobeinichev and co-workers developed a pulse heated mass spectrometer to studied the high temperature decomposition of ammonium perchlorate.[30]

Common to all these methods has been that the studies were conducted at either slow heating rate, e.g. the thermal decomposition took place in minutes, or the mass spectrometer sampling rates were slow, e.g. ~ 0.1 sec. Recently, confined thermolysis FTIR spectroscopy with a TOFMS system has allowed for the gaseous products from a high pressure thermolysis chamber.[31] Although the time resolution of the mass spectra measurement can be ~ 1 ms, the system time respond is limited by the slow sampling rate of the FTIR probe.

Despite the many efforts directed to characterizing condensed phase reactions, time resolved characterization of very rapid condensed phase reactions, particularly those associated with ignition and combustion have proved to be a formidable task. These processes, where the heating rates are usually of the order of $10^3 \sim 10^6$ K/s, are beyond the limit of current thermal analysis techniques.[7, 32]

One additional consideration is that for many of the MS and FTIR studies, experiments were conducted in an open tube condition, such that much of the chemistry occurred in the gas-phase. However to gain a mechanistic understanding one would like to separate the condensed vs. gas phase contribution. Thus, in order to understand the decomposition mechanism or the combustion process of energetic materials, it is necessary to separate the primary and secondary processes, and investigate the condensed phase reaction under the condition of rapid heating.

Our objective in developing the T-Jump-MS system was first be able to characterize chemistry under high heating rate conditions ( i.e. fast chemistry), and second to conduct the experiments under conditions where the secondary gas phase chemistry can be minimized. In the former case high heating rates correspond more closely to the environment usually encountered by energetic materials but more profoundly one should expect reaction channels to increasing favor the higher activation channels possessing the lowest entropy constraints. The later emphasis of minimizing gas-phase chemistry eliminates the possibility of bi-molecular gas phase reaction and likely much unimolecular decomposition. As a result the rapid pyrolysis of energetic materials in vacuum should be dominated by condensed phase reactions, which should ultimately allow for a more direct probe of condensed phase chemistry. The essence of the experiment is that the T-Jump probe is directly inserted into the Electron Ionization chamber of the mass spectrometer, and the species from T-Jump excitation are monitored by the TOF mass spectrometer continuously. The time-resolved mass spectrometric capabilities of the instrument enable the characterization of rapid solid state reactions, which should provide an insightful complement to conventional thermal analysis. The purpose of this initial paper is to describe the operation and capabilities of this new instrument.

**EXPERIMENTAL SECTION**

**a. EI/TOF Mass Spectrometer.**

The EI/TOF mass spectrometer is comprised of a linear Time-of-Flight chamber, adapted from a previously developed Single Particle Mass Spectrometer (SPMS)[11, 33] and includes an electron gun for ionization, and the T-Jump probe with an electrical feedthrough, as shown in figure 1. The sample loading chamber is separated from the ionization chamber by a gate valve, which enables the T-Jump probe to be rapidly changed without the need to break vacuum in the TOF chamber. An electron gun (R. M. Jordan Company, Grass Valley, CA, US) is mounted between the extraction plates of the TOF, and perpendicular to the orientation of the T-jump probe. The electron beam is nominally operated at 70 eV, and 1 mA, with the background pressure in the TOF chamber at ~$10^{-7}$ Torr.

**b. T-Jump Sample Probe.**

For the T-Jump we have primarily used a 76μm diameter platinum wire, with a total heated length of ~ 1 cm, which is replaced after each heating event. In each experiment, the wire is coated with a thin layer of either sample powder as in the case of particulates, or solution dipped to prepare organic coatings. Using an in-house built power source, the heating rate of the T-Jump probe can be varied by changing the pulse voltage or pulse width, at a rate of up to ~ 5 x$10^5$ K/s for the present filament configuration.

**c. Control and Data Acquisition System.** The schematic of the control and data acquisition system for the T-Jump/TOF mass spectrometer is shown in Figure 2. The present design is based on a previously developed Single Particle Mass Spectrometer (SPMS) which is configured for a standard laser ionization source.[11, 34] To ensure a field-free region for EI ionization, one DC high voltage power supply is used with a "T" splitter to bias both the repeller plate, and the extraction plate (V1 and V2 shown in figure 2). In the presence of a field-free region, electrons are injected between the plates and ionization takes place. After a predetermined ionization period the voltage on the extraction plate is changed by a high voltage pulser, to create the field for ion extraction region between the plates. The extracted ions drift in the linear TOF tube, and are counted at the MCP (Microchannel Plate) detector. Following the ion extraction period, the voltage on the extraction plate is pulsed back, and a new ionization period begins. Serial pulses generated from a pulse generator (DG535, Stanford Research System, Sunnyvale Inc, CA, USA) are used to trigger the high voltage pulser so that the ionization and extraction processes occur continuously. The pulse timing sequence of the high voltage pulse is also traced from the monitor signal output of the high voltage pulser. Both the detector signal and the monitor signal are recorded with a 500 MHZ digital oscilloscope and transferred to a PC for further analysis.

The heating of the T-Jump probe is also synchronized with the time-of-flight measurement system by triggering the probe power supply from the pulse generator as shown in the timing sequence diagram (There is ~2 μs delay between trigger and monitor signal, for illustration purpose we show them as the same pulse in figure 3). The temporal voltage and current of the T-Jump probe during the heating event is recorded, so that a

resistivity measurement can be obtained, and related to the instantaneous temperature, which can be mapped against the mass spectra.


**RESULT AND DISCUSSION**

Before testing the T-Jump/TOF mass spectrometer, T-Jump probe heating experiments were conducted by heating an un-coated wire to evaluate the performance of T-Jump probe. The heating rate of the probe can be varied by changing the heating pulse width and the output pulse intensity. The pulse width can be varied from ~1 ms to ~100 ms, with a maximum output voltage of ~50 V.  Figure 4 (a) shows a typical current, voltage trace, while figure 4 (b) shows the resulting temporal temperature of the platinum wire. Since the rise time of the heating pulse is in the range of 10 to ~100 us depending on the output pulse voltage, the resistance and the corresponding temperature is calculated after the rise time of the heating pulse. Thus the filament temperature is estimated to be ~400 K initially, and reaches ~1800 K after the 2.5 ms; i.e. a heating rate ~640,000 K/s.

Another important factor to consider in the design of the T-Jump/TOF mass spectrometer is the nature of the ion extraction in the presence of the T-jump probe.  The nominal configuration  of the ion extraction electrode assembly ensures a uniform extraction field between the plates[34].  However the presence of the probe and in particular its location was found experimentally to be a sensitive parameter to both signal sensitivity and resolution. One might reasonably expect that placing the probe too close to the extraction plates would distort the electric field, and result in a decrease in the mass spectrometer's resolution. Placing the probe too far away from the ionization region would lower the concentration of reaction product species in the ionization region, and consequently decrease the sensitivity of the measurement. The effect of the T-Jump probe position was examined experimentally by inserting the probe at different distances from the plates, and monitoring the ion signal from the background gas. The relative water ($H_2O$) ion intensity are plotted in figure 5 (a) as a function of probe position. Each experimental data point is an average of 40 mass spectrum measurements, and normalized by the ion intensity measured without the presence of the T-Jump probe. As a comparison to the experimental data, the effect of the T-Jump probe on the electric field and ion detection was also evaluated by conducting ion-trajectory simulations using Simion.[35] In the simulation, water ions with +1 charge were placed in the center plane of the ion extraction region with a uniform distribution, and their flight trajectories were calculated for the voltages used in the experiment. The relative ion abundance calculated from trajectory simulation is also plotted as the function of probe position in figure 5 (a). Both simulation and experimental data show that the ion signal is significantly decreased when the probe is placed close to the extraction plates. As the probe moves away from the plates, the ion signal increases, and reaches a plateau at a distance of 1.3 cm, suggesting that the presence of the grounded probe significantly perturbs the electric potential in the ion source region. Figure 5 (b) shows the calculated electric potential and ion trajectories for T-Jump probe placed 1.3 cm from the ionization region. When compared with the no-probe case in figure 5(c), it is clear that the probe induces considerable distortion to the electric potential, and ion trajectories in the region closest to the T-Jump probe, but very little change for ion trajectories in the central region. As

we further move the probe away from the ionization region, even though the effect of the probe on the electric field is minimized, a slight decrease of the ion signal in the experimental data was observed. This implies that at larger distances sensitivity will be lost for material originating from the probe, and that a distance 1.3 cm would seem to be a near optimal for this system.

Nitrocellulose and hexahydro-1,3,5-trinitro-1,3,5-triazine (RDX) samples were used to test the performance of the T-Jump/TOF mass spectrometer as examples of a slow and fast "burners". In these experiments, Nitrocellulose sample (Mallinckrodt Baker Inc. Phillipsburg, NJ, USA) or RDX was mixed with diethyl ether or acetone, and a small amount of solution (~0.07ml) is coated on the T-Jump filament surface using a dropper. While the eventual goal of this instrument is to use the temporal mass spectra, and temperature, to extract mechanistic information, the purpose of the present results is focus on illustrating the capabilities of the instrument.

The mass spectra obtained for rapid pyrolysis of nitrocellulose are shown in figure 6. The heating duration is about 9 ms with a heating rate of ~$1.3 \times 10^5$ K/s, with a total of 95 spectra sampled with a temporal resolution of 100 μs per spectrum (10000Hz). Out of the 95 spectra obtained in the experiment, we plot 17 of them in figure 6, along with a more, detailed view of a spectrum at t = 2.5 ms. Since the heating pulse is synchronized with the first EI duration, the mass spectrum at t = 0 ms is actually the background in the ion source region, which consists of water (m/z 18), $N_2$ (m/z 28), N (m/z 14), OH (m/z 17), $O_2$ (m/z 32), and H (m/z 1). We sampled up to m/z ~ 300 for each spectrum, but no heavy ions were observed, and major ions are only seen for m/z <100. At t =1.7 ms, the estimated temperature of the probe is ~575 K, and a new ion of m/z 31 appears which suggest the start of the reaction. At t = 1.8 ms which corresponds to a probe temperature ~590K, the ion signal intensity of m/z 31 increases along with ions at m/z of 15, 27, 29, 45 and 59. As the reaction time advances to t = 1.9 ms (T~ 600K), ion m/z 31 achieves its maximum intensity, and now ions at m/z 30 and 46 appear, along with m/z 16, 43, and 44. These species last for the whole duration of the heating pulse (~9ms), and some species are still present well after the end of the wire heating due to the self-burning of nitrocellulose. The time-resolved feature of the spectra allows us to extract the characteristic time of the reaction. As the highest ion intensity for most of major ions were achieved at t = 2.3 ms, following which the ion signals gradually decreases with no noticeable changes after 4 ms, it is suggested that the most aggressive reaction (ignition) happens within ~4 ms, and the whole reaction lasts ~9 ms. We compare our results for nitrocellulose thermal decomposition with experiments done at lower heating rates. Chen et al used a SMATCH (Simultaneous MAss and Temperature Change)/FTIR system to examine decomposition products of a nitrocellulose film heated at a rate of up to 320° C/s. The reaction products are noted as, NO, CO, $CH_2O$, $CO_2$, HCOOH, and $NO_2$.[36] which we also see, although we are unable to distinguish HCOOH from $NO_2$. It should also be noted that although m/z 28 is part of our background signal of $N_2$, there is significant increase for this peak during the heating event, which most like can be attributed to CO. We also compare work with that of Dauerman and co-workers who used a mass spectrometer paired with a low-pressure strand burner to examine nitrocellulose combustion.[21] This work shows multiple spectra at different times during heating, which include significant ions that are consistent with our work. The major ions cited are m/z of 14, 15, 16, 17, 18, 27, 28, 29, 30, 31, 43, 44, 45, 46, which are all seen in our

experiment excepting m/z 14, 17, 18. We are currently continuing our studies in developing a mechanism and its comparison with theoretical work by Melius which suggests possible condensed-phase initial reaction steps in nitrate ester decomposition.[37] The reaction pathway shows consistencies to our findings, and will be more fully addressed in a subsequent publication.

   RDX was used as a second example to test the T-Jump/TOF mass spectrometer. RDX decomposition has been the subject of investigation under different conditions. Behrens and co-workers have studied RDX decomposition using the simultaneous thermogravimetric modulated beam mass spectrometry (STMBMS).[27, 38, 39] The results via STMBMS provide detail information about both mechanisms and rates of reaction of RDX decomposition under low heating rate (~1K/min).   The combustion like decomposition of RDX  has been studied using a T-jump/FTIR method[2-4, 13, 16, 40] with a heating rate at ~$10^3$K/s.  In our experiments, a heating rate of ~$10^5$ K/s was used to study the ignition and combustion of RDX. Similar to the nitrocellulose experiment, we use a sampling rate of 100 μs per spectrum (10,000Hz) to capture the progression of the reaction. The heating pulse is about 8 ms at a heating rate of ~$1.5\times10^5$ K/s, and a total of 95 spectra obtained. Figure 7 shows that species, other than background species (water/$N_2$/$O_2$), only appear from 0.7 ms - 2.6 ms, which corresponds to a wire temperature of 370K to 670K.  These results clearly show as expected that RDX is more reactive than Nitrocellulose, and occurs over an interval of only ~2 ms.   Although a m/z range up to 400 was recorded for each spectrum, no heavy ions were observed above m/z 150. The major ions from RDX decomposition observed are m/z 15, 28, 29, 30, 42, 46, 56, 75 and 127. Small ions of m/z 14, 16, 41, 43, 81, 120 are also found in some spectra. The RDX mass spectra in terms of m/z values observed and their most likely ions structures are tabulated in table 1. Similar to the T-jump/FTIR method,[2-4, 13, 16, 40] species of $NO_2$, $CH_2O$, NO, CO, HNCO are also observed by our T-jump/TOF mass spectrometer. Using gas phase $CO_2$ laser photolysis of RDX, which provided extremely high heating rates,  Zhao et al. observed ions at  42, 56, 75, 81, 120 and 127, which we also see in our experiments[41].   However, HONO, HCN and $N_2O$ which are reported in both T-jump/FTIR and gas-phase infrared multiphoton dissociation experiments were not detected under our conditions. The differences point to the complex nature that heating rate and ambient environment may play in probing the decomposition pathways. For example, it is believed that two global reactions are responsible for the decomposition of RDX under flash heating condition.[13, 40] The reaction channel which leads to the formation of $N_2O$ is dominant at lower temperatures, while the reaction channel to $NO_2$ favors the higher temperatures.  Our heating rate is much higher than the heating rate employed in T-jump/FTIR experiments (~$10^5$ K/s vs. ~$10^3$K/s) it is possible that the chemistry is dominated by the $NO_2$ channel and $N_2O$ is not favored under these conditions. Moreover, as one of the motivations in developing this T-jump mass spectrometer, was to minimize or eliminate the gas phase chemistry, the failure to detect species such as HCN and HONO and possibly N2O  suggests these may be  formed primarily  in the gas phase.


   Since the purpose of this paper is to demonstrate of the operation and capabilities of the instrument, we defer further analysis on rates of reactions and mechanisms to the future. Based on the experimental results presented above, it is clear that the characteristic

reaction time for energetic materials decomposition/combustion is in the order of milliseconds or even less. We note that while a time resolution of 100μs was used to test and demonstrate the instrument, the T-Jump/TOF mass spectrometer can be operated with a scanning rate up to ~ 30kHz. The experimental results suggest that the time-resolved spectra obtained using T-jump/TOF mass spectrometer shoud have sufficient sensitivity, and time resolution to probe the reaction dynamics of extremely fast condensed state reactions at high heating rates.

**CONCLUSION**

A new Time-of-Flight mass spectrometer (TOFMS) combined with a temperature jump technique is described. The instrument allows for the time resolved characterization of the decomposition, ignition, and combustion of solid energetic materials or other highly reactive condensed state reactions. Using heating rates of up to $10^5$ K/sec, samples of nitrocellulose and RDX were ignited, and time resolved mass spectra were obtained. By monitoring the electrical characteristics of the heated wire, the temperature could also be obtained and correlated to the mass-spectra. When combined with the time dependent temperature information, the results indicate that the instrument can capture the signature of rapid condensed phase reactions in a time resolved manner.

**REFERENCES**

(1)     Vyazovkin S. *Analytical Chemistry* **2006**; *78*: 3875.
(2)     Brill TB, Brush PJ, James KJ, Shepherd JE, Pfeiffer KJ. *Applied Spectroscopy* **1992**; *46*: 900.
(3)     Brill TB, Arisawa H, Brush PJ, Gongwer PE, Williams GK. *J. Phys. Chem.* **1995**; *99*: 1384.
(4)     Thynell ST, Gongwer PE, Brill TB. *Journal of Propulsion and Power* **1996**; *12*: 933.
(5)     Furutani H, Fukumura H, Masuhara H, Kambara S, Kitaguchi T, Tsukada H, Ozawa T. *J. Phys. Chem. B* **1998**; *102*: 3395.
(6)     Roberts TA, Burton RL, Krier H. *Combustion and Flame* **1993**; *92*: 125.
(7)     Ward TS, Trunov MA, Schoenitz M, Dreizin EL. *International Journal of Heat and Mass Transfer* **2006**; *49*: 4943.
(8)     Dauerman L, Salser GE, Tajima YA. *Aiaa Journal* **1967**; *5*: 1501.
(9)     Blais NC, Fry HA, Greiner NR. *Review of Scientific Instruments* **1993**; *64*: 174.
(10)    Makashir PS, Mahajan RR, Agrawal JP. *Journal of Thermal Analysis* **1995**; *45*: 501.
(11)    Mahadevan R, Lee D, Sakurai H, Zachariah MR. *J. Phys. Chem. A* **2002**; *106*: 11083.
(12)   Trunov MA, Schoenitz M, Dreizin EL. *Propellants Explosives Pyrotechnics* **2005**; *30*: 36.
(13)    Kim ES, Lee HS, Mallery CF, Thynell ST. *Combustion and Flame* **1997**; *110*: 239.
(14)    Brill TB, Gongwer PE. *Propellants Explosives Pyrotechnics* **1997**; *22*: 38.
(15)    Brill TB, Ramanathan H. *Combustion and Flame* **2000**; *122*: 165.

(16) Hiyoshi RI, Brill TB. *Propellants Explosives Pyrotechnics* **2002**; *27*: 23.
(17) Morelli JJ. *Journal of Analytical and Applied Pyrolysis* **1990**; *18*: 1.
(18) Park K, Lee D, Rai A, Mukherjee D, Zachariah MR. *J. Phys. Chem. B* **2005**; *109*: 7290.
(19) Yang M, Ramsey JM, Kim BJ. *Rapid Communications in Mass Spectrometry* **1996**; *10*: 311.
(20) Jones DEG, Turcotte R, Acheson B, Kwok QSM, Vachon M. *International Annual Conference of ICT* **2003**; *34th*: 46/1.
(21) Dauerman L, Tajima YA. *Aiaa Journal* **1968**; *6*: 1468.
(22) Farber M, Srivastava RD. *Combustion and Flame* **1978**; *31*: 309.
(23) Fowler AHK, Munro HS. *Polymer Degradation and Stability* **1985**; *13*: 21.
(24) Blais NC, Engelke R, Sheffield SA. *J. Phys. Chem. A* **1997**; *101*: 8285.
(25) Mileham ML, Kramer MP, Stiegman AE. *J. Phys. Chem. C* **2007**; *111*: 16883.
(26) Stiegman AE, Mileham ML, Kramer MP. *Abstracts of Papers, 233rd ACS National Meeting, Chicago, IL, United States, March 25-29, 2007* **2007**: INOR.
(27) Maharrey S, Behrens R. *J. Phys. Chem. A* **2005**; *109*: 11236.
(28) Minier L, Behrens R, Bulusu, S. *Journal of Mass Spectrometry* **1996**; *31*: 25.
(29) Behrens R. *Review of Scientific Instruments* **1987**; *58*: 451.
(30) Korobein Op, Boldyrev VV, Karpenko YY. *Combustion Explosion and Shock Waves* **1968**; *4*: 19.
(31) Chowdhury A, Thynell ST. *Thermochimica Acta* **2006**; *443*: 159.
(32) Umbrajkar SM, Schoenitz M, Dreizin EL. *Thermochimica Acta* **2006**; *451*: 34.
(33) Lee D, Park K, Zachariah MR. *Aerosol Science and Technology* **2005**; *39*: 162.
(34) Wiley WC, McLaren IH. *Review of Scientific Instruments* **1955**; *26*: 1150.
(35) Dahl DA*, V.8.0 ed.; Scientific Instrument Services, Inc. www.simion.com: Ringoes, NJ.
(36) Chen JK, Brill TB. *Combustion and Flame* **1991**; *85*: 479.
(37) Melias CF, Piqueras MC. *Proceedings of the Combustion Institute* **2002**; *29*: 2863.
(38) Behrens R, Bulusu S. *J. Phys. Chem.* **1992**; *96*: 8891.
(39) Behrens R, Bulusu S. *J. Phys. Chem.* **1992**; *96*: 8877.
(40) Brill TB, Brush PJ, Kinloch SA, Gray P. *Philosophical Transactions of the Royal Society of London Series a-Mathematical Physical and Engineering Sciences* **1992**; *339*: 377.
(41) Zhao X, Hintsa JE, Lee YT. *The Journal of Chemical Physics* **1988**; *88*: 801.

**Table 1.** ions observed from mass spectra of RDX pyrolysis and their possible assignments.

| m/z | Species |
|---|---|
| 14 | N[#] |
| 15* | $CH_3$, NH |
| 16 | O |
| 17 | OH[#] |
| 18* | $H_2O$ [#] |
| 28* | $N_2$[#], $CH_2N$, CO |
| 29* | HCO |
| 30* | NO, $CH_2O$ |
| 32 | $O_2$[#] |
| 41 | $CHN_2$ |
| 42* | $C_2H_4N$, $CH_2N_2$, CNO |
| 43 | HCNO |
| 46* | $NO_2$ |
| 56* | $C_2H_4N_2$ |
| 75* | $CH_3N_2O_2$ |
| 81 | $C_3H_3N_3$ (1,3,5-triazine) |
| 120 | $CH_2N_3O_4$ |
| 127* | $C_3H_3N_4O_2$ |

(*) major ions

([#]) species also observed in background MS
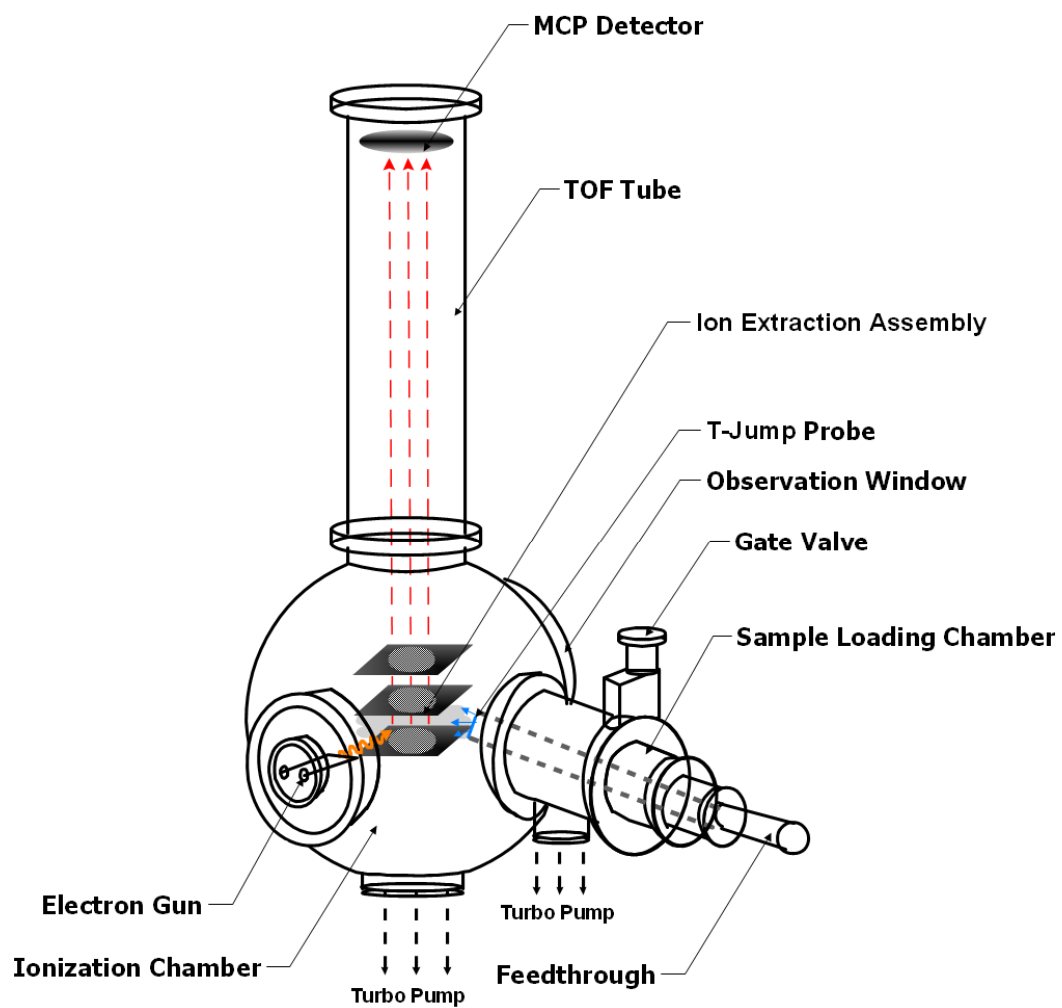
**Figure 1.** Schematic of T-Jump/TOF mass spectrometer.
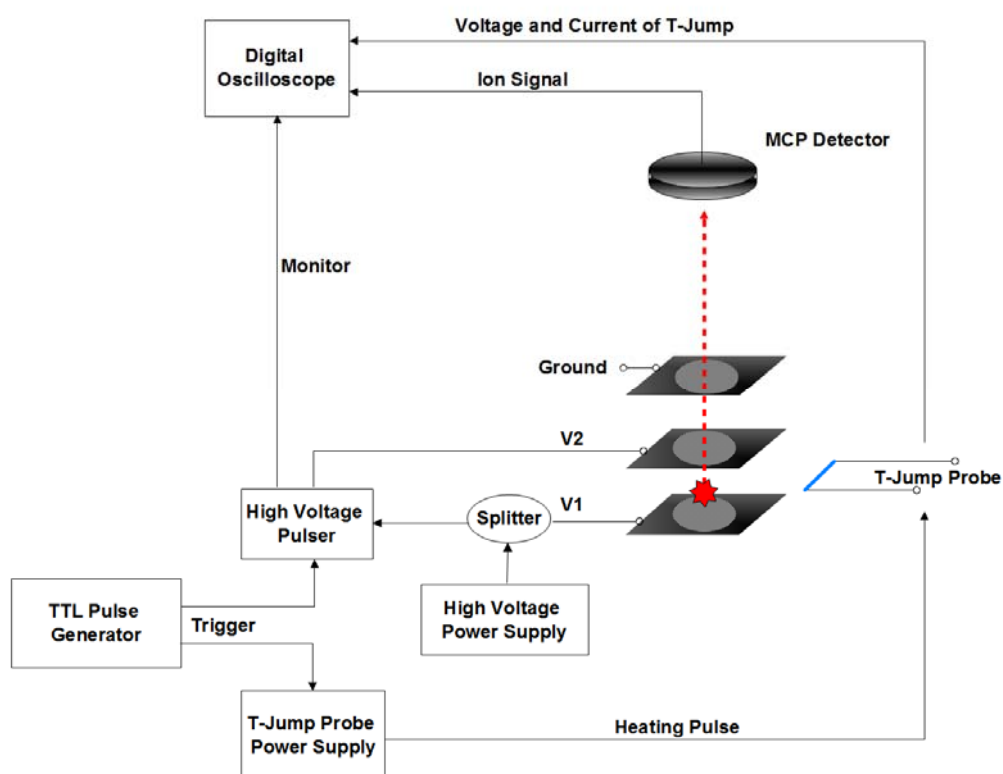
**Figure 2.** Schematic of the control and data acquisition system for the T-Jump/TOF mass spectrometer.
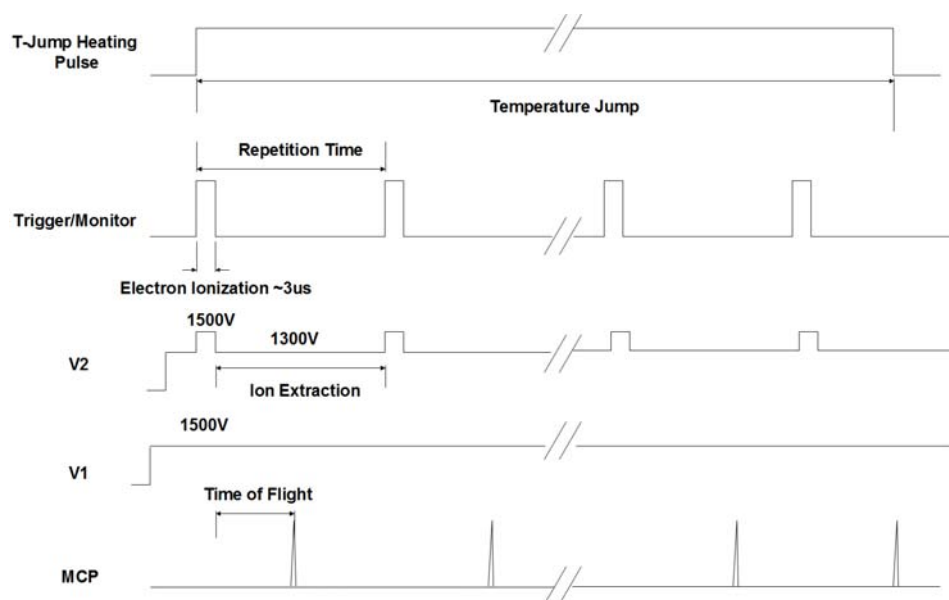
**Figure 3.** Pulse sequence used for EI ionization and ion extraction in the T-jump/TOF mass spectrometer.
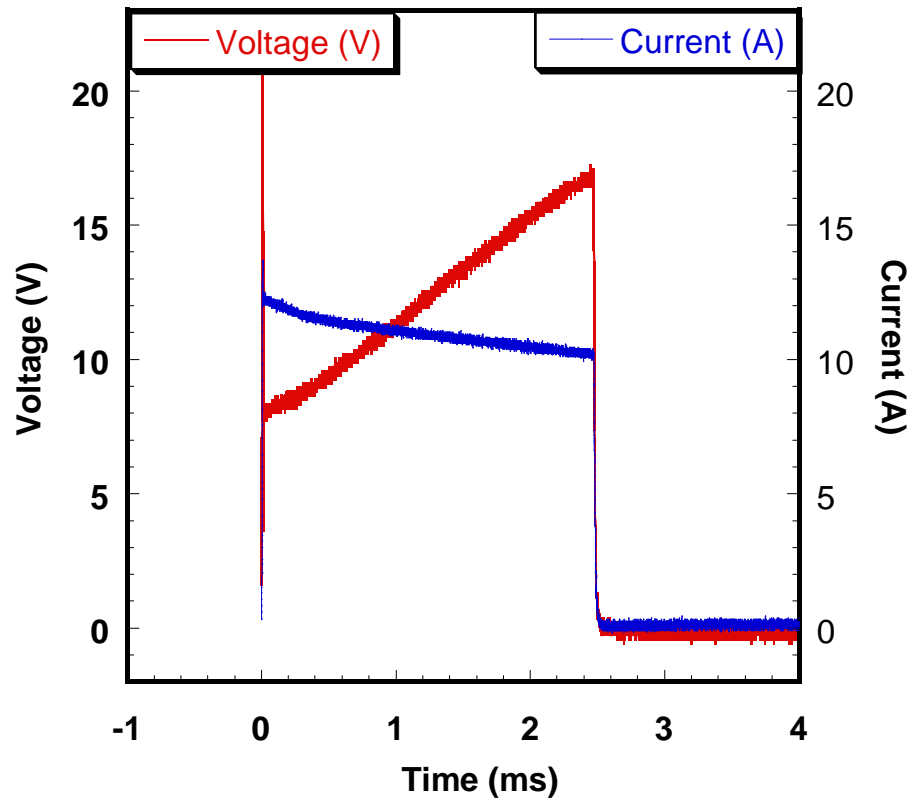
**Figure 4 (a).** Voltage and current across the T-Jump probe.
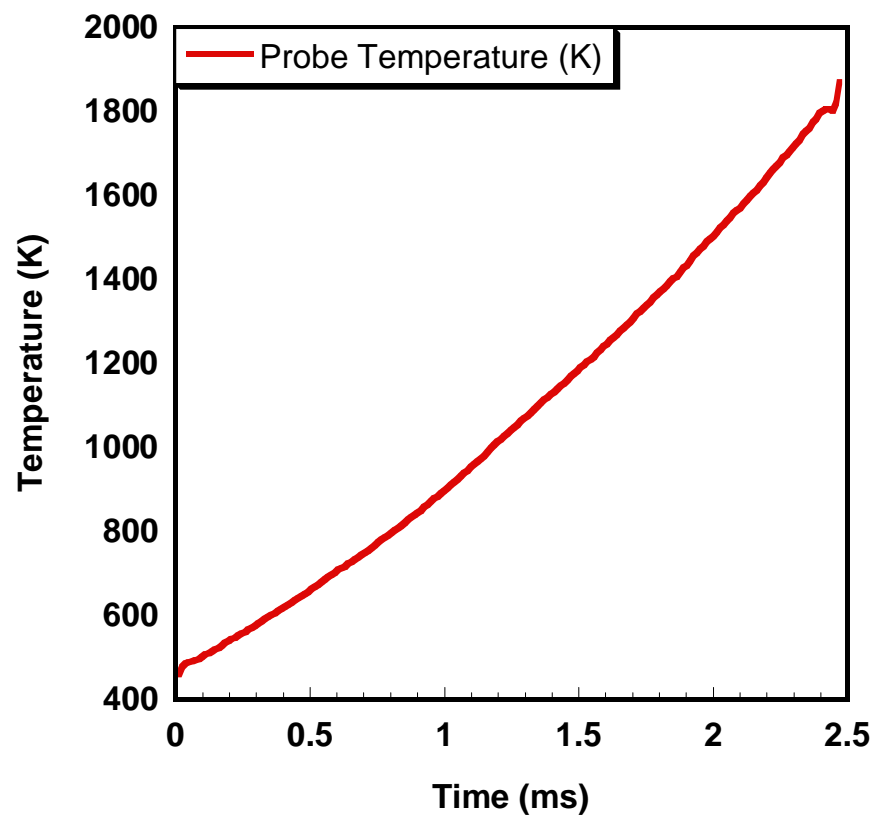
**Figure 4 (b).** Estimated probe temperature from electrical resistance
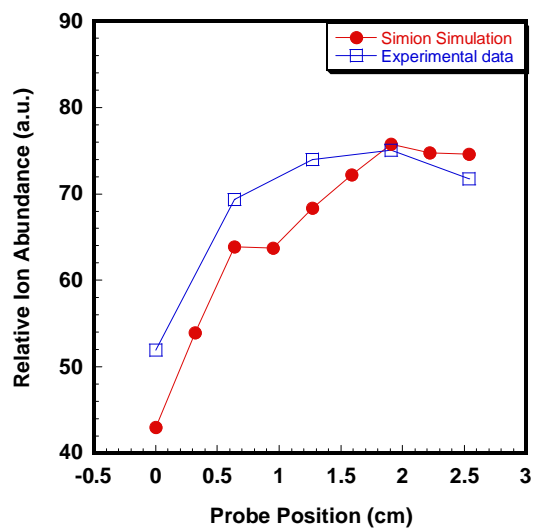


Figure 5 (a)
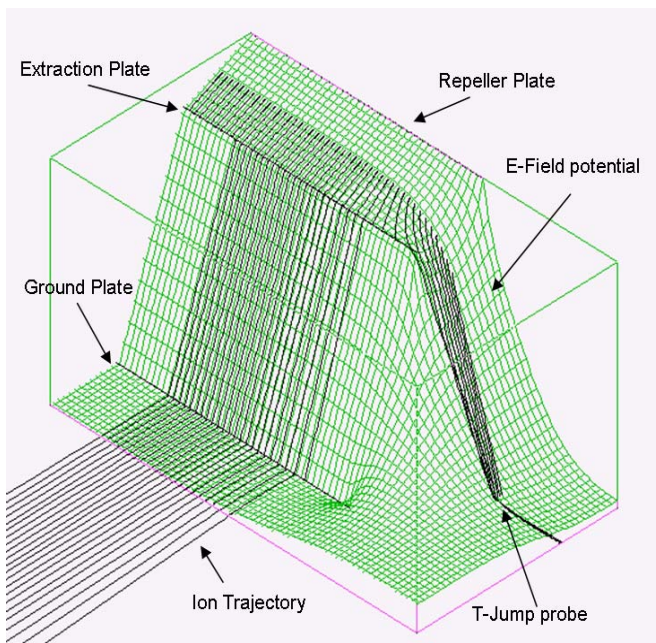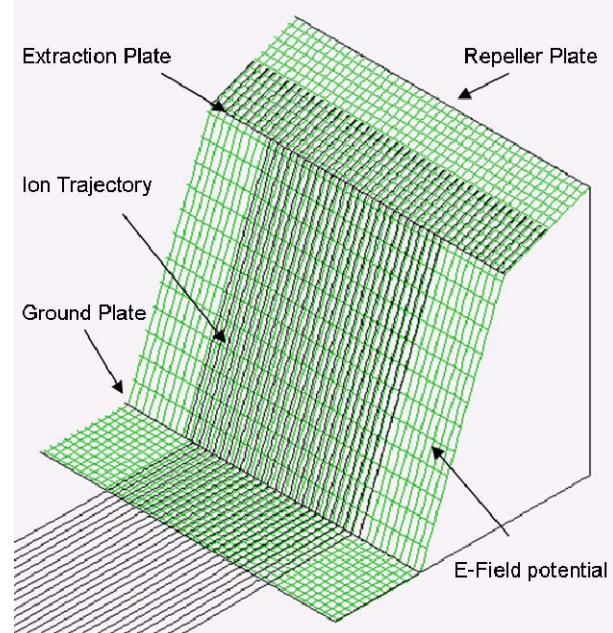
Figure 5 (b)                                    Figure 5 (c)

**Figure 5 (a).** Relative water ion abundance as a function of the probe filament position.

**(b).** Ion trajectory and electric potential at ion source region with the presence of T-Jump

probe. **(c)** Ion trajectory and electric potential calculation at ion source region without

probe.
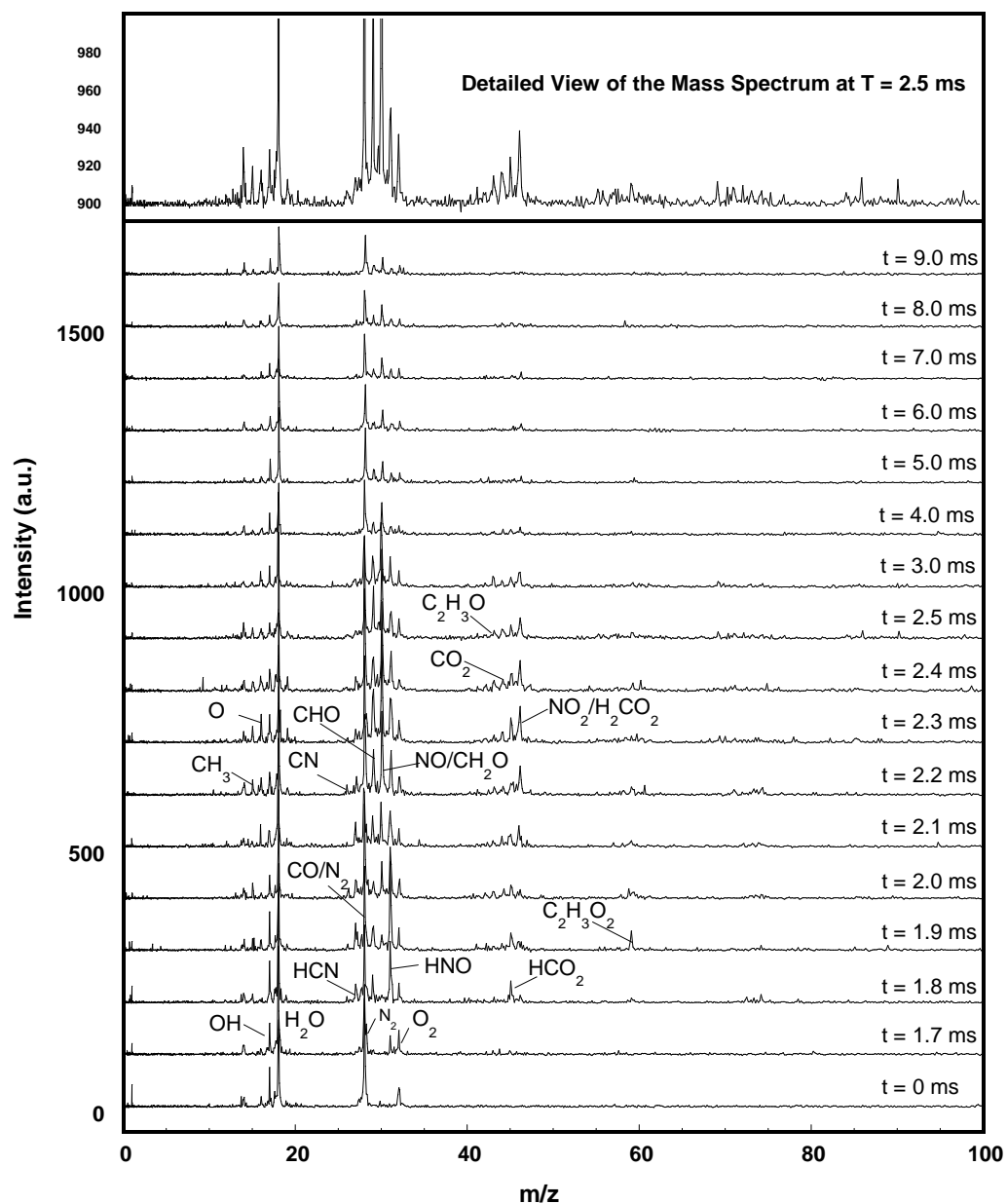
**Figure 6.** Time resolved mass spectrum from rapid heating of nitrocellulose. Heating rate

~ $1.3 \times 10^5$ K/s
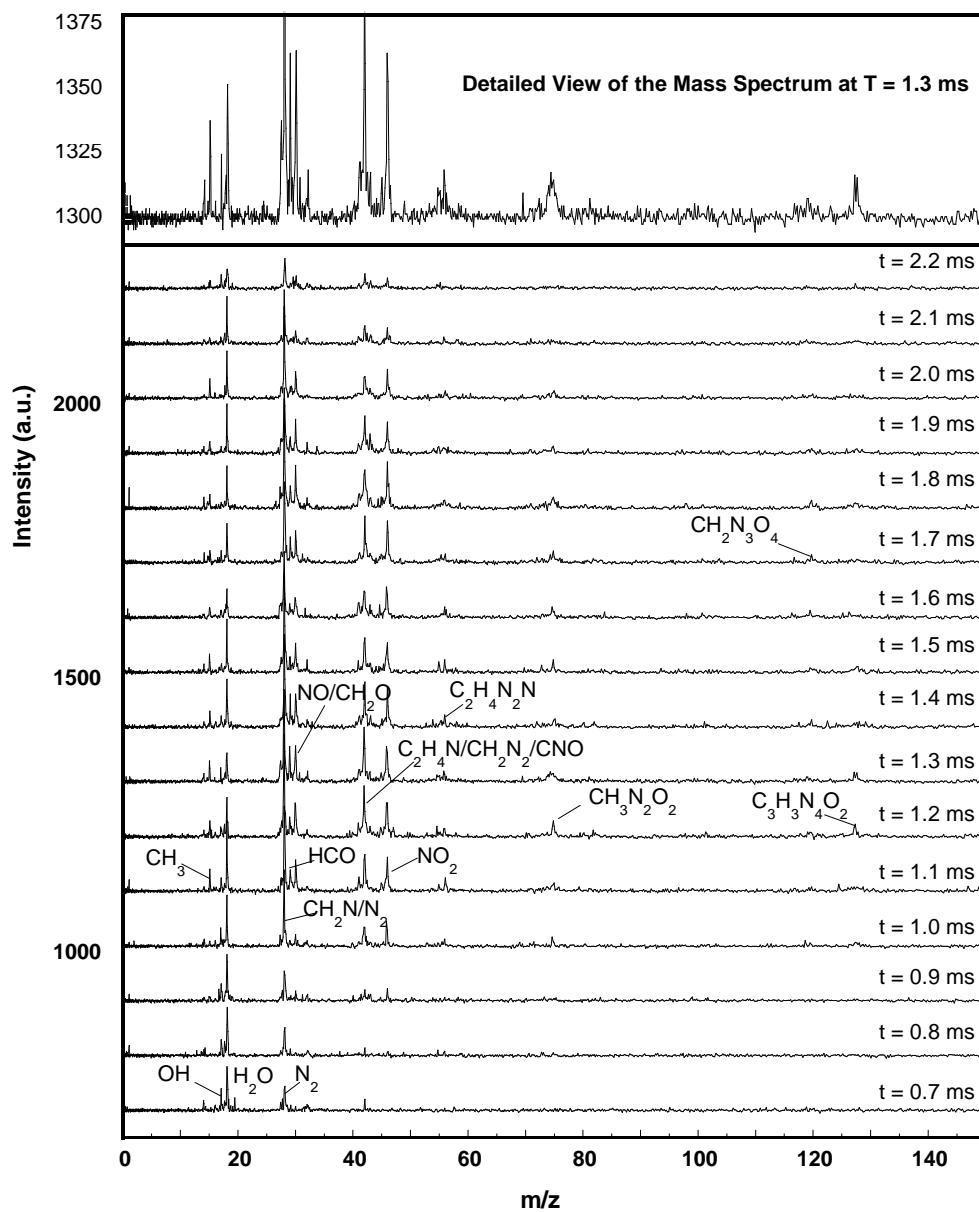
**Figure 7.** Time resolved mass spectrum from rapid heating of RDX. Heating rate ~1.5 $\times 10^5$ K/s

YEAR 3 iii. **Status of Effort**

This year we employing our T-Jump system to study a variety of thermite and high nitrogen energetic systems. We have also demonstrated the formation of single crystals of nanoaluminum.

## iv. Accomplishments
4. Studies the O2 evolution from a variety of metal oxides and correlated this results to thermite reactivity.
5. Conducted a variety of thermite reaction characterizations and determined likely reaction mechanisms.
6. Discovered that thermite ignition is accompanied with a strong current pulse, and determined the likely source.
7. Showed that ignition of aluminum based nanothermites is likely not a melt dispersion mechanism but rather a diffusion mechanism based on ignition delay data.

## v. Personnel Supported

Faculty: M.R. Zachariah
Graduate students: D. Klapawitz ( part time), S. Chowdhury, Zhou Lei ( part time)

## vi. Publications

**a.** L. Zhou; N.Piekiel; M. R. Zachariah,, T-Jump Mass Spectrometry to probe Heterogeneous Combustion JANAFF Propulsion Conference, March **2008**.

b. L. Zhou; N.Piekiel; S. Chowdhury; M. R. Zachariah, " *T-Jump/Time-of-Flight Mass Spectrometry for Time Resolved Analysis of Energetic Materials"* Rapid Comm. Mass. Spectrometry 23, 194, **2009**

c. L. Zhou, N. Piekiel, S. Chowdhury, D. Lee and M. R. Zachariah
*"Transient ion ejection during nanocomposite thermite reactions"*
Journal of Applied Physics in press

d. B. Henz, T. Hawa, and M.R. Zachariah
*"On the Role of Built-in Electric Fields on the Ignition of Oxide Coated NanoAluminum: Ion mobility versus Fickian Diffusion."*
Journal of Applied Physics in press

e.  S. Chowdhury, N. Piekiel and M.R. Zachariah
    *"Diffusive vs. Explosive Reaction at the Nanoscale"*
    *Journal of Physical Chem. C submitted.*

## vii. Interactions

f.  Presented invited paper at the E-MRS meeting in Strasbourg, Fr;  June 8 2009
g.  Two papers presented at the National Combustion Institute Conference , Ann Arbor, MI. May 18, 2009
h.  Collaborated with Dr. Curtis Johnson from China Lake on energetic biocide measurements.
i.  Collaborated with Greg Young, NSWC-IH on Alane Decomposition
j.  Collaborated with Jason Jouet , NSWC-IH on formation of Aluminum nanocrystals.

DETAILED DESCRIPTION

**On the Role of Built-in Electric Fields on the Ignition of Oxide Coated
NanoAluminum: ion mobility versus Fickian Diffusion.**

**Abstract**

Using the classical molecular dynamics method we simulate the mechanochemical
behavior of small (i.e. core diameter < 10nm) oxide coated aluminum nanoparticles.
Aluminum nanoparticles with core diameters of approximately 5nm and 8nm are
simulated with 1nm and 2nm thick oxide coatings or shells. In addition to thickness the
shells are parameterized by varying degrees of crystallinity, density, and atomic ratios in
order to study their affect on the ignition of nanoparticle oxidation. The oxide shells are
parameterized to consider oxide coatings with the defects that commonly occur during
the formation of an oxide layer and for comparison with a defect free crystalline oxide
shell. Computed results include the diffusion coefficients of aluminum cations for each
shell configuration and over a range of temperatures. The observed results are discussed
and compared with the ignition mechanisms reported in the literature. From this effort we
have found that the oxidation ignition mechanism for nanometer sized oxide coated
aluminum particles is the result of an enhanced transport due to a built-in electric field
induced by the oxide shell. This is in contrast to the currently assumed pressure driven
diffusion process. This induced electric field accounts for approximately 90% of the mass
flux of aluminum ions through the oxide shell. The computed electric fields show good
agreement with published theoretical and experimental results.

**Introduction**

Much of the interest in nanoparticles is derived from an appreciation that
chemical/physical properties often vary from that of the bulk material. Some of these
properties, including increased reactivity [1], can simply be attributed to the high surface
area to volume ratio of nanoparticles, however it is known that catalytic activity can be
significantly changed from that of the corresponding bulk [2,3]. It is also well known that
metal nanoparticles are pyrophoric and have enhanced energy release rates, which make
them attractive in propulsion [4].

Virtually all metal nanoparticles will nominally have a native oxide shell, which
for aluminum is ~2-3 nm thick. Thus any oxidative reaction or vigorous combustion must
proceed by transport of either the aluminum or oxidizer though the oxide shell. The
ignition temperature of oxide coated aluminum nanoparticles has been observed to
decrease with particle size, with a minimum temperature reached for nanoparticles near
the melting point of the aluminum core.[5] This suggests to some that a mechanism
associated with the melting of the aluminum core is responsible for ignition, whereas in
larger particles the ignition temperature is closer to the melting temperature of alumina,
namely 2327K. The closeness of the reaction temperature to the melting point of pure
aluminum indicates that the melting of the aluminum core is the possible initiator of this
reaction for nanoparticles.

It has previously been assumed that either the sudden decrease in density of the aluminum upon melting [6,7] or the lower melting temperature of the nanometer sized oxide shell [8] is the key to initiation of the oxidation process. However, in this paper we explore the possibility that built-in electric fields as opposed to Fickian diffusion drive aluminum cations through the oxide shell to the nanoparticle surface where it is possible for the oxidation process to proceed. Experimentally produced hollow aluminum oxide nanoparticles provide support for this rapid diffusion hypothesis [9,10]. These observed hollow oxide shells are an indication that the oxidation process is driven by the diffusion of aluminum cations. We will show that field mediated ion-transport is much faster than Fickian diffusion, and will be the dominant transport process in the initiation of the oxidation of nanoaluminum. Anecdotal support for this mechanism comes from numerous numerical [11,12] and experimental studies. [13,14]

**Simulation Approach**
In this work we have chosen to use the ReaxFF (Reactive Force Field) empirical potential from van Duin [15] implemented within the GRASP (General Reactive Atomistic Simulation Program) MD application. The ReaxFF potential has an advantage over traditional empirical potentials in that it is able to accurately simulate the charge transfer that occurs during metal oxidation. The other empirical potential commonly used for this material system is the Streitz-Mintmire potential [16], however we chose to use the ReaxFF potential because it is available within GRASP which can be executed in parallel. The Al-O potential parameter set used in this work comes from a previous effort that considered the sliding of $Al_2O_3$ coatings against Al and $Al_2O_3$ [17]. The computational requirement of this software is high with the largest material system considered here containing nearly 100,000 atoms and requires 96 Intel Woodcrest processor cores running at 3.0 GHz to be simulated efficiently.

**Model Description**
Two core sizes are considered here, the smaller of these consists of a 5.6nm diameter core of aluminum with either a 1nm or 2nm thick shell of Alumina ($Al_2O_3$) as illustrated by the example systems in figure 1. The larger model includes an 8nm aluminum core with a 2nm thick crystalline oxide shell. This model is used to consider scaling effects for the electric field and diffusivity.

There are four shell configurations considered for each oxide shell thickness.

1. A defect free crystalline shell that may result from extremely slow or high temperature formation. This shell is modeled by coating a bare aluminum nanoparticle with a crystalline shell made up of α-$Al_2O_3$. Although the gamma phase of alumina is more prevalent in oxide coated nanoparticles the alpha form is also observed, and is a limiting case as it is the densest phase that the oxide shell will form. A dense amorphous shell that has an atomic ratio of 2:3 aluminum to oxygen atoms (i.e. $Al_2O_3$). This shell is formed in the simulation by heating a crystalline oxide shell above its melting temperature while holding the aluminum core atom positions fixed. In this way the oxide layer melts and then is rapidly cooled and trimmed in order to obtain a slightly amorphous oxide layer with the desired thickness.

2. A dense amorphous shell 10% deficient in oxygen atoms, Al/O = 2:2.7. This shell may form during a faster rate of formation or if the environment during formation was oxygen lean. In the computer simulation this shell is formed by removing 10% of the oxygen from the previous dense oxide shell that is at the stoichiometric ratio of 2:3 aluminum to oxygen atoms.

3. Lastly, a porous amorphous shell with an atomic ratio of 2:3 aluminum to oxygen atoms. This shell has approximately one half of the density of the previously described dense shell with the same atomic ratio. This more porous amorphous shell represents oxide formation that may occur at a very fast rate with a sufficient supply of oxygen. This oxide shell is formed in the computer simulation similarly to the process used for the dense shell except that the shell is repeatedly heated to a higher temperature and rapidly cooled until a much more amorphous configuration is achieved.

Following the creation and equilibration of the oxide shell, the model systems were heated at rates of $10^{11}$K/s, $10^{12}$K/s, and $10^{13}$K/s in order to determine any rate dependencies. We found, similarly to Puri and Yang [8], that at rates below $10^{12}$K/s the heating rate appears to have little effect on the simulation results. This is an important result, as lower heating rates would increase the number of MD simulation time steps, which for this work was ~1fs to maintain energy conservation, to a level that would be unreasonable with current computing capacities. The temperature of the model systems was raised from 300K to 1000K and eventually up to 3000K, which is much higher than the melting point of the oxide layer. From experimental data available in the literature [4] it is expected that some reaction should be observed near the melting point of the aluminum core. At the melting point of the core the aluminum density decreases from, 2.7g/cm$^3$ to 2.4g/cm$^3$, resulting in a volumetric expansion of about 12%. Melting of the oxide shell requires heating the nanoparticle to above the melting point of the oxide which is 2327K for the bulk material or somewhat less for a nanoparticle shell because of the size affect. The results of each of these efforts are detailed in the following sections.

**Results of Rapid Heating Simulations**
The simulations in this section were carried out in a vacuum so that as Al cations move radially outward towards the oxide surface there are no oxygen molecules available for oxidation reactions. In simulations discussed later we have found the diffusivity of Al through the oxide layer to be more important than oxygen diffusion towards the core. For this reason we are primarily concerned in this work with the mechanism by which Al cations reach the surface of the nanoparticle, therefore limiting the scope of this effort to the ignition process. Initially, the nanoparticles were heated from 300K to about 1000K, which is above the core melting point but below the size dependent oxide melting point reported by Puri and Yang [8]. At around 900K, or slightly below the bulk melting temperature of the aluminum core, a rapid volumetric expansion of the core is observed indicating that the aluminum core has begun to melt. At 1000K the oxide shell still remains intact, with no cracking, even when maintained at that temperature for 100ps. We do see however, as illustrated in Figure 3, the initiation of aluminum cation diffusion to the particle surface.

The results in figure 3 show a slightly inhomogeneous melting of the aluminum core, which is evident in the "1000K, +0ps" plot. Some of the less dense faces of the core begin to melt while the top and bottom remain crystalline, giving the nanoparticle a slightly elongated appearance. The plots in figure 3 also demonstrate the mechanism by which oxidation will be initiated at elevated temperatures. The first observation is that the oxide shell does not crack as one might expect if diffusion were extremely limited, or the shell were brittle. This suggests that the shell is more elastic at this length scale, or the expansion of the aluminum is insufficient to cause failure in the shell, even at these elevated temperatures. One possible reason for the enhanced elasticity is the lower coordination of the atoms in the oxide shell as compared to the bulk material [18], which is incidentally also a contributing factor to the size dependent melting temperature observed in nanoparticles. In addition, we observe significant diffusion of the core atoms through the oxide shell, thus relieving the potentially high internal pressures. The primary mechanism driving this diffusion is discussed in the following sections.

**Aluminum Cation Diffusion through the Oxide Shell**

As observed by us and by others [8], at temperatures below the melting point of the oxide shell there is significant diffusion of aluminum cations through the oxide shell. Computation of the diffusivity from the mean square displacement (MSD) of the aluminum cations yields values typically found for liquids. This was unexpected because these measurements were taken at 600K, somewhat below the melting temperature of the relatively small 5.6nm aluminum nanoparticle core. Although the MSD data is somewhat noisy because of the limited simulation time and small nanoparticle sizes, there is an obvious trend of proportionally increasing diffusion rates radially through the shell with increased temperature. To support this observation the radial diffusivity is compared to the overall diffusivity in table I.

The diffusion coefficients in table I are computed using equation 1.

$$\frac{\partial \langle r^2(t) \rangle}{\partial t} = 2dD \tag{1}$$

In equation 1, the number of dimensions, $d$, available for atomic diffusion, is 3 for overall diffusion, and 1 for radial diffusion [19]. The use of the bulk diffusion equation is reasonable since during the time scales considered the movement of only the atoms initially on the surface are restricted by the particle boundary [20]. For radial diffusion we are only concerned with the MSD directed radially from the center of the nanoparticle. In equation 1, $t$ is the elapsed time, and $\langle r^2(t) \rangle$ is the MSD of the atoms being tracked. The diffusion coefficients reported are for all of the core atoms including those near the center of the nanoparticle. This is important since we would expect the mechanical and electrostatic affects to be larger near the core/shell interface, but because of the small sample sizes available, computing a radial distribution of diffusivity is unreliable.

By comparing the radial and overall diffusivities in table I an interesting trend is observed. As the temperature increases the radial diffusivity becomes a generally more important portion of the overall diffusivity of aluminum cations. This result indicates that once the aluminum core has melted the diffusion of aluminum cations is preferentially in the radial direction, as compared to the results prior to melting. This is possibly due to a high pressure gradient near the core/shell interface pushing atoms out into the shell.

Another possibility is that once the core has melted the atoms are more mobile so in addition to pressure, any other effects such as an electric field will increase diffusion. The radial diffusion data that does not correlate with this observation at 600K is for the 2nm thick crystalline oxide shells for both the 5.6nm and 8.2nm aluminum cores. These configurations show diffusion rates that are on par with the overall diffusivity, possibly indicating that one of the drivers of radial diffusion is proportionally stronger for these shell configurations at 600K. We will show in the following sections that the electric field is indeed strongest in the 2nm thick crystalline shells.

In figure 4 an Arrhenius plot of the diffusivity versus temperature is given for each of the oxide shell configurations used with the 5.6nm aluminum core in this work. From figure 4 we observe that a change in slope occurs near the melting point of the aluminum core, namely 1000K. This indicates that for temperatures above 1000K the activation energy required for cation diffusion is lower than for temperatures below 1000K. The increase in activation energy for the 1nm amorphous and dense oxygen poor shells, is likely due to a lower melting point for these oxide shells. This is not the case, for thicker or more crystalline shells where the oxide remains in the solid phase, and does not undergo any phase transformation. In the remaining model systems the activation energy drops once the melting temperature is reached, indicating a change in diffusion mechanism. The primary change that occurs at around 1000K is the melting of the aluminum core, the associated volumetric expansion, and increased mobility of the aluminum atoms. This expansion is expected to greatly increase the pressure inside of the core, and enhance the diffusion of aluminum cations radially outward through the oxide shell.

**Induced Electric Field in Oxide Shell**

One possible explanation for the computed rapid diffusion of aluminum atoms through the oxide layer is that they are driven by an induced electric field near the core/shell interface. The theory that oxidation growth proceeds via migration of charged particles is not a new one. In fact Carl Wagner proposed this theory in 1933 [13]. In a 1948 paper by Cabrera and Mott [11] the authors developed a theory focused on the growth of a thin oxide film on metal surfaces that is driven by an induced electric field. This electric field causes metal ions to migrate to the surface, increasing the oxide thickness until the induced field is prevented by the thickening surface to cause further diffusion of metal cations. The maximum thickness of the oxide layer that is formed with this process increases with temperature, up to a critical temperature above which growth of the oxide layer will continue indefinitely.

Recent theoretical and experimental evidence points to the importance of the induced electric field described by Cabrera and Mott in the oxidation of oxide coated metal nanoparticles. Zhdanov and Kasemo [21] recently performed an analysis of the induced electric field in oxide coated nanoparticles. They found that by considering the size and geometry effect of nanoparticles coated with oxide shells that the induced electric field will be much stronger than observed in a flat surface, thus increasing the associated oxidation rate exponentially in oxide coated nanoparticles. We have also observed the formation of hollow particles [9, Figure 2] during the oxidation of oxide coated aluminum, which we attributed to the faster diffusion of Al cations. Subsequently Nakamura et al [10] also observed formation of hollow metal oxide nanoparticles from

oxidation of metals and attributed the rapid diffusion of metal cations through the oxide shell to the induced electric field. In the following sections we investigate the magnitude and effect of the induced electric field on the oxide coated aluminum nanoparticle system.

In the current simulation effort, rapid diffusion of aluminum cations through the oxide layer is observed. An indicator of the strength of the electric field is the radial charge density. The radial charge density is computed through the nanoparticle at 2Å radial intervals and is averaged over 100ps of simulation time. Although noisy, which is partially caused by atomic diffusion, it is apparent that there is a negative charge gradient throughout the oxide shell. This charge gradient contributes to the out flow of positive charges, and the mass flux of aluminum cations at the core/shell interface.

The difference in charge density between the inner and outer surfaces of the oxide shell indicates that an electric field is induced which will drive aluminum cations near the core/shell interface to the outer surface where they will be exposed to oxygen and oxidize. An approximate interaction between an aluminum cation, with the core and shell can be computed using Gauss's Law. By assuming the atomic charges to be distributed approximately homogeneously in the shell and the core, the electric field on the surface of the core can be estimated as the field from a single point charge at the center of the core, through equation 2. If we assume the charge to be evenly distributed in the oxide shell then the electric field inside of the shell from the atoms in the oxide shell is zero.

$$E = \frac{Q_{core}}{4\pi\varepsilon_0 r^2} \tag{2}$$

In equation 2, $Q_{core}$ is the total charge of the core, $r$ is the radial position of the interfacial aluminum atom of interest, and $\varepsilon_0$ is the permittivity of a vacuum. Using equation 2 the electric fields from the various oxide coated models are computed in table II.

In figure 6 the volume between the core surface and outer surface of the oxide shell is assumed to be a vacuum. For the purpose of computing the electric field, this assumption is valid so long as the charges in the oxide shell are distributed radially only. With a radially distributed charge the electric field due to the oxide shell is zero everywhere for atoms at the core/shell interface or inside of the aluminum core. The most obvious trend observed in table II is that of the decreasing core charge and electric field strength with increasing temperature. This is likely due to the fact that as shown in table I, diffusivity increases as temperature increases, and smears the boundary between the core and shell. Another observed trend, albeit weaker, is an increase in the electric field as the shell becomes thicker, and more organized. So in going from an amorphous 1nm thick shell to a 2nm thick crystalline shell we observe a 100% increase in the electric field strength. This observation is supported by the analysis of Zhdanov and Kasemo [21].

A more accurate method of computing the electric field at each ion in the core and shell is to use Coulomb's Law and to sum the discrete contribution from all of the neighboring charges. Using this method is straight forward since there are a finite number of discrete charge carrying atoms. In figure 7 the computed electric field, using equation 3, is plotted at each of the core aluminum atoms.

$$E = \frac{q}{4\pi\varepsilon_0 r^2}\hat{e}_r \tag{3}$$

In equation 3 $\hat{e}_r$ is the radial unit vector coming from the neighboring atom and $q$ is the charge associated with the neighboring atom. Summing each of these vectors for all of the core atoms gives the results as shown in figure 7 for 600K, 1000K, and 2000K.

The electric field plotted in figure 7 is within one order of magnitude of the simple model results, tabulated in table II, which assumes a homogeneous charge distribution in the core and oxide shell. The direction of the computed electric field indicates that the mass flux due to the electric field is directed out through the oxide shell rather than acting to randomly rearrange the atoms. The positively charged aluminum atoms will therefore be preferentially directed towards the outer surface of the oxide shell, where they will come into contact with oxygen ions and oxidize.

With the diffusion coefficients previously computed and the electric field results computed here it is possible to analyze the mass flux due to concentration gradients ($J_d$), the electric field ($J_e$), and the internal pressure ($J_c$). The relative magnitude of the effect of the electric field on Al ion diffusion can be computed using the Nernst-Planck equation. The Nernst-Plank equation is given in equation 4 [22].

$$J = -D\frac{dC}{dx} - \frac{zFDC}{RT}\frac{d\phi}{dx} + Cv \tag{4a}$$

$$J = J_d + J_e + J_c \tag{4b}$$

If we assume a zero molar concentration of Al cations in the shell and the bulk concentration at the interface then the parameters for equation 4a are given as the following.

$$C = 0.1\,{}^{mol}\!/\!_{cm^3}$$

$$\frac{dC_{1nm}}{dx} = 1.0 \cdot 10^6\,{}^{mol}\!/\!_{cm^4}$$

$$R = 8.314\,{}^{C \cdot V}\!/\!_{mol \cdot K}$$

$$F = 96485\,{}^{C}\!/\!_{mol} \tag{5}$$

The electric field computed in table II is the negative of the charge gradient $d\varphi/dx$.

The convective flux, $J_c$ in equation 4 is the drift velocity of metal ions through the core/shell interface due to constant force acting on the ions. The force on these ions comes from the pressure gradient which is due to the expanding aluminum melt. When considering $J_c$ only the radial drift velocity, and therefore the radial pressure gradient, in equation 4a is considered so that $J_c$ can be rewritten as $C\,(Df_r/k_BT)$, where $f_r$ is defined as

$$f_r = -\frac{\partial V}{\partial r} = -\nabla p v_{Al} \tag{6}$$

In equation 6, $\nabla p$ is the pressure gradient in the radial direction and $v_{Al}$ is the solubility of Al in the $Al_2O_3$ network [23]. The maximum pressure gradients observed in the simulations range from less than 1GPa/nm at 600K to 2GPa/nm at 1000K and above. For the solubility of Al in $Al_2O_3$ we have assumed a value that comes from previous analysis of oxygen and Al diffusion through $Al_2O_3$ and should therefore be a reasonable value. Assuming a value of about $0.02nm^3$ for the solubility of Al, $v_{Al}$, it is possible to estimate the mass flux due to each term in equation 4. The diffusivity due to the drift velocity is directly proportional to $v_{Al}$ but variations here by less than one order of magnitude and would have little effect on the results in table III.

From the final column in Table III, listing the ratio of $J_e$ to $J$, it is apparent that in all cases except for two, over 90% of the mass flux through the oxide shell is due to the induced electric field present at the core/shell interface. The exceptions to this 90% observation are the 1nm amorphous and 1nm dense $Al_2O_{2.7}$ shells at 2000K, which from previous analysis appear to have undergone a phase change at this temperature. This illustrates the importance of considering the electric field in the oxide shell for any oxidation analysis of the oxide coated aluminum nanoparticle system. Another interesting trend is that the importance of the electric field in diffusion increases, as both the shell thickens and the temperature decreases. The trend associated with temperature is expected since diffusion without an electric field is strongly temperature and pressure dependent, and at low temperatures diffusion would be very slow without an electric field. The trend associated with shell thickness requires some more thoughtful analysis. By considering the computed electric fields in table II, we observe that the magnitude does indeed increase with shell thickness while the overall mass flux decreases, Table II and figure 8.

In figure 8 we observe some interesting trends not necessarily apparent in Table III. For nanoparticle systems at 600K and 1000K the degree of crystallinity in the oxide shell does not appear to have a noticeable effect on the mass flux of the aluminum cations through the oxide shell. This result is interesting because we can conclude that the reaction rate for oxide coated aluminum nanoparticles in this size range will not be dependent on how the coating was formed or upon its thickness, up to 2nm.

The most apparent trend in figure 8 is that the mass flux of aluminum atoms through the shell at 2000K decreases with increasing shell crystallinity and thickness. This result is likely due to the increased dependence of total mass flux on the concentration gradient and drift velocity terms in equation 4 as opposed to being solely due to the electric field. This decreased mass flux is observed as lower values in the last column in Table III for 2000K versus 600K and 1000K. Since the heating rate required to reach 2000K before an appreciable amount of the core has diffused into the shell is so high, greater than $10^{12}$K/s, we would not expect this to be an experimentally observable result without some sort of very rapid heating method.

**Formation of Hollow Aluminum Oxide Shells**
Recent experimental efforts by Rai et al [9] and Nakamura et al [10] have both observed the formation of hollow aluminum oxide nanoparticles as a result of the oxidation of oxide coated aluminum nanoparticles. In the work by Rai et al [9] we observed the formation of hollow spheres of aluminum oxide subsequent to the oxidation of aluminum nanoparticles at about 727K. We expected that these hollow oxide shells are produced by the outward diffusion of aluminum through the oxide shell as opposed to inward diffusion of oxygen. This observation is supported here by the high measured diffusion coefficients for aluminum cations and mass flux due to the electric field in the nanoparticle.

In order to better compare the inward diffusion of oxygen versus the outward diffusion of aluminum we have simulated a 5.6nm aluminum core with a 2nm crystalline oxide shell in a high density oxygen gas as shown in figure 9. The diffusion of oxygen ions through the shell has the potential to limit the mass flux of aluminum cations emanating from the core, producing reactions inside of the oxide shell and at the

core/shell interface as opposed to on the nanoparticle surface. Oxidation in the core would potentially increase the internal pressure of the nanoparticle from volumetric expansion resulting in mechanical failure of the oxide shell, but would be unlikely to result in the hollow shells observed by Rai et al [9].

In figure 9 it is apparent that the diffusivity of aluminum cations through the oxide shell is observably higher than the diffusion rate of oxygen anions towards the core. This result indicates that oxidation will occur on or near the outer surface of the oxide shell rather than at or near the core/shell interface. By the oxidation reaction occurring on the outer shell surface an outward growth of the oxide shell is observed which ultimately results in a hollow aluminum oxide shell as observed experimentally [9,10]. One effect that may limit the mass flux of oxygen atoms into the oxide shell is that at higher temperatures the sticking probability of the gas molecules is lower than for temperatures <623K [24].

**Conclusions**

For small oxide coated aluminum nanoparticles we have found that ignition of the oxidation process is likely to occur by rapid diffusion of aluminum cations through the oxide shell as opposed to mechanical failure or melting of the shell, for heating rates as high as $10^{12}$K/s. The high level of measured aluminum cation diffusivity is driven not only by the volumetric expansion of the aluminum core, but primarily by the induced electric field in the oxide shell. This enhanced diffusivity due to the induced electric field is supported by theoretical analysis of the Cabrera-Mott effect for oxide coated nanoparticles [21]. Oxidation initiation by rapid diffusion of aluminum ions to the nanoparticle surface is in agreement with published experimental efforts that have observed the formation of hollow aluminum oxide nanoparticles [9,10]. Diffusion of oxygen ions into the shell has also been considered but does not contribute appreciably when compared to the flux of aluminum to the nanoparticle surface.

**References**
1. X. Phung, J. Groza, E. A. Stach, L. N. Williams, and S. B. Ritchey. "Surface characterization of metal nanoparticles", *Materials Science and Engineering A*, **359**, 261–268, 2003.
2. J.H. Sinfelt. *Bimetallic Catalysis: Discoveries, Concepts and Applications.* Wiley, New York, 1983.
3. J. Uppenbrink and David J. Wales. "Structure and energetic of model metal clusters", *Journal of Chemical Physics*, **96**(11), 8520–8534, 1992.
4. A. Rai, D. Lee, K. Park, and M. R. Zachariah. "Importance of Phase Change of Aluminum in Oxidation of Aluminum Nanoparticles", *Journal of Physical Chemistry B*, **108**, 14793–14795, 2004.
5. M.A. Trunov, M. Shoenitz, and E.L. Dreizin. "Effect of polymorphic phase transformations in alumina layer on ignition of aluminum particles", *Combustion Theory and Modelling*, **10**(4), 603–623, 2006.
6. V.I. Levitas, B.W. Asay, S.F. Son, and M. Pantoya. "Melt dispersion mechanism for fast reaction of nanothermites", *Journal of Applied Physics*, **89**, 071909, 2006.

7. V.I. Levitas, B.W. Asay, S.F. Son, and M. Pantoya. "Mechanochemical mechanism for fast reaction of metastable intermolecular composites based on dispersion of liquid aluminum", *Journal of Applied Physics*, **101**, 083524, 2007.

8. P. Puri and V. Yang. "Thermo-Mechanical Behavior of Nano Aluminum Particles with Oxide Layers", 46th AIAA Aerospace Sciences Meeting and Exhibit, Reno, NV, 7-10 January 2008.

9. A. Rai, K. Park, L. Zhou, and M.R. Zachariah. "Understanding the mechanism of aluminum nanoparticle oxidation", *Combustion Theory and Modelling*, **10**(5), 843–859, 2006.

10. R. Nakamura, D. Tokozakura, H. Nakajima, J.-G. Lee, and H. Mori. "Hollow oxide formation by oxidation of Al and Cu nanoparticles", *Journal of Applied Physics*, **101**, 074303, 2007.

11. N. Cabrera and N.F. Mott. "Theory of the Oxidation of Metals", *Rep. Prog. Phys.*, **12**, 163–184, 1948.

12. A.T. Fromhold, jr, and E.L. Cook. "Kinetics of Oxide Film Growth on Metal Crystals: Thermal Electron Emission and Ionic Diffusion", *Physical Review*, **163**(3), 650–664, 1967.

13. C. Wagner. "Beitrag zur Theorie des Anlaufvorgangs", *Z. Phys. Chem.*, B**21**, 25, 1933.

14. L.P.H. Jeurgens, W.G. Sloof, F.D. Tichelaar, and E.J. Mittemeijer. "Growth kinetics and mechanisms of aluminum-oxide films formed by thermal oxidation of aluminum", *Journal of Applied Physics*, **92**(3), 1649–1656, 2002.

15. A.C.T. van Duin, S. Dasgupta, F. Lorant, and W.A. Goddard III. "ReaxFF: A Reactive Force Field for Hydrocarbons", *Journal of Physical Chemistry A*, **105**, 9396–9409, 2001.

16. F.H. Streitz and J.W. Mintmire. "Electrostatic potentials for Metal-Oxide Surface and Interfaces", *Physical Review B*, **50**(16), 11996–12003, 1994.

17. Q. Zhang, T. Çağın, A. van Duin, W.A. Goddard III, Y. Qi, and L.G. Hector, Jr. "Adhesion and Nonwetting-Wetting Transition in the Al/$\alpha$-Al$_2$O$_3$ Interface", *Physical Review B*, **69**, 045423, 2004.

18. N. Pradeep, D.I. Kim, J. Grobelny, T. Hawa, B.J. Henz, and M.R. Zachariah, "Ductility at the nano scale: Deformation and fracture of adhesive contacts using atomic force microscopy", *Applied Physics Letters*, **91**, 203114, 2007.

19. S. Ogata, H. Iyetomi, K. Tsuruta, F. Shimojo, A. Nakano, R.K. Kalia, and P. Vashishta. "Role of atomic charge transfer on sintering of TiO$_2$ nanoparticles: Variable-charge molecular dynamics", *Journal of Applied Physics*, **88**(10), 6011–6015, 2000.

20. P.P. Mitra, P.N. Sen, L.M. Schwartz, P. Le Doussal. "Diffusion Propagator as a Probe of the Structure of Porous Media", *Physical Review Letters*, **68**(24), 3555–3558, 1992.

21. V.P. Zhdanov and B. Kasemo. "Cabrera–Mott kinetics of oxidation of nm-sized metal particles", *Chemical Physics Letters*, **452**, 285–288, 2008.

22. C.G. Zoski. *Handbook of Electrochemistry*. Elsevier, 2007.

23. J. Dalla Torre, J.–L. Bocquet, Y. Limoge, J.–P. Crocombette, E. Adam, G. Martin, T. Baron, P. Rivallin, and P. Mur. "Study of self-limiting oxidation of silicon

nanoclusters by atomistic simulations", *Journal of Applied Physics*, **92**(2), 1084–1094, 2002.

24. V. Zhukov, I. Popova, and J.T. Yates. *Surface Science*, **441**, 251, 1999.

Table I. Effective diffusion coefficients for core aluminum atoms with various oxide shell configurations. The effective diffusion coefficients are for general diffusion ($D_{eff}$) and radial diffusion ($D_{radial}$).

| Shell Thickness | Type | Temperature | $D_{eff}$ $(cm^2/s*10^{-7})$ | $D_{radial}$ $(cm^2/s*10^{-7})$ |
|---|---|---|---|---|
| 1nm | Amorphous | 600K | 53 | 5.9 |
| 1nm | Amorphous | 1000K | 420 | 300 |
| 1nm | Amorphous | 2000K | 7100 | 8300 |
| 1nm | Dense | 600K | 11 | 4.0 |
| 1nm | Dense | 1000K | 340 | 280 |
| 1nm | Dense | 2000K | 1300 | 1300 |
| 1nm | Dense, $Al_2O_{2.7}$ | 600K | 2.6 | 2.1 |
| 1nm | Dense, $Al_2O_{2.7}$ | 1000K | 380 | 190 |
| 1nm | Dense, $Al_2O_{2.7}$ | 2000K | 6000 | 6700 |
| 1nm | Crystalline | 600K | 31 | 6.7 |
| 1nm | Crystalline | 1000K | 330 | 240 |
| 1nm | Crystalline | 2000K | 1000 | 1300 |
| 2nm | Amorphous | 600K | 23 | 4.6 |
| 2nm | Amorphous | 1000K | 400 | 320 |
| 2nm | Amorphous | 2000K | 770 | 660 |
| 2nm | Dense | 600K | 8.1 | 6.9 |
| 2nm | Dense | 1000K | 360 | 250 |
| 2nm | Dense | 2000K | 490 | 520 |
| 2nm | Dense, $Al_2O_{2.7}$ | 600K | 4.2 | 3.3 |
| 2nm | Dense, $Al_2O_{2.7}$ | 1000K | 370 | 180 |
| 2nm | Dense, $Al_2O_{2.7}$ | 2000K | 270 | 100 |
| 2nm | Crystalline | 600K | 8.3 | 7.8 |
| 2nm | Crystalline | 1000K | 330 | 190 |
| 2nm | Crystalline | 2000K | 490 | 520 |
| 2nm, 8nm Core | Crystalline | 600K | 6.9 | 9.9 |
| 2nm, 8nm Core | Crystalline | 1000K | 190 | 160 |
| 2nm, 8nm Core | Crystalline | 2000K | 1300 | 920 |

Table II. Total charge of aluminum core and associated electric field are given here for all of the core/shell configurations considered. Note on electric field units, N/C = 0.01 V/m.

| Shell Thickness | Type | Temperature | $Q_{core}$ (C*$10^{-18}$) | E (N/C*$10^{10}$) |
|---|---|---|---|---|
| 1nm | Amorphous | 600K | 8.28 | 1.10 |
| 1nm | Amorphous | 1000K | 5.67 | 0.75 |
| 1nm | Amorphous | 2000K | 1.47 | 0.20 |
| 1nm | Dense | 600K | 11.4 | 1.52 |
| 1nm | Dense | 1000K | 8.86 | 1.18 |
| 1nm | Dense | 2000K | 4.01 | 0.53 |
| 1nm | Dense, $Al_2O_{2.7}$ | 600K | 7.91 | 1.05 |
| 1nm | Dense, $Al_2O_{2.7}$ | 1000K | 6.38 | 0.85 |
| 1nm | Dense, $Al_2O_{2.7}$ | 2000K | 1.09 | 0.14 |
| 1nm | Crystalline | 600K | 12.7 | 1.69 |
| 1nm | Crystalline | 1000K | 10.8 | 1.44 |
| 1nm | Crystalline | 2000K | 3.04 | 0.40 |
| 2nm | Amorphous | 600K | 13.3 | 1.77 |
| 2nm | Amorphous | 1000K | 11.9 | 1.58 |
| 2nm | Amorphous | 2000K | 4.61 | 0.61 |
| 2nm | Dense | 600K | 13.8 | 1.83 |
| 2nm | Dense | 1000K | 12.7 | 1.69 |
| 2nm | Dense | 2000K | 4.21 | 0.56 |
| 2nm | Dense, $Al_2O_{2.7}$ | 600K | 11.6 | 1.54 |
| 2nm | Dense, $Al_2O_{2.7}$ | 1000K | 11.1 | 1.47 |
| 2nm | Dense, $Al_2O_{2.7}$ | 2000K | 7.80 | 1.04 |
| 2nm | Crystalline | 600K | 15.6 | 2.08 |
| 2nm | Crystalline | 1000K | 13.9 | 1.85 |
| 2nm | Crystalline | 2000K | 4.39 | 0.58 |
| 2nm, 8nm Core | Crystalline | 600K | 43.9 | 2.47 |
| 2nm, 8nm Core | Crystalline | 1000K | 42.6 | 2.40 |
| 2nm, 8nm Core | Crystalline | 2000K | 30.4 | 1.71 |

Table III. Diffusion coefficient and mass flux computed at 600K, 1000K, and 2000K for all shell configurations with the 5.6nm core unless noted. The last column labeled Ratio $J_e$ to J, is the fraction of the total mass flux due to the induced electric field, with the balance due to the concentration gradient and drift velocities.

| Shell Thickness | Configuration | Temperature | J (mol/cm$^2$·s) | D (cm$^2$/s *10$^{-8}$) | Ratio $J_e$ to J |
|---|---|---|---|---|---|
| 1nm | Amorphous | 600K | 4.20 | 1.97 | 0.98 |
| 1nm | Amorphous | 1000K | 11.97 | 13.6 | 0.96 |
| 1nm | Amorphous | 2000K | 53.45 | 424.0 | 0.83 |
| 1nm | Dense | 600K | 3.03 | 1.03 | 0.99 |
| 1nm | Dense | 1000K | 11.49 | 8.33 | 0.97 |
| 1nm | Dense | 2000K | 35.18 | 110.8 | 0.93 |
| 1nm | Dense, $Al_2O_{2.7}$ | 600K | 2.13 | 1.03 | 0.98 |
| 1nm | Dense, $Al_2O_{2.7}$ | 1000K | 8.06 | 7.88 | 0.96 |
| 1nm | Dense, $Al_2O_{2.7}$ | 2000K | 46.27 | 426.0 | 0.78 |
| 1nm | Crystalline | 600K | 5.08 | 1.55 | 0.99 |
| 1nm | Crystalline | 1000K | 14.72 | 8.75 | 0.98 |
| 1nm | Crystalline | 2000K | 35.58 | 147.0 | 0.91 |
| 2nm | Amorphous | 600K | 3.31 | 0.97 | 0.99 |
| 2nm | Amorphous | 1000K | 18.49 | 10.0 | 0.98 |
| 2nm | Amorphous | 2000K | 23.73 | 65.2 | 0.94 |
| 2nm | Dense | 600K | 1.26 | 0.35 | 0.99 |
| 2nm | Dense | 1000K | 6.13 | 3.11 | 0.98 |
| 2nm | Dense | 2000K | 11.34 | 33.8 | 0.93 |
| 2nm | Dense, $Al_2O_{2.7}$ | 600K | 3.69 | 1.23 | 0.99 |
| 2nm | Dense, $Al_2O_{2.7}$ | 1000K | 7.99 | 4.58 | 0.98 |
| 2nm | Dense, $Al_2O_{2.7}$ | 2000K | 5.27 | 8.38 | 0.96 |
| 2nm | Crystalline | 600K | 7.83 | 1.94 | 0.99 |
| 2nm | Crystalline | 1000K | 15.06 | 6.98 | 0.98 |
| 2nm | Crystalline | 2000K | 6.81 | 19.6 | 0.93 |
| 2nm, 8nm Core | Crystalline | 600K | 17.27 | 3.59 | 0.99 |
| 2nm, 8nm Core | Crystalline | 1000K | 24.31 | 8.61 | 0.99 |
| 2nm, 8nm Core | Crystalline | 2000K | 31.27 | 30.8 | 0.98 |
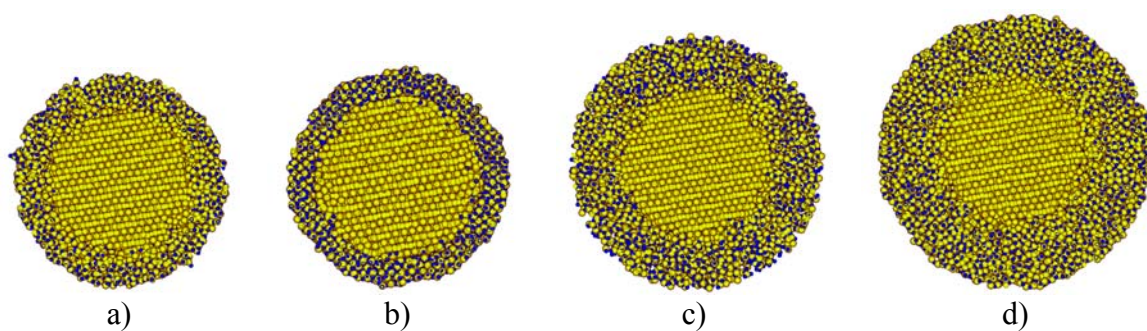
**Figure 1**. Cross sections of some of the oxide coated aluminum nanoparticle models used in this work. a) 1nm thick, dense oxide shell. b) 1nm thick, crystalline oxide shell. c) 2nm thick, amorphous oxide shell. d) 2nm thick, dense oxide shell with 2:2.7 Al:O ratio. Blue spheres represent oxygen atoms and yellow spheres denote aluminum atoms.
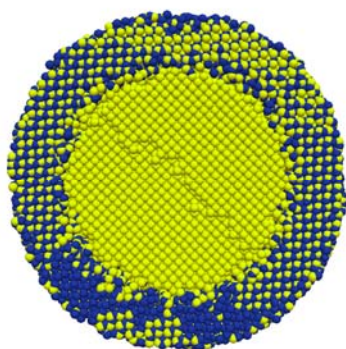


**Figure 2**. Cross section of an 8.2nm Al core with 2nm thick crystalline oxide shell. Yellow denotes Al atoms and oxygen atoms are blue.
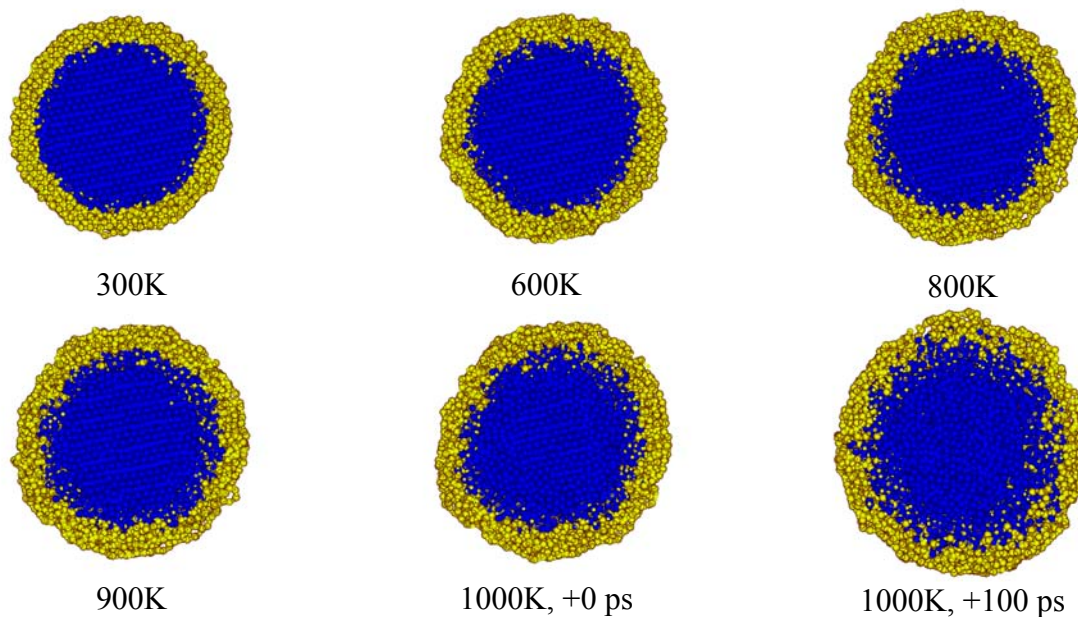
**Figure 3**. Plot showing diffusion of aluminum cations (blue) through the 1nm thick oxide shell (red) as the temperature increases from 300K to 1000K and held for 100 ps.
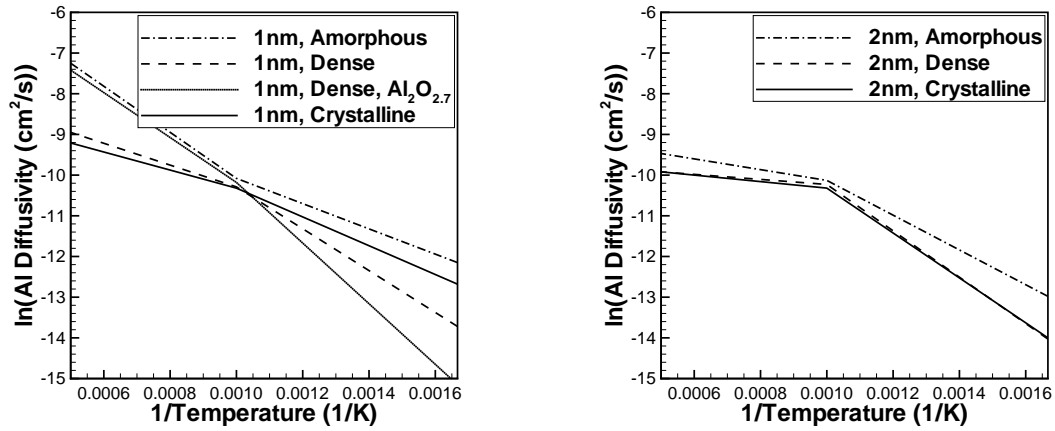
**Figure 4**. Arrhenius plot of ln(D) versus 1/T, where D is the diffusivity of the core aluminum atoms. The slope of this plot is the activation energy required for diffusion of aluminum cations and shows an expected decrease above the melting point of the core, at approximately 0.001/K.
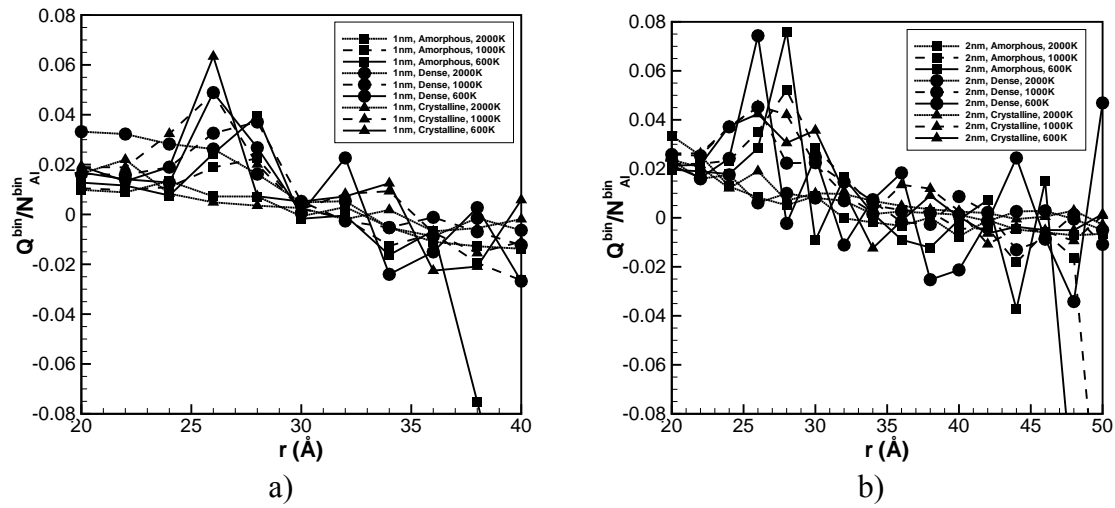


**Figure 5**. Radial charge distribution through the oxide shell for a 1nm (a) thick shell and a 2nm (b) thick shell.
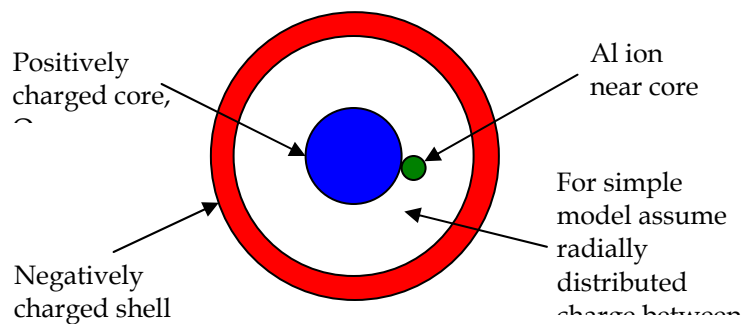
**Figure 6**. Schematic of assumed charge distributions affecting electric field around core surface aluminum atoms.
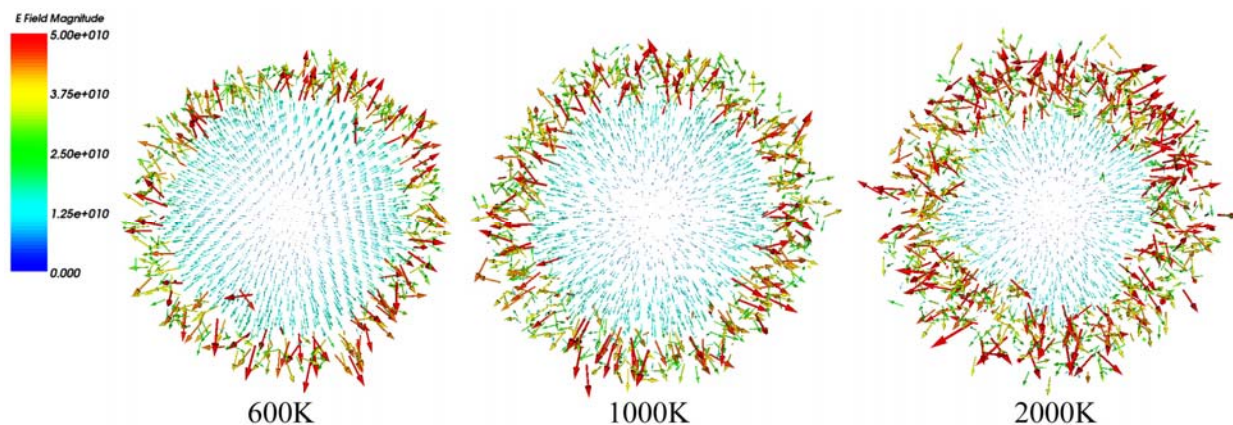


**Figure 7**. Electric field (N/C) at each of the core Al atoms in the nanoparticle core computed using Coulomb's Law. These results are for the 5.6nm core with a 2nm thick crystalline shell. Note the generally radial direction of the field.
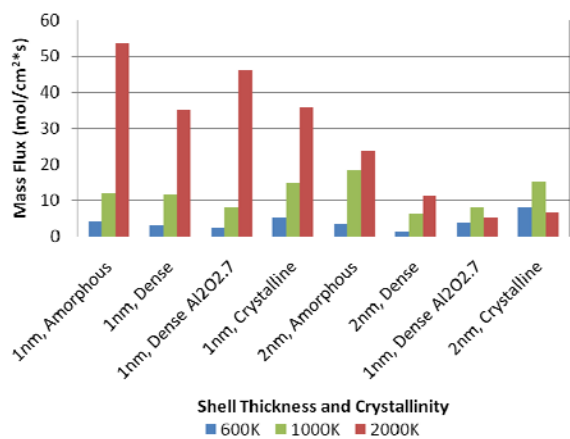


**Figure 8**. Plot of mass flux versus temperature and shell configuration.
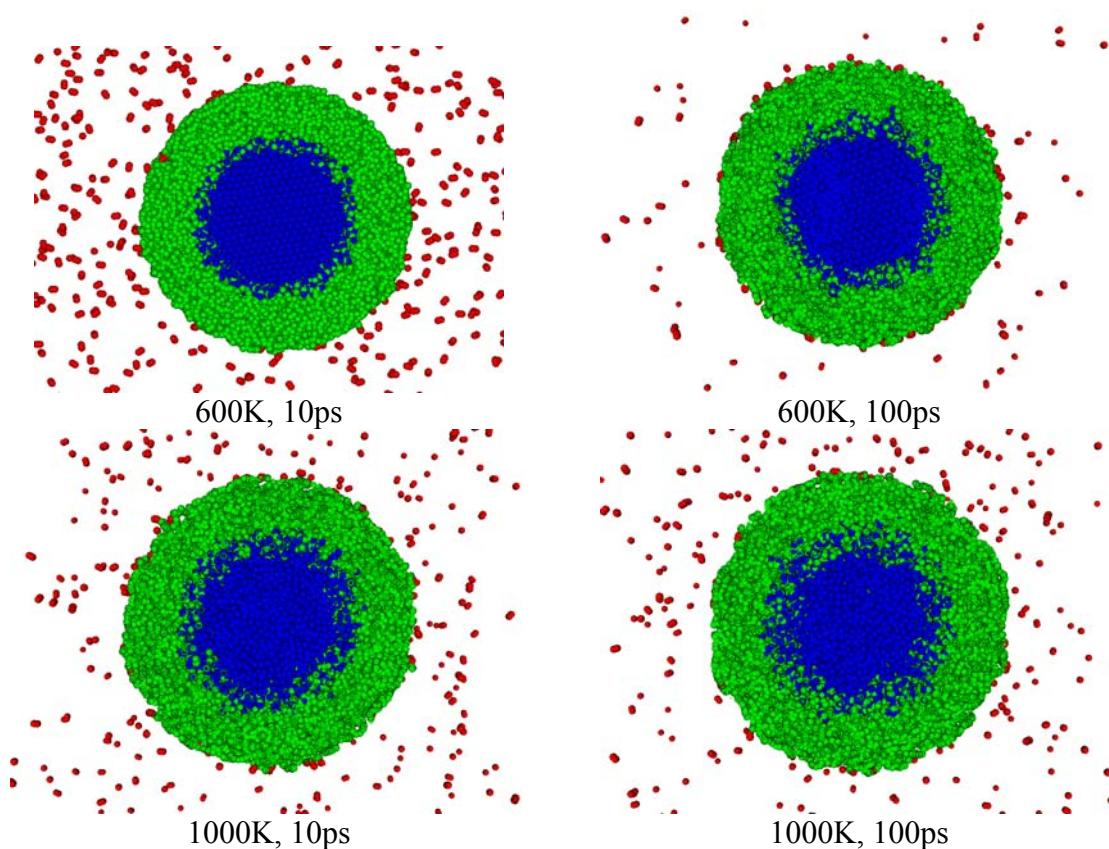
**Figure 9**. Cross section of oxide (green) coated aluminum core (blue) showing surrounding oxygen (red) atoms. Higher rates of diffusion for aluminum cations is observed by aluminum atoms moving radially outward into the oxide shell atoms while adsorbed oxygen atoms remain on the outer surface or desorb from the shell. Figures a and b are at 600K and represent 10ps and 100ps of simulation time, respectively. Figures c and d are at 1000K, after 10ps and 100ps, respectively.

# Transient ion ejection during nanocomposite thermite reactions

**ABSTRACT:**

We observe an intense ion pulse from nanocomposite thermite reactions, which we temporally probe using a recently developed Temperature Jump/Time of Flight Mass Spectrometer (T-Jump/TOFMS). These ion pulses are observed to be much shorter in duration than the overall thermite reaction time. Ion ejection appears in stages as positive ions are ejected prior to nanocomposite thermite ignition, and ignition of the thermite mixtures leads to a second ionization step which is primarily dominated by negative species. The positive species are identified from mass spectrometric measurements, and the results show that the positive ion species are comprised of Na ions with minor species of Al and K ions. This observation can be explained by a diffusion based ion-current mechanism, in which strong Al ion diffusion flux formed through the oxide shell, and the surface Na and K ions from salt contaminations are ejected by the strong electrostatic repulsion. The fact that the negative ionization step occurs during the ignition event, suggests a strong relation between the nanocomposite thermite reaction and the negative ionization process.

## INTRODUCTION

Nanocomposite thermites, also known as Metastable Intermolecular Composites (MIC), are comprised of reactive components consisting of nanostructured particles that are intimately mixed. The unique nanostructure of MICs not only enhance the reactivity, but also allow a control over the reactivity by varying parameters such as particle size, morphology and local composition.[1-3].

This class of material have not been studied as extensively as traditional organic based energetic materials. Research on thermite energetic materials typically focuses on developing new thermite formulations, as well as studying the thermite reaction mechanism. In general, a thermochemical point of view is emphasized in mechanism studies by means of characterizing combustion properties such as flame speed, reaction rate, ignition temperatures or reaction products.[4-9] On the other hand, the literature shows that complex ionization phenomena are observed through a variety of combustion systems.[10, 11] Ershov studied the detonation of solid explosives such as TNT and PETN, and observed high degrees of ionization in the detonation front. The corresponding electron density is several orders of magnitude higher than the theoretical value estimated from the Saha equation, which indicates nonthermal channels of ionization.[12] Experiments also revealed transient electric/magnetic field generation from combustion of a variety of metal-gas and metal-metal reaction systems, which may be attributed to the different diffusion rates of charge carriers through the oxide shell.[13-20] More recently, molecular dynamic simulations show that strong electric fields are intrinsically formed across the oxide shell of aluminum nanoparticles.[21] In fact, the electrical fields can be considered as inherent reaction parameter which should be accounted for in a model for thermite initiation or potentially be used as a controlling parameter though application of external fields. [22, 23]

The above experimental and theoretical investigations suggest an incomplete understanding of the origin of this behavior and if indeed it could be manipulated. Only a few studies report on ionization phenomena in nanocomposite thermites. Douglas and co-

workers took a similar approach to Ershov's work, and studied the electrical conductivity induced by nanocomposite thermite reactions. Their work showed that a conduction zone was observed in the reaction front, and that the conductivity profile was much longer than organic high explosives [24]. Korogodov and co-workers measured microwave radiation pulses from the combustion of an $Al/Fe_2O_3$ nanocomposite thermite system, to be several orders of magnitude higher than thermal radiation.[25]

Recently we reported on the development of a "Temperature- Jump/Time-of-Flight Mass Spectrometer" (T-Jump/TOFMS) that is capable of monitoring the transient reaction of organic based energetic materials (e.g. RDX, Nitrocellulose, etc).[4] However, when attempting to conduct experiments with nanothermites we found that initiation of the exothermic reaction caused a catastrophic malfunction of the high voltage bias on the ion extraction optics, and resulted in loss of mass spectra signal. This observation leads us to realize that an intense flux of charged species (ions and electrons) is ejected from the thermite reactions. Furthermore through appropriate configuration of the electric field within the mass-spectrometer we have the opportunity to probe with very high temporal resolution the nature of the current pulse, and its relationship to the combustion process. Here we apply T-Jump/TOFMS with minor modifications to clarify the characteristic nature of the ionization and its temporal correspondence to nanothermite combustion.

**EXPERIMENTAL APPROACH**

Thermite composite samples were prepared by mixing aluminum nanoparticles with oxidizer particles to obtain a stoichiometric mixture. The aluminum used was 50 nm Aluminum Explosive (ALEX) powder obtained from Argonide Corporation. Four types of oxidizers, copper oxide (CuO), iron oxide ($Fe_2O_3$), bismuth oxide ($Bi_2O_3$) and tungsten oxide ($WO_3$) nanopowders of ~ 100 nm obtained from Sigma-Aldrich, were used in a mix with aluminum particles. Nanocomposite thermite samples were mixed in hexane and the suspensions were sonicated for about 30 minutes to break the agglomerates and ensure intrinsic mixing between the fuel and oxidizer. The prepared sample suspensions were then coated on the T-Jump probe with a dropper. The T-Jump probe is a ~10 mm long platinum wire with diameter of 76 μm, for which the center ~ 5 mm of the wire is coated with a thin layer of sample comprising less than 0.3 mg.

The T-Jump/TOFMS is comprised of a linear Time-of-Flight chamber, an electron gun ionization source, and the T-Jump probe with an electrical feed-through for rapid sample heating. A detailed description of the T-Jump/TOF mass spectrometer can be found in our previous work.[4] In this work, different electric field configurations were used to extract ions of interest. The schematic of ion optics is shown in Figure 1. The ion optics consist of an ion repeller plate A1, an ion extraction plate A2, and an ion acceleration plate A3. A liner system was used to ensure a field-free ion drifting region in the Time-of-flight tube, and a Micro-Channel Plate (MCP) detector was used to measure the extracted ions. Since the primary interest in this study is to probe the intrinsic ions generated by the thermite event, the electron impact ionization source was not used for most of the experiments. The four experimental configurations of ion optics voltages and probe position are summarized in table 1.

The ion pulse was measured by inserting the T-Jump probe between the repeller plate A1 and the extraction plate A2 as shown in Figure 1. Charged species were continuously extracted by the ion optics, and consequently, the ion signal detected from the MCP is proportional to the total number of charged species generated during the thermite reaction,

but does not contain any ion mass information. To obtain an ion mass we pulse the ion optics in order to determine a drift time. In this manner the T-Jump/TOFMS was operated in the same way as we illustrated in our previous work,[4, 26] but without the electron impact ionization source. The T-Jump probe was placed outside, but near the ion extraction region, to obtain positive ion mass spectra. We were unable to obtain negative ion spectra, due to thermite reaction induced arcing in the ion-extraction region.

In addition to the ion pulse signals and mass spectra measurements, a high speed camera system (Phantom 12.1) was used to capture the optical emission from the ignition/combustion events. The camera capture images at a rate of 30 us per frame. For optical data processing purpose, we consider each image as a matrix of pixels, and the magnitude of the values in the matrix is the optical intensity for a given pixel, thus the total optical intensity from the summation of the matrix can be found for each image. The time resolved optical profile of each heating event can obtained by plotting the total optical intensity VS heating time. The optical profile can be considered as a measure of the reactivity and can be directly compared with the ion signal obtained from the same ignition event.

## RESULTS AND DISCUSSION
### Ignition Behavior Observed by Optical Emission
The ignition behavior of nanocomposite thermite samples in the T-Jump experiments was first examined from the time resolved images recorded by the high speed camera. Selected images for a Al/CuO thermite reaction are shown in Figure 2 (a) and the corresponding time resolved optical profile is presented in Figure 2 (b)., The time dependent temperature trace calculated from probe resistance change is also shown in Figure 2 (b). The result shows that the temperature rises to ~1600 K in 2.7 ms i.e. a heating rate of ~5 $\times 10^5$ K/s. This heating rate was used throughout our T-Jump experiments. It is seen from Figure 2 (a) that the optical registration is first observed at the two ends of the sample coating at time of 2.040 ms, indicating the ignition of the thermite sample. The ignition front then propagated from the two ends toward the center, and ignited the whole thermite sample at a time 2.187 ms. We define this ignition propagation time as the ignition interval as shown in Figure 2 (b). Quite clearly seen in Figure 2 (a) and (b) is that the thermite sample is also blown off the wire after the ignition, and continues to react until ~3 ms, i.e. overall reaction time ~ 1 ms. For the other nanocomposite thermite systems investigated, e.g. $Al/Fe_2O_3$ $Al/WO_3$ and $Al/Bi_2O_3$, similar ignition behavior was observed from the camera images. However, due to space limitations, we will only show the time resolved optical intensity profile in the rest of our analysis of the thermite reaction induced ion pulses.

### Ion Pulse Generation and its Relationship to Ignition
Figure 3 shows typical results of the positive ion pulse signal measurement for (a) $Al/CuO$, (b) $Al/WO_3$, (c) $Al/Fe_2O_3$ and (d) $Al/Bi_2O_3$ nanocomposite thermite mixtures. The ion signals are plotted as function of T-Jump heating time. The zoom-in views are also plotted in Figure 3 to show the fine structure of the ion signals. An important piece of information that is available from Figure 3 is the temporal evolution of the ion

generation process, which corresponds to the width of the ion signal. As we can see in the zoom-in view of Figure 3 (a), the ionization duration for Al/ CuO reaction is about ~0.3 ms (from 1.85 ms to 2.15 ms) but the major ion pulse lasts less than ~0.1 ms, Similarly, Al/WO$_3$ has an ionization interval of ~0.3 ms but has an intense current spike lasting only ~0.02 ms (Figure 3 (b)). The ion signal from Al/ Fe$_2$O$_3$ reaction (Figure 3 (c)), which lasted for about ~0.4 ms, exhibits the longest ionization period among all four nanocomposite thermites. Al/Bi$_2$O$_3$ shows the shortest ionization period among all four nanocomposite thermite systems; the ion signal in Figure 3 (d) is ~0.1 ms with the major ion peak width lasting less than ~0.03 ms.

We now turn our attention to how the positive ion pulses are related to the nanocomposite thermite combustion, by comparing ion pulse signal with the corresponding time resolved intensity profile which is shown at the bottom of each figure. Here we would like to first point out that although the camera and the heating of the probe are triggered simultaneously, the ions were detected by the MCP detector after the ions drifted in the linear TOF tube, so the ion signals are slightly delayed compared with the time resolved images. However, as the delay time is only on the order of ~10 us we will ignore this difference.

As we can see from Figure 3 (a), the Al/CuO ion signal starts to rise at ~1.85 ms, much before the first ignition event at 2.04 ms was observed optically. The whole thermite sample was ignited by 2.22 ms, so that the ignition interval is 2.04 - 2.22 ms, and the thermite sample was continuously reacting until ~3 ms as shown in the bottom of Figure 3 (a). On the other hand, the major ion peak in Figure 3 (a) occurs at ~ 2.05 ms, which roughly coincides with the first ignition event, and the ion generation process is over well before the whole sample had even ignited. This behavior is particularly obvious for Al/ WO$_3$ system as the ion current pulse in Figure 3 (b) is complete by 2.07 ms, in contrast to the ignition which did not start until ~2.2 ms. The situation for the Al/Fe$_2$O$_3$ and Al/Bi$_2$O$_3$, Figures 3 (c) and (d), respectively, are not as clear. The positive ion pulse seems to initiate prior to ignition but the bulk of the ion generation is coincident with the ignition phase, followed by a bright emission phase that lasts well after the ion pulse is over. Finally for the Al/Bi$_2$O$_3$ system we see that optical and ion signal are coincident. These results suggest a general conclusion that the positive ion generation either precedes or is coincident with thermite initiation, and therefore is not a product of combustion but rather precedes it. Secondly the ion generation is relatively short, as compared to the burning time, and is relatively independent of species type.

Similar experiments were conducted to measure the negative species (ions or electrons). Figure 4 shows the negative pulse signal for (a) Al/CuO, (b) Al/WO$_3$ and (c) Al/Fe$_2$O$_3$, and the corresponding optical signal is also plotted at the bottom of each figure. The Al/Bi$_2$O$_3$ nanocomposite thermite reaction caused arcing for this experimental configuration and will be discussed later. In general we summarize the finding that the negative currents are longer in duration than the corresponding positive currents, but perhaps what is more intriguing is that unlike positive species which were observed before ignition, negative species were generated during the ignition, suggesting there is a separate ionization process and that the negative species were closely associated with the ignition. This suggests that there is a two step ionization process which is generic and independent of the composite formulation.

From the above temporal analysis on the positive/negative signals, we can conclude that there are two primary ionization steps around the ignition point. The first ionization step happens prior to ignition and is dominated by positive ions. Then the ignition of nanocomposite thermite mixture leads to a second ionization step which primarily produces negative species. After ignition has propagated along the T-Jump probe, the reactants are blown off of the wire, but the thermite reaction continues. Analysis at later times does show that there were still some ions detected during this time, but the intensity is much lower than that of the initial ion pulse.

The peak intensities of the ion peaks correspond to the instantaneous ion density, and can be used as a relative measure of ionization rates. From Figure 3, we see that ion intensity varies as a function of composite mixture, from ~5 a.u. to 30 a.u. and provides for an ordering of ionization rates: $Al/Bi_2O_3 > Al/WO_3 > Al/CuO > Al/Fe_2O_3$. Similar analysis of Figure 4 indicates negative ionization rates are also species dependent: $Al/CuO > Al/Fe_2O_3 > Al/WO_3$

The integrated ion signal corresponds to the total current to the detector, and can be used to evaluate the overall ions densities. Figure 5 shows the integrated positive and negative currents for (a) $Al/CuO$, (b) $Al/WO_3$, (c) $Al/Fe_2O_3$ and (d) $Al/Bi_2O_3$ (only positive ion signal available). Because the positive and the negative signals are measured in separate experiments, the ignition times may be slightly different due to differences in coating thickness, wire length, etc., and one cannot directly compare the temporal evolution of the integrated curves. Nevertheless, the results for $Al/Fe_2O_3$ and $Al/CuO$ systems, and especially the $Al/WO_3$ system, clearly show that the positive species appear before the negative ones, consistent with our temporal analysis.

The integrated ion signals presented in Figure 5 are divided into three regions labeled, pre-ignition heating, ignition ionization (including both positive and negative ion currents) and post ignition. During the initial heating, the integrated ion signals remain flat, however as the wire is heated both positive and negative integrated ion signal rise sharply. Following that stage, the integrated signals continuously increased, but at a much slower rate. This result indicates that there is still ion generation taking place even after the intense ion pulse is over, but with a much lower current. This is not a surprise considering the thermite powder is still reacting after the ignition interval and the chemical reaction leads to a relatively "soft" ionization. This result also indicates that the ionization through the thermochemical channels is much less intense than the ion pulse observed around the ignition interval.

In addition to the total integrated ion signals, we also calculated the peak area of the ignition associated positive/negative ion peaks, e.g. the integral of the zoom-in view signal, and the results are also listed in each of Figures 3 and 4. The peak areas for positive ion signals are 0.46, 0.46, 0.42 and 0.53 for $Al/Fe_2O_3$, $Al/CuO$, $Al/WO_3$ and $Al/Bi_2O_3$ thermite systems, respectively. As we can see, even though the signal intensities are significantly different, peak areas observed from different nanocomposite thermite mixtures are comparable. In other words, the $Al/Fe_2O_3$ system ionizes at a slower rate but for longer time, while the $Al/Bi_2O_3$ system ionizes much more aggressively, but for a shorter duration. The result is that the overall number densities of positive ions generated from the ionization process are about the same. A similar result is also found for negative species, with peak areas for negative ion signals of 0.51, 0.57, and 0.65 for $Al/Fe_2O_3$,

Al/CuO, and Al/WO$_3$ thermite systems, respectively, and consistent with the positive current results, that total current generation is species independent.

Now as we compare the peak areas for the positive and negative species, we can see that there are slightly more negative species detected than the positive species. More evidence supporting a surplus of negative species can be found if we consider the fact that the T-Jump probe was slight positively biased during heating. The presence of the T-Jump probe tends to repel the positive species but attract negative ones, so that the positive ions may be extracted with a higher efficiency than the negative species. We found that the ionization induced arcing has a polarity preference; it only occurs when we have positively biased ion optics near the T-Jump probe. Through the course of our investigation we have concluded that in general, arcing occurs if there is an open path from the T-Jump probe to a positively biased electrode. Consequently, we are not able to conduct mass specrometry on negative species. We believe the polarity effect can be attributed to the density differences between the positive and negative ion formations. Since negative species have higher ion density than positive ones, the transient current pulse collected by the positively biased electrode is much more intense, and creates a higher possibility of arcing. Furthermore, comparing with the behavior of RDX and Nitrocellulose which did induce arcing even with positively biased ion optics,[4] we conclude that the degree of ionization from nanocomposite thermite systems is orders magnitude higher than high explosives.

**Species Identification by Mass Spectrometry**

Given the limitations discussed in the paragraph above regarding negative species induced arcing we turn our attention to identifying the positive ion species by mass spectrometry. The Al/Fe$_2$O$_3$ system showed relatively weak ion signal (Figure 3 c) and we were unable to detect any nascent ions in the TOF mass spectra. On the other hand, mass spectra for Al/CuO, Al/Bi$_2$O$_3$ and Al/WO$_3$ systems all show intense nascent ion signals. Example spectra for Al/CuO thermite is shown in Figure 6 (a). In these experiments the electron impact ionization source in our mass spectrometer was turned off to ensure the thermite reaction as the sole source of ions. However, the tradeoff of not using the electron gun is loss of resolution as compared to the normal mass spectrometer operation. An example mass spectra of the Al/CuO thermite reaction obtained with an external electron impact ionization source is shown in Figure 6 (b), and detailed analysis of this mass spectra can be found elsewhere.[26] Despite the lower resolution, ion peaks of Na (m/z = 23), Al (m/z = 27) and K (m/z = 39) can be clearly identified in figure 6 (a). A small peak at m/z = 64, corresponds to Cu, and suggests Cu ions may be generated as minor species from the thermite reaction induced ionization. Mass spectra for both Al/Bi$_2$O$_3$ and Al/WO$_3$ showed similar results to the Al/CuO. Independent of thermite compositions, the positive mass spectra all contain a strong Na peak, suggesting the positive ion species distributions are dominated by Na with minor species of Al and K for all the tested thermite systems. There is also a clear Bi peak (m/z = 209) observed for Al/Bi$_2$O$_3$ thermite system, but no W species can be found for the case of Al/WO$_3$. This observation is consistent with the fact that Al/Bi$_2$O$_3$ produces the most intense ionization.

The mass spectrometric measurement indicates that the major current generating species are not the primary components comprising the composite particles, but rather Na and K

derived salts that while a minor component on a mass basis, evidently can result in intensive ion currents. The mass spectra patterns obtained for three different thermites show similar ion peak patterns, suggesting a common ionization mechanism that governs the generation of positive ion species.

**On the Mechanism of Ion Generation**

Together with the observation of Al species in the mass spectra, we believe that the underlying ionization mechanism for positive ions should be closely related to the ion flux in the shell of the aluminum nanoparticles. Recently, we have studied the ignition behavior of nanocomposite thermites under T-Jump heating conditions (heating rate ~$10^5$ K/s), and the results suggest that the ignition of nanocomposite thermites is controlled by diffusion of molten aluminum through the oxide shell.[27] Diffusion controlled metal oxidation theories have been studied for several decades and depending on the types of metal or thickness of the oxide layer, various theoretical models have been developed to study metal oxidation.[28-30] It is believed that the diffusion of ions and electrons through the oxide shell due to concentration and pressure gradients, or an electric field within the oxide layer, is the controlling transport process for metal oxidation.[31-33] From Cabrera and Mott's thin film growth theory, a strong electric field on the order of ~$10^7$ V/cm is predicted across the oxide shell caused by tunneling electrons, and thus ion transport is driven by the electric field.[34, 35] We have also observed a similar electric field driven ion transport in aluminum nanoparticles at high temperatures through molecular dynamics simulations.[21] The simulation results show that the strong electric field is intrinsically self-generated due to the presence of the oxide shell, which provides a strong driving force for ion transport. In the case of 6 nm aluminum nanoparticles with a 2 nm oxide shell, the simulations shows an Al ion flux of ~20 mole/cm$^2$/sec at 1100 K is primarily due to the electric field as opposed to the concentration and pressure gradients. For the larger aluminum nanoparticles that we used in these experiments, an even higher ion flux should be expected.

Based on the above discussion, the positive ion generation can be explained as follows. Prior to the ignition point the aluminum particles are already at elevated temperatures and the nascent electric field is formed across the oxide shell. Assisted by the electric field, aluminum ions move radially outward through the oxide shell. On the other hand, the salts exist at the particle surface in the form of Na$^+$, K$^+$ and Cl$^-$ ions and are weakly bonded with surface atoms. As the aluminum ions reach the particle surface, electrostatic repulsion between Al$^+$ and Na$^+$ or K$^+$ eject the Na$^+$ and K$^+$ ions from particle surface. As a result, transient ion pulses composed of Na$^+$, K$^+$ and some Al$^+$ are observed just prior to the ignition of the thermites. If we assume the electrostatic repulsion force from a coulomb potential only becomes significant when two ions are within 1 nm of each other, then based on an Al ion flux of ~20 mole/cm$^2$/sec predicted by our molecular dynamic simulations,[21] aluminum ions will be moving toward a single Na$^+$ or K$^+$ ion at the rate of ~$10^{11}$ number per sec. In other words, during our observed ionization interval of ~0.1 ms, there are ~$10^7$ aluminum ions around a single Na$^+$ or K$^+$ ion. As a result of the strong electrostatic repulsion, Na$^+$ and K$^+$ ions are ejected as the most abundant species even though the salt contaminations in the thermite should be low. In addition, our experimental results suggest that the total number of positive ions produced from

different thermite reaction systems are about the same regardless of the thermite compositions, consistent with a common source of ions regardless of particle type.

To test our diffusion based ion-current theory we mix the $Al/Fe_2O_3$ thermite sample with sodium chloride salt. As expected, the total positive ion signal in Figure 7 (a) shows the same transient nature of the ion generation but a much stronger intensity than regular $Al/Fe_2O_3$ thermite sample (Figure 3 (c)) and the corresponding mass spectra in Figure 7 (b) show a strong Na, Al and K peaks, agreeing with our expectation. The result shown in Figure 7 confirms the salt contamination as the primary positive ions source, and suggests our diffusion flux based ionization mechanism for positive ion pulse generation is correct. As our experimental results suggest, the ionization is a two step process, and the negative species are emitted during the ignition of thermite reactions. However, our current mass spectrometer configuration would not allow us to obtain negative mass spectra, and consequently, it is difficult to extract complete mechanistic information without the knowledge of species identification. The fact that the negative ionization step occurs during the ignition event, suggests the strong relation between the solid phase nanocomposite thermite reaction and the ionization process.

**CONCLUSIONS**

During the development of the Temperature Jump/Time of Flight Mass Spectrometer (T-Jump/TOFMS) for studying the nanocomposite thermite reactions, we observed a strong ion pulse generation phenomenon. In this paper we investigate the characteristic features of this ion pulse arising from the combustion of $Al/CuO$, $Al/WO_3$, $Al/Fe_2O_3$ and $Al/Bi_2O_3$ nanocomposite thermite mixtures. The transient current pulse nominally occurs over ~ 0.1 ms, and is much shorter than the characteristic reaction time of typical thermite mixtures. The ion pulse signals for positive and negative species, show that the thermite induced ionization occurs close to the point of ignition of the thermite powders, and is characterized by two ionization steps. The first ionization step happens prior to ignition which primarily produces positive ions, and the ignition leads to a second ionization step which is dominated by negative species. The mass spectrometric measurements revealed that the positive ion species distributions are dominated by Na with minor species of Al and K for all the tested thermite systems. The positive ion generation was attributed to the interaction between the Al ion diffusion flux through the oxide shell and the salt contamination at the particle's surface. The strong electrostatic repulsion formed by the Al flux ejects the Na and K ions from the particle's surface. However, we are not able to obtain spectra for the negative species due to induced arcing from the strong negative ion pulse.

**REFERENCE**

1.	K. Sullivan, G. Young, and M.R. Zachariah, *Enhanced Reactivity of Nano-B/Al/CuO MICs*. Combustion and Flame., 2009. **156**: p. 302.

2.	Umbrajkar, S.M., S. Seshadri, M. Schoenitz, V.K. Hoffmann, and E.L. Dreizin, *Aluminum-rich Al-MoO3 nanocomposite powders prepared by arrested reactive milling.* J. Propul. Power, 2008. **24**(2): p. 192-198.

3.	Prakash, A., A.V. McCormick, and M.R. Zachariah, *Tuning the reactivity of energetic nanoparticles by creation of a core-shell nanostructure.* Nano Lett., 2005. **5**(7): p. 1357-1360.

4.	Zhou, L., N. Piekiel, S. Chowdhury, and M.R. Zachariah, *T-Jump/Time-of-Flight Mass Spectrometry for Time Resolved Analysis of Energetic Materials.* Rapid Communications in Mass Spectrometry, 2009. **23**(1): p. 194-202.

5.	Young, G., K. Sullivan, and M.R. Zachariah, *Combustion Characteristics of Boron Nanoparticles.* Combustion and Flame, 2009. **156**: p. 332.

6.	Sanders, V.E., B.W. Asay, T.J. Foley, B.C. Tappan, A.N. Pacheco, and S.F. Son, *Reaction propagation of four nanoscale energetic composites (Al/MoO3, Al/WO3, Al/CuO, and Bi2O3).* J. Propul. Power, 2007. **23**(4): p. 707-714.

7.	Pantoya, M.L. and J.J. Granier, *The effect of slow heating rates on the reaction mechanisms of nano and micron composite thermite reactions.* Journal of Thermal Analysis & Calorimetry, 2006. **85**(1): p. 37-43.

8.	Trunov, M.A., M. Schoenitz, and E.L. Dreizin, *Ignition of aluminum powders under different experimental conditions.* Propellants Explosives Pyrotechnics, 2005. **30**(1): p. 36-43.

9.	Plantier, K.B., M.L. Pantoya, and A.E. Gash, *Combustion wave speeds of nanocomposite Al/Fe2O3: the effects of Fe2O3 particle synthesis technique.* Combustion and Flame, 2005. **140**(4): p. 299-309.

10.	Fialkov, A.B., *Investigations on ions in flames.* Progress in Energy and Combustion Science, 1997. **23**(5-6): p. 399-528.

11.	Filimonov, I. and N. Kidin, *High-Temperature Combustion Synthesis: Generation of Electromagnetic Radiation and the Effect of External Electromagnetic Fields (Review).* Combustion, Explosion, & Shock Waves, 2005. **41**(6): p. 639-656.

12.	Ershov, A.P., *Ionization During Detonation of Solid Explosives.* Combustion Explosion and Shock Waves, 1975. **11**(6): p. 798-803.

13.	Setoodeh, M., K.S. Martirosyan, and D. Lussa, *Electrical pulse formation during high temperature reaction between Ni and Al.* Journal of Applied Physics, 2006. **99**(8).

14.	Martirosyan, K.S., M. Setoodeh, and D. Luss, *Electric-field generated by the combustion of titanium in nitrogen.* Journal of Applied Physics, 2005. **98**(5).

15.	Kirdyashkin, A.I., V.L. Polyakov, Y.M. Maksimov, and V.S. Korogodov, *Specific features of electric phenomena in self-propagating high-temperature synthesis.* Combustion Explosion and Shock Waves, 2004. **40**(2): p. 180-185.

16.	Martirosyan, K.S., J.R. Claycomb, J. H. Miller, Jr., and D. Luss, *Generation of the transient electrical and spontaneous magnetic fields by solid state combustion.* Journal of Applied Physics, 2004. **96**(8): p. 4632-4636.

17.	Igor Filimonov, D.L., *Formation of electric potential during the oxidation of a metal particle.* AIChE Journal, 2004. **50**(9): p. 2287-2296.

18.	Martirosyan, K.S., J.R. Claycomb, G. Gogoshin, R.A. Yarbrough, J.H. Miller, and D. Luss, *Spontaneous magnetization generated by spin, pulsating, and planar combustion synthesis.* Journal of Applied Physics, 2003. **93**(11): p. 9329-9335.

19. Martirosyan, K.S., I.A. Filimonov, and D. Luss, *Self-Heating by Joule Dissipation during Gas-Solid Combustion Reactions.* International Journal of Self-Propagating High-Temperature Synthesis, 2003. **12**(2): p. 91.

20. Martirosyan, K.S., I.A. Filimonov, M.D. Nersesyan, and D. Luss, *Electric field formation during combustion of single metal particles.* J. Electrochem. Soc., 2003. **150**(5): p. J9-J16.

21. Henz, B.J., T. Hawa, and M.R. Zachariah, *On the Role of Built-in Electric Fields on Oxidation of Oxide Coated NanoAluminum: ion mobility versus Fickian Diffusion.* submitted to Phys. Rev. B., 2009.

22. Munir, Z.A., *The effect of external electric fields on the nature and properties of materials synthesized by self-propagating combustion.* Materials Science and Engineering A, 2000. **287**(2): p. 125-137.

23. Carleton, F.B. and F.J. Weinberg, *Electric field-induced flame convection in the absence of gravity.* Nature, 1987. **330**(6149): p. 635-636.

24. Douglas, G.T., W.A. Blaine, C.K. James, V.E. Sanders, and F.S. Steven, *Dynamic measurements of electrical conductivity in metastable intermolecular composites.* Journal of Applied Physics, 2006. **99**(2): p. 023705.

25. Korogodov, V.S., A.I. Kirdyashkin, Y.M. Maksimov, A.A. Trunov, and R.M. Gabbasov, *Microwave radiation from combustion of an iron-aluminum thermite mixture.* Combustion Explosion and Shock Waves, 2005. **41**(4): p. 481-483.

26. Zhou, L., N. Piekiel, S. Chowdhury, and M.R. Zachariah, *Time-Resolved Mass Spectrometry of nanocomposite thermite reactions.* manuscript in preparation, 2009.

27. Chowdhury, S., K. Sullivan, N. Piekiel, L. Zhou, and M.R. Zachariah, *Diffusive vs. Explosive Reaction at the Nanoscale.* in preparation, 2009.

28. Atkinson, A., *Transport processes during the growth of oxide films at elevated temperature.* Reviews of Modern Physics, 1985. **57**(2): p. 437.

29. A. T. Fromhold, Jr., *Theory of Metal Oxidation Volume 2.* Vol. 2. 1980: North-Holland Publishing Company.

30. A. T. Fromhold, Jr., *Theory of Metal Oxidation Volume 1.* Vol. 1. 1976: North-Holland Publishing Company.

31. Rai, A., K. Park, L. Zhou, and M.R. Zachariah, *Understanding the mechanism of aluminium nanoparticle oxidation.* Combustion Theory and Modelling, 2006. **10**(5): p. 843 - 859.

32. Fromhold, A.T. and E.L. Cook, *Kinetics of Oxide Film Growth on Metal Crystals: Electronic and Ionic Diffusion in Large Surface-Charge and Space-Charge Fields.* Physical Review, 1968. **175**(3): p. 877.

33. Wagner, C., *The theory of the warm-up process.* Z. Phys. Chem. Abt. B, 1933. **21**(25).

34. Cabrera, N. and N.F. Mott, *Theory of the Oxidation of Metals.* Reports on Progress in Physics, 1948. **12**: p. 163-184.

35. Zhdanov, V.P. and B. Kasemo, *Cabrera-Mott kinetics of oxidation of nm-sized metal particles.* Chem. Phys. Lett., 2008. **452**(4-6): p. 285-288.

Table I: Summary of the configurations of ion optics voltages and probe position

| | Positive ions | Negative ions[#] | Positive mass spectra | Negative mass spectra[*] |
|---|---|---|---|---|
| Probe position | Inside | Inside | Outside | Outside |
| A1 | Ground | DC -200V | Ground | Pulsed ground to -200V |
| A2 | DC -200V | Ground | Pulsed ground to -200V | Ground |
| A3 and liner | DC -1500V | DC +1300V | DC -1500V | DC +1300V |

\# Al/Bi$_2$O$_3$ thermite mixture caused arcing in this configuration

\* All four types of thermite mixtures caused arcing in this configuration

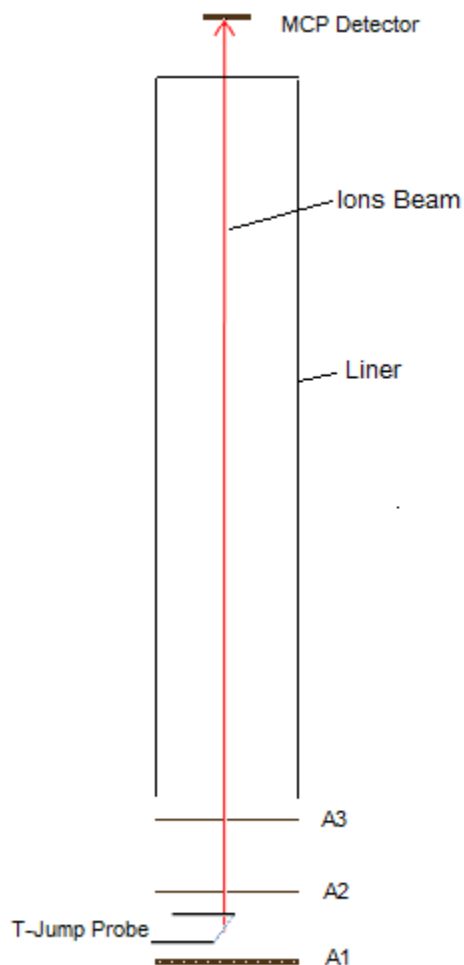**Figure 1:** Schematic of ion optics in the T-Jump/TOFMS
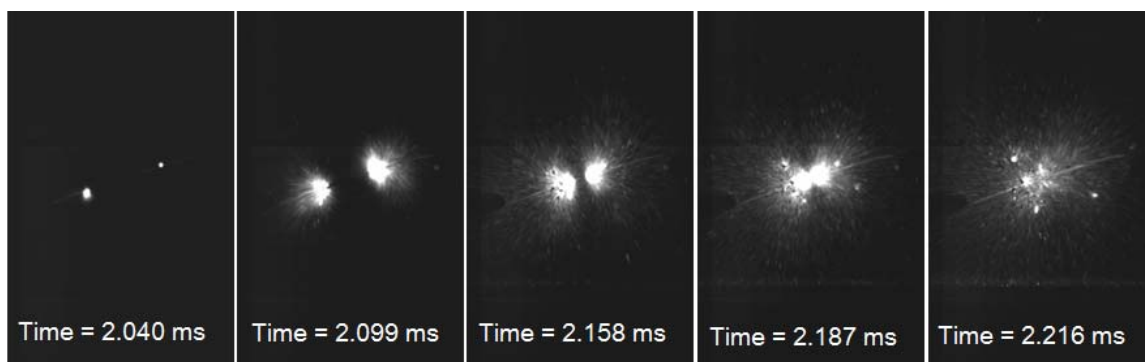


**Figure 2 (a):** Selected images for a Al/CuO thermite reaction recorded by high speed camera
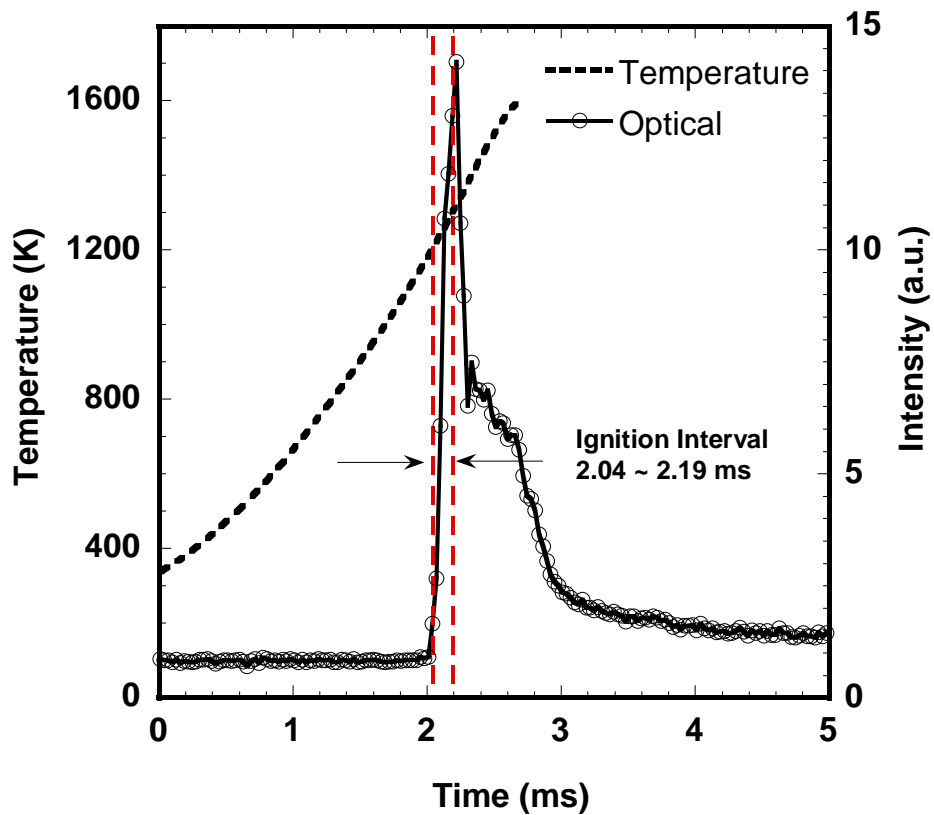
**Figure 2 (b):** The time resolved optical profile of a Al/CuO thermite reaction obtained from the high speed camera images, and the T-Jump temperature trace calculated from probe resistance measurement.
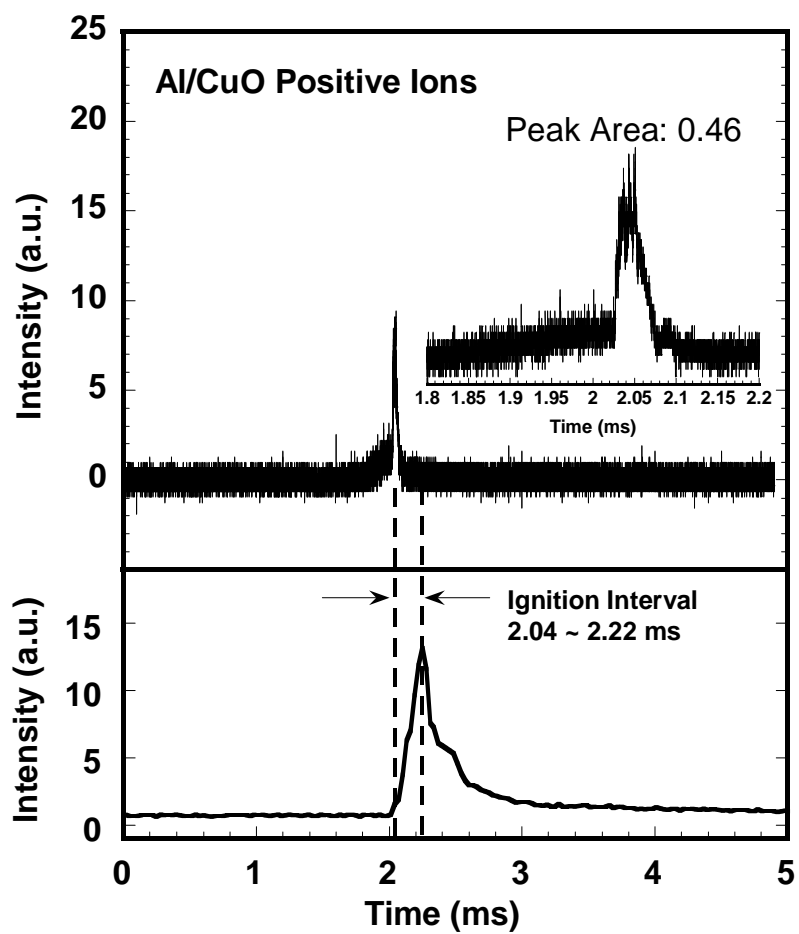
**Figure 3 (a)**
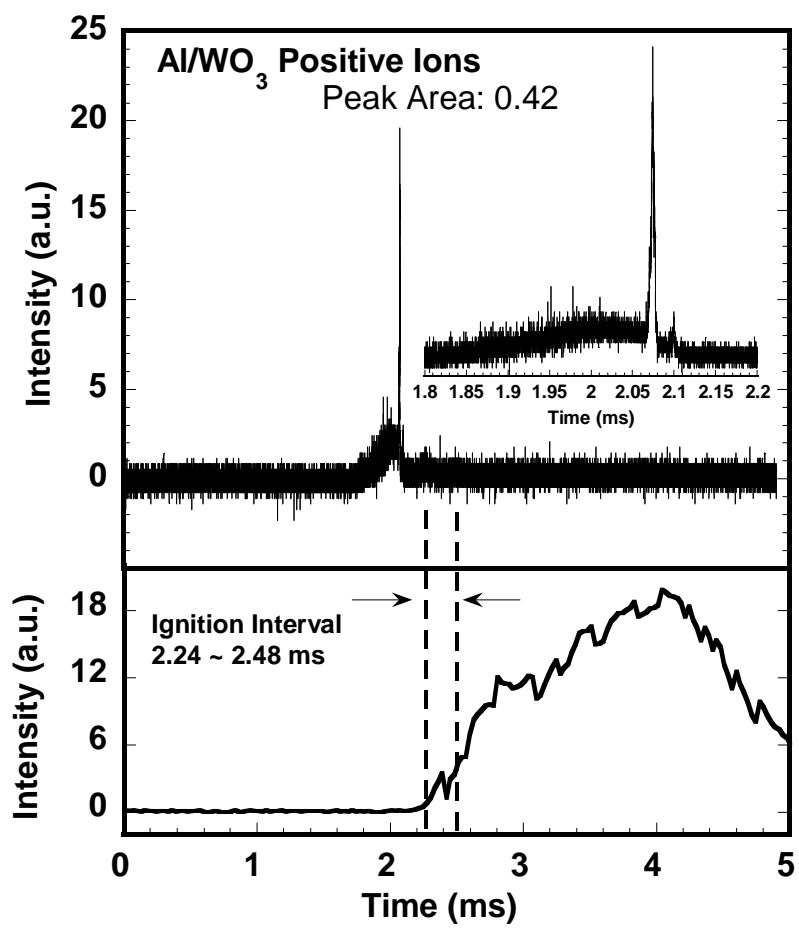
**Figure 3(b)**
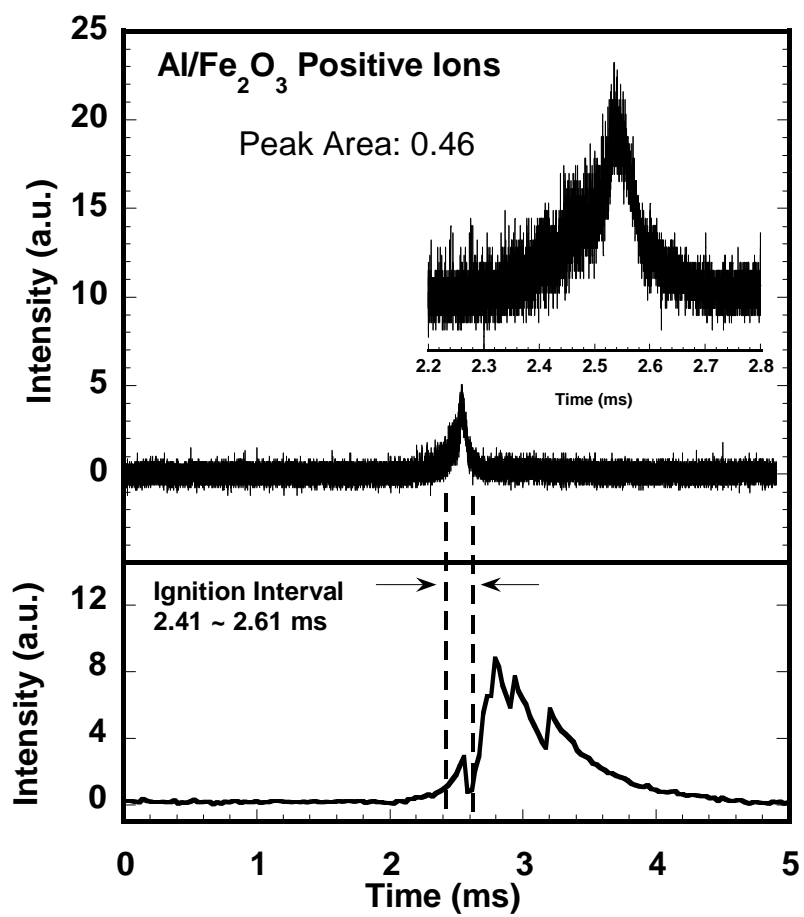
**Figure 3 (c)**
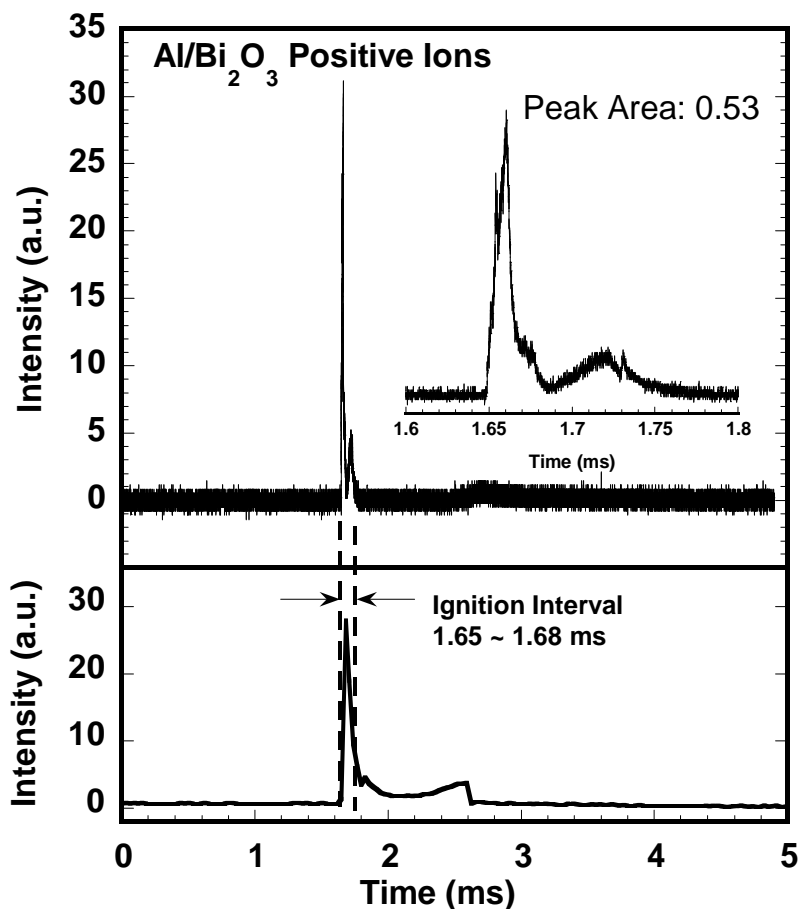
**Figure 3 (d)**

**Figure 3:** Typical results of the total positive ion measurement for (a) Al/CuO, (b) Al/WO$_3$, (c) Al/Fe$_2$O$_3$ and (d) Al/Bi$_2$O$_3$ nanocomposite thermite mixtures. The zoom-in view shows the fine structure of the ion signal. The corresponding optical profile from the high speed camera is shown in the bottom of the each figure.
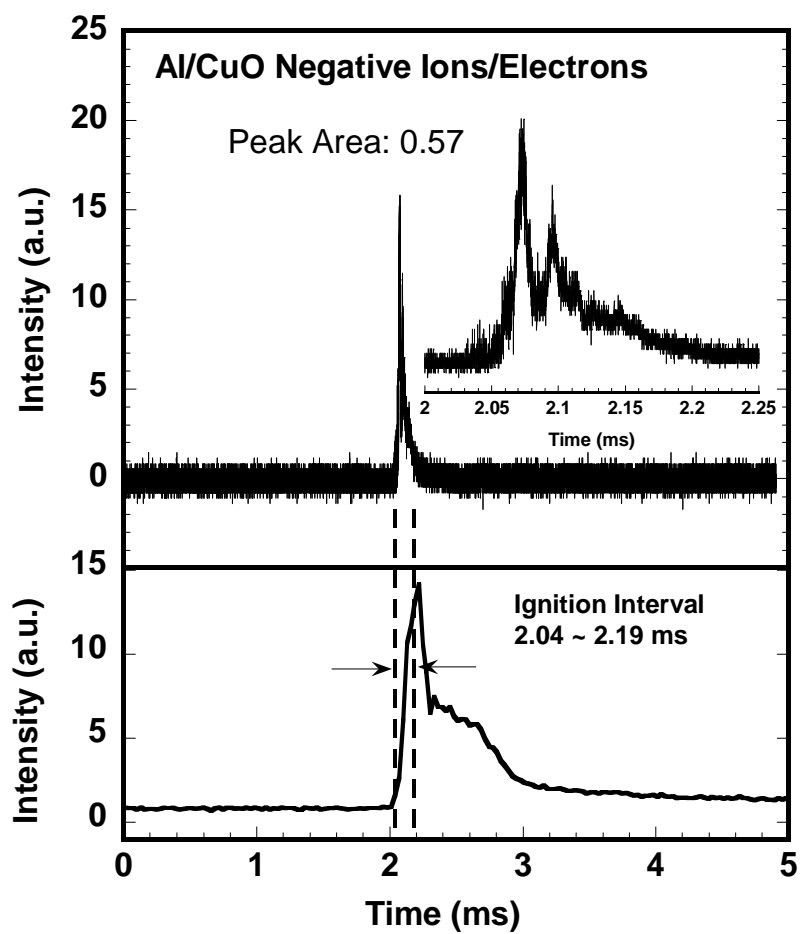
**Figure 4 (a)**
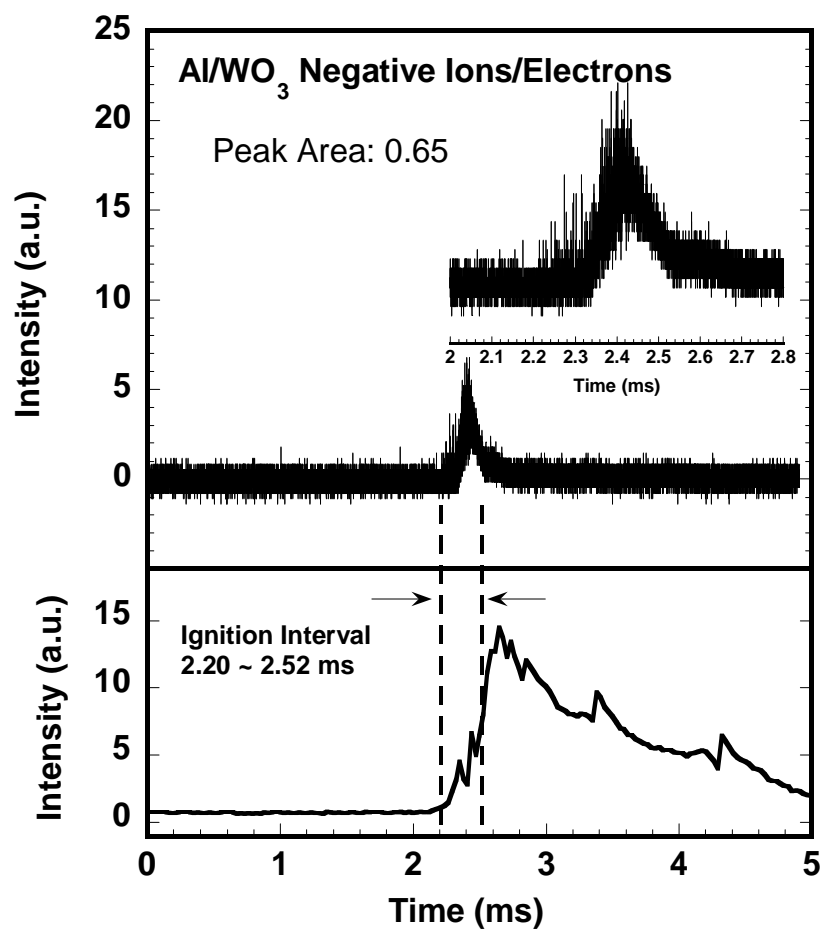
**Figure 4 (b)**
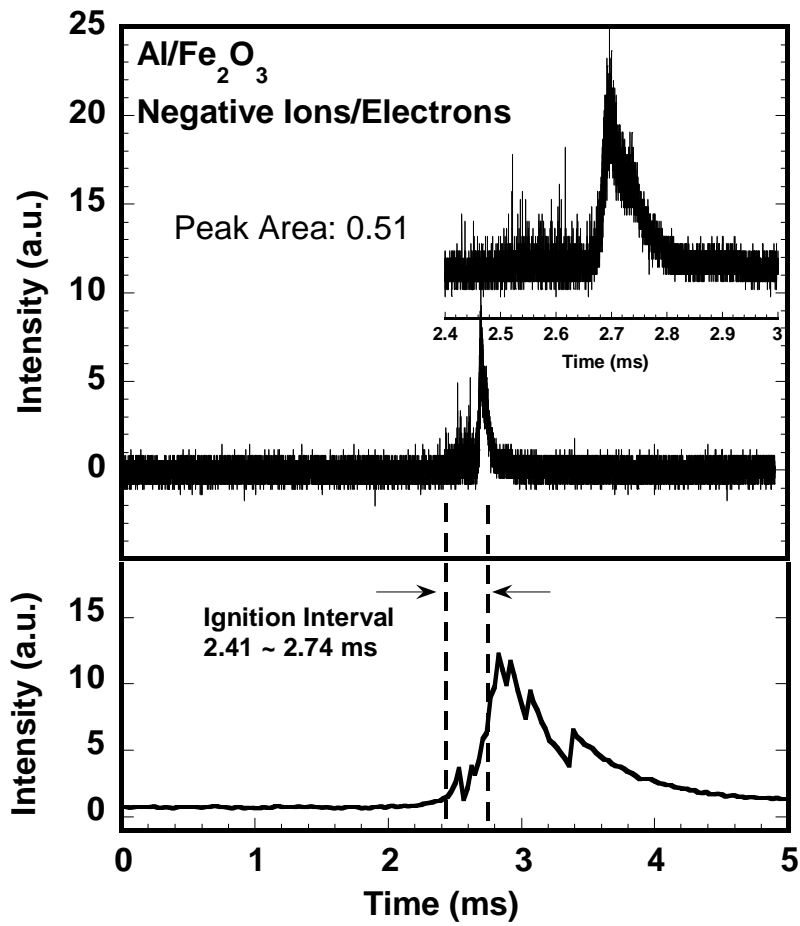
**Figure 4 (c)**

**Figure 4:** Typical results of the total negative ion measurement for (a) Al/CuO, (b) Al/WO$_3$, and (c) Al/Fe$_2$O$_3$ nanocomposite thermite mixtures. The zoom-in view shows the fine structure of the ion signal. The corresponding optical profile from the high speed camera is shown in the bottom of the each figure.

**(a)**                                                                      **(b)**

78
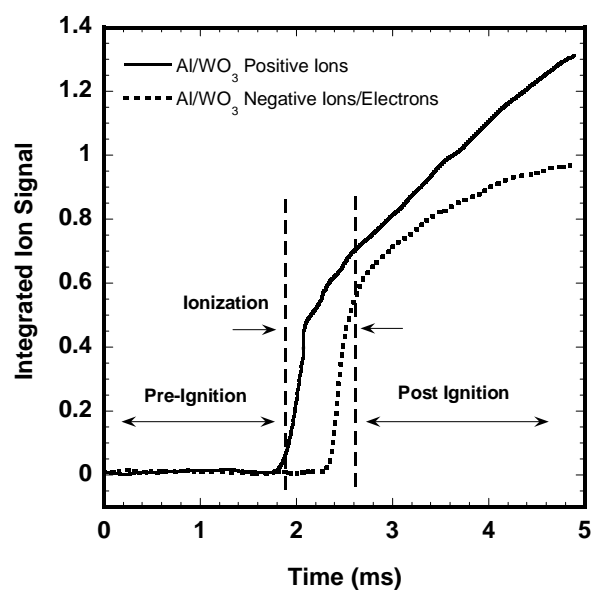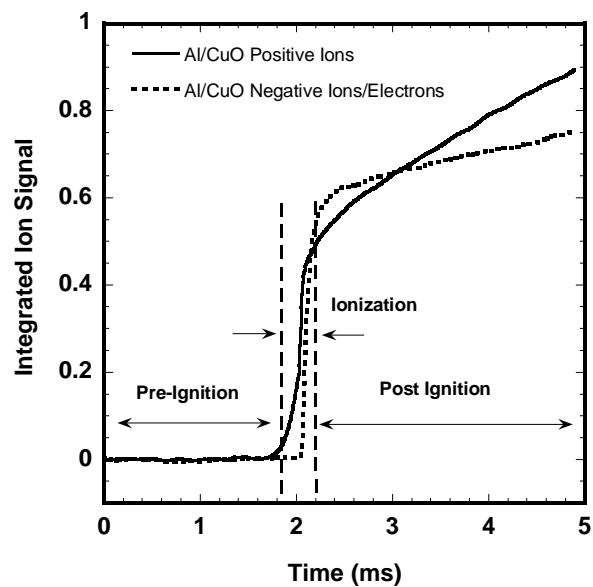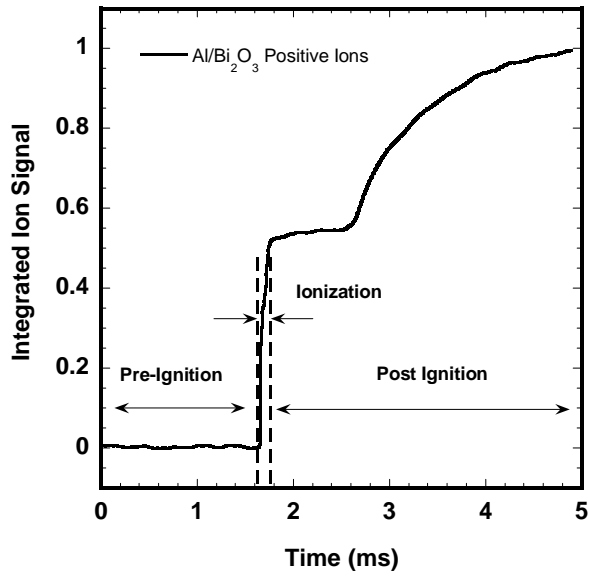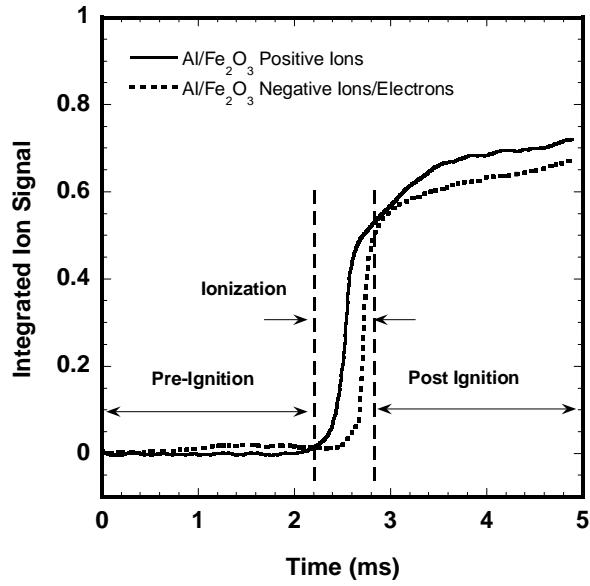
**(c)**                                           **(d)**

**Figure 5:** The integrated positive and negative currents for (a) Al/CuO, (b) Al/WO$_3$, (c) Al/Fe$_2$O$_3$ and (d) Al/Bi$_2$O$_3$ (only positive ion signal available)
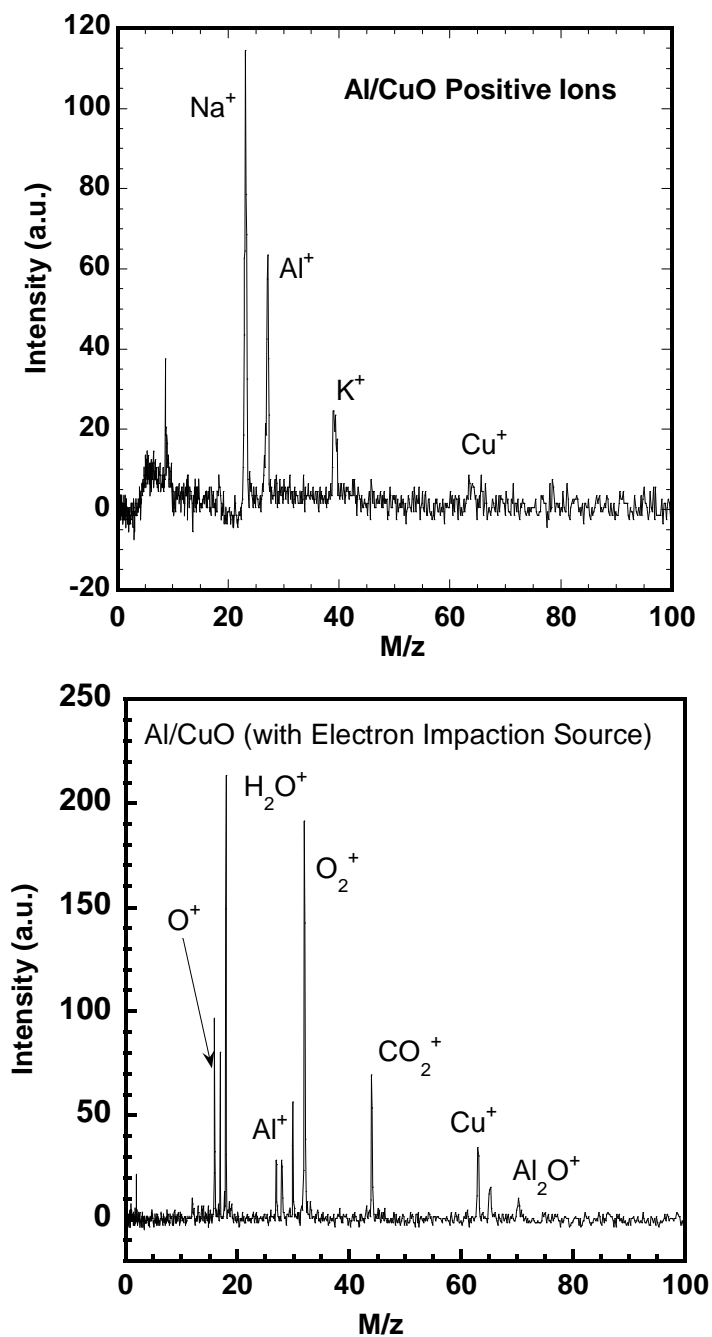
**Figure 6 (a):** Example spectra for positive ion species generated from Al/CuO thermite (without external electron impact ionization source). **and (b):** Al/CuO thermite reaction obtained with external electron impact ionization source
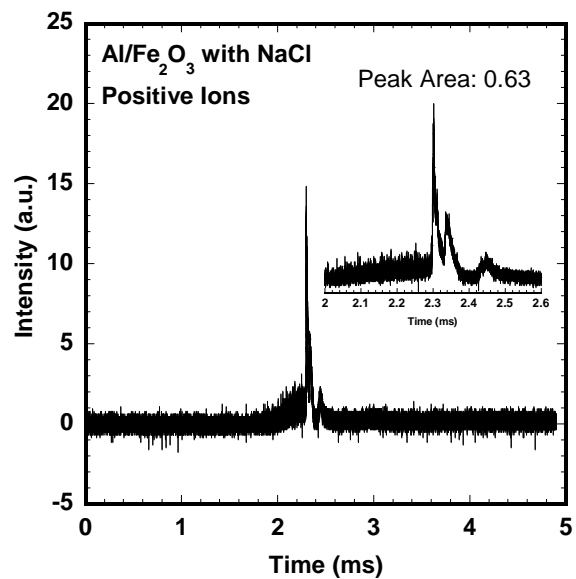
**Figure 7 (a)**
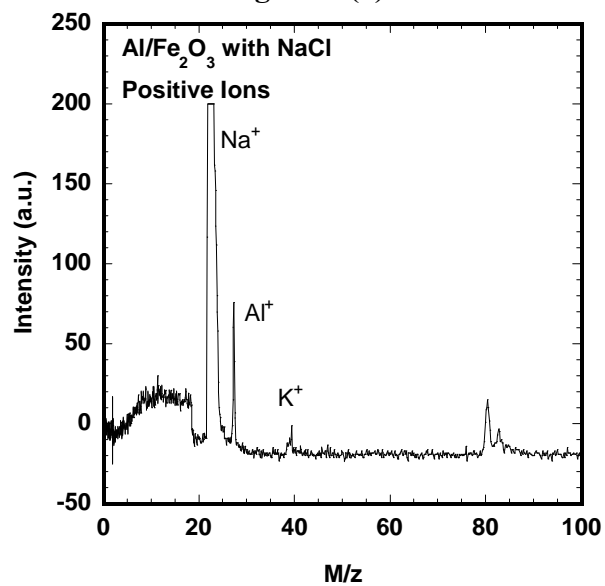


**Figure 7 (b)**

**Figure 7 (a):** the total positive ion signal for a Al/Fe$_2$O$_3$ thermite sample mixed with sodium chloride salt. **and (b):** the corresponding mass spectra measure of positive ion generated from the thermite reaction (without external electron impact ionization source)

Diffusive vs. Explosive Reaction at the Nanoscale

ABSTRACT. Solid-Solid reactions at the nanoscale between a metal passivated with a nascent oxide, and another metal oxide can have energy densities thrice that of TNT, and result in a very violent reaction. The natural question as to the mechanism has led to contrasting theories that either involves a mass-transfer (i.e. diffusive) mechanism, or alternatively, a more violent explosive mechanism. In this study using Al-CuO nanocomposites, with various oxide shell thicknesses on the aluminum particles, we find that pulsed heating at rates of $\sim 10^5$K/s results in an ignition delay. This delay is used as a probe to extract effective diffusion coefficient of the diffusing species. Fast time-resolved mass spectrometry, confirms this result. The results of this experiment are consistent with a diffusion controlled mechanism.

## 1. Introduction

Nanoscale particles composed of a metal and metal oxide can undergo a violent thermite reaction. Furthermore it is well known that making the particles smaller increases the reaction rate dramatically. An example of such reactions include Al + CuO which under stoichiometric conditions yield an adiabatic reaction temperature of 2840 K, with an energy density more than a factor of 3 over TNT on a volume basis. Nevertheless because of the interrelationship between many complex processes occurring, considerable debate continues as to the nature of initiation of the thermite event. Close proximity of the fuel and oxidizer reduces the diffusion length and increases their reaction rate[1]. Fuel nanoparticles usually have lower melting point than their micron size counterparts[2,3] making them easier to ignite. However, at those length scales, heat transfer rates are extremely fast and hence reaction characteristics such as onset of reaction/ignition temperature, ignition delays etc. are known to depend on the particle size[4-6]. In this letter, we will address some key issues on ignition behavior.

We consider the Al/CuO nanoscale thermite system as representative of the wide class of such reactions. The aluminum fuel component is actually a core shell structure of an aluminum core with an aluminum oxide passivation layer. Typically such layers are on the order of a few nanometers[7]. Nominally we consider the nanoscale regime to be those where both components (metal and metal oxide) are below 100 nm in diameter.

It is important, before proceeding further, to define some terminologies. Ignition temperature is defined as the temperature at which a particle/mixture can sustain chemical reaction on its own, without the aid of an external heat source. Ignition temperature is a strong function of experimental conditions as well as material property. Ignition delay is defined as the time taken to preheat the particle to its ignition temperature and hence would depend strongly on heating rate.

Briefly, let us review our current knowledge about ignition of aluminum particles. For micron sized particles, ignition temperature has been reported to correspond close to the melting of the oxide shell. Using a variety of methods several researchers have

corroborated that for the ignition of micron sized aluminum based reactives, ignition temperatures close to the melting point of the metal oxide are observe[8-14]. On the other hand, aluminum nanoparticles/nanopowders exhibit much lower ignition/oxidation temperature under some circumstances[15-19]. In other cases reaction but not ignition occurs at well below the melting point when probed by low heating rate experiments (10's K/min). For e.g., Umbrajkar et al.[16] reports that reaction starts at lower temperature at lower heating rates. However, the powder would not ignite unless it is externally heated. In shock tubes with heating rates of $\sim 10^6$ K/s the oxidation temperature of nanoaluminum has been observed to be in the range 1200-2100 K at elevated pressures[13]. Nanoaluminum, thus, has been reported to have a wide range of ignition temperature as compared to micron sized aluminum. Studies also report the effect of the type of shell and its thickness on the chemical reactivity of the particle. Jones et al.[20] found that the reactivity of aluminum nanoparticles with aluminum oxide and teflon coatings have remarkable difference in reactivity towards water. Levitas et al.[21] has suggested that reactions occurring via the melt dispersion mechanism (described below) would be promoted if the temperature of formation of the oxide shell is increased.

Two different mechanisms have been proposed in the literature to explain the observed behavior for nanoaluminum. These mechanisms differ significantly in the way ignition occurs. The first mechanism states that the reaction of nanoaluminum is a diffusion based mechanism where participating species diffuse across the oxide shell. Rai et al.[22] has shown that even with low heating rate, the aluminum core melts and exerts pressure on the oxide shell causing it to crack (not violently). The melt dispersion mechanism, proposed by Levitas et al.[21], requires the mechanical rupture of the shell and thereby releasing the aluminum for ignition/reaction. According to this mechanism, under high heating rates the oxide shell explodes due to the volume expansion of the melting metal core causing the liquid aluminum to be suddenly exposed to the oxidizer[21]. However, the current knowledge about the exact physical mechanism is still unclear.

A resolution of the two opposing views is the subject of this letter. The assessment of the prevailing mechanism is done by systematically changing the thickness of the oxide shell to determine the ignition temperature and characteristic reaction time. Our studies will show that this highly violent reaction is likely based on a diffusion mechanism.

## 2. Experiment

In this study we prepare mixtures of Al/CuO nanoparticles that are coated on a fine wire. The wire is joule heated using a pre-programmed voltage pulse and the point of ignition is recorded with a photomultiplier tube. In addition, time resolved Time-of-flight mass-spectrometry enables us to obtain temporal speciation of the reaction. The key point is the preparation of metal with different oxide thicknesses, and our ability to accurately measure temperature during heating rates of $\sim 10^5$ K/sec.

### a) Sample Preparation

Commercially available aluminum powder ALEX procured from Argonide Corporation has been used in this study. The particles have a nominal size of ~50 nm with an active aluminum content of $\sim$ 70% determined by thermogravimetric analysis (TGA). This would indicate an aluminum oxide shell thickness of $\sim$ 2 nm which is consistent with TEM analysis. To increase the oxide thickness, particles were oxidized at

500 $^0$C, (i.e. below the melting point of aluminum) for various lengths of time, and subsequently weighed to determine the oxide growth. This ensures that the oxide shell thicknesses are formed at the same temperature, an important criterion in the melt dispersion mechanism. Measurements indicate that the gain in weight would correspond to thickening of the oxide shell to ~3 nm and 4 nm. The active aluminum content in those samples is thus changed to 59 and 50 % respectively. These measurements have an accuracy of ±3% limited by precision of the balance (0.1 mg). Appropriate amount of copper (II) oxide nanopowders (< 100 nm size) from Sigma Aldrich is weighed and mixed with the aluminum powders with different shell thicknesses to make 3 stoichiometric mixtures. Hexane is then added to the samples and sonicated for ~ 30 minutes to break up the aggregates. Table 1 below shows the preparation and composition of the three samples.

Table 1 Samples used in experiments and their preparation

| Sample | Wt. of Al for oxidation (mg) | Time in preheated furnace at 500 $^0$C (mins) | Wt. gain (mg) | Shell Thickness (nm) | Activity (%) | Amt. of CuO mixed (mg) |
|--------|--------|--------|--------|--------|--------|--------|
| 1 | 30.0 | - | - | 2 | 70 | 132.7 |
| 2 | 30.8 | 5 | 2 | 3 | 59 | 85.4 |
| 3 | 31.1 | 10 | 3.9 | 4 | 50 | 76.8 |

**b) Experimental Setup**

A very thin platinum wire (length ~ 12 mm, diameter ~ 76 um) is electrically heated by a measurable and controllable voltage pulse generated by a home built power source. For any applied voltage (i.e. heating rate) the temperature to which the wire is heated can be controlled by varying the duration of the pulse, during which the current passing through the circuit is measured by a current probe. A small portion of the central region of the wire (~ 3-4 mm) is coated with a micropipette with the samples and the solvent is allowed to evaporate. The ignition event is recorded using a photomultiplier tube (PMT), and is identified by the appearance of a sudden emission of light above the background signal from the heated wire. In the context of this paper, ignition delay is defined as the time difference between the appearance of the ignition signal, identified as a sharp spike in the optical detector, and the end of the applied voltage pulse.

From the recorded voltage and current data, the temperature of the wire at the point of ignition can be calculated from the well known Callender- Van Dusen equation[23]. A new wire is used each time a sample is heated.

**3. Results**

Figure 1 (a) shows the temperature of the wire and the PMT signal recorded as a function of time for such an event, for the three samples in Table 1 under condition of a heating rate of 1.7E5 K/sec. Heating rates were fairly repeatable with uncertainty ~ $10^4$ K/s. The uncertainty associated with the measurement of maximum temperature is ± 50 K. The sharp rise in the PMT signal indicates the start of the reaction. The results show an apparent increase in ignition temperature from 1275 K to 1450 K as the shell thickness is increased. Please note that in this case, the wire temperature is being ramped even after

84

ignition occurs. In a second experiment we vary the heating rate of 1.7e5 and 5.2e5 K/s and plot the result in Figure 1(b) for a particle with a 2 nm shell. Clearly observed is that the ignition temperature is heating rate independent in the range of heating rates carried out in this study. Similar behavior is observed for sample 2 and 3. The maximum heating rate is limited by the power supply and the shortest pulse duration that would not melt the platinum wire.

A next set of experiments are conducted where we turned off the pulse. One key observation is illustrated in Figure 2(a) where we restricted the maximum temperature attained by the wire to ~1250 K, which is just around the lowest ignition temperature of any of the particles determined in Figure 1(a). Figure 2(a) reveals that in all three samples, ignition occurs after the pulse is shut off - *there is actually a delay associated with ignition.* The ignition delays were fairly repeatable, sample 1 (~ 20 µs) and 2 (~50 µs) show lesser variability than sample 3 (~100 µs). In this case in the absence of any reaction, the system would be cooling. Despite this, a thermite event occurs, and the event time correlates with oxide shell thickness. *This is the key result of this paper which we will interpret.*

Finally time resolved time of flight mass spectrometry of Al-CuO MIC is also conducted on the samples as a qualitative tool to verify the delay in ignition. A description of the instrument, its operating procedures and verification could be found elsewhere[24]. Figure 3 shows time resolved mass spectra taken at 100 µs intervals for sample 1, the 2 nm shell thickness case. Species with strong signals, such as $H_2O^+$ (m/z = 18) and $N_2^+$ (m/z = 28) are background species while $HCHO^+$ (m/z = 30) and $CO_2^+$ (m/z=44) appears from small amount of copper carbonate formed on the surface of CuO. In this experiment, the heating pulse was turned off around 2.35 ms. Very relevant is that no $Al^+$ (m/z = 27) is seen before 2.35 ms, but appears at ~ 2.4 ms. $Cu^+$ (m/z = 63.0) starts appearing at ~ 2.5 ms, suggesting an ignition delay of ~ 150 µs. This compares very closely to the optical measurement which has better time resolution. Cu is never observed when CuO alone is heated and its appearance in mass spectrometry is analogous to the sharp rise in the PMT signal, as Cu is present only as a product species, and indicates start of the reaction. $O_2^+$ (m/z = 32) appears from the decomposition of CuO, 2CuO --> $Cu_2O + \frac{1}{2} O_2$ and is seen before the pulse is turned off. Cu always appears in the same or after one spectrum of the appearance of Al. Another product species $Al_2O^+$ (m/z=70) appears around the same time as copper. A more detailed description of the mass spectrometric measurements on Al-CuO thermites is available in[25]. Similar results were seen for sample 2 and 3, except that copper seemed to appear even later in the spectrum with increase in shell thickness.

## 4. Discussion

The independence of ignition temperature on heating rate for any given shell thickness is possibly a first suggestion against the melt dispersion mechanism, as it is expected to be very sensitive to heating rate. However, the range of heating rates is fairly small in our case, which is restricted by the power supply. The change in ignition temperature in Figure 1(a) with oxide thickness could be explained as due to a longer path to diffusion through the oxide shell, rather than an increase in temperature. This point is most reinforced by the key observation in this work (Figure 2), where ignition occurs

considerably after energy input to the system ceases. Furthermore, the thicker the oxide shell, the greater the ignition delay - again consistent with a diffusion mechanism.

According to the melt dispersion mechanism, reaction would occur at the melting point of aluminum owing to the maximum mismatch in thermal expansion coefficient between molten aluminum and the oxide shell. A simplified model simulation was carried out to estimate the actual powder temperature based on the model developed by Ward et al[26]. Results show that the powder temperature is <5 K from the wire temperature. Also, once the pulse is shut off, the heat loss from the wire due to convection and radiation is minimal, which over the relevant time of the experiment decreases no more than ~ 50 K. This would indicate the ignition temperature of the powder exceeds the melting point of aluminum (~ 933 K) and contrary to what is expected according to the melt dispersion mechanism. The characteristic heat transfer time across a nanoparticle is on the order of a few nanoseconds, so that melting should occur essentially instantaneously once the melting point is exceeded. This would cause a huge buildup in internal pressure, and hence explode violently, in time scales ~ ns. However, we see no evidence of reactions at such time scales, rather we see delay times of ~100's of microseconds.

The melt dispersion mechanism is expected to happen at very high heating rates of $10^6$-$10^8$ K/s[27]. This was phenomenologically suggested from the rise time observed in pressure traces in burn tube experiments[1]. However, in those experiments, the powder was set off by an electrical igniter. The external heating rate is thus unknown and hence, the above mentioned rate is clearly the "intrinsic" heating rate once the powder has ignited. The adiabatic flame temperature of Al-CuO mixture is ~2840K and the ignition temperature seen in this study is ~1200 K. The rise time (time for the optical signal to go from 0 to 1 in Fig. 2(a)) observed in the optical signal is ~ 100 μs. This would suggest an intrinsic heating rate of ~ 1.6e7 K/s, which is within the range of the melt dispersion mechanism. As a result, we would assume that the "intrinsic" heating rate of the powder is sufficient to observe the melt dispersion mechanism if it were to happen.

An order of magnitude estimate of the effective diffusion coefficient (= $L^2/t_{delay}$) is presented in Table 2 for the tested samples. The delay times are an average of 2 experiments. The characteristic diffusion length (=L) is assumed to be the thickness of the shell. The extracted diffusion coefficients look very reasonable[28].

Table 2 Ignition delay and effective diffusion coefficient with oxide shell thickness

| Oxide shell thickness, L (nm) | $t_{delay}$ (us) | $D_{eff}$ (cm$^2$/s) |
|---|---|---|
| 2 | 100 | 4.0E-10 |
| 3 | 500 | 1.8E-10 |
| 4 | 2000 | 8.0E-11 |

The appearance of $Cu^+$ signal in mass spectrometry follows the same trend that we see in our optical experiments. Copper formed during the reaction has a low boiling point which is less than the adiabatic temperature of the reaction. Any copper formed would thus be in the gas phase and would be detected. Appearance of copper later in the spectrum for samples 2 and 3 (relative to sample 1) indicates a delay in the initiation of those reactions. This qualitatively supports the statement that the reaction is diffusion controlled.

86

Based on the ignition temperature, the aluminum core would be molten. Although the purpose of this paper is not to determine the diffusion species, it is the aluminum ions from the molten core which are more likely to diffuse because of their smaller size. Evidence of the dominance of the diffusion of aluminum has been observed in other studies too. Rai et al.[28] have shown the formation of hollow particles during aluminum oxidation where the molten aluminum in the core has leaked out and reacted. Similar hollow particle formation has also been reported by Nakamura et al.[29] Henz et al.[30] has also recently showed that built in electric fields within the nanoparticle promote the movement of aluminum ions through the oxide shell, which significantly enhance the initial transport over Fickian diffusion.

Figure 4 summarizes the ignition delay observed for the various cases tested. Ignition delay increases with increase in shell thickness, with 4 nm shell showing the longest delay. The mass spectrometric data compares well qualitatively with the optical data and shows the same trend as identified by the appearance of the Cu signal. These points to an initiation mechanism governed by diffusion across the oxide shell.

## 5. Conclusions

Experiments were conducted at high heating rates to investigate the ignition mechanism of nano-thermites. Samples with different shell thicknesses on aluminum particles mixed with CuO were probed at high heating rates of ~$10^5$ K/s. We find the ignition temperature is well above the melting point of aluminum. Furthermore *an ignition delay consistent with a diffusion limited reaction is observed.* The delay increased with increase in shell thickness of aluminum particles in the samples and from which effective diffusion coefficients are extracted. Fast time-of-flight mass spectrometry shows that the appearance of copper, which is a product species, is progressively delayed in the mass spectra with shell thickness and agrees with the order of ignition delay observed. Based on our data, we would conclude that ignition under the heating rates investigated is a *diffusion governed mechanism.*
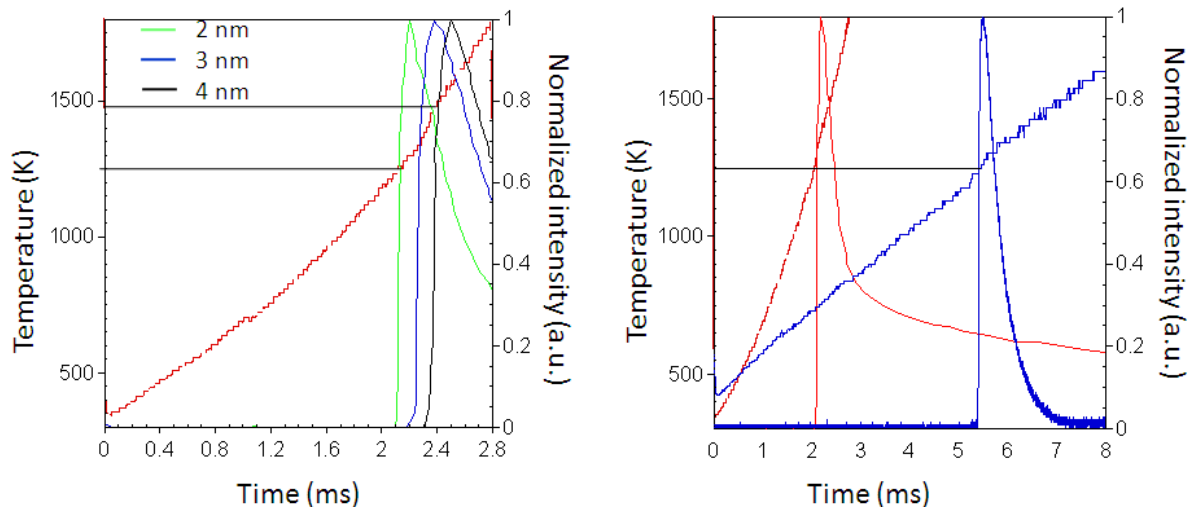
Figure 1(a) Ignition temperature for sample 1, 2 and 3 at 5.3e5 K/s and 1(b) Effect of heating rate - 1.7e5 K/s (blue) and 5.2e5 K/s (red) on ignition temperature of sample 1.
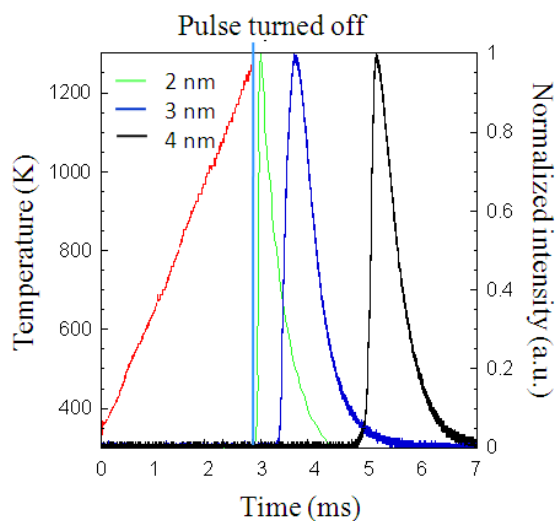


Figure 2 Ignition delay as observed with samples having different oxide shell thickness on aluminum. The maximum temperature attained by the wire is 1250 K as indicated by the red curve. The wire cools down ~ 50 K in the longest times scales seen here after the pulse is turned off. Heating rate is ~ 3.2e5 K/s.

.
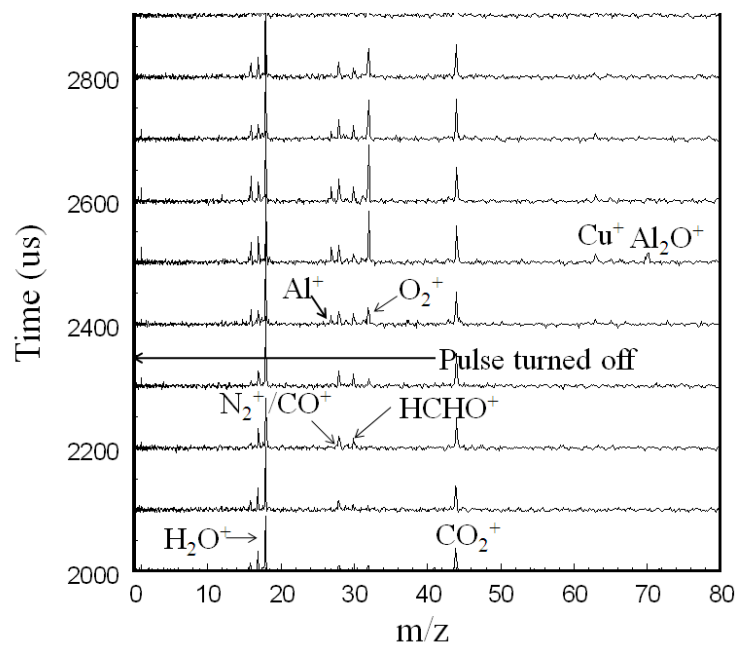
Figure 3 Time of flight mass spectrometric measurements for sample 1. The temperature of the wire when the pulse is turned off is around 1300 K. Species mentioned before the pulse is turned off emanates from background[25].
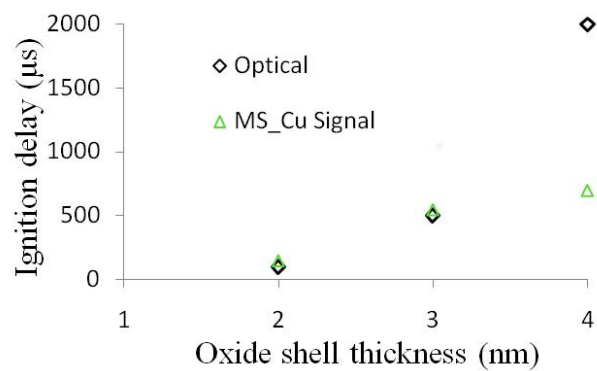


Figure 4 Ignition delay time as a function of various oxide shell thicknesses

**References**

1. B.S. Bockmon, M.L. Pantoya, S.F. Son, B.W. Asay and J.T. Mang, J. of App. Phys. 98, 064903,

   2005.

2. P. Puri and V. Yang, J. of Phys. Chem. C 111, 2007.

3. S. Alavi and D.L. Thompson, J. of Phys. Chem. A, 2005.

4. K. Moore and M.L. Pantoya, J. of Prop. and Power 23, No. 1, 2007.

5. J. Sun, M.L. Pantoya and S.L. Simon, Thermochimica Acta 444, 2006, 117-127.

6. C.J. Bulian, T.T. Kerr and J.A. Puszynski, 31st International Pyrotechnics Seminar, Fort Collins,

   CO,  USA, July 12-14, 2004, pp. 237.

7. D.E. Wilson and K. Kim, 30th AIAA/ASME/SAE/ASEE Joint Prop. Conf., 2003, Reno, Nevada.

8. E. L. Dreizin, Combust. Flame 105, 541-546, 1996.

9. R. Friedman and A. Macek, Combust. Flame 1962, 6, 9.

10. A.G. Merzhanov, Y.M. Grigoriev and Y.A. Galchenko, Combust. Flame 1977, 29, 1.

11. M.A. Trunov, M.  Schoenitz, X. Zhu and E.L. Dreizin, Combust. Flame 2005, 140, 310.

12. M.A. Trunov, M.  Schoenitz and E.L. Dreizin, Joint Meeting of the U.S. Sections of the

   Combustion Institute, Philadelphia, PA, 2005.

13. T. Bazyn, H. Krier and N. Glumac, Combust. Flame 145 (2006), 703-714.

14. T. Bazyn, N. Glumac, H. Krier, T.S. Ward, M. Schoenitz and E.L. Dreizin, Combust. Sci. and

   Tech., 179, 457-476, 2007.

15. C.E. Aumann, G.L. Skofronick and J.A. Martin, J. of Vac. Sci. Technol. B 13(3), May/June 1995.

16. S.M. Umbrajkar, M. Schoenitz and E.L. Dreizin, Thermochimica Acta 451, 2006, 34-43.

17. M.L. Pantoya and J.J. Granier, J. of Thermal Anal. And Calorimetry, Vol. 85 (2006)1, 37-43.

18. K. Park, D. Lee, A. Rai, D. Mukherjee and M.R. Zachariah, J. of Phys. Chem B, Nov 2004.

19. M.A. Trunov, M. Schoenitz and E.L. Dreizin, Propellants, Explosives, Pyrotechnics 30 (2005),

   No. 1.

20. D.E.G. Jones, R. Turcotte, R.C. Fouchard, Q.S.M. Kwok, A.M. Turcotte and Z.A. Qader,

   Propellants Explosives Pyrotech. 28, 2003, 120-131.

21. V.L. Levitas, B.W. Asay, S.F. Son and M.L. Pantoya, Appl. Phys. Lett 89, 071909 (2006).

22. A. Rai, D. Lee, K. Park and M.R. Zachariah, J. of Phys. Chem. B, 108 (39), 2004.

23. P.R.N. Childs, "Practical Temperature Measurement", Butterworth-Heineman, 2001, Chapter 6,

   pp 149.

24. L. Zhou, N. Piekiel, S. Chowdhury and M.R. Zachariah, Rapid Commun. Mass Spectrom. 2009;

   23:194-202.

25. L. Zhou, N. Piekiel, S. Chowdhury and M.R. Zachariah, (in preparation).

26. T.S. Ward, M.A. Trunov, M. Schoenitz and E.L. Dreizin, Intl. J. of Heat and Mass Transfer **49**,

   2006, pp 4943-4954.

27. V.I. Levitas, M.L. Pantoya and K.W. Watson, Appl. Phys. Lett **92**, 201917 (2008).

28. A. Rai, K. Park, L. Zhou and M.R. Zachariah, Combustion Theory and Modelling, Vol. **10**, No.

   5, Oct 2006, pp 843-859.

29. R. Nakamura, D. Tokozakura, H. Nakajima, J.G. Lee and H. Mori, J. of Appl. Physics **101**,

   074303, 2007.

30. B. Henz, T. Hawa and M.R. Zachariah, J. of Appl. Physics, in press.

YEAR 4   iii. **Status of Effort**

This year we employing our T-Jump system to study a variety of thermite and high nitrogen energetic systems.   We have also employed novel high temperature high speed TEM characterization of thermite reactions.

**iv. Accomplishments**

Studies on the Burning of MIC's
This work investigates the reaction mechanism of Metastable Intermolecular Composites (MICs) by collecting simultaneous pressure and optical signals during combustion in a constant-volume pressure cell. Nanoaluminum and three different oxidizers are studied; $CuO$, $SnO_2$, and $Fe_2O_3$. In addition these mixtures are blended with varying amount of $WO_3$ as a means to perturb the gas release in the system. The mixtures with $CuO$ and $SnO_2$ exhibit pressure signals which peak on timescales faster than the optical signal, while the mixtures containing $Fe_2O_3$ do not show this behavior. The burn time is found to be relatively constant for both $CuO$ and $SnO_2$, even when a large amount of $WO_3$ is added. For $Fe_2O_3$, the burn time decreases as $WO_3$ is added and the temperature increases. The results are consistent with the idea that oxidizers such as $CuO$ and $SnO_2$, which decompose at relatively low temperatures, show an initial fast pressure rise followed by combustion over a longer time scale. In this case the burning is rate limited by the aluminum, and is similar to the burning of aluminum in a pressurized oxygenated environment. For the $Fe_2O_3$ system, the oxidizer decomposition to release oxygen only occurs significantly at the adiabatic flame temperature, and is the rate limiting step.

Nano-Aluminum Initiaion

One of the questions that has been debated is how the aluminum is initiated. The two primary competing theories have been solid-state diffusion through the oxide shell or the "Melt-Dispersion" mechanism. The latter involves a violet explosion of the oxide shell. To address this point the ignition of nanoscale Al/CuO thermites with different aluminum oxide shell thicknesses was investigated on a fast heated Pt wire. ($\sim 10^5 K/s$). Ramping the wire temperature to ~1250K, and then shutting off the voltage pulse results in ignition well after the pulse it is turned off- ***i.e. an ignition delay is observed***. The delay is used as a probe to extract effective diffusion coefficient of the diffusing species, which is confirmed by fast time- resolved mass spectrometry. The results of this study are consistent with a diffusion controlled ignition mechanism.

Time resolved characterization of Thermite Chemistry/Physics

Heterogeneous nanocomposite reactions of Al/CuO, Al/Fe$_2$O$_3$ and Al/ZnO systems were characterized using a recently developed T-Jump/TOF mass spectrometer. Flash-heating experiments with time-resolved mass spectrometry were performed at heating rates in the range of ~$10^5$ K/s. We find that molecular oxygen liberated during reaction is an active ingredient in the reaction. Experiments also conducted for neat Al, CuO, Fe$_2$O$_3$ and ZnO powders show that the oxygen are produced by decomposition of oxidizer particles. Mass spectrometric analysis indicates that metal oxide particles behave as an oxygen storage device in the thermite mixture, and release oxygen very fast to initiate the reaction. A clear correlation is observed between the capability of oxygen release from oxidizing particles, and the overall reactivity of the nanocompoiste. The high reactivity of Al/CuO mixture can be attributed to the strong oxygen release from CuO, while Fe$_2$O$_3$ liberates much less oxygen and leads to moderate reactivity, and ZnO's poor oxygen release capability caused the Al/ZnO mixture to be completely not reacting, even though the reaction is overall exothermic. It is likely that the role of the oxygen species is not only as a strong oxidizer, but also an energy propagation medium that carries heat to neighboring particles.

An experimental investigation on the ignition behavior of α-Aluminum Hydride (α-AlH$_3$) was also conducted.   In this study the ignition characteristics were determined through the use of two separate  modified T-jump experiments.  Both ignition and hydrogen release temperatures were studied for heating rates ranging from $10^4$ K/s to $10^5$ K/s.  Both the hydrogen release and ignition temperature increased as the heating rate increased.   Hydrogen release temperatures ranged from approximately 650 K to 1200 K, while ignition was observed to range from below the melting temperature of aluminum (933 K) to approximately 1500 K.  Activation energies for hydrogen release were ~ 27 kJ/mol, and are well below those reported by others at much lower heating rates. This result is consistent with the affects of higher heating rates transitioning the rate limiting step from one of chemical kinetics to intra-particle hydrogen diffusion.  For conditions in which the particles would ignite it was found that the environment did not play a significant role in the ignition temperature, beyond a critical oxygen mole fraction of $X_{O2} > 0.05$.  Ensemble average burning times were found to increase by a factor of about three when the oxygen mole fraction was increased from 0.1 to 0.5.

Plasma Generation and the Role of Built in E-Fields.
One very interesting observation was that intense ion pulse originate from nanocomposite thermite reactions. We  temporally probed them the Temperature Jump/Time of Flight Mass Spectrometer (T-Jump/TOFMS). These ion pulses are

observed to be much shorter in duration than the overall thermite reaction time. Ion ejection appears in stages as positive ions are ejected prior to nanocomposite thermite ignition, and ignition of the thermite mixtures leads to a second ionization step which is primarily dominated by negative species. This observation can be explained by a diffusion based ion-current mechanism, in which strong Al ion diffusion flux formed through the oxide shell, and the surface Na and K ions from salt contaminations are ejected by the strong electrostatic repulsion. The fact that the negative ionization step occurs during the ignition event, suggests a strong relation between the nanocomposite thermite reaction and the negative ionization process.

Using the classical molecular dynamics method we simulate the mechanochemical behavior of small (i.e. core diameter < 10nm) oxide coated aluminum nanoparticles. Aluminum nanoparticles with core diameters of approximately 5nm and 8nm are simulated with 1nm and 2nm thick oxide coatings or shells. In addition to thickness the shells are parameterized by varying degrees of crystallinity, density, and atomic ratios in order to study their affect on the ignition of nanoparticle oxidation. The oxide shells are parameterized to consider oxide coatings with the defects that commonly occur during the formation of an oxide layer and for comparison with a defect free crystalline oxide shell. Computed results include the diffusion coefficients of aluminum cations for each shell configuration and over a range of temperatures. The observed results are discussed and compared with the ignition mechanisms reported in the literature. From this effort we have found that the oxidation ignition mechanism for nanometer sized oxide coated aluminum particles is the result of an enhanced transport due to a built-in electric field induced by the oxide shell. This is in contrast to the currently assumed pressure driven diffusion process. This induced electric field accounts for approximately 90% of the mass flux of aluminum ions through the oxide shell. The computed electric fields show good agreement with published theoretical and experimental results.

On the Role of Reactive Sintering.
One of the open questions in understanding the reactivity of nanometric metal/metal oxide composites is the relative role of gas-solid vs. condensed state reactions. We investigated several nano-Al based thermites subjected to very rapid heating rates.. Ignition was seen to occur above the melting temperature of aluminum, and closer to the melting/decomposition temperature of the metal oxide. Samples were also rapidly heated in-situ within electron microscopes to provide direct imaging before and after heating. The sintering of agglomerated particles into larger, spherical particles was experimentally observed in all cases, and the fuel and oxidizer were found to be in surface contact suggesting that condensed-phase reactions had at some point occurred. High resolution image

sequences of thermites ignited on the Pt wire were collected using a real time phase contrast imaging technique at the Advanced Photon Source at Argonne National Lab. The timescale of the sintering event was experimentally seen to occur on a faster timescale than the onset of optical emission, suggesting some degree of condensed phase reaction precedes thermal runaway and intense optical emission. The results suggest that a reactive sintering mechanism occurs early in the reaction, causing rapid melting and coalescence of aggregated particles.  This dramatically changes the initial size and morphology of the constituents before the remainder of the material burns. The results calls into question the idea that a decrease in particle size will necessarily lead to an enhancement in reactivity, since large amounts of sintering occurs early in the reaction.

## Aluminum NanoCrystal Growth
We show a low temperature gas-phase synthesis route to produce faceted aluminum crystals in the aerosol phase.  Use of triisobutylaluminum whose decomposition temperature is below the melting point of elemental aluminum enabled us to grow nanocrystals from its vapor. TEM shows both polyhedral crystalline and spherical particle morphologies, but with the addition of an annealing furnace one can significantly enhance production of just the polyhedral particles. The results on surface passivation with oxygen suggest that these nanocrystals are less pyrophoric than the corresponding spherical aluminum nanoparticles, and combustion tests show an increase in energy release compared to commercial nanoaluminum.

**v. Personnel Supported**

Faculty: M.R. Zachariah
Graduate students:  D. Klapawitz  ( part time), S. Chowdhury, K. Sullivan, L, Zhou

**vi.**                                                                        **Publications**

1. L. Zhou, N. Piekiel, S.Chowdhury, D. Lee and M. R. Zachariah *Transient ion emission during nanocomposite thermite reaction J. Appl. Phys.* 106, 083306 (2009)
2. G. Young, S. Chowdhury, and M.R. Zachariah *Ignition Behavior of -Alane* Comb. Sci. Tech. 182: 1341–1359, 2010
3. K. Sullivan and M.R. Zachariah *Simultaneous Pressure and Optical Measurements of Nanoaluminum Thermites: Investigating the Reaction Mechanism* Journal of Propulsion and Power, 26, 467 (2010)
4. S. Chowdhury, K. Sullivan, N. Piekiel, L. Zhou and M. R. Zachariah *Diffusive vs. Explosive Reaction at the Nanoscale* J. Phys. Chem. C. 114, 9191 (2010)
5. L. Zhou, N. Piekiel, S. Chowdhury, M.R. Zachariah, *"Time Resolved Mass Spectrometry of the Exothermic Reaction between Nanoaluminum and Metal Oxides: The Role of Oxygen Release"* J. Physical Chemistry C. 114, 14269 (2010)
6. K. Sullivan, C. Johnson, M.R. Zachariah *Ignition and Combustion Characteristics of Nanoscale Al/AgIO3: A Potential Energetic Biocidal System* Combustion Science and Technology, in press
7. K. Sullivan, W-C Chiou, R. Fiore and M.R. Zachariah *In-situ microscopy of rapidly heated nano-Al and nano-composite thermites* Appl. Phys. Lett. 97, 133104 ( 2010)
8. D. Kaplowitz, J. Jouet and M.R. Zachariah "*Aerosol Synthesis and Reactive Behavior of Faceted Aluminum Nanocrystals*" J. of Crystal Growth, 312, 3625 (2010)

**vii. Interactions**

k. Collaborated with Dr. Curtis Johnson from China Lake on energetic biocide measurements.
l. Collaborated with Greg Young, NSWC-IH on Alane Decomposition
m. Collaborated with Jason Jouet , NSWC-IH on formation of Aluminum nanocrystals.
n. Collaboration with Luke Currano at ARL on porous silicon based energetics

DETAILED DESCRIPTION
# Reactive Sintering: An Import Component in the Combustion of Nanocomposite Thermites

**ABSTRACT**

One of the open questions in understanding the reactivity of nanometric metal/metal oxide composites is the relative role of gas-solid vs. condensed state reactions. This work is an investigation of several nano-Al based thermites subjected to very rapid heating rates. The ignition temperature of thermites, as measured by the onset of optical emission, was measured using a rapidly heated Pt wire. Ignition was seen to occur above the melting temperature of aluminum, and closer to the melting/decomposition temperature of the metal oxide. Samples were also rapidly heated in-situ within electron microscopes to provide direct imaging before and after heating. The sintering of agglomerated particles into larger, spherical particles was experimentally observed in all cases, and the fuel and oxidizer were found to be in surface contact suggesting that condensed-phase reactions had at some point occurred. High resolution image sequences of thermites ignited on the Pt wire were collected using a real time phase contrast imaging technique at the Advanced Photon Source at Argonne National Lab. The timescale of the sintering event was experimentally seen to occur on a faster timescale than the onset of optical emission, suggesting some degree of condensed phase reaction precedes thermal runaway and intense optical emission. The results suggest that a reactive sintering mechanism occurs early in the reaction, causing rapid melting and coalescence of aggregated particles. This dramatically changes the initial size and morphology of the constituents before the remainder of the material burns. The results calls into question the idea that a decrease in particle size will necessarily lead to an enhancement in reactivity, since large amounts of sintering occurs early in the reaction. It is suggested that improvements in reactivity can be achieved by improving interfacial contact area, and also through the use of architectures which may reduce the effect of sintering.

**Keywords:** High heating, thermites, aluminum, phase contrast imaging, microscopy, nanoparticles

## Introduction

Nanocomposite thermites, or metastable intermolecular composites (MICs) are intimate mixtures of metal and another metal/metal oxide nanoparticles, and typically have the consistency of a loose powder. Using

97

nanoparticles greatly reduces mass diffusion lengths between the fuel and oxidizer, and also increases the interfacial contact and homogeneity of mixing. Upon ignition, these materials give rise to a self-propagating reaction with a characteristically high temperature, and low to moderate gas production. Research on MICs can be traced back about fifteen years to when Aumann et. al.[1] showed that using nanoparticles of $Al/MoO_3$ resulted in several orders of magnitude increase in combustion characteristics over similar mixtures with micron-sized particles. Since then, research efforts have increased to understand the ignition and combustion mechanism, so that improvements in safety and performance can be achieved.

MICs have been experimentally shown to exhibit pressures and flame velocities somewhere in between propellants and explosives.[2] Flame velocities range between 10's and 1000's of meters per second, while the pressures range between a few to nearly 1,000 atmospheres. The pressure and flame velocity in MICs is something that can be tuned through easily-adjusted parameters using various techniques, such as changing the method and uniformity of mixing,[3,4,5] particle size and distribution,[6,7,8] choice of materials and stoichiometry,[9] or by other techniques such as electrostatic assembly[10] or creating new types of core-shell oxidizers.[11] This tunability, along with other attributes such as high mass/volumetric energy densities and the production of environmentally benign products, make MICs very attractive energetic systems. Nano-sized aluminum has been found to be an excellent fuel, and nano-Al based MICs are currently being investigated for uses in propellants, explosives, and pyrotechnics.

Despite the amount of experimental results available in the literature, the ignition and combustion mechanism remains poorly understood. A major problem has been designing experimental techniques which can probe the intrinsic reaction while replicating the environment these materials are subject to, during the self-heating in the freely propagating reaction. This means very rapid and uniform heating, speculated to be somewhere in the range of $4 \times 10^4$ K/s to upwards of $10^8$ K/s (an ad-hoc calculation assuming thermites can reach an ignition temperature of ~1000 K in 10 μs, which is an experimentally observed pressure rise time).[12, 13] Furthermore, in order to understand the thermite mechanism, the ignition and combustion mechanism of nano-Al itself must first be well understood.

It is well known that nano-Al forms an oxide shell when exposed to air. This shell is amorphous and uniform,[14] and typically has a thickness of 2-3 nm.[15] The oxide shell can occupy a relatively large portion of the particle's mass, and in some cases can even exceed 50 Wt%.[16] The interaction between the low melting point core (933 K) and the high melting point shell (2327 K) is speculated to be critical in understanding why the ignition temperature of nanoaluminum is experimentally observed to occur close to the melting temperature of Al, and not near the melting temperature of the $Al_2O_3$ shell, as is seen for large aluminum.[17] Two schools of thought have prevailed for rapidly heated nano-Al: one suggests

that the melting and volumetric expansion is enough to completely rupture the oxide shell, followed by the ejection of small clusters of molten aluminum at high velocities,[18,19,20] while the other suggests that the melting and expansion of the core causes the shell to crack and/or break down via phase transitions, exposing the aluminum core and rendering a diffusion-based mechanism.[15,21,22,23, 24] It has also been shown through molecular dynamics simulations that built in electric fields in the oxide shell can greatly enhance the diffusion rate of aluminum through the shell,[22] thus allowing for enhanced reactivity. Understanding the mechanism of ignition is a crucial prerequisite in understanding the mechanism of combustion.

Only a few works have examined the combustion of nano-Al at very high heating rates. One experimental technique which accomplishes the appropriate heating is a shock tube, and Bazyn et. al. have conducted several experiments of nano-Al burning in varying environments inside a shock tube.[25,26,27] The authors use pyrometry to measure the combustion temperature of the particles as a function of pressure and gas composition, and suggest that the burning cannot be modeled by a "droplet burning" model, but instead large heat losses characteristic of nanoparticles cause the flame to sit much closer, if not directly on the particle surface. This suggests that heterogeneous reactions between the gas and the particle are prominent in the combustion mechanism. The authors have also investigated the ignition and combustion of nanocomposite $Al/Fe_2O_3$ and $Al/MoO_3$ using the same technique, and measured the ignition temperatures in an inert environment to be 1400 and 1800 K, respectively.[28] It should be noted that these ignition temperatures are significantly higher than the melting temperature of Al, which in some cases has been experimentally observed to be very close to when nano-Al ignites in a gaseous oxidizing environment.[17] The authors also measure the combustion temperatures of the composites to be in the range of 2750 – 3350 K (close to the boiling point of Al), and find that combusting in an oxygenated environment can raise the temperature several hundred degrees, indicating some degree of reaction with the gas.

Besides the aforementioned shock tube experiments, there have been limited other studies of the ignition and combustion of nanocomposite materials which:

a) Avoid the negative effects of studying a bulk sample such as packing density, mixing, differences in heating, etc.
b) Probe intrinsic properties
c) Uniformly and rapidly heat the samples

These considerations have led to the development of temperature jump (T-Jump) techniques, which can ramp the temperature of a small amount of sample very quickly. In these experiments a thin wire or filament is supplied a tunable voltage pulse and rapidly heats (~$10^6$ K/s) through resistive heating. The ignition and combustion event can be monitored optically,[29,30] or in a mass

spectrometer[31] to probe transient species evolution. Chowdhury et al.[30] used this setup to examine the ignition delay in a nano-Al/CuO composite as a function of aluminum oxide shell thickness. The authors concluded that the diffusion of Al through the oxide shell was responsible for the delay, since an increasing delay time was measured with increasing oxide shell thickness. This work raised questions about what is actually the appropriate temperature to report for ignition, especially when a delay is present in a rapidly heated environment. If some mass transfer rate limiting step (i.e. diffusion of Al through $Al_2O_3$) occurs in a very rapidly heated environment, then the apparent ignition temperatures could possibly be higher than what would be measured using an experimental apparatus which slowly heats the sample.

One other phenomenon which has received little attention in nanoparticle combustion studies and will be a topic of discussion in this work is the sintering of adjacent particles. This directly impacts the question of size dependence to reactivity, and what is the "effective" particle size of the reacting material. Commercially available nanoparticles are almost always highly agglomerated, and the "size" specified by a supplier oftentimes is the average size of the primary particles within these aggregates. Surface tension forces will of course drive the particles to coalesce if the temperature is sufficiently high to make the particles liquid-like.[32, 33] In a reacting thermite, nanoparticles can be heated and sintered by heat transfer from the surroundings, as well as from the energy liberated during an exothermic chemical reaction. The latter is referred to as reactive sintering, and is a phenomenon which, for example, has been shown to be important in Al/Ni reacting systems.[34, 35]

The key point we will have to consider is whether the kinetic timescale for sintering[31] is compatible with reactive timescales we observe experimentally. If it is, then this consideration might change the manner in which one considers the effect of particle size on reactivity. It will also raise two very important questions:

1) Do nanoparticles maintain their high surface area morphology during combustion, and if not, then what is the appropriate "size" to report?
2) Is there an advantage of using agglomerated nanoparticles below a certain critical size?

The current work is a compilation of various experiments of both nano-Al and nano-Al thermites subjected to rapidly heated conditions. Several different types of thermite systems were tested both on a rapidly heated Pt wire, and within electron microscopes equipped with a rapid heating holder.

## Experimental

In this work several thermite systems are compared to determine whether there are mechanistic similarities. Not all systems were studied using each

experimental technique, largely due to time constraints on borrowed equipment or facility usage. The particular thermite studied in each case, therefore, was selected based on what would give the clearest representation of the steps involved in the nanocomposite thermite reaction for the particular experimental technique. The nano-Al used in this work is termed "50 nm ALEX," and was purchased from the Argonide Corporation. The primary particle size is specified by the supplier to be 50 nm, and the elemental portion of the particles was found to be 70% by mass, as measured using thermo gravimetric analysis (TGA). A representative image of the nano-Al is shown in Figure 1. The primary particles are largely spherical in nature, and are highly agglomerated. One of the samples of CuO, which we will term "6nm CuO", was synthesized by a wet chemical technique (using copper nitrate and sodium hydroxide), and the primary particle diameter was found by electron microscopy to be ~6 nm. A representative image of the as-prepared material is shown in Figure 2. The particles are spherical and relatively monodisperse, with varying degrees of aggregation. All other oxidizers were purchased from Sigma Aldrich, and also were spherical and agglomerated. These include $Bi_2O_3$ (90-210nm), $WO_3$ (<100nm), $Fe_2O_3$ (<50nm), and CuO (<50nm) with the sizes specified by the supplier. Table 1 provides a summary of the materials used.

To prepare thermites, stoichiometric amounts of the nano-Al and oxidizer were weighed and added to either a ceramic crucible or glass vial along with a few milliliters of hexane. The samples were then sealed and placed into a sonicating bath, followed by ultrasonication for ~30 minutes to ensure intimate mixing. For the wire experiments, the hexane/sample mixture was directly pipetted onto the wire, and the hexane was allowed to evaporate before testing. To prepare the grids for microscopy, the hexane was allowed to evaporate and then a small amount of ethanol was added to pipette the sample onto the grid. Ethanol was simply chosen based on experience that it evaporated easier from the microscopy grids.

Three separate experiments were conducted in this work, and as previously mentioned, not all samples were run for each experiment. The first used a temperature jump (T-Jump) setup to investigate the ignition temperature of the thermite sample rapidly heated on an ultra thin wire in air. The wire is made of Pt, with a diameter of 76 μm, and through utilization of a tunable voltage pulse, can be resistively heated to a maximum temperature of ~1800 K at a rate of approximately $5 \times 10^5$ K/s.[30, 31] A photomultiplier tube (PMT) is used to monitor the optical emission, and ignition is said to have occurred at the onset of the emission. An example of the data produced by this method is given for an Al/CuO thermite in Figure 3. Secondly, a specially designed heating holder (Aduro holder, Protochips, Inc.) was used to heat samples with a tunable heating pulse in-situ inside an electron microscope, from room temperature up to a maximum of 1473 K and at a rate as fast as $~10^6$ K/s. The holder can be held at the desired temperature for a user-specified amount of time before being shut

off.  The specially fabricated grids are small thermal loads, and thus once the voltage is turned off, very rapidly cool to room temperature.  Pure nano-Al, Al/6nmCuO, and Al/WO$_3$ thermites were rapidly heated using this holder inside an electron microscope (transmission or scanning, TEM or SEM), and the before and after images were compared to draw conclusions about the mechanism.  Finally, x-ray phase contrast imaging experiments were performed at the Advanced Photon Source (APS).  We took the T-Jump system to APS, where a coherent x-ray beam was used to view the thermites rapidly heated on the Pt wire in real time at a frame rate of 135,780 Hz (7.4 μs per frame).  The per-frame exposure time was actually much shorter ~500 ns, and was controlled by the pulse width of the synchrotron bunch structure.   The high coherence of the undulator x-ray source at APS means that the relative phase of the x-rays (and not simply differential x-ray absorption) contributes to image contrast, making this technique extremely sensitive to gradients in electron density.[36]  In addition, the PMT setup was used simultaneously used to monitor the optical emission, thus providing a correlation between the images and the emission of light.  The various systems studied, along with which experimental techniques were used, are summarized in Table 2.

## Results and Discussion

*T-Jump/PMT Ignition Temperature*

The ignition temperature, defined as the onset of optical emission during the rapid heating of the sample on the wire in air, is summarized for various thermite systems in Table 3.  Also included in the table is the melting point of the oxidizer.  The "melting" of an oxidizer is not a very clear terminology, and generally involves some form of thermal decomposition to a suboxide.  Upon melting/decomposing, certain oxidizers can release gaseous O$_2$, or other gaseous oxidizing species.  For example, CuO and Fe$_2$O$_3$ decompose to Cu$_2$O and Fe$_3$O$_4$ when heated, coupled with the release of O$_2$ gas.  We have recently argued, through temporally resolved mass spectrometry, that the O$_2$ release for these particular oxidizers plays an important role in the ignition and combustion process.[37] Upon rapid heating, a critical partial pressure of gaseous oxygen may be reached, which facilitates the ignition of the aluminum fuel.  This idea could be extended to oxidizers such as WO$_3$, SnO$_2$ and MoO$_3$, which can produce other gaseous oxidizing species, such as WO$_2$, SnO, and MoO$_3$ vapor.

What can be seen in Table 3 is that the experimentally measured ignition temperatures are all above the melting temperature of aluminum (933 K), which is approximately where nano-Al is experimentally observed to ignite for lower heating rate experiments.[17]   In other words, at high heating rates it's not sufficient for only the aluminum to have melted, but the oxidizer must also have reached a temperature closer to its melting point.  In some cases, ignition is seen to occur very close to the melting temperature of the metal oxide, while in other

cases, the ignition temperature is significantly below the melting temperature of the bulk material. In all samples, there is a distribution of particle sizes, and thus a range of melting temperatures. Also, the melting/decomposition mechanism varies between the oxidizers. Certain metal oxides ($Bi_2O_3$ and $WO_3$) melt, whereas others (CuO and $Fe_2O_3$) decompose to a suboxide before melting, and this transition can release $O_2$. The decomposition can begin to occur below the bulk melting temperature, and in fact the decomposition temperature is much closer to the experimentally measured ignition temperatures. In any case, the results suggest that the melting or decomposition of the metal oxide plays a role in the ignition mechanism at high heating rates. For further investigation, we can now turn to the results of the high heating microscopy experiments.

*High-Heating Microscopy*

For the following discussion, all heating pulses used the maximum heating rate of $10^6$ K/s, and the sample always starts at room temperature. At this heating rate the system takes approximately 1 ms to heat the sample to 1000 K. The sample is then "held" at the maximum temperature for a user-specified amount of time (1 ms is the minimum) before the electronics can turn off the voltage. The sample then rapidly cools by a rate governed by heat transfer, and since the substrate is a very small thermal load, this rate is expected to be comparable in magnitude to the heating rate. The parameters which are varied in the following section are the maximum temperature, along with the amount of time the sample is held before the voltage shuts off and quenches the heating. All images are taken at room temperature, and are compared before and after being heated.

Before investigating the thermite systems, a sample of nano-Al with no oxidizer was prepared and investigated in-situ with a Transmission Electron Microscope (TEM, JEOL JEM 2100 Lab6). The results are presented in Figure 4. The nano-Al was first given a heating pulse to 1273 K, held for 1 ms, and turned off. Practically no morphological changes in the particle could be observed visually, aside from evidence of aluminum crystallization (Figure 4b). Typical burning times for nanoaluminum in rapidly heated oxygenated environments are on the order of several hundred microseconds,[26] so the observation of no change on a timescale of 1 ms was unexpected. Next, a second heating pulse was employed up to the maximum temperature of 1473 K, and this time the sample was held for 10 ms before the pulse was turned off (Figure 4c). In this case there was some obvious deformation of several particles, and visual evidence of the aluminum core diffusing out. We note that the changes are not very dramatic, and the particles maintain their shapes for the most part. Clearly no sign of violent "spallating" were observed, as has been suggested by the "Melt Dispersion Mechanism".[18,19,20] Finally, the particles were given a heating pulse from room temperature to 1473 K, and this time were held for 1 s before the pulse was shut off (Figure 4d). In this case a dramatic change was observed in all

particles. It was clear that the aluminum had melted and either evaporated or possibly reacted with the underlying thin carbon film to form $Al_4C_3$. We do want to point out, however, that the structure of the oxide shell is still visible, indicating that the aluminum core had in some way migrated outwards through the shell during the heating.

Next we turn to thermites. The first system looked at was nano-Al/6nmCuO in the TEM. This particular system was chosen primarily because the small monodisperse nature of the CuO made it easy to visually distinguish from the larger, polydisperse nano-Al. At the time of this study, the holder had not yet been modified for use with in-situ elemental analysis, so the sample was removed and the product was confirmed via elemental analysis in a separate microscope. The heating pulse used for this sample was to the maximum temperature of 1473 K, held for 10 ms, and then turned off. This particular pulse was chosen primarily because of the observations from Figure 4, showing that no obvious morphological changes occurred at the lesser heating pulse. The before and after heating images are shown in Figure 5, and clearly show that all particles have undergone a dramatic morphological change. The very fine 6 nm particles, which were the CuO, have all formed a much larger and nearly spherical copper product. The aluminum particles are significantly deformed and the oxide product is found to be in contact with the copper. The results suggest that a large amount of sintering had occurred, however, it could not be distinguished at what point the sintering had occurred, and thus whether sintering precedes reaction or vice versa.

To provide a more qualitative understanding of how the Al/CuO formed the morphology shown in Figure 5, two samples of pure CuO were prepared and studied with a high resolution SEM. In this case, commercially available CuO (Sigma-Aldrich) was used, simply because the particle sizes are polydisperse and thus it gives a more representative picture of what occurs. At the time of this experiment, the sample holder had been modified for in-situ use with an SEM, therefore allowing for simultaneous elemental analysis. Both samples were given a heating pulse at the maximum rate of $10^6$ K/s and held for 1 ms before being shut off, however, one sample was heated to 1250 K while the other was heated to the maximum temperature of 1473 K. Before and after images are shown in Figure 6. The sample heated to 1250 K showed only mild amounts of sintering, while the sample heated to 1473 K showed a dramatic morphological change. Agglomerates which were several microns in size had completely sintered into much larger "pools" of $Cu_2O$, confirmed by energy dispersive x-ray spectroscopy (EDS). CuO can decompose according to the mechanism:

$$4CuO \text{ (cr)} \rightarrow 2Cu_2O \text{ (cr, L)} + O_2$$

The melting temperature of bulk $Cu_2O$ is 1517 K, however, with a wide range of particle sizes present, there will also be a range of melting temperatures. Once melting occurs, the kinetics of sintering are dramatically accelerated, and this point will be revisited later in this work. Another consideration worth

mentioning is that sintering is an exothermic event, and this could also serve to self-accelerate the process, causing the particle temperature to rise, and for very small particles (<10 nm), by as much as a few hundred degrees.[33]

In any case, from these results it is quite clear that the highly agglomerated nanoparticles have sintered into particles with much larger characteristic lengthscales, and on a timescale faster than 1 ms. The sample was next given a series of subsequent heating pulses, however, the morphology remained unchanged. Comparing these results to the nano-Al/CuO thermite (Figure 5), we do not observe the formation of spherical copper particles from heating of the pure CuO. This comparison confirms that the exothermic reaction is indeed occurring to further reduce the $Cu_2O$ and produce the spherical Cu product. In order to render the morphology seen in Figure 5, we propose that the Al and $Cu_2O$ (or CuO) have come into surface contact and a heterogeneous reaction ensues. The heat liberated by the reaction serves to further drive the sintering process as energy is conducted through the aggregates. As material is melted during this process, capillary/surface tension forces serve to rapidly bring the constituents together, thus rapidly delivering oxidizer to the fuel. The results suggest that a reactive sintering mechanism could be occurring for the nano-Al/CuO thermite, however, is cannot be resolved whether the sintering preceded the reaction, or vice versa.

Next we turn to a nano-Al/$WO_3$ sample studied in an SEM in order to determine whether similarities exist between different thermites. An SEM has the advantage of constructing a backscattered electron (BSE) image, which is well known to introduce contrast based on atomic weight (Higher weight → brighter in image). Aluminum and $WO_3$ can thus be easily distinguished in BSE image, and this is one reason $WO_3$ was chosen. The nano-Al/$WO_3$ was given a heating pulse to 1473 K, held for 1 ms, and turned off. The maximum temperature was chosen in an effort to heat as close to the experimentally measured ignition temperature as possible (1523 K for nano-Al/$WO_3$, as seen in Table 3). A shortened heating pulse was chosen to minimize film stability issues that were seen in the nano-Al/6nmCuO, and to also minimize any effects which may have been induced by additional heating from the holder. Typical burning times measured using the T-Jump setup for nano-Al/$WO_3$ are on the order of 1-2 ms, so this pulse was very appropriate to probe the intrinsic behavior during the ignition process. The rapid quenching of the sample holder allows for the "freezing" of the reaction shortly after ignition.

The before and after images of nano-Al/$WO_3$, along with the corresponding BSE images, are shown in Figure 7. The bright areas in the BSE image correspond to W-containing species, while the dark spots correspond to Al species (separately confirmed by elemental analysis). Unlike the nano-Al/CuO results, the selected area has both the thermite along with the pure oxidizer within the picture, thus allowing for a direct comparison between the two subjected to an identical heating pulse. The results show that two very different

types of behavior can be seen; for fuel and oxidizer in close proximity significant sintering has occurred and the products are found to be in surface contact, while WO$_3$ which was isolated from the fuel shows practically no morphological changes other than minor amounts of sintering. These observations suggest that the heating pulse alone had not been sufficient to melt the WO$_3$ ($T_{melt}$ = 1746 K), however, in the areas where the fuel and oxidizer had been intimately mixed, the exothermic reaction had been vigorous enough to further melt the adjacent particles. Consistent with what was seen for nano-Al/6nmCuO, the results imply that a reactive sintering mechanism has occurred. The exothermic reaction leads to further melting of adjacent material, and capillary/surface tension forces cause the newly melted material to rapidly migrate towards the interface where the reaction is occurring.

The sample was given a second identical heating pulse for an additional 1 ms. The image/BSE image pair after the second heating pulse can be seen in Figure 8. It should be noted that a large portion of the un-melted WO$_3$ broke away from the particle, and cannot be seen since this particular image was taken at a higher magnification to emphasize the structure. Also shown in Figure 8c is an elemental linescan plotting the intensity of W, O, and Al as a function of position (Figure 8c) across the particles (white line marked in Figure 8b). The concentration profile indicates that there is some overlap between the species, implying that inter-mixing of the constituents may occur near the interface, an indicator that a condensed-phase reaction mechanism is happening. In addition, the BSE image (8b) shows the emergence of several small bright "spots", when compared to Figure 7d. The spots are likely small clusters of solid tungsten which form during the heterogeneous reaction, and the second heating pulse is allowing for a further extent of reaction. The tungsten which forms is, not surprisingly, solid due to its high melting point (3680 K). As a comparison, the Cu product previously discussed (Figure 5) has a low melting temperature (1356 K). Even if both thermites had reacted by similar mechanisms, the observed morphology may differ depending on the ability of the product to form larger spherical particles within the timescale of the heating pulse.

All of the results from the heating microscopy studies show large morphological changes, with evidence suggesting significant sintering of adjacent particles. The thermites showed different behavior relative to the pure materials, and the changes were most dramatic where the fuel and oxidizer were in close proximity, suggesting that the exothermic reaction can further drive the sintering process. The results also show the aluminum to be in surface contact with the product, suggesting that the constituents may have come into surface contact and reacted via a condensed-phase mechanism at the interface. Unfortunately, from these experiments we cannot pinpoint exactly at what point sintering occurred, and thus how it may be important to the ignition mechanism. In one extreme, a critical temperature may be achieved where condensed phase species begin to rapidly sinter, bringing fuel and oxidizer particles into surface

contact and reacting at the interface. In another extreme, an alternate mechanism of ignition (i.e. $O_2$ release from the oxidizer and heterogeneous reaction at the Al surface) may occur, and large thermal gradients from the exothermic reaction drive the sintering of neighboring particles into the observed morphologies. What is also missing in the microscopy experiments is a more accurate timescale of the very fast processes. The minimum amount of time the sample could be held with the holder is 1 ms, and even that may be too fast to capture the processes of interest. The next section investigates the burning of thermites on a rapidly heated wire, and will place a more accurate timestamp on the sintering processes.

*Real-Time Phase Contrast Imaging*

In this section, high resolution image sequences of samples rapidly heated on the wire are presented. The images are created by a real time x-ray phase contrast technique, which provides much better structural resolution than traditional x-ray radiography. These experiments were performed using synchrotron x-rays from the Advanced Photon Source. The same T-Jump wire as discussed earlier was used to ramp the temperature of the samples from room temperature to ~1800 K at approximately $5 \times 10^5$ K/s. Simultaneous optical emission was monitored for the thermites using a photomultiplier tube (PMT). As a preliminary test, rapidly heated nano-Al was investigated, however, no morphological changes were seen to occur other than a small volumetric change as the material slowly melted. Thermites and the pure oxidizers, on the other hand, showed very dramatic behavior that was imaged with ~7.4 µs time resolution.

Figure 9 is an image sequence of the nano-Al/CuO thermite being heated on the wire. The images labeled as t = 0 µs correspond to the first image where a morphological change can be visually seen. The particles are seen to blow off the wire, through a propagation process that moves from left to right along the wire. This behavior has been observed in previous work, and is presumably due to the evolution of $O_2$ gas from the CuO.[38] The onset of optical emission, as measured by the PMT, is labeled in the figure, and is more commonly referred to as the "ignition temperature" when using this setup. What can be seen in Figure 9 is that larger particles form rapidly in time, and well before the onset of the optical emission. The exact shape or size distribution of the particles is not something which can accurately be measured due to the limited spatial resolution of the x-ray phase contrast imaging technique (~2 µm), but many of the particle sizes appear to be on the order of micrometers. Another important observation is that the results appear to be consistent with the microscopy results of Figure 5, where it was shown that sintering of agglomerated nanoparticles led to the formation of larger, nearly spherical particles (~1 µm in some case). While the experimental technique used in Figure 9 does not spatially resolve the intricacies that an electron microscope can, the qualitative similarities lead us to believe that the

mechanisms are similar, and thus in this case a reactive sintering mechanism also occurs to form larger nearly spherical particles early in the burning.

As a comparison, pure CuO was also heated with the same pulse, and the image sequence is shown in Figure 10. The material was observed to volumetrically shrink, followed by evidence of "bubbling" over the next several milliseconds of heating. These results can be compared to the microscopy results (Figure 6), where large agglomerates of nanoparticles rapidly formed "pools" of $Cu_2O$ once a critical temperature as achieved. On the wire, the CuO (cr) likely decomposes into molten $Cu_2O$, and simultaneously evolves $O_2$ gas. The wire heating alone is insufficient to rapidly decompose the $Cu_2O$ (L), and thus a large amount of oxygen remains trapped in the condensed phase. The $O_2$ which was released (or continues to be released via $Cu_2O$ decomposition) is trapped inside the melt and forms pockets of gas as it migrates out through the matrix, experimentally seen as the formation of bubbles within the material.

It is evident from these results that the CuO is indeed releasing gaseous $O_2$, and thus is serving as a gas generator. In the presence of nano-Al, an exothermic reaction can serve to greatly accelerate the oxidizer decomposition. What cannot be resolved is whether the nano-Al reacts with the released $O_2$ gas, or whether it reacts with the $Cu_2O$ (L). In fact, it could be a combination of both. Since reaction under vacuum was clearly observed for nano-Al/CuO (Figure 5), it would lead us to believe that at least some amount of reaction proceeds in the condensed phase, since a large amount of $O_2$ gas should escape into the high vacuum and thus not participate in the reaction.

Based on the experimental evidence and discussion thus far, it's plausible to speculate that what happens for the nano-Al/CuO thermite is that the sample is heated to a critical temperature where CuO can start decomposing/melting. If there is no exothermic reaction, a $Cu_2O$ melt is formed, and thus only a portion of $O_2$ is released. With added Al, however, an exothermic reaction can initiate presumably at the interface between Al and $Cu_2O$ (L) (or possibly $O_2$). Modeling this interfacial reaction is beyond the scope of this work, however, it should be noted that built-in electric fields[22] could potentially play an important role to accelerate the kinetics if the fuel and oxidizer are brought in very close proximity. The energy liberated serves to rapidly melt/decompose adjacent particles of CuO into $Cu_2O$ (L). As molten $Cu_2O$ is produced during this process, capillary/surface tension forces cause the material to rapidly be delivered towards the interface where it continues to react. Experimentally, this is consistent with the observations that many micron-sized particles form during the thermite reaction, and not for the pure CuO. As the reactive sintering mechanism occurs, a significant amount of $O_2$ gas which did not participate in the reaction may be released, either during the CuO decomposition to $Cu_2O$ or during the $Cu_2O$ decomposition to Cu. The gas released serves to convectively propagate the energy and support a fast self-propagating reaction. Once latent processes and decomposition are complete, some amount of unreacted

aluminum continues to burn in a gaseous oxidizing environment, and this is where the temperature can be seen to rise, experimentally seen as a delayed optical signal relative to the phase changes.

As a direct comparison, a nano-Al/$Fe_2O_3$ thermite was also studied using the setup. In a previous work,[13] we argued that $Fe_2O_3$ does not decompose very efficiently due to the fact that it forms FeO (L), which does not completely dissociate until a temperature (~3300 K) even exceeding the adiabatic flame temperature (~3100 K). Therefore, it traps a significant amount of oxidizer in the suboxides it produces, even in the presence of a hot exothermic reaction. The image sequence of the thermite rapidly heated on the wire is shown in Figure 11. What can be seen is that much larger spherical particles are formed, and some even appear to be hollow. Hollow particles indicate that some gaseous $O_2$ is released into a molten $Fe_xO_y$ matrix and thus forms "bubbles," analogous with what was seen for pure CuO in the absence of an exothermic reaction (Figure 10). The gas release is not nearly as rapid for the nano-$Fe_2O_3$ thermite as it is for the nano-Al/CuO thermite, and this is likely attributed to high dissociation temperatures of the suboxides of $Fe_xO_y$ produced. Directly comparing the image sequences for the two thermite (Figures 9 and 11), it appears as though a more intense gas release is visually seen as the formation of much finer particles.

Although the spatial resolution of the x-ray image sequences is clearly inferior to an electron microscope, the image sequences provide an estimate of the time resolution of the sintering processes. The approximate timescale for larger particle formation (sintering) can be visually approximated for the thermites from the image sequences. Using Figures 9 and 11, the sintering time is roughly estimated as the difference in time between the first visual evidence of a reaction (t = 0 μs) and when most of the material appears to exist off of the wire as larger particles. This is a very rough approximation, but it's interesting when compared to other measured quantities. The sintering timescale is tabulated in Table 4, along with the apparent ignition point (onset of optical emission) and the FWHM burning time for comparison. What's interesting is that the apparent sintering time for the nano-Al/CuO is on par with the pressure rise time of 10.4 μs experimentally measured during combustion experiments in a previous work.[13] In this previous work, we had argued that the pressure rise was evidence of some partial reaction, followed by a prolonged burning in a gaseous oxidizing environment, experimentally seen as a prolonged optical signal. What can be added based on the results of the current work is an explanation for the mechanism of the "partial reaction." The sintering timescale appears to have some relevance, at least for the nano-Al/CuO thermite, and thus the next section will be a discussion of this timescale.

**Characteristic Reaction and Sintering Times**

Up to this point, we have shown that sintering is indeed occurring, however, we have only really discussed it in the context of a reactive sintering

mechanism. That is, the exothermic reaction initiates, and this causes rapid melting/fusion of adjacent particles. In all cases, the maximum temperatures experimentally achieved were close to or just above the decomposition temperature. In some practical applications, however, it's possible that the heating can occur even more vigorously and to higher temperatures. Therefore, it may be possible that a large amount of sintering can be thermally activated on timescales even faster than the reaction. If this occurs, then the size and morphology of the particles may be drastically altered from their initial states, and this may be a critical consideration in applications where nanoparticles are being investigated in energetic applications. Specifically, two examples where the kinetic timescale of the sintering event may be particularly important are:

1)  Self-heating by convection of intermediate gases in a self-propagating thermite
2)  Addition of nanoparticles to a high explosive, where the ambient temperature may rapidly rise to high temperatures (i.e. ~3000 K behind a shock front)

The following section presents a simple estimate of the timescale for sintering of nanoparticles convectively heated by a hot gas, which, should be relevant to the two cases above. Since we are ignoring the local heat of reaction in this analysis, the results may be considered an overestimate of the characteristic sintering time.

*Reaction Time Scale*

An estimate of the reaction timescale depends on the particular combustion system and configuration, and for the following analysis, we limit ourselves to our own studies. In a previous work using a combustion bomb,[13] we showed that the pressure rise occurred on the order of 10 μs, whereas the FWHM burning time was approximately 200 μs. Since we are interested in seeing whether sintering is occurring to affect the combustion process, we choose a characteristic reaction time that is a small fraction (5%) of the optically-measured burning time. This leads to a characteristic reaction time of 10 μs, which is coincidentally also the pressure rise time. We ignore particle size effects on burn time for simplicity.

*Sintering Time Scale*

To estimate an appropriate sintering timescale, two separate calculations must be included:

1)  Time to heat and completely melt nanoparticles
2)  Fusion of adjacent particles into a single particle, i.e. the "sintering" process

In a thermite system, there are actually three materials present; aluminum, an aluminum oxide shell, and the metal oxide. The metal oxide could sinter with

other metal oxide particles, or the aluminum may sinter with neighboring aluminum (in which case it likely does not occur until the melting of the $Al_2O_3$ shell occurs). Given that most of the experimental evidence and discussion have focused on the oxidizer, the calculations focus on sintering time of two identical particles of CuO.

To calculate the heating timescale, an approach from a previous work is followed.[39] For simplicity, particles are not treated as agglomerates, but instead as single spheres surrounded by a hot gas, and with radiation losses assumed to be negligible. A lump-capacitance model of heating is assumed, which assumes that the heat transfer within the particle is fast relative to the heat transfer between the gas and solid interface, and therefore the particle temperature is uniform throughout at any instance in time. The particle temperature profile is thus governed by the heat transfer from the surrounding gas to the particle, and the rate can be written as:

$$\frac{dT_p}{dt} = \frac{hA}{\rho V c_p}(T_{gas} - T_p) \tag{1}$$

Where $T_p$, A, V, $C_p$ refer to the temperature, surface area, volume, and temperature-dependent heat capacity (calculated with fitting parameters available on the NIST webbook) of the particle, t is time, and $T_{gas}$ is the gas temperature. h is the heat transfer coefficient, defined in terms of the Nusselt number (Nu), thermal conductivity of the gas and particle diameter ($d_p$) as:

$$h = \frac{Nu k_g}{d_p} \tag{2}$$

The Nusselt number of the particles is estimated from the modeling results of Filippov et al.[40] for a large gas to particle temperature ratio and accommodation coefficient of 0.3.

For the heating calculation, the gas temperature was assumed to be fixed at 1700 K, just above the melting temperature of CuO (1599 K). This temperature is chosen so as to provide a source of heat to melt the particles (i.e. above the chosen melting point). It should be noted that it is not known what temperature the surrounding gas will be, and in fact it may even be as high as the adiabatic flame temperature (~3000 K). Since the experimental results tabulated in Table 4 suggested that apparent sintering occurs before the onset of optical emission was detected, it is more likely that the gas temperature is well below the adiabatic flame temperature. In any case, the use of 1700 K is a conservative choice, and any increase in the temperature will result in a decrease the sintering time.

To calculate the timescale of the actual fusion process ($\tau_{fus}$), the approach laid out in Mukherjee et al. is followed.[31] Below the melting point, particles can fuse via solid state grain boundary diffusion, whereas above the melting point surface tension forces dominate and the timescale can be estimated by a viscous flow mechanism.[41] Preliminary calculations suggest that the timescale becomes orders of magnitude faster once the melting temperature is reached and the mechanism changes. Therefore, we make the assumption that no morphological

changes occur until the particle has been completely melted.  Once this occurs, the fusion time can be approximated by:

$$\tau_{fus} = \frac{\mu d_{eff}}{2\sigma_l}$$ (3)

where $d_{eff}$ is the instantaneous effective particle diameter ($\sim 2d_p$) , $\mu$ is the size dependent liquid viscosity calculated by an empirical fit[42] ($\sim 100$ mPa*s), and $\sigma_l$ is the surface tension of the liquid ($\sim 0.7$ J/m$^2$).[43]

Equation (1) was numerically integrated in two steps; time to sensibly heat CuO from room temperature to the melting point, followed by the time to melt the particle at a constant temperature of 1599 K.  The latent heat of fusion of $Cu_2O$ (112 kJ/mol, ICT database) was used, since this is what CuO decomposes to as it melts.  The heating time is reported as the sum of these two times.  Equation (3) was used to calculate the subsequent fusion time at 1599 K.  The heating time is compared with the fusion timescale in Figure 12, and as a function of particle diameter.  The total sintering time is the sum of the time to heat, melt, and fuse two identical particles with initial diameter $d_p$.  From Figure 12, it can be seen that the actual fusion of particles happens on a much faster timescale than the heating time of the particles.  In other words, if melting can be achieved then a calculation of the "sintering timescale" of particles can be reduced to a calculation of the time it takes to heat and melt the particles.  Most important, however, is that sintering time is comparable to the characteristic reaction timescale.  Thus, it is reasonable to expect that sintering processes and their effects (heat release, wetting, change in size, etc.) directly participate in the reaction dynamics of nanothermite mixtures.  The reaction rate is therefore coupled to the sintering rate, and this correlation supports that a reactive sintering mechanism is occurring.  In a real self-propagating thermite, the reaction may occur in two steps: reactive sintering which rapidly decomposes the oxidizer and pressurizes the system, followed by the combustion of the remaining aluminum in a pressurized, oxygenate environment.  These results are consistent with the findings in our previous work,[13] but further expand on how a two step mechanism may be possible.

The calculation can be extended to the addition of nano-Al (or thermites) to a high explosive, where temperatures are expected to exceed 3000 K, well above the melting point of the oxide shell in aluminum.  The model predicts sintering times that are orders of magnitude smaller than some experimentally measured reaction times scales, and suggest that, depending on the particular heating environment, significant sintering may precede much of the combustion.  If nanoparticles are indeed sintering into larger particle much faster than the characteristic reaction timescale, then this would entirely change our conceptual understanding of how reactivity should scale with particle size.  In several examples, authors have experimentally shown a very low diameter dependence on nanoparticle burning times,[44, 45] even though the burning time has traditionally been speculated to scale directly with diameter according to a  "$d^1$"

112

law.  In many works, however, the designation of particle size is somewhat ambiguous, as nanoparticles are often found to be highly aggregated.  If early sintering occurs, then instead of classifying the particle dimensions in terms of the average primary particle diameter or the exposed surface area, it may perhaps be more appropriate to calculate the average volume of an aggregate and report the size of an equivalent-volume sphere.  Also, experimental techniques which utilize slow heating rates may give different results than high heating experiments.  For example, if the reaction of nano-Al in a gas is being studied using thermogravimetric analysis, the intense heat losses may prevent the particle from ever reaching the melting point of $Al_2O_3$, and thus the particles may maintain their morphologies during the oxidation and display strong size dependence.  If, however, nano-Al is shocked to a very high temperature at a high heating rate, the thermal heating alone may serve to melt and sinter particles early, and thus a size-dependence may not be observed.

When one collectively looks at all the experimental results along with the predictions of the model, it should become quite clear that particle sintering is an important phenomenon to consider for energetic applications involving agglomerated nanoparticles.  In the thermites, it's suggested that the sintering is directly coupled to the reaction by a reactive sintering mechanism.  However, particle sintering can also be thermally activated in situations where the heat transfer is vigorous to rapidly raise the temperature above the melting point, and thus the particles become fluid-like.  The results pose new questions about the commonly held belief that smaller particles sizes necessarily lead to an enhancement in reactivity.

## Conclusion

This reaction mechanism of nano-Al based thermites using several high heating techniques was investigated.  First, thermites were rapidly heated on an ultra thin Pt wire, and the optical emission was monitored to determine the ignition temperature.  It was found that the four nano-Al based thermites (CuO, $Fe_2O_3$, $WO_3$, $Bi_2O_3$) ignited above the melting temperature of Al, and closer to the melting/decomposition temperature of the metal oxide.

High heating microscopy experiments were conducted for pure nano-Al and CuO, along with nano-Al/6nmCuO and nano-Al/$WO_3$ thermites.  For nano-Al, the results indicate a significant heating pulse was required before large morphological changes were observed.  For the thermites, both systems showed evidence that a reactive sintering mechanism involving condensed phase reactions had occurred.  The results showed very different behavior for the pure metal oxide than what was seen in region where the fuel and oxidizer were in close proximity, suggesting the exothermic reaction largely drives the observed morphological changes.

High resolution image sequences of a thermite of nano-Al/CuO heated on the wire was next collected using a phase-contrast imaging technique, along with

images of just the pure oxidizer. The results are consistent with the microscopy experiment in that larger, more spherical particles indicative of reactive sintering were observed. In addition, the images showed the timescale of sintering was much faster than the onset of optical emission, indicating some reaction precedes thermal runaway. It was shown that the CuO is indeed the gas generator, and it is suggested that in the presence of an exothermic reaction, some amount of the oxidizer rapidly decomposes to release gas. A nano-Al/$Fe_2O_3$ was also viewed on the wire, and exhibited much larger particle formation, along with evidence of oxygen being trapped and bubbling out over a longer timescale. The results show qualitative differences between thermites with an oxidizer which can rapidly decompose (CuO) versus one which does not ($Fe_2O_3$).

Finally, the sintering timescale of CuO nanoparticles is estimated via a simplistic model and compared with a characteristic reaction timescale. The results show that the sintering time is comparable to an experimentally measured pressure rise time, suggesting that a reactive sintering mechanism occurs early and rapidly pressurizes the system. The model was also extended for nano-Al heated by hot gases behind a shock front, and show that in some cases sintering may occur orders of magnitude faster than the reaction.

All of the results suggest a reactive sintering mechanism is occurring early during the burning of nanocomposite thermites, and the model results suggest that convective heating can activate sintering processes on fast timescales, with or without an exothermic reaction. Large morphological changes accompany sintering, thus greatly changing the particle size and morphology. Overall, the results and discussion within this paper provide insight into a new mechanism for nanocomposite thermites which can occur on fast timescales. A reactive sintering mechanism is seen to occur, and suggests that we must re-think our understanding of critical parameters in nanocomposite thermites, such as particle size, morphology, interfacial contact, stoichiometry, etc.

**Table 1: A summary of the materials used in this work. The sizes were all as-specified by the supplier except for the synthesized 6nmCuO, where the size was measured by TEM.**

| Material | Source | Size (primary particle) |
|---|---|---|
| Nano-Al (70% Al, 30% $Al_2O_3$ measured by TGA) | Argonide Corp | 50 nm |
| 6nmCuO | Prepared by wet chemical synthesis | 6 nm (TEM) |
| CuO | Sigma Aldrich | <50 nm |
| $Fe_2O_3$ | Sigma Aldrich | <50 nm |
| $WO_3$ | Sigma Aldrich | <100 nm |
| $Bi_2O_3$ | Sigma Aldrich | 90-210 nm |

**Table 2: Summary of the thermite systems studied by several different high heating experimental techniques. TEM and SEM are transmission and scanning electron microscope, respectively.**

| Material or Thermite | T-Jump/PMT setup for ignition Temp | T-Jump/Movie at ANL | High Heating TEM (JEOL JEM 2100 LaB6 TEM) | High Heating SEM (Hitachi SU-70 SEM) |
|---|---|---|---|---|
| Nano-Al | No | Yes | Yes | No |
| Nano-Al /6nm CuO | Yes | No | Yes | No |
| Nano-Al/CuO | Yes | Yes | No | No |
| Nano-Al/$Fe_2O_3$ | Yes | Yes | No | No |
| Nano-Al/$WO_3$ | Yes | No | No | Yes |
| Nano-Al/$Bi_2O_3$ | Yes | No | No | No |
| CuO | N/A | Yes | No | Yes |
| $Fe_2O_3$ | N/A | Yes | No | No |

**Table 3: A comparison of the ignition temperature measured for various thermites and the melting temperature of the metal oxide. The ignition temperature was measured using the rapidly heated Pt wire experiment and monitoring the onset of optical emission via a photomultiplier tube.**

| Thermite | Ignition Temperature | Oxidizer Melting Temperature (Bulk |
|---|---|---|

|  | (K) +/- 40 K | values) (K) |
|---|---|---|
| Al / CuO | 1217 | 1599 |
| Al / WO$_3$ | 1292 | 1746 |
| Al / Fe$_2$O$_3$ | 1508 | 1735 |
| Al / Bi$_2$O$_3$ | 1067 | 1098 |

**Table 4 Various timescales estimated from the movies of the thermites rapidly heated on the wire. Note that in all cases, larger spherical particles form on a faster timescale than when ignition occurs, and much faster than the measured burning times.**

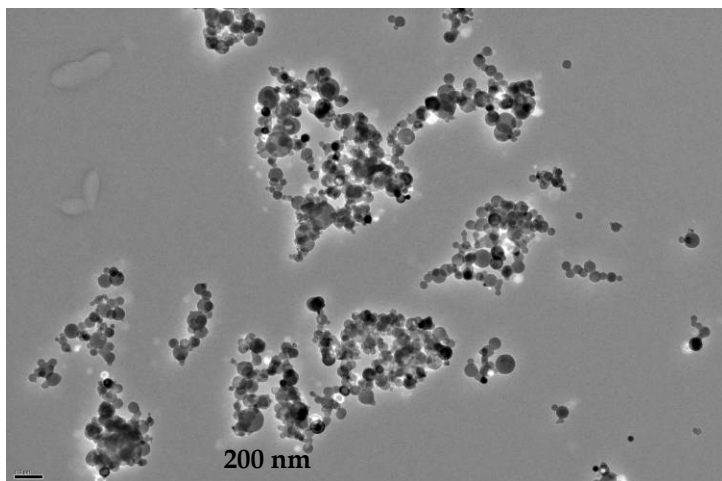| Thermite | Approximate time to form larger spherical particles μs | Onset of Optical Emission (Ignition Point) μs | FWHM Burn Time μs |
|---|---|---|---|
| Al / Fe$_2$O$_3$ | ~44 | 456 | 1900 |
| Al / CuO | ~15 | 140 | 960 |



200 nm

**Figure 1: Representative transmission electron microscope image of "ALEX" nano-Al. The particles have an average primary diameter of 50nm as specified by the supplier. A native passivating oxide shell with a thickness of 2-5nm is also present, though it cannot be resolved at this magnification.**
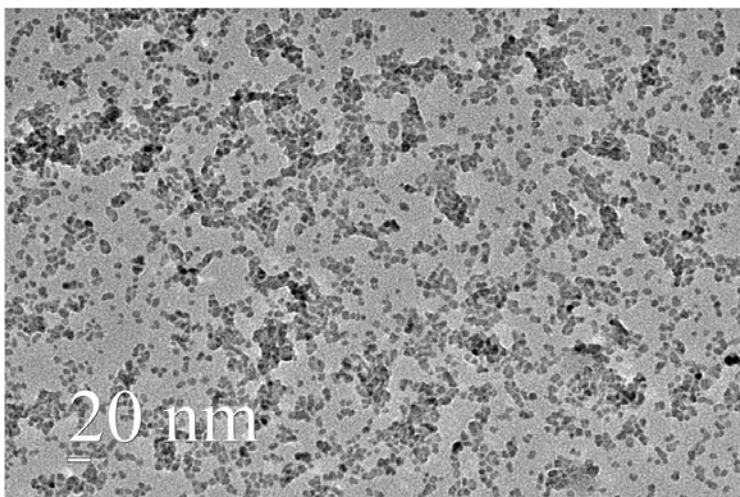
**Figure 2: Representative TEM image of the as-prepared CuO. The primary particle size is ~6nm, as measured by TEM. The particles are spherical with varying amounts of agglomeration. A higher resolution image of the CuO can be seen in Figure 4c.**
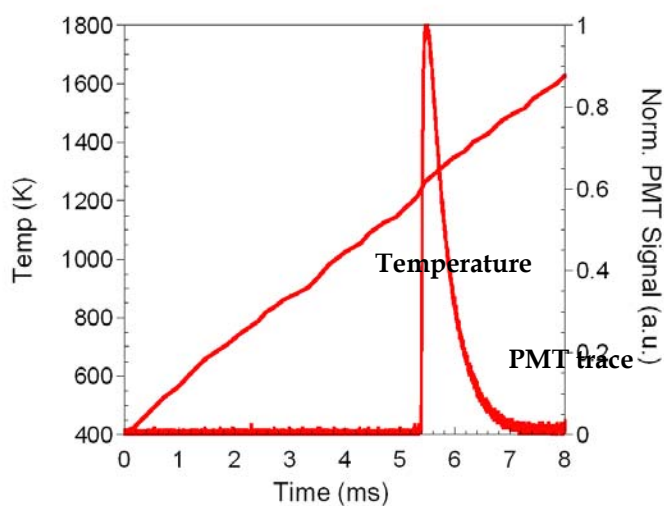


**Figure 3: Typical experimental data for determining the ignition temperature of a thermite (nano-Al/CuO) on a rapidly heated Pt wire. The temperature is calculated for the wire based on resistivity, and the ignition temperature is measured at the onset of optical emission as measured by a PMT.**
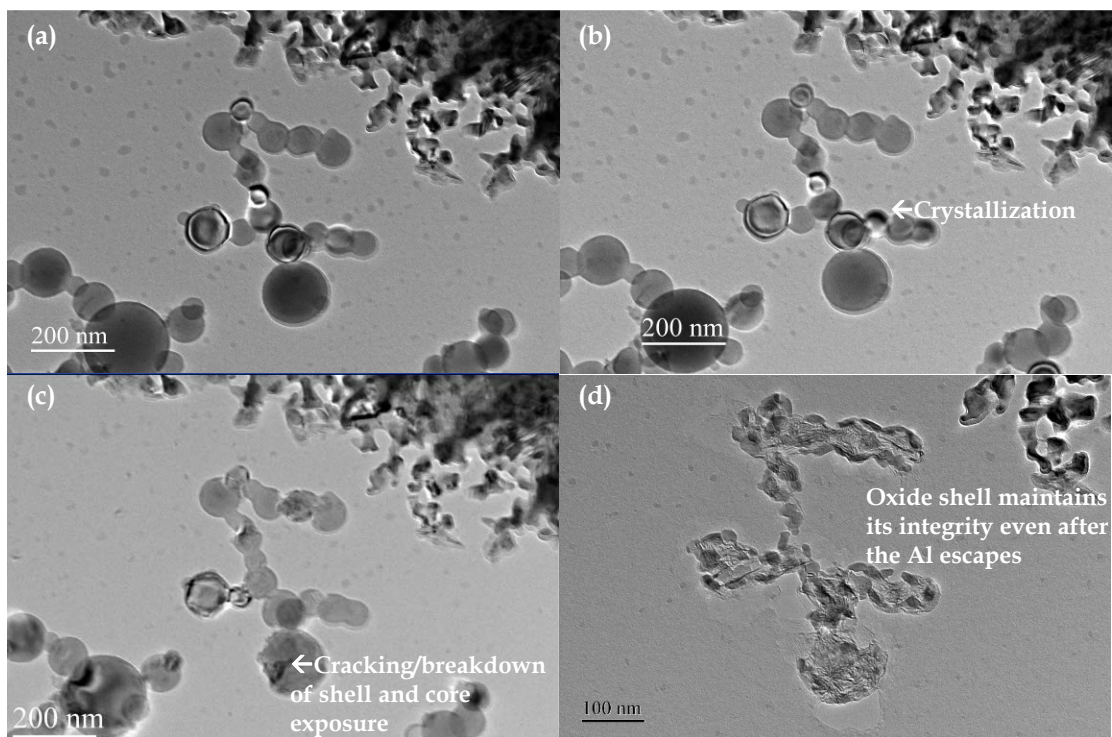
**Figure 4: Nano-Al rapidly heated ($10^6$ K/s) via a special holder inside a transmission electron microscope. The heating pulses used in figures a-d are as follows: (a) unheated, (b) 300-1273 K, held for 1 ms, off, (c) 300-1473 K, held for 10 ms, off, (d) 300-1473 K, held for 1 s, off. Notice how the oxide shell remains mostly intact, implying that the aluminum has melted and diffused through the shell to escape. There is a possibility that the molten aluminum reacts with the carbon film in (d).**
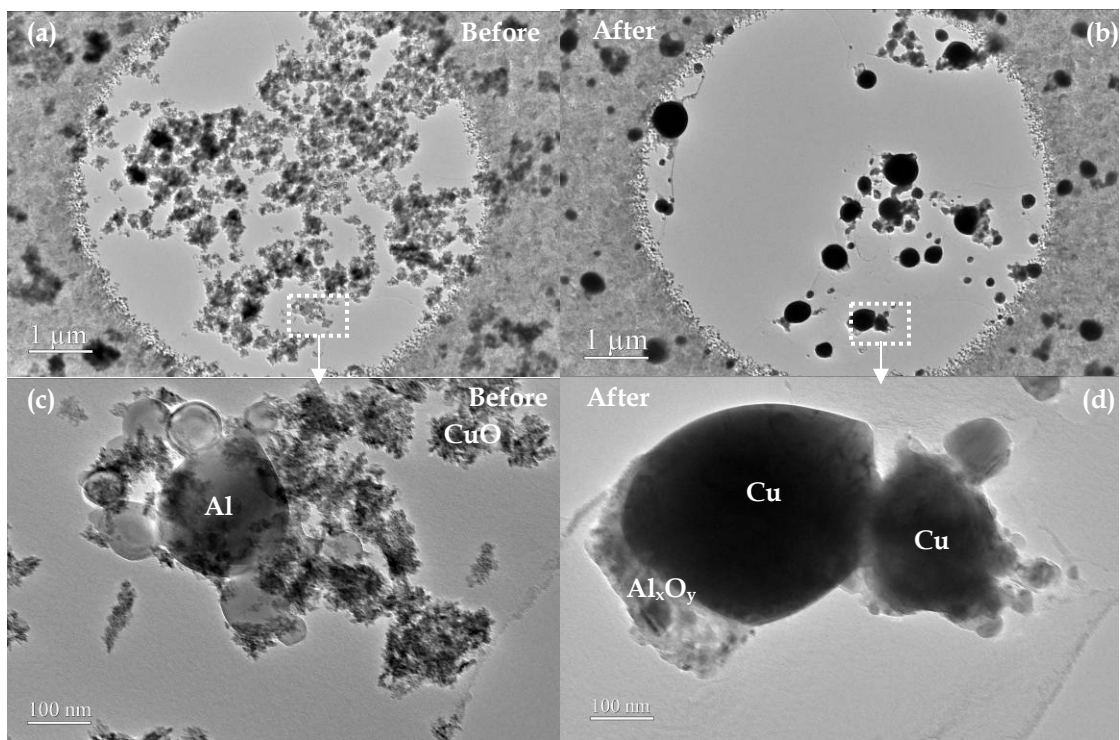
**Figure 5: Before (left) and after (right) images of Al/6nmCuO reacted in-situ in a TEM. Images (c) and (d) are higher magnification images of the boxed regions in (a) and (b). The products were separately confirmed by elemental analysis in a separate microscope. The results suggest a reactive sintering mechanism has occurred to produce the observed morphology.**
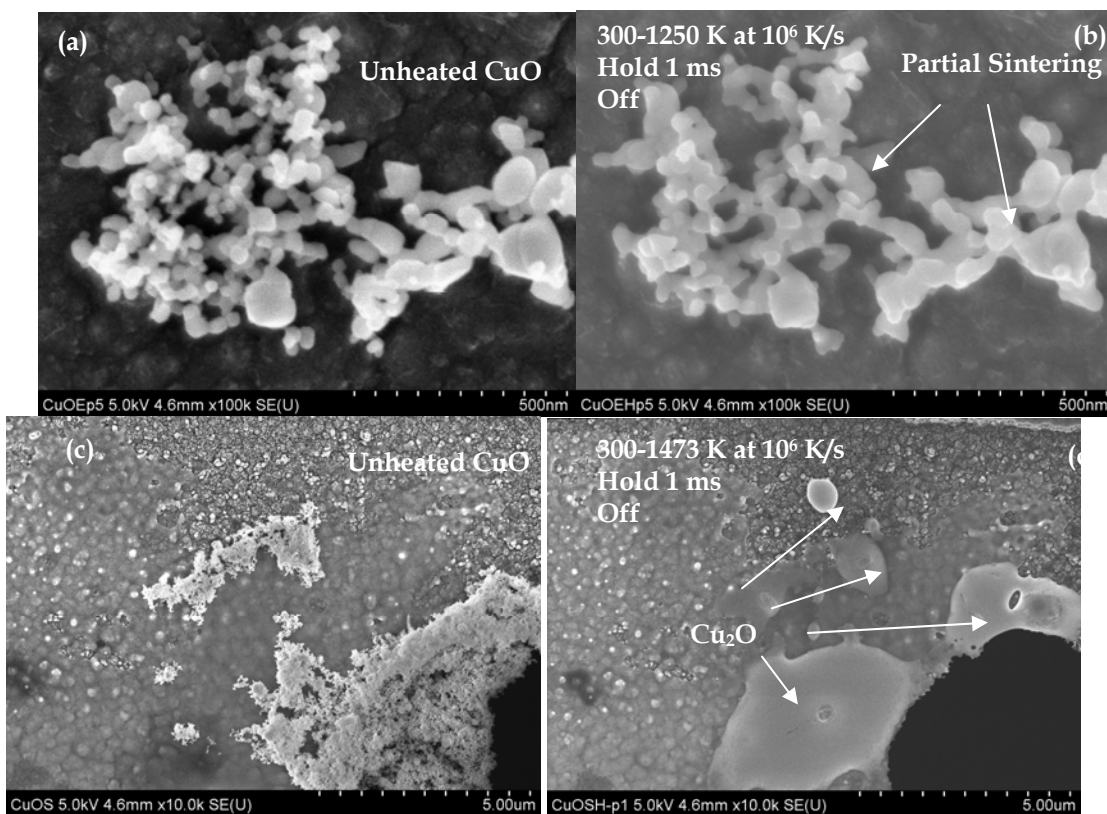
**Figure 6: Images of CuO before (a/c) and after (b/d) rapid heating. The top sample was heated to 1250 K while the bottom sample was heated to the maximum of 1473 K. While a small amount of sintering is seen when the sample is heated to 1250 K, the changes are subtle compared to changes observed when heated to 1473 K. Note that the complete sintering of even micron-sized agglomerates occurs very quickly, in this case in a sub 1 ms timescale.**
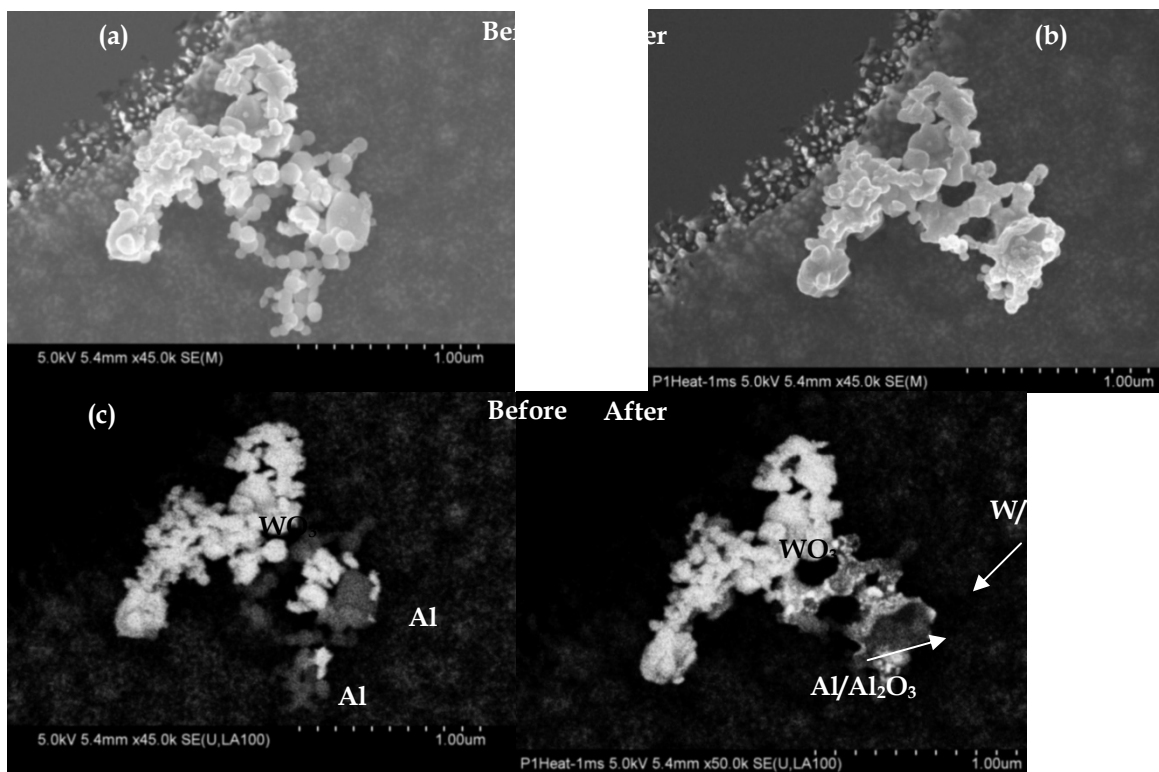
**Figure 7: Secondary electron (a, b) and backscattered electron (c, d) images of a nano-Al/WO$_3$ thermite sample before (a/c) and after (b/d) heating from 300-1473 K at 10$^6$ K/s, held for 1 ms, off. The labeled species were separately confirmed using energy dispersive x-ray spectroscopy (EDS). Note that significant morphological changes only occurred in regions where the fuel and oxidizer were closely mixed, indicating that a reactive sintering mechanism again drove the melting/fusion of adjacent particles. The WO$_3$ not in close proximity to Al did not undergo much change, likely because the pulse was not hot enough to melt the WO$_3$ (MP 1746 K).**
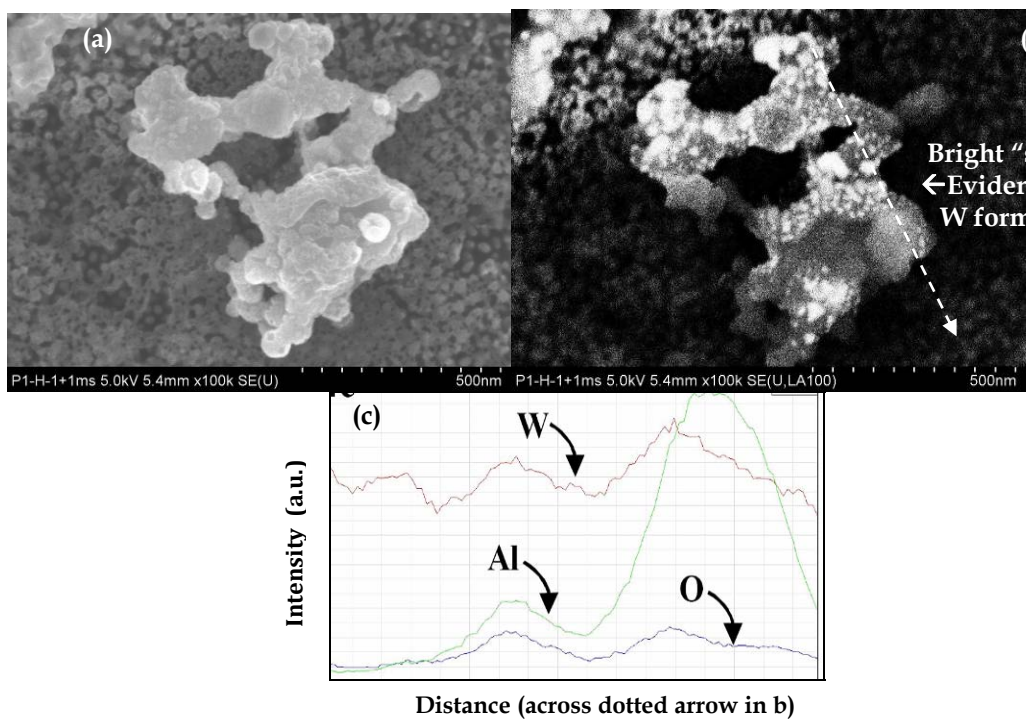
**Figure 8: Nano-Al/WO₃ image/BSE pair (a/b) from Figure 7, after a second identical heating pulse. Note the formation of small white spots in (b), indicating the formation of solid tungsten as the reaction proceeds. An elemental linescan is shown in (c), which plots the intensity of the W, Al, and O signal as a function of position across the dotted arrow in (b). This linescan indicates that interdiffusion of Al/WO₃ has occurred, indicative of condensed phase reactions at an interface.**
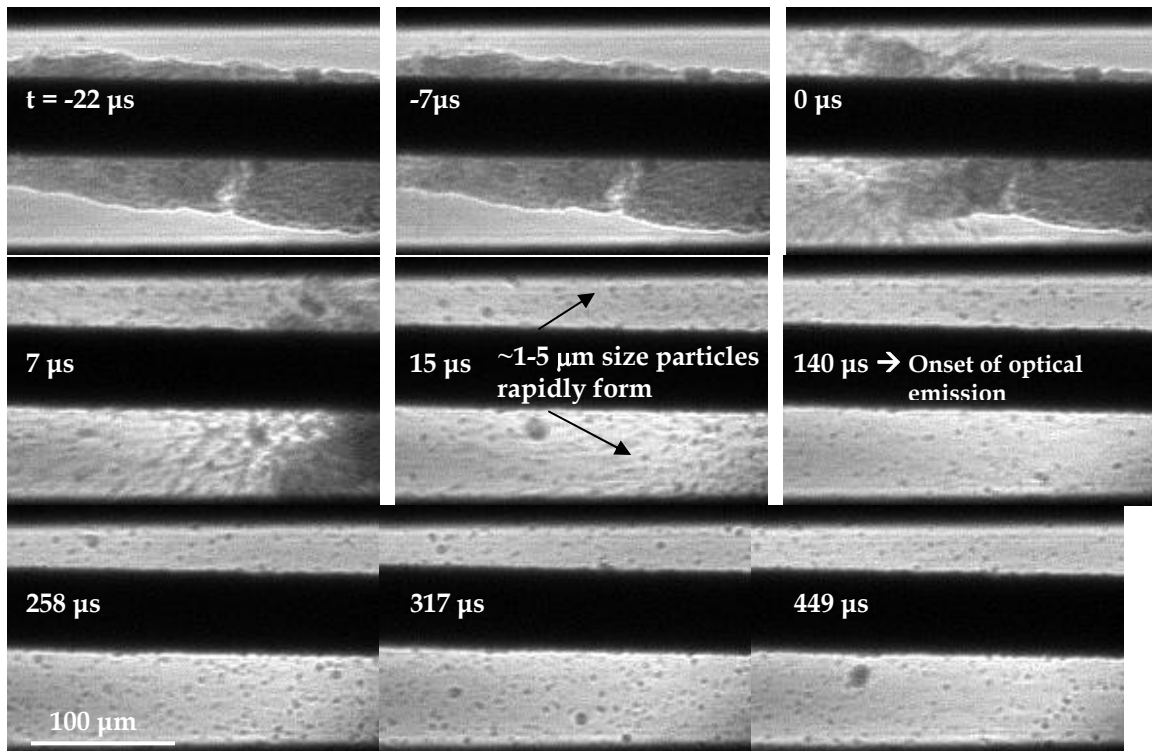
**Figure 9: Series of snapshots of nano-Al/CuO thermite reacted on the wire (dark area in images). Spherical particles with diameters on the order of a few microns were observed to form very early, and well before the onset of optical emission. The results are qualitatively consistent to the observations in Figure 5, and suggest the formation of large spherical particles in this case is also attributed to a reactive sintering mechanism.**
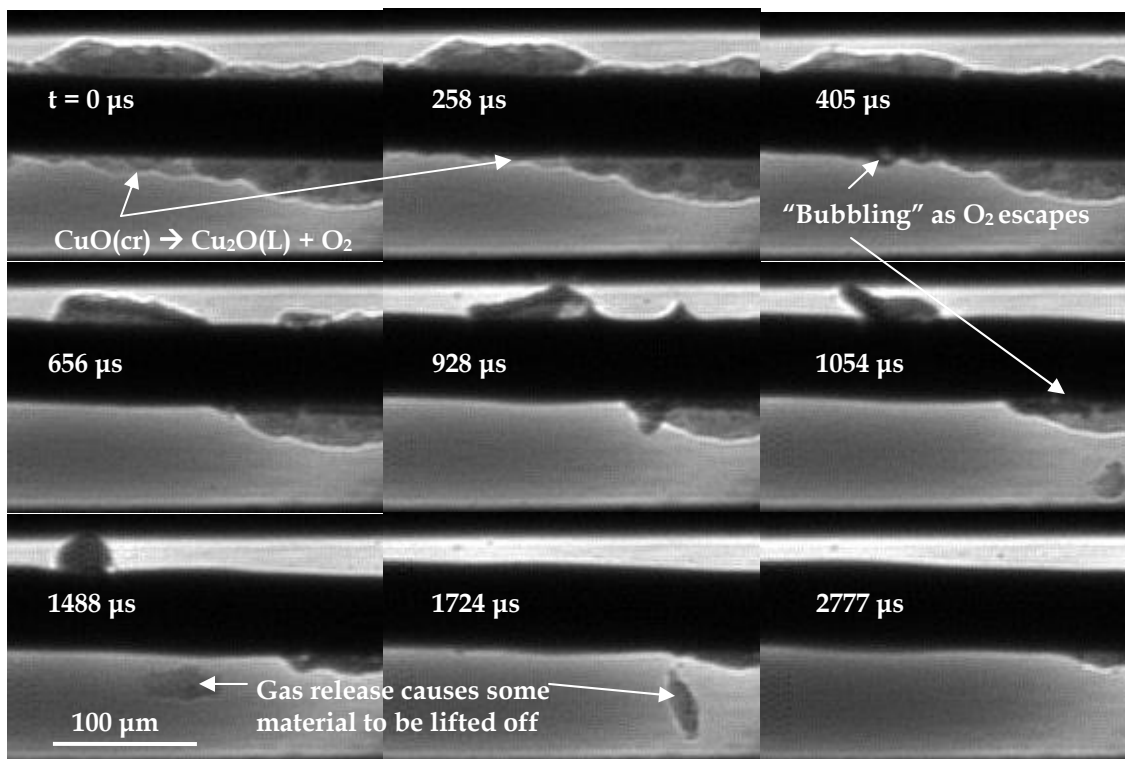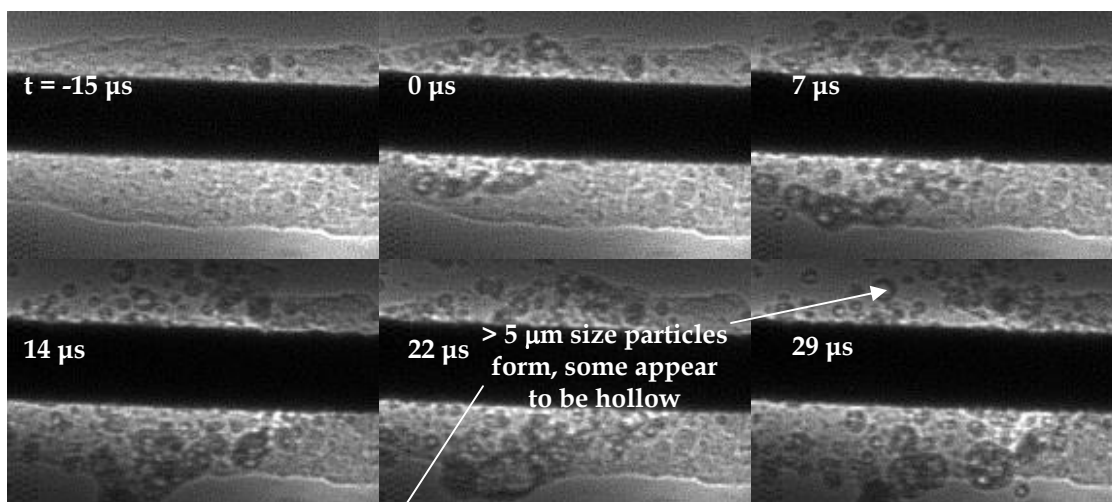
**Figure 10: Series of snapshots nanosized CuO heated on the wire. The video shows signs of "bubbling" indicating that pockets of $O_2$ are trapped within molten $Cu_2O$. The gas release causes some material to be lifted off the wire. Overall, the material is removed from the wire much slower than was observed for the thermite.**
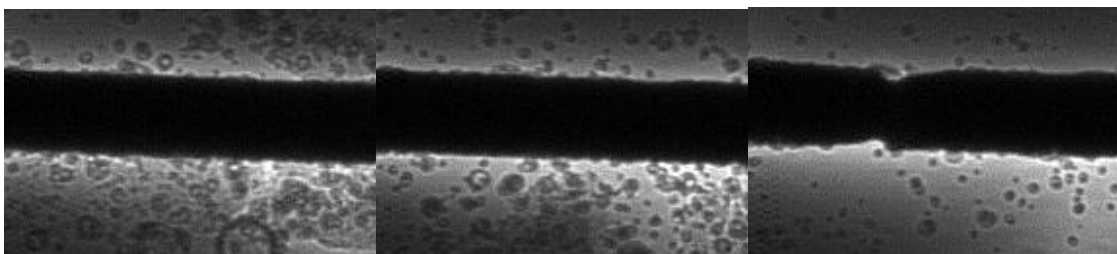
**Figure 11: Series of snapshots of nano-Al/Fe₂O₃ thermite reacted on the wire. Note the formation of micron-sized spherical particles, in this case much larger than was observed for the nano-Al/CuO thermite (see Figure 9). Some particles appear to be hollow in this case. The formation of spherical particles occurs well before the onset of optical emission was measured.**
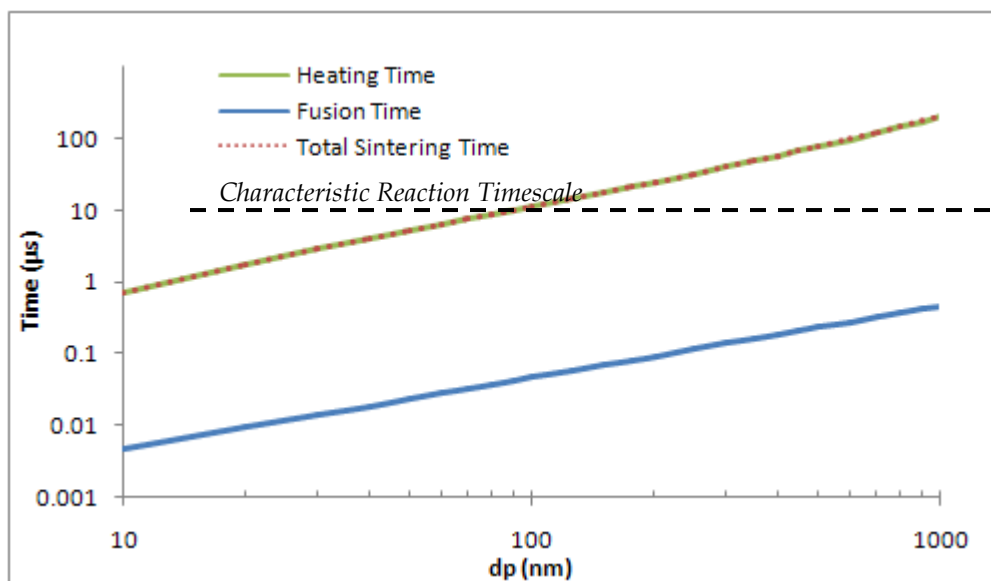


**Figure 12: Model predictions of the total time to sinter CuO nanoparticles in air at 1700 K relative to a characteristic reaction timescale. The total sintering time is assumed to be the sum of two components depicted in the figure; the heating (sensible and latent) time of nanoparticles to the melting temperature, along with the time to fuse the particles calculated by a viscous flow mechanism. The timescale of fusion is found to be much faster than the heating time, therefore, the calculation of the total sintering time can be reduced simply to a calculation of the time it takes to heat and melt nanoparticles. The results show the sintering and reaction timescales are comparable, indicative of a reactive sintering mechanism.**

1.      C. E. Aumann; G. L. Skofronick; J. A. Martin, *Journal of Vacuum Science & Technology, B: Microelectronics and Nanometer Structures* **1995,** 13, (3), 1178-83.

2.      D. E. Wilson; K. K. Kim in: *Combustion of Consolidated and Confined Metastable Intermolecular Composites*, 43rd AIAA Sciences Metting and Exhibit, Reno, NV, January 10-13, 2005; Reno, NV, 2005.

3.      J. A. Puszynski; C. J. Bulian; J. J. Swiatkiewicz, *Materials Research Society Symposium Proceedings* **2006,** 896, (Multifunctional Energetic Materials), 147-158.

4.      D. Prentice; M. L. Pantoya; B. J. Clapsaddle, *Journal of Physical Chemistry B* **2005,** 109, (43), 20180-20185.

5.      M. Schoenitz; T. Ward; E. L. Dreizin, *Materials Research Society Symposium Proceedings* **2003,** 800, (Synthesis, Characterization and Properties of Energetic/Reactive Nanomaterials), 85-90.

6.      M. L. Pantoya; J. J. Granier, *Propellants, Explosives, Pyrotechnics* **2005,** 30, (1), 53-62.

7.      D. S. Moore; S. F. Son; B. W. Asay, *Propellants, Explosives, Pyrotechnics* **2004,** 29, (2), 106-111.

8.      J. A. Puszynski, *Materials Research Society Symposium Proceedings* **2003,** 800, (Synthesis, Characterization and Properties of Energetic/Reactive Nanomaterials), 223-232.

9.      V. E. Sanders; B. W. Asay; T. J. Foley; B. C. Tappan; A. N. Pacheco; S. F. Son, *Journal of Propulsion and Power* **2007,** 23, (4), 707-714.

10.     S. H. Kim; M. R. Zachariah, *Advanced Materials* **2004,** 16, (20), 1821-+.

11.     A. Prakash; A. V. McCormick; M. R. Zachariah, *Nano Letters* **2005,** 5, (7), 1357-1360.

12.     K. S. Martirosyan; L. Z. Wang; A. Vicent; D. Luss, *Propellants Explosives Pyrotechnics* **2009,** 34, (6), 532-538.

13.     K. T. Sullivan; M. R. Zachariah, *In press- Journal of Propulsion and Power* **2010**.

14.     L. P. H. Jeurgens; W. G. Sloof; F. D. Tichelaar; E. J. Mittemeijer, *Physical Review B: Condensed Matter and Materials Physics* **2000,** 62, (7), 4707-4719.

15.     M. A. Trunov; M. Schoenitz; X. Zhu; E. L. Dreizin, *Combustion and Flame* **2005,** 140, (4), 310-318.

16.     J. J. Granier; M. L. Pantoya, *Combustion and Flame* **2004,** 138, (4), 373-383.

17.     M. A. Trunov; M. Schoenitz; E. L. Dreizin, *Propellants, Explosives, Pyrotechnics* **2005,** 30, (1), 36-43.

18.     V. I. Levitas; B. W. Asay; S. F. Son; M. Pantoya, *Journal of Applied Physics* **2007,** 101, (8).

19.     V. I. Levitas; M. L. Pantoya; B. Dikici, *Applied Physics Letters* **2008,** 92, (1), 011921/1- 011921/3.

20.     V. I. Levitas, *Combustion and Flame* **2009,** 156, (2), 543-546.

21.     A. Rai; K. Park; L. Zhou; M. R. Zachariah, *Combustion Theory and Modelling* **2006,** 10, (5), 843-859.

22.     B. J. Henz; T. Hawa; M. R. Zachariah, *Journal of Applied Physics* 107, (2).

23.     S. Chowdhury; K. Sullivan; N. Piekiel; L. Zhou; M. R. Zachariah, *Journal of Physical Chemistry C* **2010,** 114, (20), 9191-9195.

24.     T. Bazyn; H. Krier; N. Glumac, *Proceedings of the Combustion Institute* **2007,** 31, 2021-2028.

25.     T. Bazyn; H. Krier; N. Glumac in: *Shock Tube Measurements of Combustion of Nano-Aluminum*, 44th AIAA Aerospace Sciences Meeting and Exhibit, Reno, Nevada, 2006; Reno, Nevada, 2006; pp 1-8.

26.     T. Bazyn; H. Krier; N. Glumac, *Combustion and Flame* **2006,** 145, (4), 703-713.

27.     T. Bazyn; H. Krier; N. Glumac, *Proceedings of the Combustion Institute* **2007,** 31, (Pt. 2), 2021-2028.

28.     T. Bazyn; N. Glumac; H. Krier; T. S. Ward; M. Schoenitz; E. L. Dreizin, *Combustion Science and Technology* **2007,** 179, (3), 457-476.

29.     M. Schoenitz; S. Umbrajkar; E. L. Dreizin, *Journal of Propulsion and Power* **2007,** 23, (4), 683-687.

30.     S. Chowdhury; K. Sullivan; N. Piekiel; L. Zhou; M. R. Zachariah, *Journal of Physical Chemistry C Letters*.

31.     L. Zhou; N. Piekiel; S. Chowdhury; M. R. Zachariah, *Rapid Communications in Mass Spectrometry* **2009,** 23, (1), 194-202.

32.     T. Hawa; M. R. Zachariah, *Physical Review B* **2007,** 76, (5).

33.     K. E. J. Lehtinen; M. R. Zachariah, *Journal of Aerosol Science* **2002,** 33, (2), 357-368.

34.     B. J. Henz; T. Hawa; M. Zachariah, *Journal of Applied Physics* **2009,** 105, (12).

35.     K. J. Blobaum; D. Van Heerden; A. J. Gavens; T. P. Weihs, *Acta Materialia* **2003,** 51, (13), 3871-3884.

36.     Y. J. Wang; X. Liu; K. S. Im; W. K. Lee; J. Wang; K. Fezzaa; D. L. S. Hung; J. R. Winkelman, *Nature Physics* **2008,** 4, (4), 305-309.

37.     L. Zhou; N. Piekiel; S. Chowdhury; M. R. Zachariah, *J Phys Chem C* **2010**.

38.     L. Zhou; N. Piekiel; S. Chowdhury; D. Lee; M. R. Zachariah, *Journal of Applied Physics* **2009,** 106, (8).

39.     K. T. Sullivan; G. Young; M. R. Zachariah, *Combustion and Flame* **2007**.

40.     A. V. Filippov; D. E. Rosner, *International Journal of Heat and Mass Transfer* **1999,** 43, (1), 127-138.

41.     P. Tandon; D. E. Rosner, *Journal of Colloid and Interface Science* **1999,** 213, (2), 273-286.

42.     T. Iida; H. Sakai; Y. Kita; K. Murakami, *High Temperature Materials and Processes* **2000,** 19, (3-4), 153-164.

43.     S. Y. Sun; L. Zhang; S. Jahanshahi, *Metallurgical and Materials Transactions B-Process Metallurgy and Materials Processing Science* **2003,** 34, (5), 517-523.

44.    R. A. Yetter; G. A. Risha; S. F. Son, *Proceedings of the Combustion Institute* **2009,** 32, 1819-1838.

45.    G. Young; K. Sullivan; M. R. Zachariah; K. Yu, *Combustion and Flame* **2009,** 156, (2), 322-333.

**YEAR 4:   The report has two sections**
1. **Ignition Initiation of Various Nanothermites**
2. **Alane as a dopant in MIC'S**


# 1. Ignition Initiation of Various Nanothermites

## Introduction

Prior work has shown proof of a diffusion based mechanism behind the ignition initiation of a nanothermite reaction at heating rates on the order of $10^5$ K/s. However, due to the nature of the experiments, we were unable to detect if this initiation was caused by the diffusion of the aluminum ions outwards across the shell. Here we employ a set of experiments for various nanothermites to promote further understanding of the ignition mechanism. These set of experiments are crafted by judicious choice of the oxidizer to verify our current understanding and test/predict/propose similar/alternate phenomenological mechanisms.

## Literature Survey

Although nanoparticles of boron [41] and silicon [42] have been explored in nanothermites, nano-sized aluminum (Al) is predominantly the fuel of choice due to a combination of its high energy density, reactivity, low cost, and nontoxic nature.  A variety of oxidizers have been studied, and the choice often depends on the particular application. Copper oxide (CuO) [9, 43], iron oxide ($Fe_2O_3$) [43], molybdenum oxide ($MoO_3$) [5, 6, 18, 44-47], tungsten oxide ($WO_3$) [47] and bismuth oxide ($Bi_2O_3$) [47, 48] are the commonly used oxidizers in nanocomposite thermite formulations.

The nature of the morphology of the fuel and oxidizer particles is important as they play a significant role in the reaction rate/mechanism.  When exposed to air, a portion of the aluminum oxidizes, creating an amorphous aluminum oxide shell surrounding the elemental core of aluminum. This shell generally is very thin ($\sim$ 2-5 nm thick), and protects the particle from further oxidation in air.  These particles are typically aggregates of spherical primary particles although recent work has shown the formation of single domain aluminum crystals [49]. For nanoparticles, the oxide shell can represent a significant portion of the particle mass.  Oxidizer particles, on the other hand, display various morphologies. They have been used in the form of platelets [46, 47], crystalline sheets [47], powders [43, 48] and nanorods [46, 47, 50].

Particles of nanoscale dimensions exhibit properties that are different from their micron sized counterparts. Lower activation energy for nanoaluminum activation has been reported by Aumann et al. [3]. Aluminum nanoparticles in various MIC formulations have exhibited lower reaction temperatures [6, 9, 44], smaller ignition delays [18, 45] and higher flame velocity/burning rates [10, 11, 47]. The ignition mechanism of aluminum in air is something which has received considerable attention in the literature.  Nano-sized aluminum has been experimentally shown to ignite much closer to the melting temperature of aluminum (933 K), whereas larger aluminum ignites closer to the melting temperature of $Al_2O_3$ (2327 K).  Trunov et al. [8] proposed a

diffusion based mechanism to explain the ignition mechanism of aluminum particles. The authors claim that polymorphic phase transformations in the alumina shell occur as the particles are heated, and can expose the elemental aluminum to oxidizer as the shell undergoes these transformations. Micron-sized particles can react and "heal" the shell, whereas nanoparticles cannot and thus ignite at a lower temperature. Rai et al. [38] investigated the reactivity of aluminum particles in air using a furnace and online aerosol sampling techniques, and using electron microscopy, showed the formation of hollow $Al_2O_3$ particles above 1250 K. The authors also used hot stage TEM to study the thermal response of nanoaluminum in vacuum, and showed the outwards migration of aluminum through the shell, starting around 1000 K [28]. This suggests that the molten aluminum core can leak out through the shell. Nakamura found similar evidence of the formation of hollow particles by oxidation [39]. In a recent study by our group, Sullivan et al. [15] used a specially-designed heating holder to heat nano-Al at $10^6$ K/s inside an electron microscope. In this particular study, a significant heating pulse (300-1473 K, held for 10 ms) was necessary before evidence of shell breakdown and outwards migration of Al could visually be identified. A lesser heating pulse, although above the melting temperature of Al, induced no changes within the very fast heating and cooling timescale of this experimental technique.

In all of the studies on ignition, it is evident that understanding the thermally-induced interaction of the low melting core with the high melting shell is important in describing the ignition mechanism of nano-sized Al. While there is a considerable body of data at lower heating rates, very little data is available on ignition behavior at high heating rate conditions. Levitas et al. [31] proposed that at high heating rates (~$10^7$-$10^8$ K/s) the aluminum core melts and exert mechanical stress on the solid oxide shell. This causes spallation of the shell, and is predicted to happen near the melting temperature of the aluminum core, viz. 933 K. The violent rupture of the shell causes tensile stress on the molten Al core, thus unloading small molten clusters of aluminum at high velocities. The reaction rate in this mechanism is inherently not rate-limited by the diffusion of oxidizer/fuel through the shell. This mechanism is termed "Melt Dispersion" which has been discussed in details in Chapter 2. In contrast, results from our previous work in Chapter 2 using aluminum/CuO nanothermites reveals that an ignition delay is observed which increased as the oxide shell was thickened. This measured ignition delay was used to estimate an effective diffusion coefficient of ~ $10^{-10}$ cm$^2$/s, consistent with another experimental result of effective diffusion of ~ $10^{-8}$ cm$^2$/s [38], implying that the ignition could be explained by a diffusion mechanism. In a separate study [35] using time resolved mass spectrometry of rapidly heated (~$10^5$ K/s) nanocomposites, no evidence for aluminum clusters were found but only elemental aluminum was detected. Based on our previous work and the lack of aluminum clusters being detected, our current speculation is that aluminum migrates through its shell via a diffusion mechanism. The outwards migration of aluminum through the shell has been experimentally reported by several authors [15, 28, 39].

This work deals largely with the ignition of nanocomposite thermites. In air, the oxidizer exists as a gas, while in nanocomposite a metal oxide is essentially serving as a condensed-phase medium to store the oxidizer in close proximity to the fuel. At the current time, it's not clear whether the ignition mechanism will be similar between the two systems. The ignition mechanism of nanocomposite thermites remains poorly

understood and only a select few studies have used experimental techniques which utilize high heating rates. Bazyn et al. [12] studied the ignition temperature and burn time of Al-MoO$_3$ and Al-Fe$_2$O$_3$ at high heating rates ($\sim$10$^6$ K/s) using a shock tube. They found evidence for ignition of both materials at 1400 and 1800 K respectively. It's important to note that these temperatures are significantly higher than the melting temperature of aluminum, which is experimentally where nano-Al has been shown to begin reaction in air using low heating rate experiments.

The findings of ignition temperatures well above the melting temperature of aluminum, and the fact that ignition temperature depends on oxidizer type [35], indicate that the oxidizer must play some role in the ignition mechanism at high heating rates. The thermal response of a metal oxide depends on the particular oxidizer; some materials can melt, others decompose into sub-oxides prior to melting, some can even sublimate. Using time resolved mass spectrometry coupled with a high heating rate ($\sim$5 x 10$^5$ K/s) we detected the release of molecular oxygen from CuO and Fe$_2$O$_3$ in the reaction of Al-CuO and Al-Fe$_2$O$_3$ thermites [35]. The liberated O$_2$ was one of the first species to be detected in time, thus suggesting that O$_2$ release played a critical role in the ignition mechanism. However, these studies were limited to oxidizers which don't technically melt, but undergo decomposition to a sub-oxide and release O$_2$. Some other oxidizers, such as WO$_3$ and Bi$_2$O$_3$ which undergo melting prior to decomposition were not included in the prior study and thus are included in the current work to cover a broader range of oxidizers. Some other oxidizers like MoO$_3$ which are known to sublimate without melting are also included.

This work is a study on the ignition of several nanothermite systems subjected to high heating rates (4.5 x 10$^5$ K/s). The selection of oxidizers was made to compare and contrast oxidizers which decompose prior to melting, or vice versa, sublimates or release oxygen at different temperature.

## *Experimental*

### Sample Preparation

Commercially available aluminum nanopowder (Argonide Corp.) was used for all the experiments. The nominal size of the particles as specified by the supplier is 50 nm, and was determined to be 70% active using thermogravimetric (TGA) analysis, indicating a shell of $\sim$ 2 nm in thickness. All materials used, their respective particles sizes and the suppliers are listed below in Table 4.1. The particle sizes are specified by the manufacturer.

**Table 4.1 Oxidizers, procurer and primary particle size**

| Material | Supplier | Particle size (nm) |
|---|---|---|
| ALEX | Argonide Corp. | 50 |
| Copper oxide (CuO) | Sigma-Aldrich | < 50 |
| Micron copper oxide (CuO) | Sigma-Aldrich | 1000-3000 |
| Iron oxide (Fe$_2$O$_3$) | Sigma-Aldrich | < 50 |
| Tungsten oxide (WO$_3$) | Sigma-Aldrich | < 50 |
| Bismuth oxide (Bi$_2$O$_3$) | Sigma-Aldrich | < 50 |

| | | |
|---|---|---|
| Silver iodate (AgIO$_3$) | China Lake | ~ 236 |
| Diiodine pentoxide (I$_2$O$_5$) | Sigma-Aldrich | < 50 |
| Tin (IV) oxide (SnO$_2$) | Sigma-Aldrich | < 50 |
| Cobalt(II, III) oxide (Co$_3$O$_4$) | Sigma-Aldrich | < 50 |
| Molybdenum oxide (MoO$_3$) | US Research Nanomaterials | 13-80 |
| Antimony (III) oxide (Sb$_2$O$_3$) | US Research Nanomaterials | 80-200 |

For oxygen release tests, described below, a small amount (~ 10 mg) of the oxidizer is taken and is sonicated in hexane for about 10 minutes to break down the aggregates. To prepare the stoichiometric nanothermite samples, appropriate amounts of aluminum and the corresponding oxidizer are weighed and dispersed in hexane. The dispersion is thereafter sonicated for 25 min before being subjected to ignition tests.

### Experimental Approach

In order to achieve the high heating rates used in this study, a thin platinum wire (length ~ 12 mm, diameter ~ 76 um) is joule-heated by a tunable voltage pulse generated by a home built power source. For any applied pulse duration, the maximum temperature to which the wire is heated (i.e. heating rate) can be controlled by varying the applied voltage, up to a maximum value of ~1600-1700 K, which is below the melting point of platinum. The transient current passing through the circuit is measured by a current probe. A small portion of the central region of the wire (~ 3-5 mm) is coated with the samples by pipetting a dispersion of the samples in hexane onto the wire, then allowing the hexane to evaporate. The material coating the wire is estimated to be ~ 300 µg. From the recorded voltage and current data, the temperature of the wire at the point of ignition can be calculated from the resistivity of the wire using the well known Callender- Van Dusen equation [33]. As the validity of this equation is below 950 K, the platinum wire is optically calibrated for its resistance against a standard blackbody source that can reach a maximum temperature of 1373 K. Since the maximum temperature attained in the platinum wire could be higher, as is evident through melting of the wire, the calibration is extrapolated up to about 1800 K. The calibration procedure is detailed in Appendix 1. The maximum uncertainty associated with the determination of temperature is approximately ± 50 K. Heating rate is defined as the ratio of the difference in maximum temperature and initial temperature to the pulse duration.

The optical emission is monitored using a photomultiplier tube (PMT), and the ignition temperature is taken as the wire temperature corresponding to the sudden onset of optical emission, and above the background emission from the heated wire. Optical emission measurements are naturally biased to observing the hottest period during the combustion, so low-temperature reactions may go undetected. For each test, a new wire is used since reacted material may adhere to the wire and change the electrical properties, thus presenting uncertainty in the temperature calculation.

In addition to light emission we also conduct time-resolved speciation, using a custom built time-of-flight mass spectrometer (TOFMS). Details of the experimental and working procedure for our TOFMS system are given in a previous work [34]. For experiments involving the heating behavior on the oxidizers alone, this setup was used

without further modification. For nanothermite ignition studies in the mass spectrometer, the setup was modified by adding a photomultiplier tube (PMT) to a visible port in the setup, thus allowing for simultaneous collection of the mass spectra and the optical emission. This enables a direct comparison between the optical emission, commonly used as a measurement of ignition, and the time-resolved species evolved during the reaction. The TOFMS setup can collect a spectrum of the products formed during the course of the reaction every 100 μs, and at a heating rate of $5 \times 10^5$ K/s, this presents an uncertainty of ~50 K in the temperature of the species detection.

## Experiments Conducted

There are three types of experiments that are carried out in this study. They are

i) **Gas release experiments**: The first set of experiments is performed in TOFMS to determine the temperature of gas release from the oxidizer upon heating. These may be termed as gas release experiments. In these tests, a small amount of the sonicated oxidizer is coated on the platinum wire and is heated. The goal of these experiments is to know the behavior of the oxidizers when they are subjected to heating rates $\sim 4 \times 10^5$ K/s. This includes knowledge of the temperature at which the oxidizer releases gas as well as a qualitative idea of the amount of gas released upon decomposition. A light detector, such as the PMT, was not utilized for these experiments.

ii) **T-jump TOFMS with optical emission:** A second set of experiments are performed in TOFMS to determine the temporal speciation during the reaction along with the optical detection of ignition by attaching a PMT to a visible port of the TOFMS. The setup is described in section 4.3.2. This enables simultaneous measurement of the ignition time as observed through the PMT (and therefore the temperature) and the speciation occurring during the reaction.

iii) **T-jump experiments in air:** A third set of experiments are carried out in a chamber in air detailed in section 4.3.2. The goal of these studies is to find out the ignition temperature of the nanothermites in air.

The set of experiments conducted via method (ii) and (iii) are different from one another in the fact that the ambient pressure is different. The ambient pressure in the vacuum chamber is $4 \times 10^{-6}$ Torr in experiments conducted by method (ii) whereas the ambient pressure in experiment type (iii) is 1 atmosphere. It is important to conduct experiments both in air and vacuum as it is known that gas release during the reaction, if any, would be affected by pressure.

### *Thermodynamic prediction of the behavior of oxidizers upon heating*

Before discussing any results, we start with the individual oxidizers. While a reported "melting temperature" can be found for all of the oxidizers studied, its definition is somewhat ambiguous. Certain oxidizers melt directly to the liquid, whereas other oxidizers decompose first to form a sub-oxide, which then melts and decomposes upon further heating. Melting temperatures are generally not sensitive to the surrounding atmosphere or pressure, whereas decomposition temperature involving the formation of gaseous products will be.

In order to determine some of the thermodynamically predicted phase changes, and the products of decomposition, constant temperature-pressure (T, P) calculations were carried out using the NASA-CEA software [51]. For every oxidizer, calculations were run under two different pressure conditions: 1. P=1 atm and 2. P=$10^{-9}$ atm which is representative of the conditions existing in the mass spectrometer chamber. For each of the above pressures mentioned, the temperature of the oxidizer is increased in steps of 100 K. When decomposition is found to have occurred, the increment is successively reduced and then fixed within an accuracy of 10 K. The decomposition/melting as observed in the equilibrium calculations for some of the metal oxides listed in Table 4.1 are given below in Table 4.2 and 4.3. Table 4.2 shows equilibrium predictions at a pressure of P=1 atm while table 4.3 shows the same at a pressure of P=$10^{-9}$ atm. No predictions are made for some of the oxidizers as those oxidizers do not exist in the CEA database. Wherever possible, phase change data from other sources have been provided in the table for these oxidizers.

**Table .2 Behavior of the oxidizers on heating showing decomposition/phase change temperatures and the primary products at 1 atm pressure. The product phases are shown in parentheses.**

| Oxidizer | Temperature (K) | Event | Products | Temperature (K) | Event | Main Product |
|---|---|---|---|---|---|---|
| CuO | ~1300[a] | Decomposes | $Cu_2O$ (s), $O_2$ (g) | 1516[b] | Melts | $Cu_2O$ (l) |
| $Fe_2O_3$ | ~1550[a] | Decomposes | $Fe_3O_4$ (s), $O_2$ (g) | 1870[b] | Melts | $Fe_3O_4$ (l) |
| $WO_3$ | 1746[b] | Melts | $WO_3$ (l) | ~3000[c] | Decomposes | $WO_2$[c] (g) |
| $Bi_2O_3$[*] | 1098[b] | Melts | $Bi_2O_3$ (l) | NA | NA | NA |
| $Sb_2O_3$[*] | 929[b,f] | Melts | $Sb_2O_3$ (l) | 1823[b], 1703[f] | Sublimation | $Sb_2O_3$ (g) |
| $SnO_2$ | 1700[l] | Decomposes | SnO (g), $O_2$ (g), $SnO_2$ (s) | 1903[b] | Melts | $SnO_2$ (l) |
| $AgIO_3$[*] | 678[b,d] | Decomposes | AgI (s)[d], $O_2$(g) | 831[f] | Melts | AgI (l)[f] |
| $I_2O_5$[*] | 573[f] 663-723[e] | Decomposes | $I_2$ (g)[e], $O_2$[e] (g) | NA | NA | NA |
| $Co_3O_4$[*] | 1173[f] | Decomposes | CoO (s), $O_2$ (g) | 2103[f] | Melts | CoO (l)[f] |
| $MoO_3$ | 1075[f] | Melts | $MoO_3$ (l)[f] | 1428[f] | Boil | $MoO_3$ (g)[f] |

[a] Reference [43]. The decomposition likely occurs over a wide range of temperature, and ultimately

depend on the surrounding local atmosphere.

[b] ICT Thermal Database [52].

[c] Some minor species (mole fractions <1e-6) are seen even at 1600 K in equilibrium calculations.

[d] Reference [53]

[e] Reference [54]

[f] Reference [55]

[*]Equilibrium calculations could not be performed as these species are not included in CEA.

[!]Decomposition initiates at this temperature. Not completely decomposed until >2200 K.

Table 4.2 shows that under atmospheric pressure, CuO and $Fe_2O_3$ first decompose upon heating to condensed phase sub-oxides ($Cu_2O(s)$ and $Fe_3O_4(s)$) with the generation of molecular oxygen [35], and then undergo melting when heated by an additional 200-300 K. $AgIO_3$ on heating decomposes into AgI (s) and $O_2$ (g)[53]. AgI (s) then undergoes melting at 831 K. Cobalt (II, III) oxide ($Co_3O_4$) decomposes around 1173 K into CoO (s) and $O_2$ (g). The decomposition product CoO (s) is comparatively stable and does not melt until 2103 K [55].

On the contrary, there exist oxidizers which decompose directly into gaseous products without producing any solid phase sub-oxide. Iodine (V) pentoxide ($I_2O_5$) would fall in this category of oxidizers, decomposing into the respective elements $I_2$ (g) and $O_2$ (g).

Alternatively, oxidizers such as $WO_3$, $Bi_2O_3$, $Sb_2O_3$ and $Co_3O_4$ melt first. For $WO_3$, the thermochemistry predicts melting into $WO_3$ (l) at 1746 K, followed by decomposition into multiple sub-oxides at higher temperatures (~3000 K at 1 atm), $WO_2$ (g) being one of them. $Bi_2O_3$ is reported to melt at 1098 K. Not much is known about the behavior of $Bi_2O_3$ above its melting point. On the other hand, antimony (III) oxide ($Sb_2O_3$) melts around 929 K, and then sublimates at 1823 K producing $Sb_2O_3$ (g). $MoO_3$ melts at 1075 K and then boils at 1428 K without decomposition. However, the data for $MoO_3$ in the literature is a little inconsistent. While reference lists $MoO_3$ as a sublimate, another reference [55] has no mention of its sublimation properties but lists its melting temperature as 1075 K. As a consequence, the data available in the literature is sometimes ambiguous and should be treated with some caution. However, they still serve as a preliminary guide as what to expect during heating of the oxidizers.

**Table .3 Behavior of the oxidizers under heating at ~ $5x10^{-9}$ atm. This is representative of the pressure existing in the mass spectrometer chamber. Only oxidizers which exist in the CEA database are shown. Phase change temperatures for other oxidizers are given in Table 4.2.**

| Oxidizer | Temperature (K) | Event | Products | Temperature (K) | Event | Main Product |
|---|---|---|---|---|---|---|
| CuO | ~800 | Decomposes | $Cu_2O$ (s), $O_2$ (g) | 1100 | Decomposes | Cu (s), $O_2$ (g) |
| $Fe_2O_3$ | ~1100 | Decomposes | $Fe_3O_4$ (s), $O_2$ (g) | 1500 | Decomposes | Fe (g), $O_2$ (g) |
| $WO_3$ | 1200 | Decomposes | $(WO_3)_2$ (g) $(WO_3)_3$ (g) etc. | - | - | - |

| | | | | | | |
|---|---|---|---|---|---|---|
| SnO$_2$ | 1175 | Decomposes | SnO (g), O$_2$ (g) | - | - | - |
| MoO$_3$ | | | | | | |

Table 4.3 above shows the predicted decomposition temperature and products from CEA equilibrium calculations for an ambient pressure of $5 \times 10^{-9}$ atm, which is characteristic of the pressure existing in the mass spectrometer chamber. CuO and Fe$_2$O$_3$ are predicted to decompose at lower temperatures than under atmospheric pressure. CuO decomposes at 800 K and Fe$_2$O$_3$ at 1100 K into oxygen and their respective sub-oxides, a decrease of around 300-550 K in their decomposition temperature. SnO$_2$ would decompose at 1175 K as compared to 1700 K where it starts decomposition at 1 atm pressure. Not only is the temperature almost 525 K lower, the decomposition products are also different. SnO$_2$ decomposes completely into SnO (g) and O$_2$ (g) at 1175 K in vacuum when compared to decomposition at a pressure of 1 atm. WO$_3$ is an interesting material as in vacuum it decomposes at 1200 K which is below its melting temperature of 1746 K. Only gas phase decomposition products, like (WO$_3$)$_2$, (WO$_3$)$_3$ etc. are predicted as listed in Table 4.3 from this decomposition. Oxidizers absent in the CEA database are not listed in this table.

The selection of the oxidizers for this study is guided by the intention to pick materials whose oxygen release temperatures are different, while also including oxidizers which melt before decomposition and vice versa. In chapter 3, we have indicated that diffusion of aluminum through its shell is responsible for an ignition delay for a rapidly heated Al-CuO thermite. It is our intention to see how the ignition temperatures from various other nanothermites suggest and support such a scheme. However, it must be remembered that any comparison of the equilibrium calculations shown should be done with an appreciation that at the very high heating rates it is highly likely that we are probing transient species and events that are very far from equilibrium. Only knowledge of the species produced during heating of the oxidizers can lead to corroboration of the predicted results. This is described in the next section.

## *Results and Discussion*

### Gas release experiments

Gas release experiments are important to ignition as the ignition temperature is known to vary with the oxidizer. [35] Visual evidence of the release of gases on heating of an oxidizer (e.g. CuO) is provided by high speed video images from experiments conducted at the Argonne National Laboratories, Chicago. In this experiment, CuO is heated on a platinum wire and was imaged by an X-ray beam using phase contrast imaging. Figure 4.1 presents a sequence of such snapshots during this event.
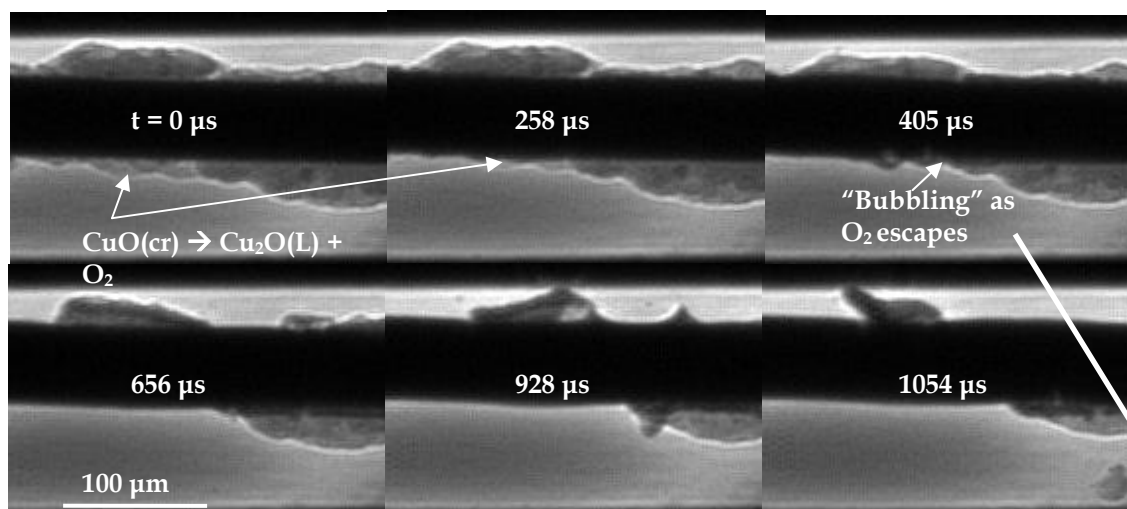
t = 0 µs     258 µs     405 µs

"Bubbling" as $O_2$ escapes

$CuO(cr) \rightarrow Cu_2O(L) + O_2$

656 µs     928 µs     1054 µs

100 µm

**Figure .1 Sequence of images depicting the heating of CuO in air. Bubbles are noticed suggesting entrapped gas inside a liquid.**

Figure 4.1 shows a series of snapshots depicting the heating of CuO particles. The time t=0 refers to the time when we first see bubbles appear. A snapshot showing "bubbling" makes us conclude of the presence of trapped gas inside a liquid. CuO is predicted to decompose to $Cu_2O$ and $O_2$ as has been listed in Table 4.2 and $Cu_2O$ can melt under the temperature attained by the wire. Once a critical pressure is exceeded, part of this trapped oxygen gas escapes from inside the liquid droplet, carrying away with it a chunk of the material. This is shown in the last snapshot. The evidence of bubbling also suggests that oxygen release is not instantaneous, but most likely occurs over a time span on the order of a millisecond. As time progresses during heating, we can clearly see that the surface of the wire gets exposed, most likely due to the formation of a pool of liquid which usually tends to form a spherical droplet due to the forces of surface tension. This necessitates an understanding of the gas species released from oxidizers under heating.

The TOFMS is used detect the species evolved/gas produced during heating of the oxidizers. A description of the instrument is given elsewhere. In short, this instrument can detect the time when oxygen/gases are released during heating and can be correlated to the temperature of the wire. Figure 4.2 below shows the concentration of oxygen that is being released on heating CuO as a function of time. Also shown on the same plot is the time history of the temperature of the platinum wire. The heating rate is around $4x10^5$ K/s. It is clear that oxygen release from CuO starts at around 980 K.
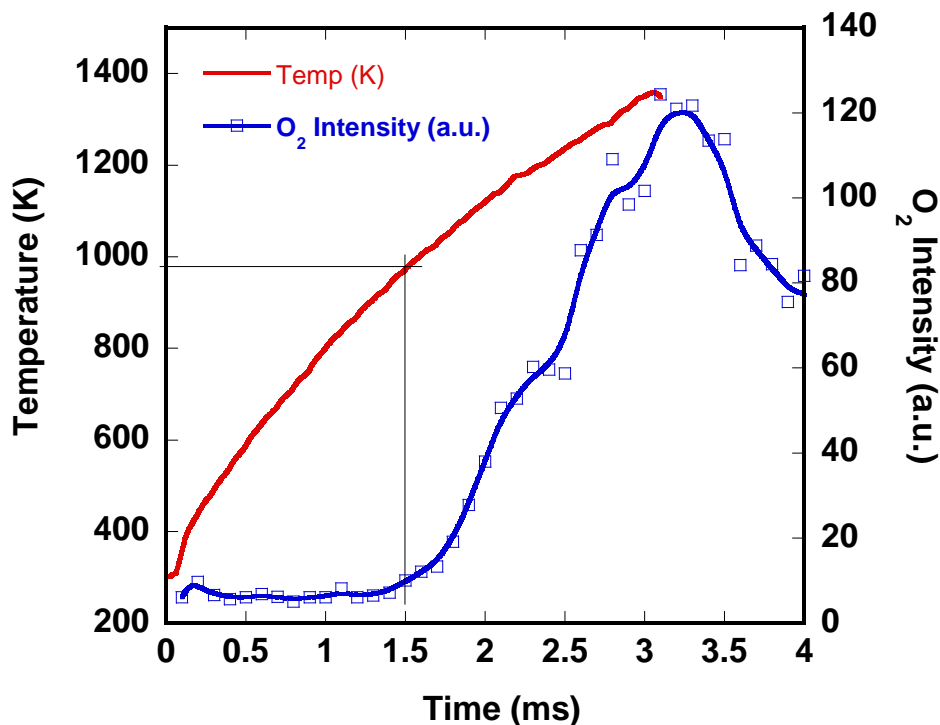
**Figure .2 Representative plot showing the temperature of oxygen release from CuO when heated at ~ 4x10^5 K/s. The intensity shown on the secondary y-axis should only be treated qualitatively, as the amount of material is not coated on the wire in a controlled manner.**

The temperature of gas release and the primary gas species detected during the gas release experiments conducted on the oxidizers listed in Table 4.2 are shown in Table 4.4. The data presented here is an average of 2 experiments. Most of the oxidizers release $O_2$ (except for $Bi_2O_3$ which, in addition to $O_2$, generates Bi gas) while some oxidizers do not. CuO (both nano sized and micron sized), $Fe_2O_3$, $Bi_2O_3$, $I_2O_5$, $AgIO_3$, $SnO_2$ and $Co_3O_4$ release oxygen on decomposition which has been detected in the mass spectrometer. No gaseous species were detected for $WO_3$, $MoO_3$ and $Sb_2O_3$ when these oxidizers are heated.

**Table .4 Gas release temperature and primary gas species detected during heating of the bare oxidizers.**

| Oxidizer | Gas release temperature (K) | Primary gas species detected |
|---|---|---|
| Copper (II) oxide (CuO) | 975 | $O_2$ |
| Micron copper oxide (CuO) | 1190 | $O_2$ |
| Iron (III) oxide ($Fe_2O_3$) | 1340 | $O_2$ |
| Tungsten (VI)oxide ($WO_3$) | - | - |
| Bismuth (III) oxide ($Bi_2O_3$) | 1615 | $O_2$, Bi, $Bi^{+2}$ |
| Silver iodate ($AgIO_3$) | 892 | $O_2$ |
| Diiodine pentoxide ($I_2O_5$) | 796* , 976 | $O_2$ |
| Tin (IV) oxide ($SnO_2$) | 1675 | $O_2$ |
| Cobalt(II, III) oxide ($Co_3O_4$) | 1025 | $O_2$ |
| Molybdenum oxide ($MoO_3$) | - | - |
| Antimony (III) oxide ($Sb_2O_3$) | - | - |

* Only minor amount of oxygen is released at this temperature

The oxygen release temperature for an oxidizer is unique and specific. This presents us with the opportunity to prepare nanothermite mixtures wisely to gain an understanding of the effect of oxygen release on the ignition/reaction of the corresponding nanothermite.

The oxygen release temperature for the various oxidizers are spread over a range of ~ 700 K. Towards the lower end of the range lies $I_2O_5$ (which is known as a strong oxidizer) and is found to release oxygen at a temperature of around 800 K and below the melting point of aluminum (933 K). On the other end of the range lies $SnO_2$ releasing oxygen at 1672 K. If gas phase oxygen is essential for ignition initiation/combustion, then one would expect Al-$I_2O_5$ mixture to ignite at much lower temperatures than Al-$SnO_2$. Another important fact to keep in mind is that the oxygen release temperature for micron sized particles is around 200 K more than corresponding particles in the nanometer range as is seen for CuO particles.

One aspect that is not evident from the data is the amount of oxygen produced by the various oxidizers. For example, CuO produces a lot more oxygen on decomposition than $Fe_2O_3$, $Bi_2O_3$ or $SnO_2$. A general observation can be made in this regard. Oxidizers releasing oxygen late during heating produces less oxygen than those which release oxygen early. The $I_2O_5$ used in these experiments most likely contained a mixture of $HIO_3$ and $I_2O_5$ as $I_2O_5$ is hygroscopic in nature. Thus, a lot of water vapor is released in addition to oxygen when $I_2O_5$ is heated. There are two oxygen release temperatures for $I_2O_5$. A minor amount of oxygen coinciding with the release of water is observed at 796 K while most of the oxygen is released at a higher temperature of 976 K. Consequently, is value is used as oxygen release temperature. Although we try to coat the platinum wire uniformly every time, the exact amount of material deposited on the wire is beyond our control. Consequently, the results of these gas release experiments should only be looked at qualitatively and not in a quantitative manner.

$Bi_2O_3$ needs a special mention as it is different from the other oxidizers in the fact that along with $O_2$, bismuth gas is also produced as bismuth has a very low boiling point. $Bi_2O_3$ melts at 1098 K under heating at atmospheric pressure while in vacuum, the gaseous products Bi and $O_2$ are detected at 1610 K in the mass spectrometer, which is well above the melting temperature of $Bi_2O_3$ (1098 K).

With a knowledge of the gas(es) released/species generated during heating of the oxidizers, we can now compare our results with the predictions from CEA. For example, CEA predicts $SnO_2$ to produce $O_2$ as well as tin (II) oxide (SnO (g)) at 1175 K, both in gas phase. Any gas phase species produced in the mass spectrometer chamber would be ionized by the electron gun and detected if produced. No such species were detected. Similarly absence of $(WO_3)_3$ (g) and Fe (g) were not detected during heating of $WO_3$ and $Fe_2O_3$. The fact that only $O_2$ (g) is detected for $SnO_2$ and $Fe_2O_3$ suggests alternate decomposition mechanisms may be probable for these oxidizers. Additionally they may be evidence of the non-equilibrium states under rapid heating. It must be remembered that oxygen release temperature also depends on the heating rate. In our experiments, the heating rate is maintained between $3-5 \times 10^5$ K/s.

## T-jumpTOFMS with optical emission

The previous section describes the behavior of only the oxidizers under heating. In this section the results of the experiments of stoichiometric mixtures of nano-aluminum and the oxidizers mentioned in Table 4.2 are discussed. The only change made in the experimental setup is the attachment of an optical detector (PMT) to identify the relative time of ignition as compared to the release of oxygen from the oxidizers.
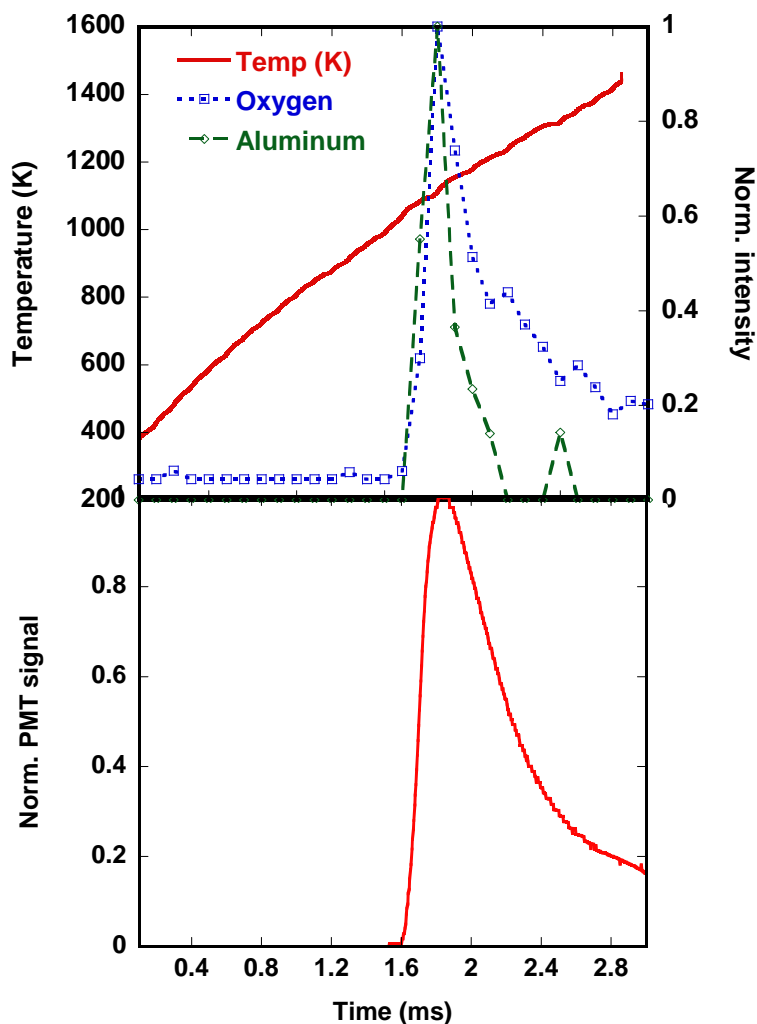


**Figure .3 (top) Plot of the temperature of the platinum wire showing the appearance of aluminum and oxygen during the reaction of Al-CuO nanothermite mixture of stoichiometric composition. (bottom) Optical emission showing ignition as recorded by a PMT during the same event. The heating rate is ~ 3.8x10$^5$ K/s.**

The appearance of oxygen and aluminum during the reaction of Al-CuO nanothermite is shown above in the top part of Figure 4.3 while the bottom part shows the optical emission during the reaction. The ignition as identified by broadband optical emission is around 1037 K, and is close to the temperature at which oxygen is released from the bare oxidizer (975 K). The optical signal is found to be correlated with the appearance of both the aluminum and oxygen species in this case. This raises an important question as to whether the release of oxygen gas is an essential precondition to

ignition. To verify this hypothesis, we must resort to other oxidizers and see if our hypothesis is valid for other nanothermite mixtures.

The ignition temperature observed for other nanothermites is given below in Table 4.5 below. The temperature at which oxygen is detected during the nanothermite reactions is also shown. Oxygen release temperature from bare oxidizers is also shown in the same table to facilitate comparison.

**Table .5 Ignition temperature of various nanothermites in vacuum listed in terms of the oxidizer. The oxygen release temperature from the nanothermite reactions and the bare oxidizer as detected by TOFMS is given alongside for a comparison.**

| Oxidizer | Ignition temperature (K) | $O_2$ release temperature in thermite (K) | $O_2$ release from bare oxidizer (K) |
|---|---|---|---|
| $AgIO_3$ | 889 | 881 | 892 |
| $I_2O_5$ | 1057 | 989 | 976 |
| $CuO$ | 1037 | 1047 | 975 |
| $Fe_2O_3$ | 1408 | Below detection limit | 1340 |
| $Co_3O_4$ | 1368 | 1021 | 1025 |
| $Bi_2O_3$ | 845 | 925 | 1615 |
| $Sb_2O_3$ | 950 | - | - |
| $MoO_3$ | 853 | - | - |
| $WO_3$ | 1227 | - | - |
| $SnO_2$ | 1049 | MS shutdown | 1675 |

Before we discuss the ignition temperature results, it is worth noting that the temperature of oxygen release from the oxidizer during a nanothermite reaction is usually the same as during heating of the bare oxidizer. Except for $Bi_2O_3$, most of the oxidizers do not show any significant change (< 100 K) in their oxygen release temperature. The amount of oxygen produced is below the detectable limit for oxidizers which release less amount of oxygen (e.g. $Fe_2O_3$). For $SnO_2$ mixtures, there is an intermittent shutdown in the operation of the MS due to arcing of the plates caused by a surge of combustion generated ions. Another important aspect is that the rate of oxygen release may be increased or decreased in the thermite reactions as compared to the oxidizer itself. This oxygen release rate has been found to increase in the case of Al-CuO reactions. Being aided by the exothermic behavior of the reaction, the oxidizer can release oxygen at a faster rate. Conversely, part of the oxygen may be used up in reactions prior to ignition and its subsequent rate of release might be less. This may be attributed to the fact that condensed phase reactions might occur before ignition happens. We shall touch upon this aspect later in the chapter.

The large change in the oxygen release temperature for $Bi_2O_3$ nanothermite from the oxidizer itself suggests that oxygen release in the thermite is primarily driven by the heat of the reaction as opposed to being heated by the wire. Consequently, we would assume that the ignition for this thermite is not contingent upon oxygen release.

Write a paragraph on ignition stuff.

# T-jump experiments in air
### Ignition temperature
In this set of experiments, the same samples tested in the previous section were heated in air with a maximum heating pulse of ~ 4.5 x $10^5$ K/s in air.  Table 4.6 lists the measured ignition temperature for all the samples tested. All the mixtures are of stoichiometric proportions ($\phi$=1.0). The data presented here is an average of 3 experiments. Al-$Bi_2O_3$ has the lowest ignition temperature (857 K) and ignites below the melting point of aluminum and $Bi_2O_3$. All other thermites ignite close to the melting point of aluminum (<50 K) or above the melting point of aluminum. Furthermore, CuO, $Fe_2O_3$, $SnO_2$, ignited below the decomposition temperature of the corresponding oxidizers where oxygen is released. $WO_3$ is odd as it ignites at a temperature below both the melting and decomposition temperatures. The relevance of the melting temperature to a few select oxidizers is discussed in the next section.

**Table .6 Ignition temperature for various stoichiometric nanothermites as observed in T-jump experiments in air.**

| Oxidizer | Ignition temperature (K) |
|---|---|
| $Bi_2O_3$ | 857 |
| $Sb_2O_3$ | 890 |
| $AgIO_3$ | 923 |
| $MoO_3$ | 962 |
| CuO | 1037 |
| $WO_3$ | 1065 |
| $SnO_2$ | 1075 |
| $I_2O_5$ | 1106 |
| $Fe_2O_3$ | 1269 |
| $Co_3O_4$ | 1343 |

Insert Ig temp in air vs vacuum, A paragraph on ignition temp in air vs vacuum
Reactive sintering
### Effect of stoichiometry
Since reactivity is also affected by stoichiometry, some chosen nanothermites were also tested for the effect of stoichiometry on ignition temperature. For these set of experiments, CuO, $Fe_2O_3$, $Bi_2O_3$ and $WO_3$ are chosen. The first two oxidizers are chosen as their ignition is known to occur simultaneously with the release of oxygen. However, the ignition temperature of the nanothermites would be expected to be sensitive to stoichiometry as CuO and $Fe_2O_3$ releases different amounts of oxygen upon decomposition. $Bi_2O_3$ is chosen as it is the only candidate that reacts below the melting point of aluminum. $WO_3$ was chosen due to its uniqueness of igniting below its melting and decomposition temperature.
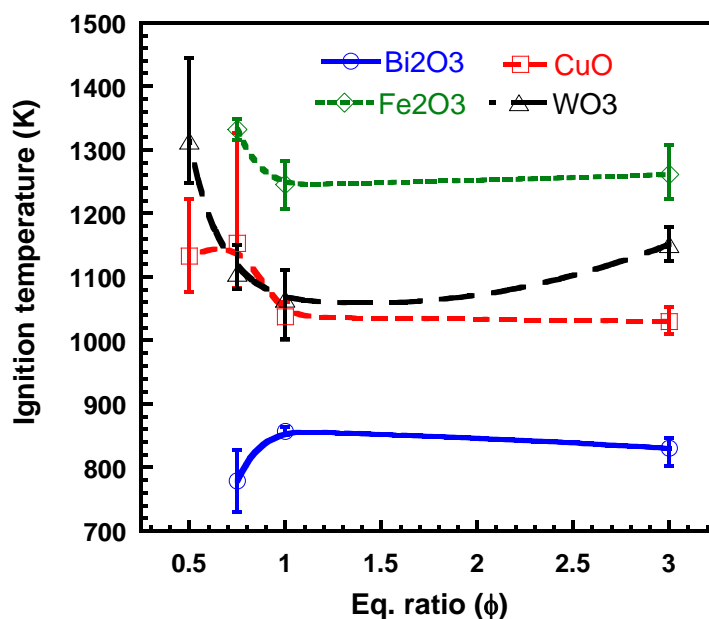
**Figure .4 Plot of ignition temperature for various nanothermite mixtures as a function of equivalence ratio. The heating rate is ~ 4x105 K/s. The legend shows only the oxidizer. Nanoaluminum is the common fuel for all the mixtures.**

For fuel-rich mixtures the Al-CuO and Al- $Fe_2O_3$ show a slight decrease in ignition temperature from their corresponding stoichiometric compositions as excess fuel is added. For Al- $WO_3$, the ignition temperature is seen to increase marginally as the sample is made fuel rich. The ignition temperature for fuel-rich Al-$Bi_2O_3$ mixtures was nearly identical to the ignition temperature of a stoichiometric mixture. But despite these differing trends, the essential feature is ignition temperature has low sensitivity to the exact value of the stoichiometry on the rich side. In either a stoichiometric or a fuel rich scenario, once the ignition process is initiated, thermal runaway occurs. Another point which is relevant is that having an excess of fuel will shift the equilibrium product towards $Al_2O$, from $Al_2O_3$. From an ignition standpoint, the formation of volatile $Al_2O$ may help facilitate the ignition by either aiding the convective energy propagation, or by "scrubbing" the aluminum surface. If Al is diffusing outwards through its shell, then forming a volatile aluminum sub-oxide may be beneficial in the ignition and combustion process by serving as a mechanism to transport Al away from the surface. Prior mass spectrometry studies have confirmed that the primary volatile aluminum containing product species observed was $Al_2O$ which increased under fuel rich conditions [35].

## *Reaction initiation*

### Correlation to melting of aluminum

The results reported in Section 4.5 depict a clear message about the ignition of various nanothermites. With the exception of Al-$Bi_2O_3$ and Al-$MoO_3$, almost all of them ignite above or around (±50 K) the melting temperature of aluminum (933 K). Observed ignition temperatures above 933 K further strongly suggests that the melt dispersion mechanism is not valid under the heating rates used in this study. Ignition below the melting point of aluminum would indicate diffusion of the oxidizers into the aluminum core as under such temperatures the core will remain solid and fairly immobile as

144

compared to the oxidizer species. *This is a clear indication that ignition cannot occur unless the solid aluminum core melts and becomes mobile.* In fact, this is directly in line with previous observations that significant diffusion of Al through the shell was observed at temperatures above the melting point of Al [28, 56]. These results, along with the current findings, indicate that there may in fact be a critical temperature where the diffusion rate of aluminum significantly increases, and this may represent a lower limit to the ignition temperature in rapidly-heated thermite systems. The exact process is beyond the scope of this work, but a mechanism similar to what has been suggested by Trunov et al [8] may occur, where some phase change in the oxide shell renders it much more permeable to the aluminum core. Nevertheless, melting of aluminum to make it more mobile would seem to be the first prerequisite to any significant reaction.

Alternatively, a reaction can occur in the condensed phase if the ignition is below the melting point of either aluminum or the oxidizer. There has been evidence of condensed phase reactions in Al-$Bi_2O_3$. This is discussed in greater details in Section 4.6.3.

### Correlated to $O_2$ release: CuO, $Fe_2O_3$, $AgIO_3$, $I_2O_5$

A previous study by our group [35]  has found that ignition is simultaneous to oxygen release in CuO and $Fe_2O_3$. The study was limited to those oxidizers only. To emphasize this point, we plot the oxygen release temperature versus the ignition temperature for the various nanothermites that release oxygen. This is shown in Figure 4.4 below. The diagonal line shown on the figure represents a perfect one to one correspondence of ignition with oxygen release. The closer the data point to the line, the greater is the correlation between oxygen release and ignition temperature. Table 4.5 shows that the ignition temperature for $AgIO_3$, CuO, $Fe_2O_3$ and $I_2O_5$ is close to the oxygen release temperature from the thermites in vacuum. Since the amount of oxygen from $Fe_2O_3$ is below the detectable limit, we use the oxygen release temperature from the bare oxidizer. For $Bi_2O_3$ we have used the oxygen release temperature from the oxidizer as a huge change is noticed in the oxygen release for the thermite suggesting that gas phase oxygen is not playing a major role in the initiation of this thermite.
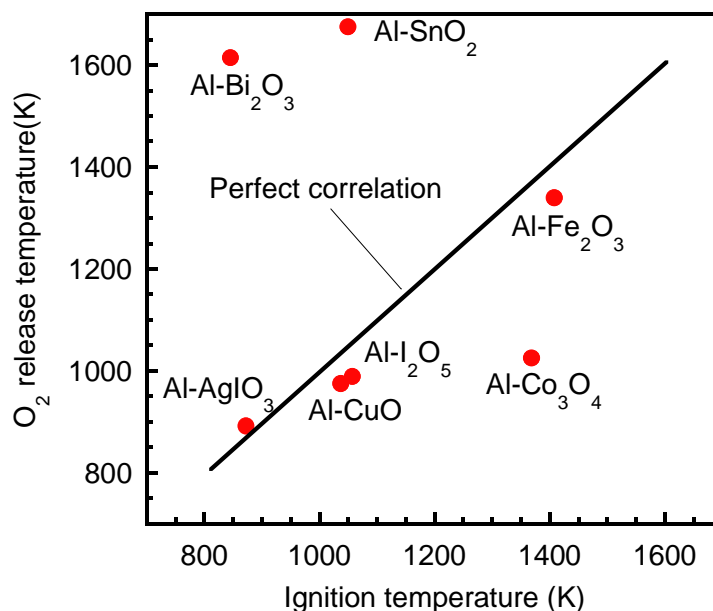
**Figure .5 Oxygen release temperature versus ignition temperature for various nanothermites in vacuum. Heating rates are on the order of 3-4x10$^5$ K/s. Oxidizers that do not release any oxygen are not shown.**

It is clearly observed from Figure 4.4 above that for oxidizers like CuO, Fe$_2$O$_3$, AgIO$_3$ and I$_2$O$_5$, there is good correspondence between oxygen release and ignition temperature of the thermite. This does not conclusively prove that initiation occurs only when gas phase oxygen around aluminum. Any gas released in the MS chamber would immediately escape from the site of the reaction. However due to the nature of the coating process, the layers in contact/close to the wire might release gases which can be trapped causing a buildup in local pressure before the gas can finally escape. Another possibility is initiation via heterogeneous condensed phase reactions and the oxygen released plays no role in initiation. Evidence of condensed phase reactions is seen from the work of Sullivan et al. through high heating microscopy (10$^6$ K/s) in vacuum. Reaction is confined in the region of contact between aluminum and copper oxide. Initiation at the area of contact leads to heat release causing further decomposition of the oxidizer. This may in turn affect the reaction rate and cause thermal runaway which is detected as ignition. We speculate that the same initiation mechanism maybe at play for oxidizers which release oxygen around ignition.

Oxidizers like Bi$_2$O$_3$ and WO$_3$ ignite much below their oxygen release temperature or melting temperature and they are discussed in the Section 4.6.3 below.

## Condensed phase initiation: Bi$_2$O$_3$ and WO$_3$

It has been pointed out in the foregoing sections that Bi$_2$O$_3$ reacts (845 K) below the melting point of aluminum (933 K) and much below its own melting point (1098 K). This makes it a strong contender for condensed phase reactions. In order to test whether it is indeed a condensed phase reaction, we use a fuel that cannot vaporize until extremely high temperature. The aluminum is thus replaced by carbon (C) powder. A C-Bi$_2$O$_3$ stoichiometric mixture is made and is tested in the TOFMS. The carbon dioxide (CO$_2$)

146

evolved during heating of $Bi_2O_3$, C and $C-Bi_2O_3$ are compared and shown in Figure 4.6 below as a function of time.
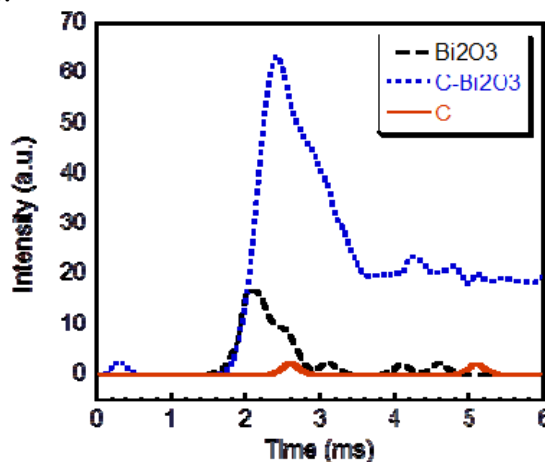


**Figure .6 CO$_2$ release profile from Bi$_2$O$_3$ and C powder, and C-Bi$_2$O$_3$ thermite under similar heating rates.**

A careful look at Figure 4.6 shows that the $CO_2$ release from the carbon powder occurs around 2.2 ms while the $CO_2$ release from $Bi_2O_3$ powders occurs much earlier at ~ 1.6 ms. When the $C-Bi_2O_3$ thermite is heated, the $CO_2$ release seem to be at 1.6 ms, around the same time when $Bi_2O_3$ releases $CO_2$. The intensity of the $CO_2$ signal from the thermite exceeds the individual oxidizer and the carbon powder and is indicative that excess $CO_2$ has been formed as a result of the reaction with the oxygen from $Bi_2O_3$ in the thermite. No oxygen is detected in the mass spectra for the $C-Bi_2O_3$ reaction. We thus conclude that the entire oxygen has been reacted with carbon. Moreover, this reaction necessarily has to be in condensed phase as any oxygen released from $Bi_2O_3$ would have escaped from the site of the reaction. The $CO_2$ seen from $Bi_2O_3$ and C powders is due to the fact that they have been sonicated in hexane. Appearance of $CO_2$ in the spectra for materials sonicated in hexane is quite regular.

WO$_3$ does not release any gas on heating but reacts above the melting point of aluminum. To probe its initiation mechanism, we turn to high heating rate electron microscopy to show that Al-WO$_3$ reactions are governed by condensed phase initiations. For this purpose, stoichiometric mixtures are of Al-WO$_3$ are put on a SEM holder (Aduro holder from Protochips Inc.). The sample was heated at $10^6$ K/s to 1473 K and held for 1 ms inside the SEM chamber. Figure 4.7 below shows a backscattered SEM image before (left) and after (right) the event. It may be noted that in this image brighter regions correspond to heavier elements (W) and the darker regions correspond to lighter elements (Al).
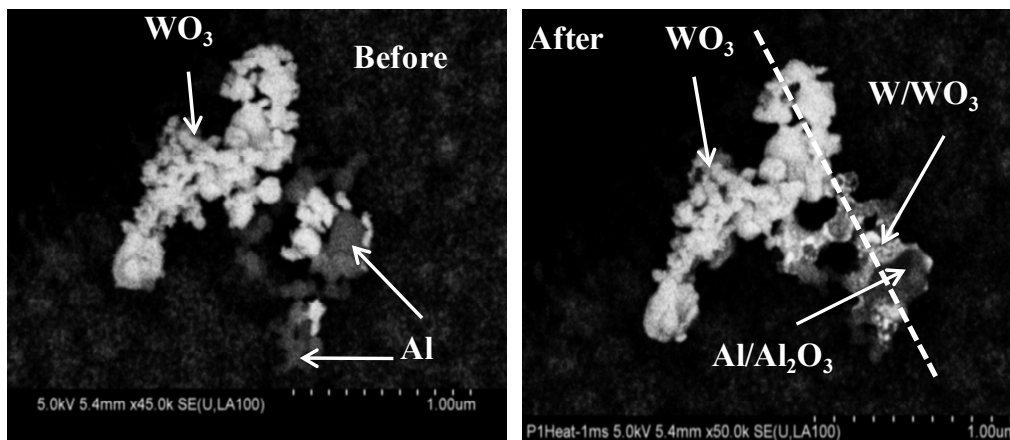
**Figure .7 Backscattered SEM image of Al-WO₃ nanothermite mixtures before and after subjecting the mixture to a heating pulse of 106 K/s to 1473 K and held for 1 ms. The bright parts indicate heavier elements (W) and the darker regions represent the lighter element (Al).**

It is interesting to note in Figure 4.7 that reaction has happened only in areas where there is interfacial contact between aluminum and $WO_3$. Movement of materials showing mass transport is observed along the line of contact in the figure after the event. Local melting seems to have taken place. To confirm the assumption that a reaction has taken place, an elemental mapping was conducted along the line by energy dispersive spectroscopy (EDS). This is shown below in Figure 4.8. It is clearly noticed that a considerable overlap of the W, O and Al towards the lower right areas in areas of interfacial contact, suggesting that a reaction has taken place in the condensed phase.
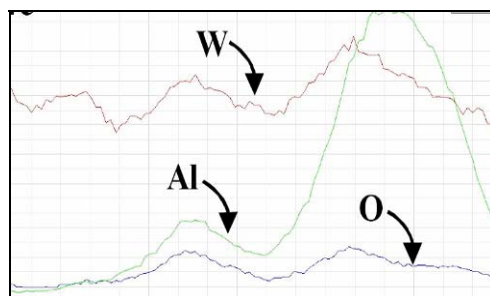


**Figure . 8 Elemental mapping via EDS along the dotted line from top left to bottom right**

## Initiation for other thermites: Sb₂O₃, Co₃O₄ and SnO₂

The thermites described here lacks conclusive evidence of an initiation mechanism. However, based on the collective knowledge of the other oxidizers mentioned in the above two sections, we put forward a hypothesis towards the same. This is based on the fact that the physical and chemical behavior of the oxidizers on heating is analogous to the oxidizers already discussed in Section 4.6.3 and 4.6.4.

Let us start with Al-Sb₂O₃ thermite. Sb₂O₃ does not release oxygen but reacts at 950 K. Its melting temperature is 970 K and thus it is very close to its melting point. According to the reactive sintering mechanism, the oxidizer can melt and facilitate contact with aluminum causing a reaction to initiate. It is highly probable that reactive

sintering during this process would enhance the mixing of the fuel and the oxidizer leading to a self-sustained reaction.

$Co_3O_4$ is odd among the entire group of oxidizers because it releases oxygen (at ~ 1025 K), both from the oxidizer as well as in the thermite, almost 350 K before it ignites. Evolution of oxygen from $Co_3O_4$ would leave behind CoO which is known to melt at a very high temperature of 2000 K. This makes the behavior of CoO similar to $WO_3$ and we would speculate it to initiate via condensed phase reactions.

$SnO_2$ releases oxygen at a very high temperature (1675 K) but ignites at ~1050 K, well below its oxygen release temperature. Furthermore, it causes an intermittent shutdown in the MS due to the arcing caused by the formation of combustion generated ions. This makes its behavior similar to $Bi_2O_3$. $Bi_2O_3$ thermite reactions have often led to loss of mass spectra during the reaction due to its enhanced capability of generating ions during ignition. These ions have been observed as a precursor to ignition as has been shown in a prior study. Based on the observation of similar "ignition symptoms", a condensed phase initiation mechanism may be in play for $SnO_2$ thermites. However, the role of the ions needs to be studied further and is mentioned as part of the future work.

## 1. Alane as a dopant in MIC'S

### Introduction

Aluminum hydride or alane is an interesting material for a wide variety of applications. It has been studied as a potential fuel in rocket propellants, air breathing propulsion systems, explosives, and as a hydrogen storage medium. There are as many as six crystalline phases of alane, of which α-alane is the most stable and is also the subject of this work[1].

While alane is an interesting material for a wide variety of applications, a relatively small amount of literature exists on its combustion behavior. Sinke[2] determined the heat of formation as -2.7 kcal/mole by bomb calorimetry in one of the earliest publications on alane. There have been a number of studies involving the decomposition of the various polymorphs of alane under non-isothermal conditions, but these are typically conducted at very low heating rates [5, 6, 7, 8, 9]. In this study we only consider the most stable form of alane, -AlH3, which decomposes in a single endothermic reaction [5].

$$AlH_3 \rightarrow Al + 3/2\ H_2 \qquad\qquad (1)$$

Graetz [5, 6, 7] demonstrated that during the decomposition of the and polymorphs, they transition to the phase at about 100 $^o$C. After further heating, the phase decomposes to H$_2$ gas and aluminum. For the temperature range conducted in their study ($60 < T\ (^oC) < 160$), Graetz et. al[5] determined that the kinetics of the aluminum hydride polymorphs were controlled by nucleation and growth in two and three dimensions, and not by the diffusion of H$_2$ through a surface oxide. Similarly, Ismail [8] determined that the single endothermic reaction of alane decomposition proceeds in two steps; 1) a rate limiting two dimensional nucleation reaction, and 2) growth of crystals. Ismail also determined that after the hydrogen is liberated from the particle, the resulting products are amorphous and crystalline aluminum. Numerous studies [5, 6, 7, 8, 9] at heating rates on the order of a few K/min to 10's of K/min found that the onset of decomposition occurred between 400 – 500 K. In two separate studies, Bazyn et. al. [9,10] proposed that in general combustion environments aluminum hydride would react via a two-step mechanism, with the first step being the decomposition reaction shown in equation 2 and the second step given by equation 3:

$$Al + ¾\ O_2 \rightarrow ½\ Al_2O_3 \qquad\qquad (2)$$

In shock tube studies, Bazyn[10] concluded that the decomposition step occurs significantly faster than ignition and that once the hydrogen has been released the remaining aluminum burns similarly to traditional aluminum of similar size (micron-scale).

Il'in [11] studied the products of combustion of alane in air and found that AlH$_3$ combustion in air had three stages; 1) A hydrogen flame, separated from the sample with a nonluminous zone, 2) once the hydrogen was consumed, the flame descended and touched the sample resulting in ignition and low-temperature combustion, similar to ultradispersed aluminum powder (UDAP), and 3) a high-temperature stage in which the sample reached 2000-2400 $^o$C. Il'in [11] analyzed the final combustion products and found a substantial amount of AlN content, which was consistent with earlier studies on UDAP.

More recently, we studied the decomposition and ignition behavior of alane at much higher heating rates ($10^4 - 10^5$ K/s) than previously published [12] by filament heating. During our study, we found that the ignition temperature of alane was a function of heating rate, but it was very similar to that of nanoaluminum while having a particle size ranging from a few microns to more than twenty microns. In addition, at these higher heating rates we found that the decomposition of alane became limited by the transport of hydrogen gas through the aluminum crystal.

Loose-powder nanocomposite thermites, often termed MICs, are currently being investigated for uses in propellants, pyrotechnics, and explosives. Nanoaluminum-based MICs give rise to high adiabatic flame temperatures, and produce relatively low amounts of gas. While the reaction mechanism in MICs remains poorly understood, the mode of energy propagation is speculated to be via convection of hot gases [13-15]. One potential way to enhance the reactivity of MICs is to introduce a gas generating constituent, so long as it does not affect the kinetic timescales of the system. We have shown that nanoboron can enhance the reactivity of nanoaluminum/CuO MICs in a recent publication [16], but only when boron was added as the minor component of the fuel. The goal of the current work is to investigate whether aluminum hydride can also enhance the reactivity of a nanoaluminum/CuO system. As discussed, an attractive characteristic of aluminum hydride is its ability to release hydrogen upon thermal decomposition at a relatively low temperature. The liberated hydrogen may therefore serve to enhance the reactivity by improving both the pressurization and convective mode of energy propagation.

## *Experimental Approach*

For this work, samples (MICs) were prepared with the fuel being composites of nanoaluminum, -aluminum hydride with nanoaluminum, micron-sized aluminum with nanoaluminumm, and the oxidizers which consist of copper oxide (CuO), iron oxide ($Fe_2O_3$), and bismuth trioxide ($Bi_2O_3$). In each case nanoaluminum was the predominant fuel with aluminum hydride or micron-sized aluminum added as a minor component. The minor components were added in terms of the molar percentage of either in the fuel. For example, a 30%$AlH_3$ sample meant that 30% of the fuel was aluminum hydride, 70% was nanoaluminum, and the corresponding amount of oxidizer was added to make the mixture of interest. In the case of experiments using $AlH_3$, the calculated stoichiometry assumed that any hydrogen produced did not participate in the reaction such that the final products of combustion were $Al_2O_3$, $H_2$, and the respective metal corresponding to the oxidizer of interest. The nanoaluminum used was obtained from the Argonide Corporation, and designated as "50 nm ALEX" by the supplier. ALEX is a nano-sized aluminum formed from the electroexplosion of an aluminum wire[17]. Thermogravimetric Analysis (TGA) was performed on the ALEX samples to determine the amount of elemental metal (active content) in the particles. TGA showed the ALEX to be 70% active. As previously mentioned, the alane used in this study was alpha alane which were rhombohedral crystals that ranged from a few microns to approximately 25 m in size as seen in figure 1. Since the alane used in this study was on the micron scale, we also substituted micron-sized aluminum in place of the nanoaluminum to make a direct comparison. The micron-sized aluminum was obtained from Atlantic Equipment Engineers, and had a size of 1-5um as per the supplier. The oxidizers copper(II) oxide, iron(III) oxide, and bismuth(III) oxide nanopowders, were all purchased from Sigma Aldrich, and had an average primary particle diameter specified by the supplier to be <50 nm, <50 nm, and 90-210 nm, respectively.

MICs were prepared by mixing the fuel and oxidizer in hexane and sonicating for 20 minutes to ensure mixing. The hexane was then allowed to dry and the sample was

gently broken apart with a spatula until the consistency for each sample was that of a loose powder.

Three different experimental techniques were used to evaluate the reactivity of alanized MIC formulations. First, we used the pressurization rate inside a small combustion cell as a measurement of the reactivity. A fixed mass (25 mg) of the sample powder was placed inside a constant-volume (~13 mL) pressure cell. A schematic and more details of the pressure cell can be found in a previous publication [18]. A nichrome wire coupled to a voltage supply was placed in contact with the top of the powder, and served as an ignition source through resistive heating of the wire. A piezoelectric pressure transducer was used in series with an in-line charge amplifier and a signal conditioner, and the resultant voltage trace was captured on an oscilloscope upon ignition of the sample. The pressurization rate was calculated by converting the voltage rise to pressure, and dividing by the rise time in microseconds. This was repeated three times for each sample, and the average pressurization rate (psi/ sec) was recorded. Reference 16 provides a detailed interpretation of the typical pressure signal.

In order to extract the rise time in a consistent way, we always took the first major peak in the system (usually the maximum voltage) and applied a linear fit. We have reported the average of three tests, and the uncertainty was calculated from the standard deviation of the data.

The decomposition behavior of the $AlH_3$-based MIC under rapid heating was investigated by coupling a Temperature-jump (T-Jump) [19] with a time-of-flight (TOF) mass spectrometer [20]. The T-jump employs a ~76 m diameter platinum wire, which is resistively heated at a rate of up to ~6 x $10^5$ K/s. This experimental setup has been described thoroughly in reference 20. We used this technique to characterize the release of $H_2$ in alane as well as the decomposition of the corresponding oxidizer when mixed together in the form of a MIC.

Finally we measured flame propagation velocity in a burn tube to compare the performance of the $AlH_3$-based MIC with the standard nanoaluminum MIC. Previously, such tests have been conducted by Bockmon et. al. [15] for various nanoaluminum-oxidizer mixtures to study the burn rates for various MICs. Our experimental setup is similar to the one used by Bockmon et. al. [15] except that we used two photodiodes at known distances from each other to calculate the average velocity. The light emission was recorded on an oscilloscope as the flame front passed the photodiodes. From the photodiode signal, we selected 5% of the maximum signal as the measure of time for when the flame front passed. The flame propagation velocity was then calculated by dividing the distance between photodiodes by the time difference between the two photodiodes to achieve 5% of maximum signal intensity. The packing densities for the mixtures were approximately 10% for the thermite mixtures.

**Results and Discussion**

1. Combustion Studies

In this study, we considered baseline MIC's of nanoaluminum-Metal Oxides and incrementally replaced the nanoaluminum with micron-scale alpha aluminum hydride and in some cases micron-scale aluminum. Initially we used stoichiometric mixtures of the MIC's and tested them in our pressure cell to determine the relative performance as a function of alane content. In some cases the result was an increase in performance, which defined an optimum amount of additive. Initially, it was uncertain whether the $H_2$ released from the system would oxidize to form $H_2O$ during the initial pressure rise of our constant volume experiment. In order to gain some insight into the role of $H_2$ in the system, we tested two samples using CuO as the oxidizer. In one sample we assumed a stoichiometry in which the products included $H_2$ and in the other we provided sufficient

oxidizer for the products to form $H_2O$.   The mixture which assumed $H_2$ in the product was found to be more reactive (i.e. gave higher pressurization rates) than the mixture which assumed $H_2O$. Therefore, we only considered the aluminum content in the alane as reactive.  Figure 2 shows the results of stoichiometric mixtures of alane as an additive to nanoaluminum-metal oxide MIC's in terms of pressurization rates in a constant volume pressure cell.  In addition figure three shows the relative performance when micron-sized aluminum replaces nanoaluminum in a CuO based MIC.  The pressurization rates have been normalized by the pressurization rate of a pure nanoaluminum-corresponding metal oxide MIC.

As figure 2 shows, the addition of micron scale aluminum hydride to a nanoaluminum-copper oxide MIC enhances the pressurization rate of the MIC, while adding aluminum in a similar size decreases the pressurization rate.  The decrease in pressurization rate from the baseline MIC of the micron aluminum substituted MIC can be attributed to the time scales associated with micron-sized aluminum combustion. Since micron-sized aluminum takes significantly longer to burn than the nanoaluminum, the addition of micron-sized aluminum slows down the heat release rate relative to the nanoaluminum thus reducing the performance.

At its optimum performance (20-30% $AlH_3$), the alanized/CuO MIC had a pressurization rate that is about a factor of two greater than the baseline nanoaluminum MIC even though it is on the same size scale as the micron sized aluminum.   After about 30% $AlH_3$ by mole, the pressurization rate decreases dramatically to well below the levels observed with 100% nanoaluminum.   The increase in pressurization rate over the baseline with alane can at least partially be attributed to the increased gas production associated with alane decomposition, which proceeds as shown in equation 2.  In shock tube studies Bazyn [10] concluded that the dehydrogenation of alane occurs significantly faster than the ignition process, which would imply a significant amount of gas is produced just prior to ignition.  However, thermochemically, the effect of increasing alane content is to lower the adiabatic flame temperature due to the endothermic decomposition of alane.   While thermochemically, the alane serves to continue to produce gas the extended time scales of the remaining micron scale aluminum and the decrease in flame temperature at some point become the controlling parameters on performance.   The thermochemical behavior of two types of $CuO/nAl/AlH_3$ MIC systems is shown in terms of adiabatic flame temperature in figure 3.  The first provides enough CuO to oxidize all of the fuel including the hydrogen gas generated from alane decomposition.  The second contains only enough CuO to oxidize all of the aluminum in the system.  Figure 3 demonstrates two interesting features.  As mentioned earlier the addition of alane decreases the flame temperature in both systems.  Furthermore, the adiabatic flame temperature of the system containing enough CuO to oxidize the hydrogen gas to water vapor becomes considerably lower than having hydrogen gas as one of the main combustion products under equilibrium conditions.  This does not necessarily mean that the hydrogen does not participate in the thermite reaction.  It is quite possible that the hydrogen may react with oxygen and or the metal oxide as an intermediate step, but in either case the flame temperature is highest when hydrogen is one of the primary combustion products as opposed to water vapor.  This in part may help to explain some of our results of an optimum system that contains only enough oxidizer to react with the aluminum. As the flame temperature drops with the addition of CuO to balance the entire system (i.e. react the hydrogen), the flame temperature begins to approach the vaporization temperature of aluminum.  In the event that the flame temperature drops below the vaporization temperature of aluminum, a change in combustion mechanism would take place. The system would have transitioned from homogeneous to heterogeneous reactions which would significantly slow down the reaction rate resulting in poor performance as observed in the experiments.

153

Interestingly, the alanized MIC's using $Fe_2O_3$ and $Bi_2O_3$ did not show the same enhancement in pressurization rate that the copper oxide MIC did. In fact the MIC based on $Fe_2O_3$ saw a dramatic decrease in pressurization rate almost immediately as alane is added. A simple thermochemical analysis shown in figure 4 provides a possible explanation for the poor performance of the $Fe_2O_3$ system. Again the addition of alane reduces the flame temperature to levels near or even below the vaporization temperature of aluminum resulting in a shift of combustion mechanism from homogeneous to heterogeneous At the same time, the $Bi_2O_3$ based MIC appeared relatively insensitive to the addition of alane in terms of pressurization rate all the way up to about 50% $AlH_3$ by mole. After about 50% $AlH_3$ the pressurization rate of the $Bi_2O_3$ based MIC falls off dramatically, similar to the CuO MIC. Figure 4 indicates that the further increase in alane content drives the adiabatic flame temperature towards the melting point of alumina. Failure to reach this temperature would significantly alter the combustion mechanism further slowing the reaction rate down. The thermochemical calculations for the CuO and $Fe_2O_3$ MICs were performed using the NASA CEA computer codes with the UV option. The calculations for the $Bi_2O_3$ MICs were performed with the CHEETAH code using the constant volume explosion option.

With the exception of the $Fe_2O_3$ based MIC, all of the other samples had similar pressure signal rise times as the nanoaluminum MIC's as seen in figure 5 up until the optimum amount of alane is added. This result implies that the increase in peak pressure observed in the alanized MIC occurs on the same time scale as the baseline, meaning that if the increase in peak pressure is solely a result of hydrogen release, then the hydrogen release must occur within this time scale. In the case of the $Fe_2O_3$ system, the rise times are immediately higher than the baseline

## 2. Time Resolved Speciation Measurements

During the next part of the study we employed a T-Jump TOF mass spectrometer to gain a better understanding of the decomposition of the alanized MIC. During the experiments, the input voltage and resulting current were recorded. From the recorded voltage and current, and the known length of the platinum wire, the temperature time history can be found as a function of wire resistance using the Callendar-Van Dusen equation:

$$\frac{R}{R_o} = 1 + \alpha T + \beta T^2 \qquad (4)$$

Where $\alpha$ = 3.91 x $10^{-3}$, $\beta$ = -5.78 x $10^{-7}$, $R_o$ is the reference resistance obtained from the length of the wire at ambient temperature.

Figure 6 shows the temporally resolved mass spectra for the alane-based MIC at a heating rate of ~6 x $10^5$ K/s. The spectrum observed at t=0 ms corresponds to the background and consists primarily of $H_2O$ (m/z=18), OH (m/z=17), and $N_2$ (m/z=28). Hydrogen and oxygen are clearly observed in the spectra, along with smaller quantities of aluminum. Figures 7 and 8 provide examples of the hydrogen and oxygen temporal release, and the evolution of aluminum vapor for a 100% Alane fuel MIC, and a 25% Alane fuel (the balance of the fuel was nanoaluminum) MIC respectively. Interestingly, in both systems the release of $H_2$ occurs at approximately the same temperature (see figures 7 and 8) and at similar rates. On the other hand, while the $O_2$ appears to be released at similar temperatures in each sample, the 25% Alane fuel mixture clearly shows $O_2$ released at much higher rates in comparison to the 100% Alane fuel. This is a clear indication of a reaction that is propagating faster (25% Alane). The corresponding

temperature of the release of hydrogen ranges between 800 °C (1073 K) and 900 °C (1173 K) from experiment to experiment with a heating rate of approximately $6 \times 10^5$ K/s. This is within reasonable agreement with our previous study[12] on the decomposition of alane on its own at similar heating rates. At much lower heating rates alane decomposition has been shown to begin at much lower temperatures, typically around 150 °C (423 K) [5,6,7,8,9]. The difference in temperature of decomposition can be directly attributed to the heating rates used in this study, and consequently the operating temperatures. At the lower heating rates, and thus lower temperatures, chemical kinetics is the rate limiting process; however, as the heating rate is increased, and thus the operating temperature is increased significantly, diffusion or mass transfer becomes the limiting process[12]. Another interesting observation is the presence of copper in the 25% alane mixture which does not appear in the 100% alane MIC, which is an indictor that the 100% case has a lower flame temperature.

The T-jump mass spectrometer shows that hydrogen is released from the alane at approximately the same time and temperature as the oxygen from the copper oxide, but provides no information to indicate if hydrogen participates in the reaction with the oxygen or the rest of the MIC. Regardless, however, of whether or not the hydrogen reacts with the oxygen or the metal oxide, our experimental results and thermochemical analysis indicate that the system is optimized when the $H_2$ is considered as product species.

Figures 9 and 10 show the time resolved species profiles for the $Bi_2O_3$ based MIC for the 100% alane and 25% alane fuels respectively. In this system we note that the rate of Bi release is significantly increased for the 25% AlH3 fuel in comparison to the 100% $AlH_3$ case. Again this demonstrates that the Alane is significantly altering the reaction rate of the system, most likely due to a shift in combustion mechanism between the 25% and 100% $AlH_3$ fuel case and a higher temperature to form vapor phase Bi. This is supported in the thermochemical calculations shown in figure 4. At 25% AlH3 the flame temperature is between the vaporization temperature of aluminum and the melting temperature of alumina.. While at 100% $AlH_3$ the flame temperature has dropped below the melting point of alumina

Figures 11 and 12 show the time resolved species profiles for the $Fe_2O_3$ based MIC for the 100% and 25% $AlH_3$ fuels respectively. Unlike the CuO and $Bi_2O_3$ MIC's we do not observe any significant changes in the speciation rates at the two different conditions with $Fe_2O_3$. Equilibrium calculations suggest that at both of these $AlH_3$ loading levels, the flame temperature is below the vaporization temperature of aluminum, but still above the melting temperature of alumina. Thus while the performance continues to degrade with increasing alane content, the rate of degradation is not as stark as it is in the $Bi_2O_3$ cases studied. This result is consistent with our earlier conclusion that the addition of alane has altered the reaction rate of the $Fe_2O_3$ based MIC and that it is most likely operating as a heterogeneous system with any addition of alane, yet still above the melting temperature of alumina.

3. Flame Velocity

We also examined the effect of alane on the propagation velocity in the MIC in a burn tube test [15]. Taking our optimum mixture (25% alane by mole) with an equivalence ratio of 1 (again assuming the hydrogen does not take part in the reaction), we found that the propagation velocity was increased with alane by about 25% over that of the baseline nanoaluminum-copper oxide MIC.

While the mass spectrometer results indicate a simultaneous release of $O_2$ and $H_2$, with a time resolution of ~100 ms, bulk materials (from pressure cell data) show rise times an order of magnitude faster and is nominally associated with convective heat transfer effects. Thus for bulk flame propagation small differences in the $H_2$ vs $O_2$ release may in fact be significant. If $H_2$ is released first it should, based on higher thermal conductivity and diffusivity be a very effective medium for convective heat transfer.

Therefore the benefit of alane to a MIC may be two fold.  First the increased gas production from decomposition of alane, and second the increase in heat transfer rates associated with $H_2$ convection.  Thus the increased burning rate occurs despite the fact that the adiabatic flame temperature is lower.


## *Discussion*

In this study, we have observed that micron-sized alane can enhance the performance of baseline MIC in terms of pressurization rate and peak pressure in a constant volume pressure cell, and the propagation velocity in a burn tube when it is a minor component of the fuel.  At the same time, with similar size aluminum particles we see no enhancement of the baseline MIC in any of the experiments.  We have attributed this to the release of hydrogen from the alane contributing to convection heat transfer as a means of enhancement..  However, we should also consider that the ignition temperature of alane is very close to that of nanoaluminum (~1000 K) [12, 23], while micron sized-aluminum typically does not ignite until it reaches ~2300K[24-28].  This would suggest that the aluminum component of alane might also be contributing to the overall heat release of the system through the oxidation of aluminum beginning earlier in time and at a lower temperature in comparison traditional micron-scale aluminum.  However, in shock tube studies of alane combustion, Bazyn[10] found that after the release of hydrogen, the remaining aluminum burns on a similar time scale to that of similarly size aluminum.  Similar to our earlier study [12] we found that burning times were on the order of milliseconds, compared to the microsecond scales expected of nanoaluminum [23].  So while there may be a small benefit from earlier and lower starting temperature aluminum oxidation of alane, the overall contribution from the aluminum portion of the alane in our MIC system is likely to be minimal.  Our results also showed that there is an optimum amount of alane that can be added (20-30% by mole) to enhance the MIC system.  The fact that there is an optimum amount of alane suggests that there is a balance between the positive contribution of the hydrogen in terms of pressurization and convection, and the negative aspects of longer burning times not contributing to the main reaction, thus creating an optimum amount of alane above which performance suffers.  This would imply that if the alane particles were on the nano-scale rather than the micron-scale that it would be a far superior fuel to aluminum in a MIC system.


## Conclusions

During this study we examined the effects of the addition of micron-scale alane on the combustion performance of three typical thermite systems, CuO/nAl, $Bi_2O_3$/nAl, and $Fe_2O_3$/nAl.  In constant volume pressure cell testing we found that the addition of alane to a CuO/nAl MIC as a minor fuel component could enhance pressurization rates by a factor of about two.  Above approximately 30% alane by mole of fuel, the performance drops off drastically to well below baseline performance.  At the same time the addition of micron-scale aluminum to the CuO/nAl MIC results in a gradual degradation of performance. The enhanced performance of the alanized MIC can be directly attributed to the release of $H_2$ upon alane decomposition.  The additional gas aids in pressurization and helps to improve the convective heat transfer of in the system even though it lowers the adiabatic flame temperature.

The addition of alane to a $Bi_2O_3$ based MIC leaves performance largely unaffected until alane becomes the majority fuel component.  For an $Fe_2O_3$ MIC, alane addition results only in degraded performance at all addition levels.  In each case the performance degradation can be attributed to a transition in combustion mechanism.  As an example, once alane is added to the iron oxide MIC, the flame temperature drops

below the vaporization temperature of aluminum resulting in a change from homogeneous to heterogeneous combustion.  Similarly, in the bismouth oxide system, at very high loadings of alane, the flame temperature drops below the melting temperature of alumina, thus severely altering the combustion mechanism of the aluminum fuel.

Burn tube studies of an alanized CuO based MIC found that the propagation velocity of the alanized MIC was about 25% higher than that of the baseline.  The release of hydrogen in the alane increases the amount of gas in the whole system, which would contribute to enhancing the energy propagation in the system by convection.

Alane ultimately lowers the flame temperature of these traditional MIC systems while at the same time improving performance under appropriate conditions.  This suggests a degree of tunability with certain mixtures is possible.  Alane's ability to generate additional gas and  ignite at low temperatures allows it to enhance performance over more traditional fuels, but with limits.  These limits appear to be associated with temperatures which govern the overall combustion mechanism.

## <u>References</u>

[1] M.A. Petrie, J.C. Bottaro, R.J. Schmitt, P.E. Penwell, D.C. Bomberger, "Preparation of Aluminum Hydride Polymorphs, Particularly Stabilized   -AlH$_3$", U.S. Patent No. US 6,228,338 B1, 8 May 2001

[2] Finholt, A. E.; Bond, A. C., Jr.; Schlesinger H. I. *J. Am. Chem. Soc.* **1947**, *69*, 1199

[3] F.M. Brower, N.E. Matzek, P.F. Reigler, H.W. Rinn, C.B. Roberts, D.L. Schmidt, J.A. Snover, K. Terada, J. Am. Chem. Soc. 98 (1976) 450

[4] G.C. Sinke, L.C. Walker, F.L. Oeting, D.R. Stull, *Journal of Chemical Physics*, 47 (8) (1967) 2759-2761

[5] Graetz, J., Reilly, J.J. (2005) Decomposition Kinetics of the AlH$_3$ Polymorphs. *Journal of Physical Chemistry B*, 109, 22181-22185

[6] Graetz, J, Reilly, J.J. (2006) Thermodynamics of the   ,   , and   polymorphs of AlH$_3$. *Journal of Alloys and Compounds*, 424, 262-265

[7] Graetz, J., Reilly, J.J., Kulleck, J.G., Bowman, R.C. (2007) Kinetics and Thermodynamics of the aluminum hydride polymorphs. *Journal of Alloys and Compounds*, 446-447, 271-275

[8] I.M.K. Ismail, T. Hawkins, *Thermochimica Acta*, 439 (2005) 32-43

[9] T. Bazyn, H. Krier, N. Glumac, N. Shankar, X. Wang, T.L. Jackson, *Journal of Propulsion and Power*, 23 (2) (2007) 457-464

[10] T. Bazyn, R. Eyer, H. Krier, N. Glumac, *Journal of Propulsion and Power*, 20 (3) (2004) 427-431

[11] A.P. Il'in, N.V. Bychin, A.A. Gromov, *Combustion, Explosion, and Shock Waves*, 37 (4) (2001) 490-491

[12] G. Young, N. Piekiel, S. Chowdhury, M.R. Zachariah, *Combustion, Science, and Technology*, Vol. 182, Issue 9, September 2010, pp. 1341-1359

[13] Son, S. F., Asay, B. W., Foley, T. J., Yetter, R. A., Wu, M. H.,Risha, G. A., Combustion of nanoscale Al/MoO3 thermite in microchannels. Journal of Propulsion and Power 23(4), 2007.

[14] B. W. Asay; S. F. Son; J. R. Busse; D. M. Oschwald, *AIP Conference Proceedings* **2004,** 706, (Pt. 2, Shock Compression of Condensed Matter--2003, Part 2), 827-830.

[15] B. S. Bockmon; M. L. Pantoya; S. F. Son; B. W. Asay; J. T. Mang, *Journal of Applied Physics* **2005,** 98, (6), 064903/1-064903/7.

[16] K. Sullivan, G. Young, M.R. Zachariah, *Combustion and* Flame, 156 (2) (2009) 302-309

**2.2.1.1.1.1** [17] J. Katz, Tepper, F., Ivanov, G.V., Lerner, M.I. and V. Davidovich in: CPIA Publication 675, JANNAF Propulsion Meeting, 1998; 1998.

[18] A. Prakash, A.V. McCormick, M.R. Zachariah, *Advanced Materials (Weinheim, Germany)*, 17 (7) (2005) 900-903

[19] T.B. Brill, P.J. Brush, K.J. James, J.E. Shepherd, K.J. Pfeiffer, *Applied Spectroscopy*, 46 (6) (1992) 900-911

[20] L. Zhou, N. Piekiel, S Chowdhury, M.R. Zachariah, *Rapid Communications in Mass Spectrometry*, 23 (194) (2009) 194-202

[21] Granier, J. J., and Pantoya, M. L., "Laser Ignition of Nanocomposite Thermites,"Combustion and Flame, Vol. 138 (4), 2004, 373–383.

[22] Wang, Y., Jiang, W., Cheng, Z., Chen, W., An, C., Song, X., Li, F., "Thermite reactions of Al/Cu core-shell nanocomposites with $WO_3$," *Thermochimica Acta*, Vol. 463 (1-2), (2007) 69-76

[23] Bazyn, T., Krier, H., Glumac, N. (2006) Combustion of Nanoaluminum at Elevated Pressure and Temperature Behind Reflected Shock Waves. *Combustion and Flame*, 145 (4), 703-713

[24] Brossard, C., Ulas, A., Yen, C.L. Kuo, K.K. (1997) Ignition and Combustion of Isolated Aluminum Particles in the Post-Flame Region of a Flat-Flame Burner. *16th International Colloquim on the Dynamic Explosions and Reactive Systems*, Krakow, Poland

[25] Brzustowski, T.A., Glassman, I. (1964) Spectroscopic investigation of metal combustion. Prog. Astronaut. Aeronaut., 15:75

[26] Friedman, R., Macek, A. (1962) Ignition and Combustion of Aluminum Particles in Hot Ambient Gases. *Combustion and Flame*, 6, 9-19

[27] Friedman, R., Macek, A. (1963) Combustion Studies of Single Aluminum Particles. *Proc. Comb. Instit.*, 9, 703-709

[28] Kuehl, D.K. (1965) Ignition and Combustion of Aluminum and Beryllium. *AIAA Journal*, 3 (12), 2239-2247
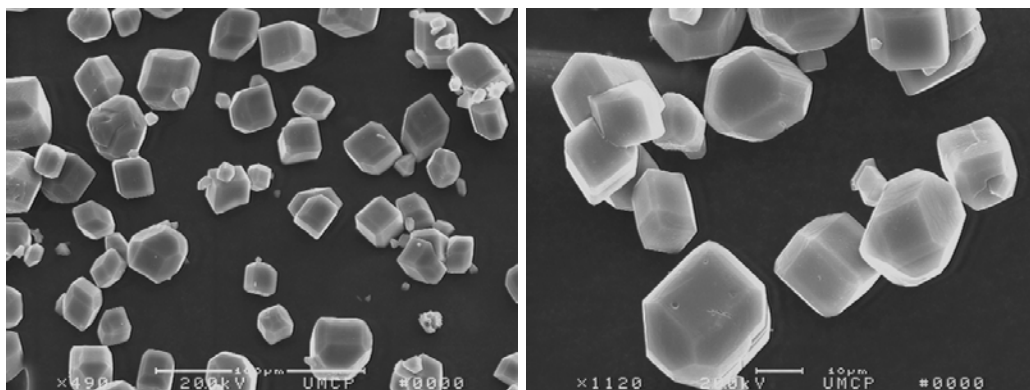
**Fig. 1 SEM image of  -Aluminum Hydride**
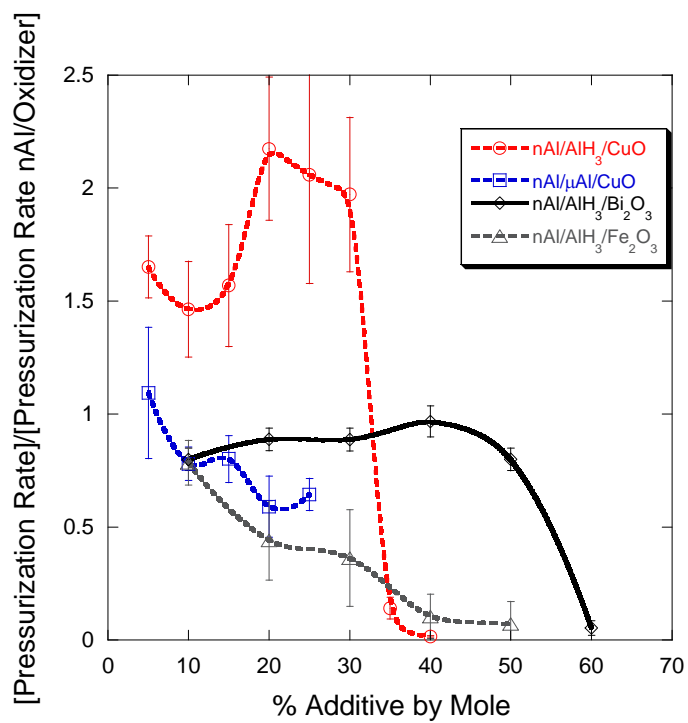


**Fig. 2 Normalized pressurization rate as function of fuel additive for stoichiometric mixtures**
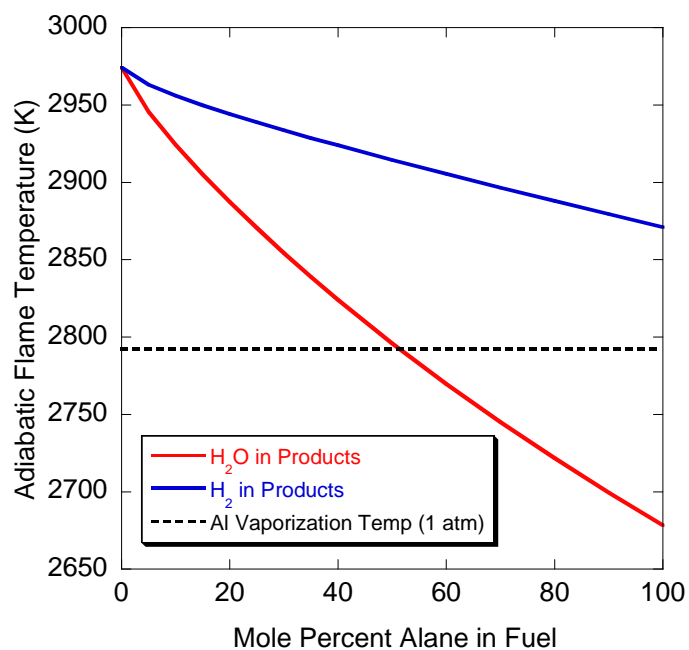
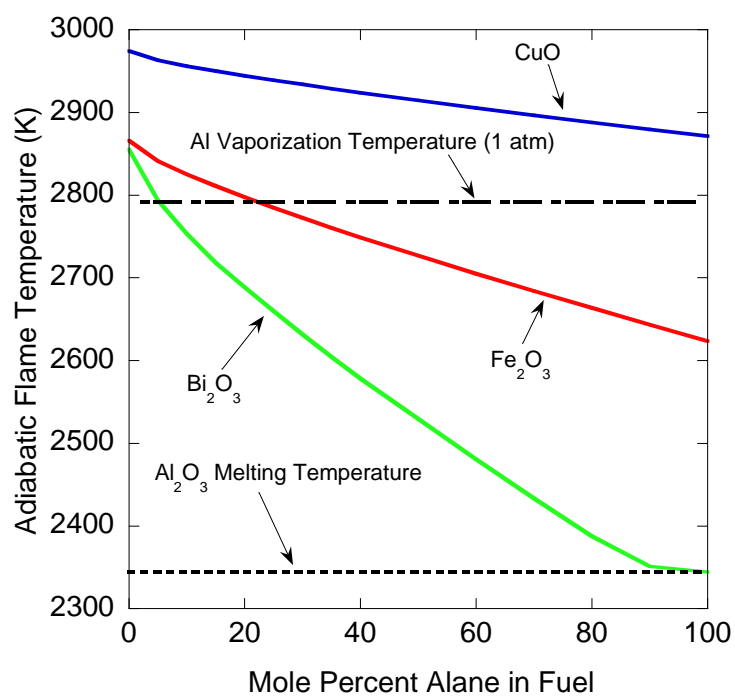**Fig. 3 Adiabatic flame temperatures of CuO/nAl/AlH$_3$ mixtures**



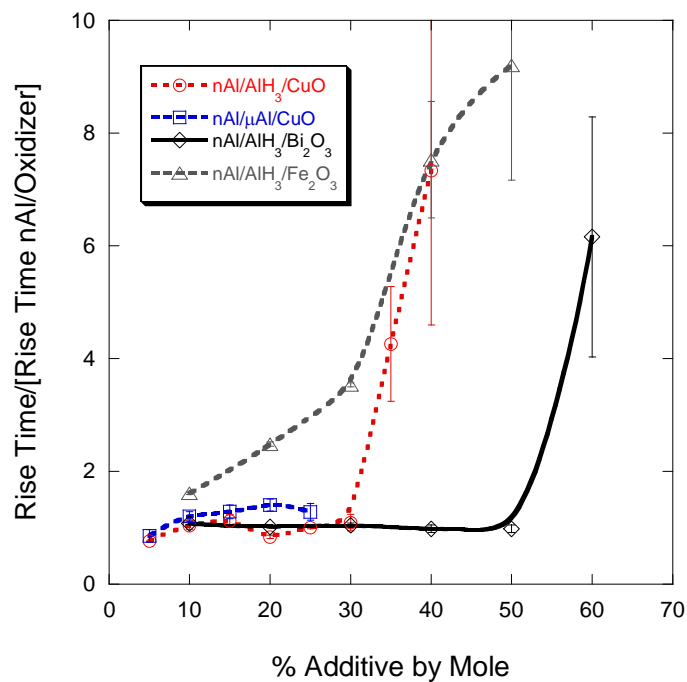**Fig. 4 Adiabatic flame temperatures of alane MIC systems with different metal oxides**

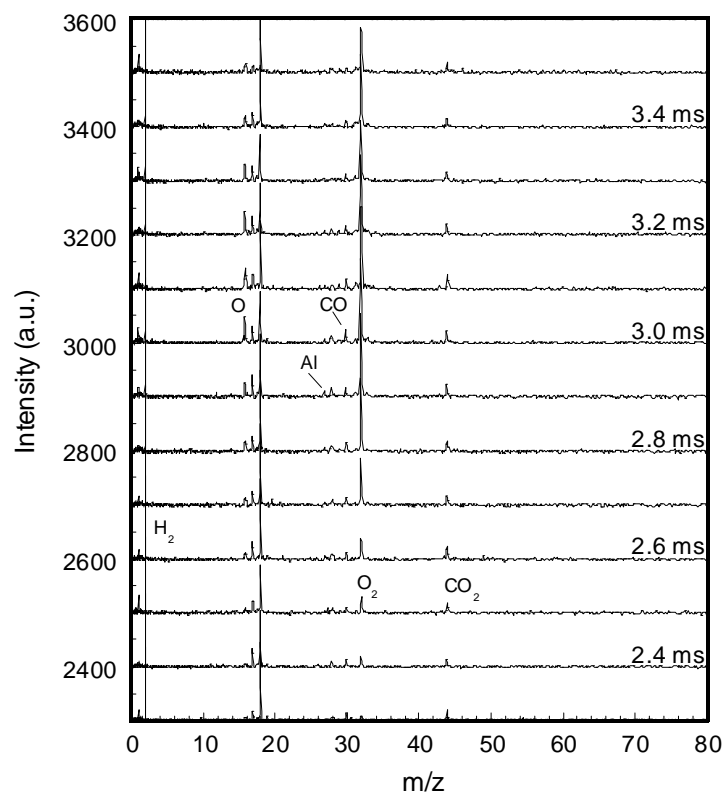**Fig. 5 Rise times of MIC's as a function of fuel additive**

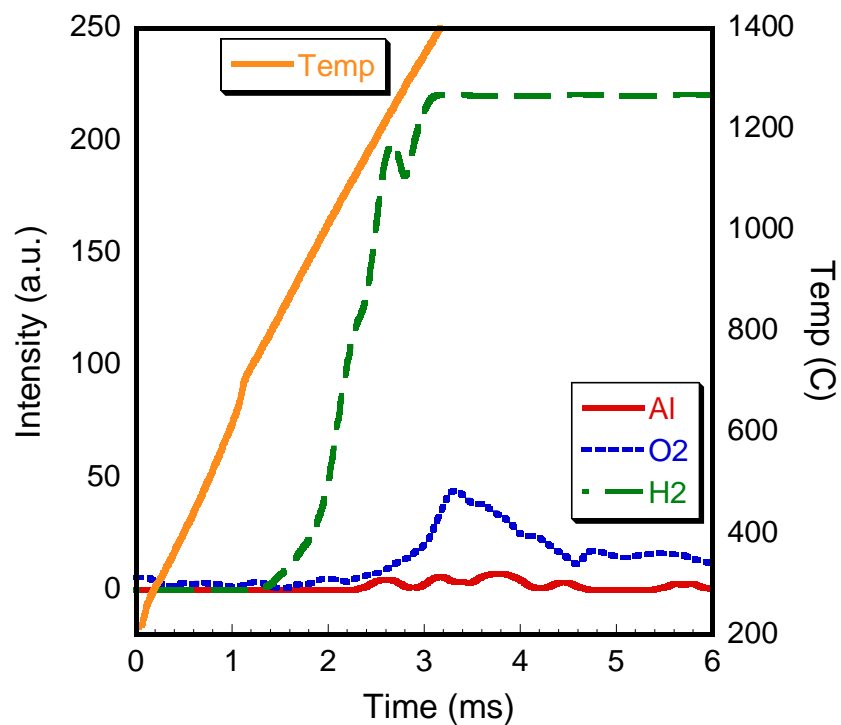**Fig. 6 Temporally resolved T-Jump TOF mass spectra for a heating rate of 5.7 x 10^{5} K/s**



**Fig. 7 Species profiles obtained in T-Jump TOF mass spectrometer for 100% AlH₃ Fuel-CuO MIC**
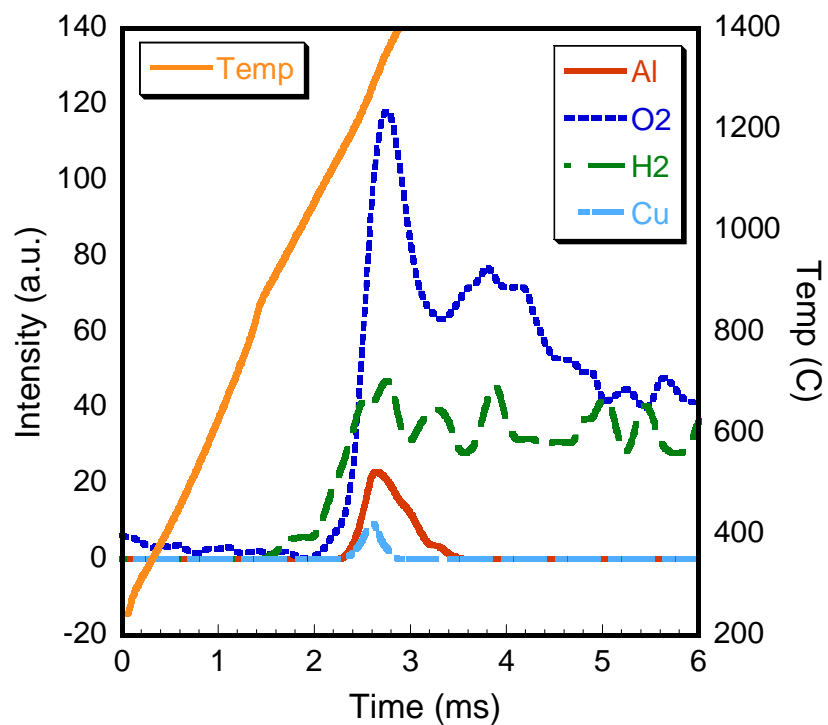
Fig. 8 Species profiles obtained in T-Jump TOF mass spectrometer for 25% AlH$_3$ Fuel (balance is nanoaluminum)-CuO MIC
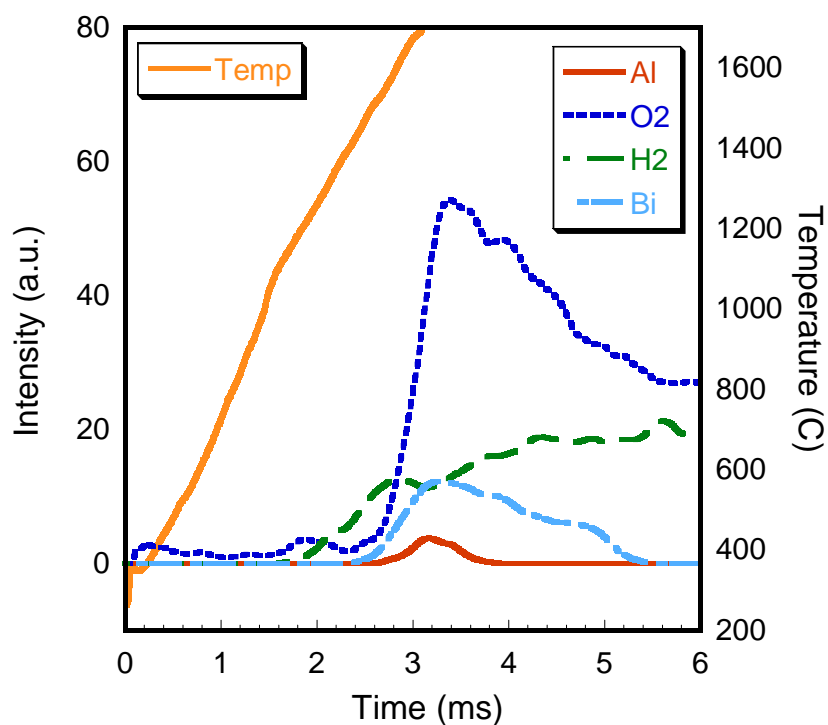
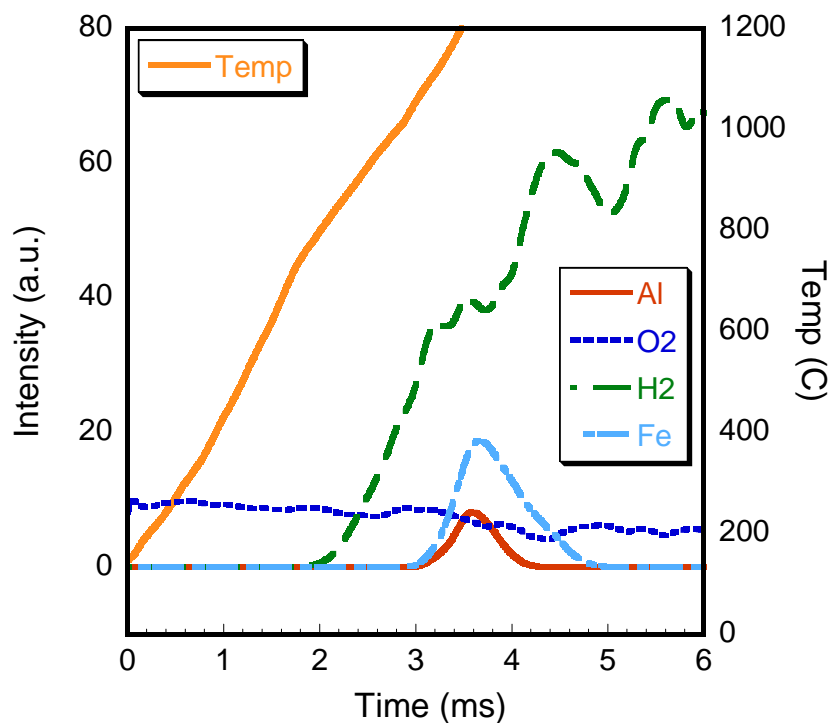**Fig. 9 Species profiles obtained in T-Jump TOF mass spectrometer for 100% AlH₃ Fuel-Bi₂O₃ MIC**
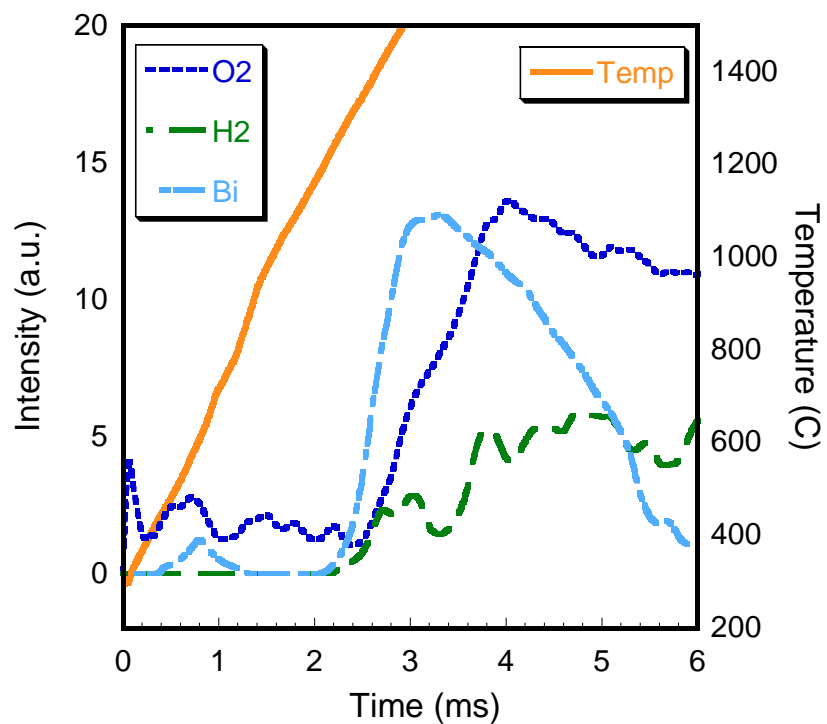


**Fig. 10 Species profiles obtained in T-Jump TOF mass spectrometer for 25% AlH₃ Fuel (balance is nanoaluminum)-Bi₂O₃ MIC**
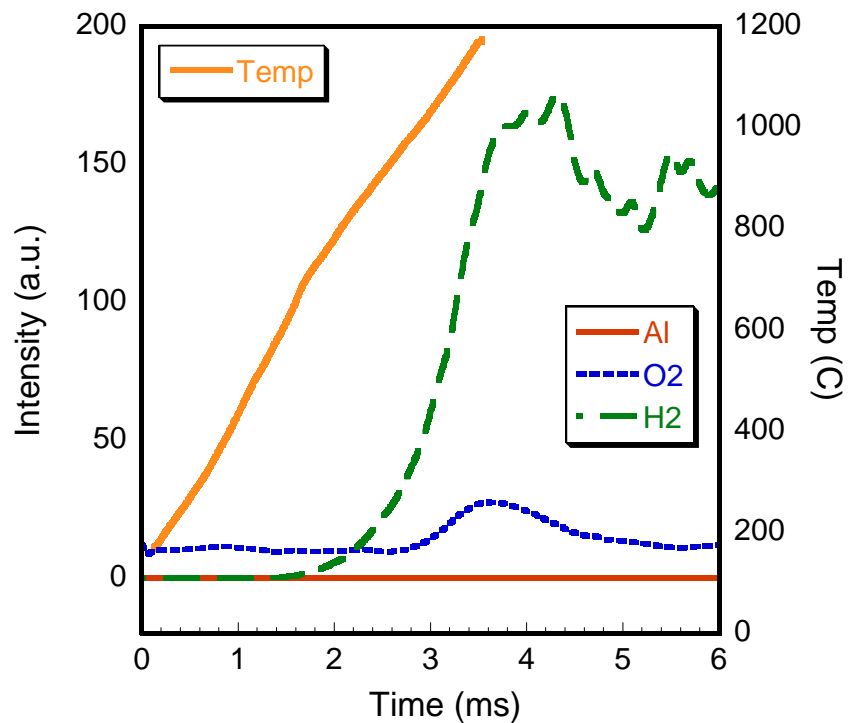
**Fig. 11 Species profiles obtained in T-Jump TOF mass spectrometer for 100% AlH$_3$ Fuel-Fe$_2$O$_3$ MIC**



**Fig. 12 Species profiles obtained in T-Jump TOF mass spectrometer for 25% AlH$_3$ Fuel (balance is nanoaluminum)-Fe$_2$O$_3$ MIC**

**Abstract**

It is axiomatic that the burning time dependence on particle size follows an integer power law dependence. However, a considerable body of experimental data show a power dependence less than unity. In this paper, we focus on what might be responsible for the fractional power dependence observed for the burning time for nanoaparticles ( e.g. Al and B). Specifically we employ reactive molecular dynamics simulations of oxide-coated aluminum nanoparticles (Al-NPs). Since most nanomaterials experimentally investigated are aggregates, we study the behavior of the simplest aggregate – a doublet of two spheres. The thermo-mechanical response of an oxide coated Al-NP is found to be very different than its solid alumina counterpart, and in particular we find that the penetration of the core aluminum cations into the shell significantly softens it, resulting in sintering well below the melting point of pure alumina. For such coated nanoparticles, we find a strong induced electric field exists at the core-shell interface. With heating, as the core melts, this electric field drives the core Al cations into the shell. The shell, now a sub-oxide of aluminum, melts at a temperature that is lower than the melting point of aluminum oxide. Following melting, the forces of surface tension drive two adjacent particles to fuse. *The characteristic sintering time (heating time + fusion time) is seen to be comparable to the characteristic reaction time, and thus it is quite possible for nanoparticle aggregates to sinter into structures with larger length scales, before the bulk of the combustion can take place.* This calls into question what the appropriate 'effective size' of nanoparticle aggregates is.

**Introduction**

Aluminum nanoparticles ( $Al$ -NPs) are the subject of considerable research in energetic materials due to their high energy density, low cost, and high reactivity. Two particular applications relevant are the addition of $Al$-NPs to high explosives to boost the energy density, and the use of $Al$-NPs as a fuel in binary thermite systems. In either case the use of nanometric scale particles is primarily to increase reactivity by reducing the characteristic mass transport length scales. In both applications, the particles are subjected to very intense heating, a fact that complicates experimental investigations. On exposure to air, aluminum particles form a native oxide ($Al_2O_3$) coating. This shell is typically uniform and amorphous, with a thickness of 2-5 nm [1]. While micron-sized aluminum particles have been reported to have an ignition temperature that is very close to the melting point of the oxide shell (~2300K), $Al$-NPs have experimentally been observed to ignite closer to the melting temperature of $Al$ (~930K). Thus understanding the interaction of the low melting Aluminum core with the high melting $Al_2O_3$ shell during rapid heating is critical in understanding the ignition mechanism of Al-NP's. At present there are two non-complementary explanations for the ignition mechanism of $Al$-NPs subjected to rapid heating are:

a. Melt dispersion mechanism – under high heating rate, the aluminum core melts and expands in volume, exerting high stress on the solid shell. If high enough, the

stress causes the oxide shell to rupture, and tensile forces subsequently unload the aluminum as small molten clusters at high velocities [2].

b. Diffusion mechanism – the shell undergoes some transition, i.e. physical cracking or polymorphic phase transitions, allowing aluminum to diffuse through the shell. The mass transport is governed by an effective diffusion coefficient of the aluminum through the permeable shell [3].

The exact physical mechanism for this ignition phenomenon is currently unclear, and this is largely due to the lack of experimental techniques. This paper however will not deal directly deal with this debate, but consider the rather curious behavior observed in the scaling laws for burning, as particle size gets smaller.

In studies on the combustion characteristic of boron nanoparticles [4], the particle size dependence of burning time ($t_b$) is found to decrease as the particle size decreases into the nanometer range. The burning times of larger particles, 30-100 $\mu m$ [5, 6], have long been known to be consistent with the $d^2$-law (diffusion-limited burning). A transition from diffusion-controlled to a kinetically-controlled is seen to occur at particle sizes of ~ 10 $\mu m$. However below ~ 10 $\mu m$ particles burning time which should be expected to roughly scale as ~ $d^1$ (kinetic limited regime) [7-9] actually are seen to demonstrate dependencies less than unity; see Figure 6 of [10]. As has been pointed out [10], the exact exponent cannot be determined due to uncertainty in the size distribution and particle agglomeration. Nevertheless, given the significant deviations from integer dependencies, it is also possible that other physical characteristics are at play not captured in a shrinking–core model. The size dependence further reduces to ~ $d^{<0.5}$ for sub-micron particles, see Figure 17 of [4]. Thus there is "apparently" only minimal gain in reducing particle size in the sub-micron range/nanoscale. Nano-Aluminum also exhibits a similar size independence in the nanoscale regime with $t_b$ ~ $d^{0.3}$ [11]. While more data is needed in the small size regime, in general we can conceptually summarize the experimental data in Figure 2. This leaves open an explanation of this behavior.
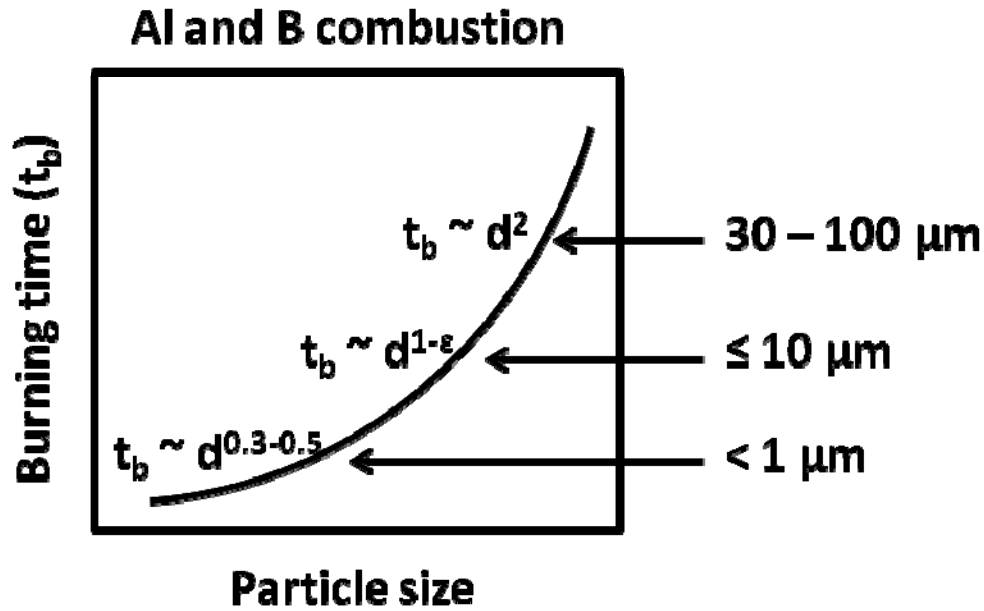
**Figure 2: Conceptual figure showing experimentally determined diameter dependence on burning time.**

Much of what is known about how super-micron particles burn is through direct imaging. But while burning can be directly imaged for large particles, nanoparticles pose a particularly challenging experimental problem. It is difficult to design experiments mimicking both the rapid heating, speculated to be around $10^8$ K/s [12], and observe the physical changes occurring. A few experimental studies have recently emerged [3, 13], to directly observe reaction on time scales relevant to combustion. In a recent work [13], a mixture of Al-NPs/ $WO_3$ (fuel/oxidizer) was imaged in a high resolution Scanning Electron Microscope (SEM). The images before and after heating are shown in Figure 3.
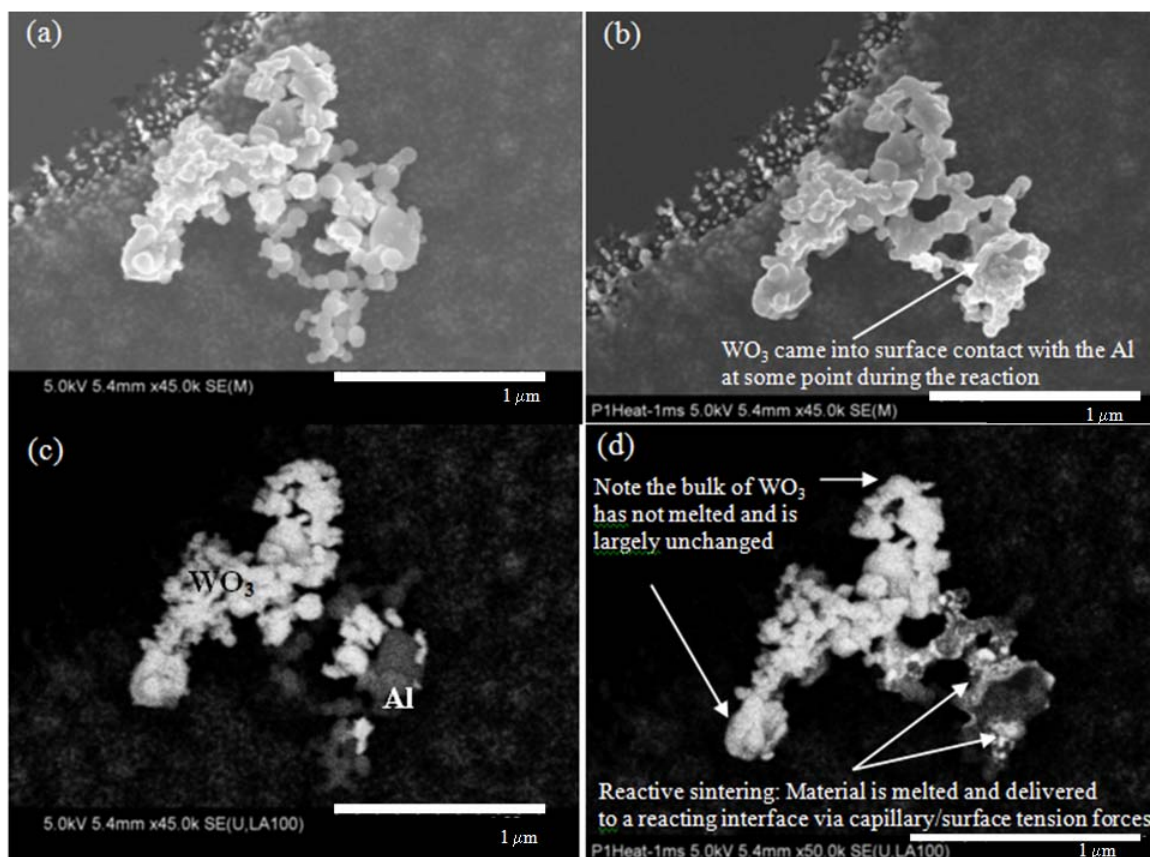
**Figure 3: SEM images of Al-NPs/WO3 (a) before and (b) after heating to 1473K at ~10⁶K/s. (c) and (d) panels are the respective backscattered electron (BSE) images: the bright particles are W/WO3, the darker particles are Al/Al2O3. Figure taken from [13]**

In the region of proximity of the fuel (Al) and oxidizer ($WO_3$), significant changes are seen (bulk of $WO_3$ does not melt and remains unchanged). It is argued that the Al and $WO_3$ come into surface contact and react at the interface. The heat generated melts adjacent particles leading to sintering. Chung et. al. [14] modeled the oxidation enthalpy of Al-NPs as a function of the Al-NP size. They found the reaction enthalpy of Al-NP (aggregated)→ bulk- $Al_2O_3$ to increase with decreasing particle size. The increased energy released with decreasing primary size would lead to faster sintering of the aggregates into bulk alumina. The results raise strong questions about the "effective" particle size and how it would impact reactivity, since large amounts of sintering serves to completely change the size and morphology of the particles. This is important since nanoparticles are mostly agglomerated.

One possible explanation then for the low size dependence of burning times for nanoparticles, seen conceptually in Figure 1, is that nanoparticles, when heated, cease to exist as single primary particles, and instead sinter to form structures with characteristically larger length scales. The goal of this work is to investigate the thermal response of oxide coated aluminum nanoparticles using molecular dynamics simulation to address the question of the likelihood of nanoaluminum sintering on a time scale commensurate with the characteristic reaction time. *The relevant question, applicable for both Al-NPs in a high explosive and binary thermites, is whether nanoparticles sinter*

170

*into characteristically larger structures well before the bulk of reaction can take place* ? On the basis of this work, the answer appears to be yes.


### Simulation Details

Molecular Dynamics (MD) methods are ideally suited to study such a problem because of the small particle sizes being considered and the lack of physical property data to implement a phenomenological model. We employed the ReaxFF (reactive) potential [15] to describe the interactions between the atoms which has been shown to accurately predict the dynamical and reactive processes of aluminum/aluminum oxide systems [16]. In contrast to traditional empirical potentials, the reactive potentials have the advantage of being able to simulate bond breaking, bond formation and charge transfer, and thus off-stoichiometry cation-anion interactions. The force field parameters for Al/$Al_2O_3$ system was developed and optimized using the results of first principles calculations. The charges of Al and O in $\alpha$-$Al_2O_3$ were found to be in good agreement with Quantum Mechanical (QM) results. The authors studied solid-Al/$\alpha$-$Al_2O_3$ interface and found it to be sharp with an equilibrium separation that agreed well with density functional theory (DFT).

However, the advantages offered by ReaxFF, also result in at least an order of magnitude more expensive than traditional MD simulations in addition to a significantly larger memory requirement. The ReaxFF potential has been integrated into the large scale parallel MD software Lammps [17] which has been used for the present study. The MD simulations were carried out on the TACC Ranger system as part of the TeraGrid network, using 8 to 128 processor cores. The equations of motion were integrated using the Verlet algorithm employing a time-step of 1 fs. Temperature was controlled by rescaling the velocities to the desired temperature at every time-step if the difference between the target and desired temperature exceeded 10K.

Here we studied two different particle sizes (8 and 16 nm in diameter) – the smaller 8nm particle consists of an ~ 5 nm diameter aluminum core coated with an ~ 1.5 nm oxide shell. A pure Al particle was first created from an *fcc* crystal by considering only the atoms within a 2.5 nm radius. It was subsequently equilibrated at 300 K. Following equilibration, the Al particle was coated with a crystalline $Al_2O_3$ shell. The coated particle was then heated to 500 K and the temperature maintained at 500 K for equilibration. A true equilibrium was, however, never reached – due to a (very) slow continuous diffusion of core Al atoms into the shell resulting in a continually decreasing potential energy profile. The diffusion being slow at 500 K, a configuration obtained after 1 ns of equilibrations was taken as the (pseudo) equilibrated structure. For comparison purposes a pure oxide particle of diameter 8 nm was built as well. The larger, 16 nm, particle, built similarly, consists of an ~ 12 nm core aluminum coated with an ~ 2 nm oxide shell (a total of ~ 200,000 atoms).

Three simulations were carried out using each of these particles. The system consisted of a particle and its translated image placed adjacent to each other, with the minimum distance between the surfaces being ~ 2-3 Å. This system was then enclosed in a box and heated rapidly at the rate of $10^{13} - 10^{14}$ K/s: from 500 K to 2000 K. Obviously this heating rate is considerably faster than that experienced in a real combustion event. We are however constrained by the total time, of the order of

nanoseconds, that can be realistically simulated in a molecular dynamics simulation. Using a parametric study, Puri et al. [18] found that a heating rate in the range $10^{13} - 10^{14}$ K/s is sufficient to equilibrate particles as well as to resolve calculated thermodynamic and structural properties. The final temperature was intentionally kept below the bulk melting point of alumina (~2400 K). Subsequently, the system temperature was held at 2000 K.

## Results and Discussion

To evaluate the sintering and combustion times we begin by simulating the sintering of oxide coated aluminum. Two small (8 nm) coated particles, equilibrated at 500K, are placed adjacent to each other and heated rapidly at the rate of $10^{14}$ K/s (total time of 15 ps). The temperature is then held at 2000K for another 1 ns. To compute the timescale for sintering, the normalized moment of inertia (MOI) is tracked throughout the simulation. The normalized MOI converges to unity when the two particles have fused completely to form a sphere. Figure 4 plots the normalized MOI along with cross-sectional views of six temporal snapshots of the simulation. Snapshots at 0 and 15 ps are for the configurations before and after heating. Heating causes the particles to undergo a volumetric expansion with melting of the core aluminum. Since the coefficient of thermal expansion of aluminum is considerably greater than that of alumina (linear coefficient of aluminum being approximately four times that of alumina), one would expect the core pressure to increase significantly, possibly leading to rupturing of the shell. However no mechanical failure was observed. The core Al atoms, were instead seen to diffuse into the oxide shell with the shell becoming richer in aluminum. The shell Al and O atoms on the other hand diffused inwards leading to a more homogeneous overall composition than the original core-shell structure.

The remaining snapshots show that after the inter-diffusion of core Al into the shell, fusion between particles begins and continues. The sintering time, time to heat the particles, plus the time to fuse completely, can be read off directly from the normalized MOI curve to be ≈ 0.7 ns. The important point here is that the 2 coated Al-NPs, heated to 2000 K, sinter completely despite that fact that the final temperature is held some ~ 400 K below the melting temperature of alumina. However, at the onset of sintering (~ 100 ps) it would be incorrect to consider the shell as alumina. The shell is clearly a sub-oxide of aluminum and is expected to have very different thermo-mechanical properties. In other words, very rapidly the shell is no longer alumina, and any phenomenological based model that uses the properties of alumina, even if there were in principle applicable to these length scales, would be in significant error.

To demonstrate this point more rigorously, an identical temperature-ramp simulation was conducted with two 8 nm oxide (alumina) particles. Figure 5 shows that even though the particles show thermal expansion effects, and form a covalent bridge, no significant neck growth can be observed. This would seem to confirm that core-shell aluminum-alumina particles would sinter well below the bulk melting point of alumina, due to the internal core-to-shell diffusion of aluminum ions.
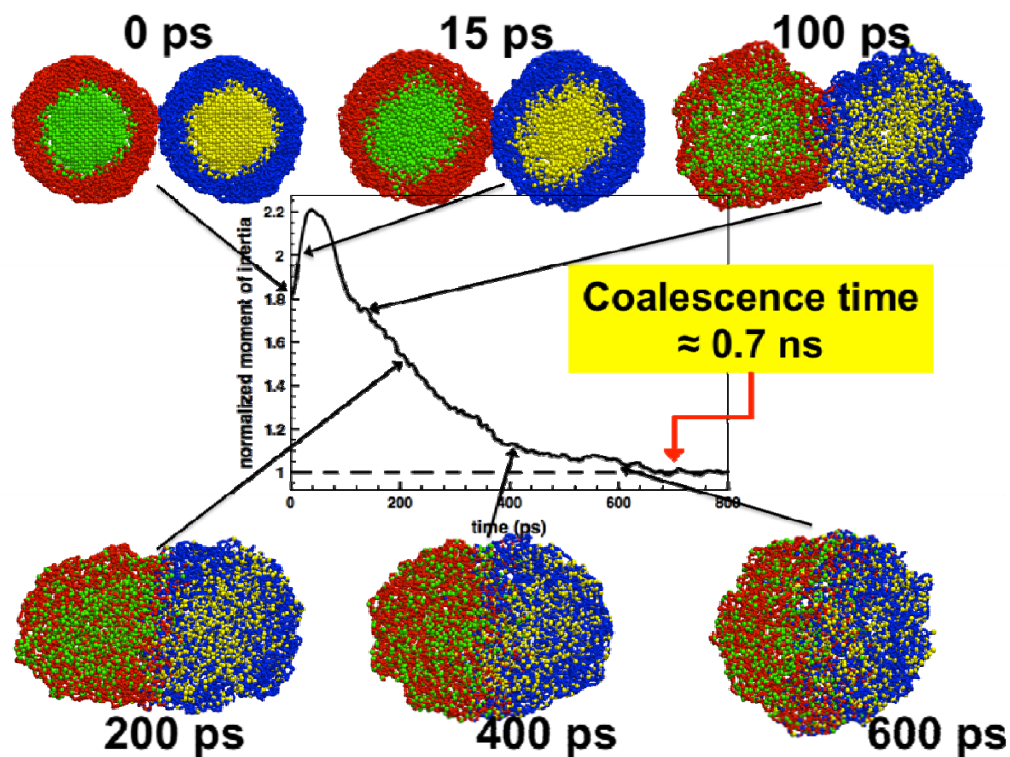
**Figure 4: Sintering of two 8nm aluminum particles with oxide shell - (a) initial configuration. (b) system at the end of rapid heating. Panels (c) to (f) represent subsequent configurations when the temperature is held at 2000 K. Colors: blue and red represent the shell (oxide) atoms whereas yellow and green represent the core (aluminum) atoms.**
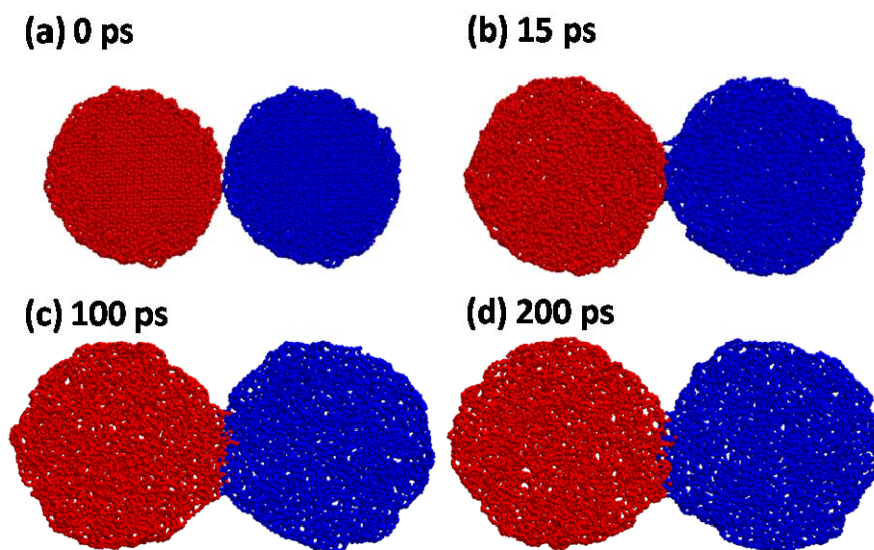


**Figure 5: simulation of a system consisting of two alumina particles. i.e no sintering in the case of alumina. Temperature ramp is identical to the case depicted in fig 3.**

173

To study the structural differences between the pure oxide, and the coated particles, the Al-O atom radial distribution function, g(r), was computed. g(r) gives the local atomic arrangement and is a tool to distinguish between solids and liquids. While crystalline solids are characterized by a repeating sequence of sharp peaks (indicating long-range order) separated by distances between neighbors, g(r) for liquids has few peaks at short distances and no long range order. The radial distribution functions for the coated and oxide particles at 200 ps are plotted in Figure 6. The sharp peak and practically no long-range order in the case of the oxide particle indicate that the oxide particle is an amorphous solid. The Al-O radial distribution function for the coated particle, on the other hand, exhibits the shape typically found for liquids – diffused peak (with fewer nearest neighbors) and no long-range order – indicating that the shell has melted and is in the liquid state. Thus, while the oxide particles remain solid at 2000 K, the coated particle is in a molten or near molten state, such that the forces of surface tension can drive the fusion.
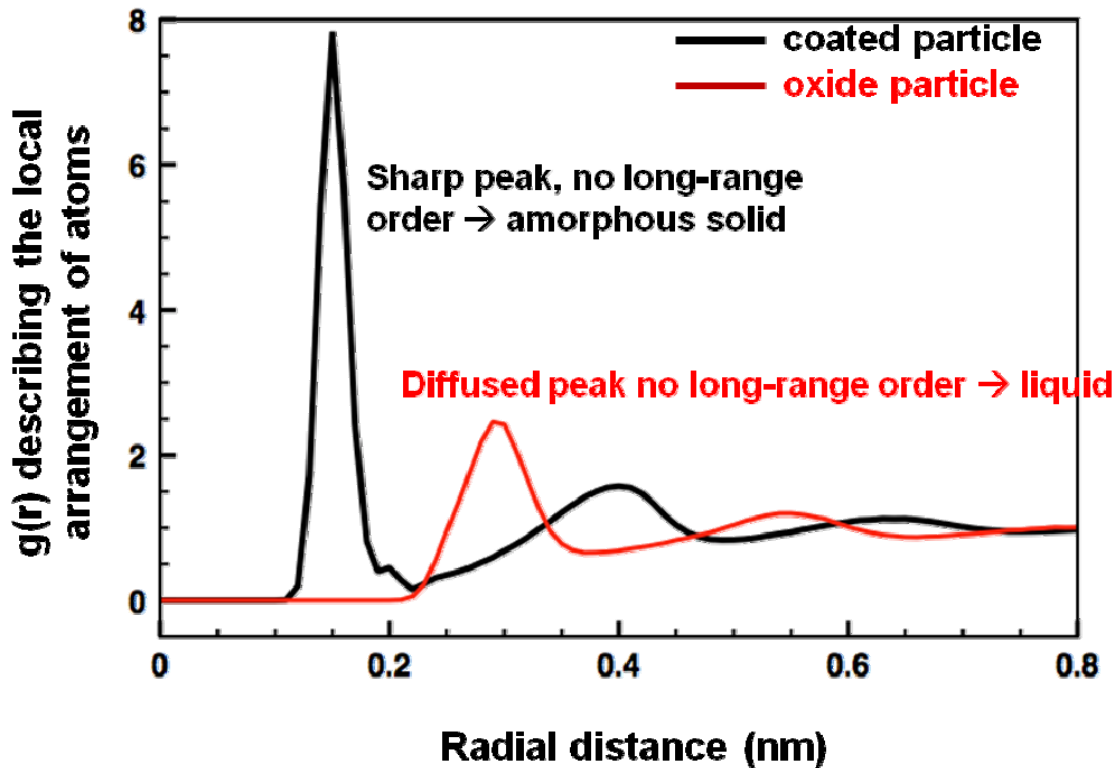


**Figure 6: Al-O atomic radial distribution functions for oxide coated nanoaluminum and aluminum oxide particles at 200 ps.**

To explore the sintering behavior in more detail a third sintering simulation was carried out with two larger (16 nm) coated particles placed adjacent to each other and heated at the rate of $10^{13}$ K/s (over a period of 150 ps) – an order of magnitude slower than the case with smaller particles. In the following, structural changes due to heating and its effects on the induced electric field/mass transfer are probed for this larger (16 nm) particle followed by a comparison of sintering and reaction timescales.

174

Radial atomic density

Figure 7 shows the radial density at different times ,indicating were each atom type is as a function of time.  Radial density [19] was calculated by considering concentric spherical shells centered at the center-of-mass of the particle. The density at a distance $r$ from the center-of-mass was then computed as the total mass inside the shell at distance $r$ divided by the shell volume. Averaging over snapshots over 40 ps of simulation time resulted in the density plots.
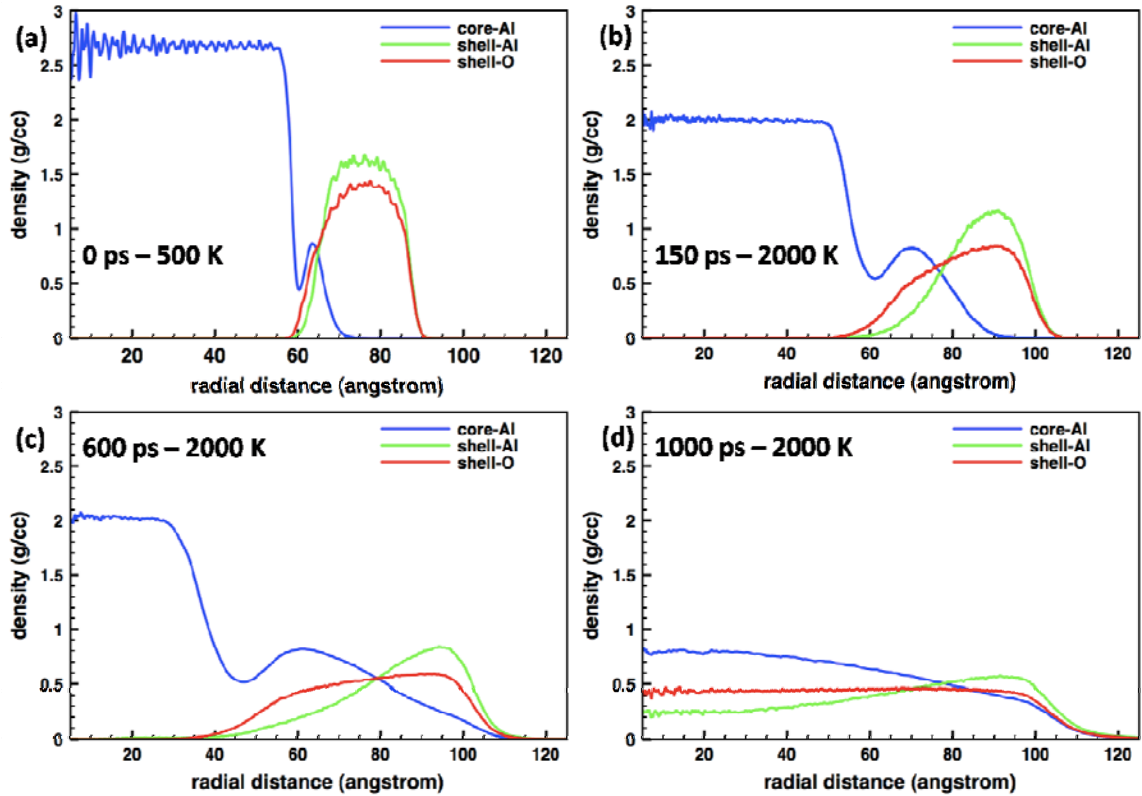


**Figure 7: Radial density plots at different times, shows movement of Al and O ions.**

Initially at 500 K, (a), the particle exhibits a core-shell structure defined by a clear interface at ~ 60 Å. The core Al had a density of 2.7 g/cc, consistent with the bulk density of solid Al. The shell, however, expanded in volume to a density of 3.1 g/cc from the prescribed initial density of 4.0 g/cc. It is interesting to note some diffusion of core Al atoms into the shell. As mentioned earlier, this diffusion is an ongoing process, much slower at lower temperature and speeding up with the melting of the Al core. As a result of heating, (b), the core melts, as is evidenced by a reduced density (2.0 g/cc). With the core Al becoming more mobile, significantly more core Al atoms diffuse into the shell – panels (b) and (c) – along with diffusion of shell atoms (both Al and O) inwards. The shell can no longer be considered to be pure alumina. Instead the shell becomes aluminum rich forming a sub-oxide. As the temperature is held constant at 2000 K, the

pure aluminum core shrinks along with an inwards expansion of the increasingly aluminum-rich shell. Finally, a near homogeneous distribution of species in the particle is obtained – panel (d).

Induced Electric Field Driving Transport

In a recent work on core-shell particles [20], the radial diffusivity of the core Al atoms was computed at different temperatures and compared with the overall diffusivity. It was found that an 'induced electric field' (rather than Fickian diffusion) drives the diffusion of core Al into the shell. The idea that oxidation growth occurs through the 'migration of charged species' was first proposed by Carl Wagner in 1933 [21]. In 1948, the Cabrera-Mott model [22] was developed that described the growth of thin oxide films on metal crystals driven by an induced electric field that causes metal ions to migrate to the surface. More recently a modified form of the Cabrera-Mott model was applied to nanometer-sized particles [23]. The induced electric field was found to be much stronger in such small particles compared to a flat surface, thereby increasing the oxidation rate significantly. Dreizin et. al. [24] further modified this model to account for volume changes in the shrinking core and expanding shell.

Figure 8 plots the radial charge density before and after heating. The plots are obtained by averaging over 40 ps of simulation time. The positively charged core, coupled with a negatively charged shell (in the initial configuration, both the core and shell were charge neutral) results in an electric field induced in the particle, most prominently at the core-shell interface.
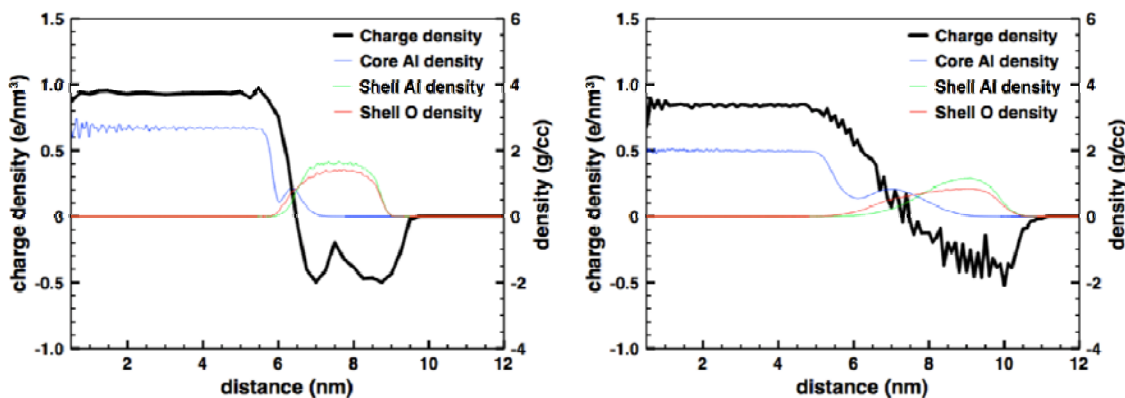


**Figure 8: Charge density in the left particle in aggregate before and after heating. For comparison, the density plot is also included.**

The electric field at each ion of the particle was then computed directly using Coulomb's law by summing over contributions from all neighboring atoms at a distance greater than 0.15 nm – to exclude the effect of the covalently bonded ions (the nearest neighbor peak in the radial distribution function for the covalently bonded shell atoms occurred at 0.15 nm). Figure 9 shows the radial component of the electric field (along with the density profile for comparison) in the particle at various times. A positive value indicates a radially outwards electric field.. Thus the core Al atoms in the interfacial

region are under a radially outward electric field. Figure 9a shows the electric field profile for the particle at 500 K – before heating. This electric field at the interface accounts for the slow continuous diffusion of core Al atoms into the shell despite the fact the core has not melted and is not under enhanced pressure. Figure 9b represents the field at 2000 K, at the end of heating. With time, the electric field moves inwards along with the core-shell interface and dissipates, Figure 9c, d. Also note that the electric field changes sign across the thickness of the shell region. This is clearly visualized by plotting the electrical force on the O atoms. Similar to the electric field calculations, the electrical force on O atoms was computed using Coulomb's Law by summing over contributions from all neighboring atoms excluding the bonded atoms. Figure 10 shows the direction of the electrical force on the oxygen atoms. As indicated by the changing sign of the electrical field, the O atoms closer to the interface experience an inward electrical force while the O atoms near the particle surface experience an outward electrical force. This is a probable explanation for the initial expansion of the shell during equilibration of the particle at 500 K.
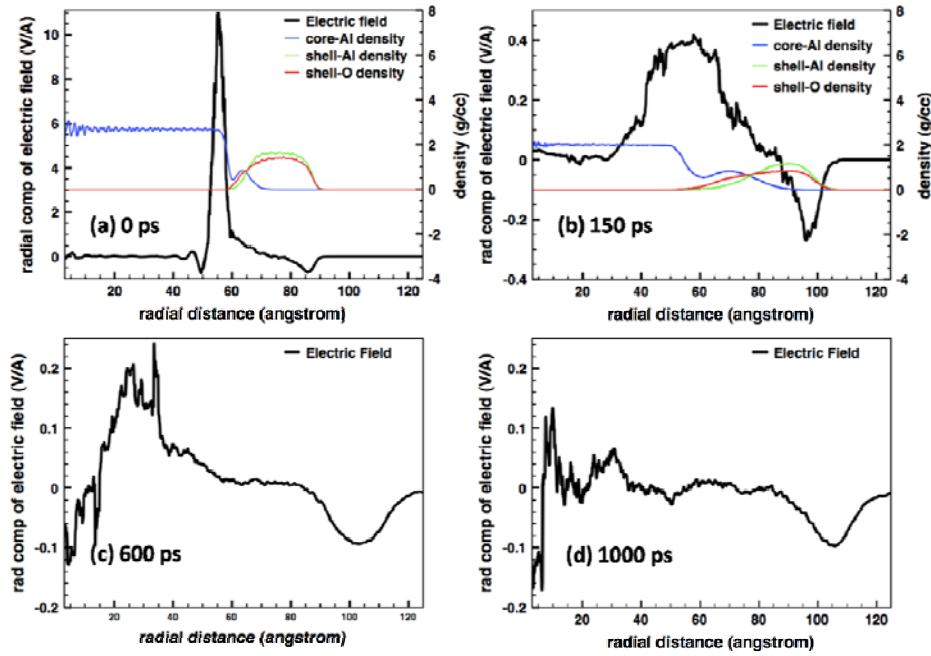


**Figure 9: Radial component of the induced electric field (volt/Angstrom) acting on the particle. With time, the peak of the electric field moves inwards and dissipates.**
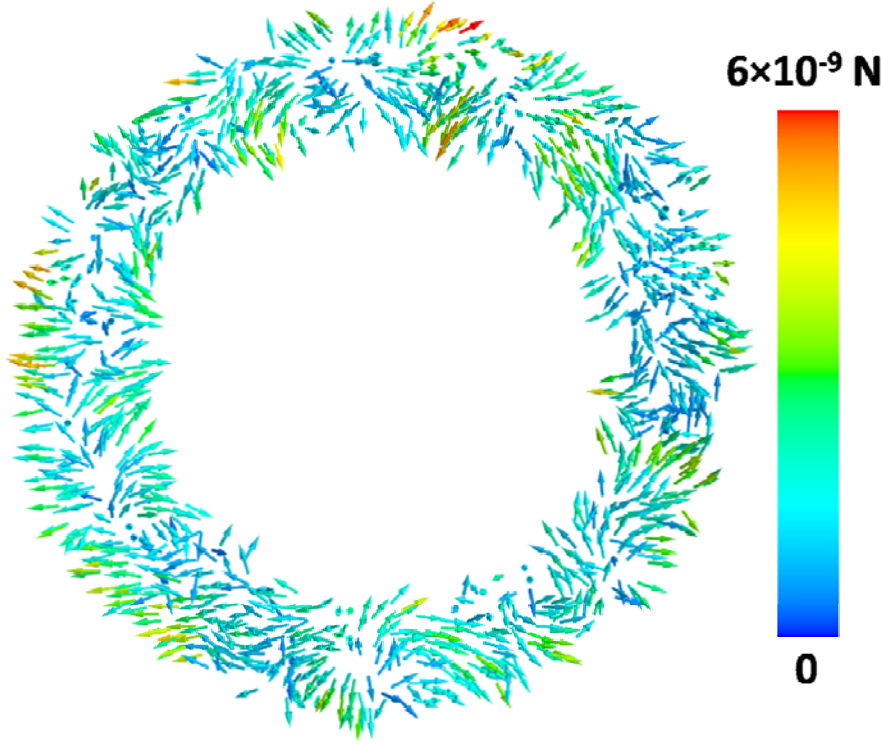
**Figure 10: Electrical force on O atoms in the shell at 500 K. O atoms closer to the core experience an inward electric force, while O atoms near the surface experience an outward electric force.**

Mass transport within a particle

Henz et. al. [20] showed that at 2000K, almost all (> 99%) of the core Al atom flux is due to the induced electric field, with the remainder due to concentration and pressure gradients. They estimated the flux of the core Al atoms using the Nernst-Planck equation [25] to be ~31 $\frac{mol}{cm^2 s}$. In this work, we compute the flux directly. The flux at time $t_i$ across a sphere of radius $r$, centered at the center of mass of the particle, is calculated as

$$J(r, t_i) = \frac{N(t_{i-1}) - N(t_i)}{4\pi r^2 (t_i - t_{i-1})} \tag{1}$$

where $N(t)$ is the number of atoms, of a particular species, inside a sphere of radius $r$ at time $t$. By construction, a positive value of the flux indicates an outward motion of atoms. Averaging over a period of 40 ps, the flux of core Al and shell O ions, for different times is plotted in Figure 11. During the period of heating (0 − 150 ps), the flux of core Al atoms at the interface increases from a nearly zero net flux to a value of

~38 $\frac{mol}{cm^2 s}$. This value is consistent with the previously estimated value.

Using the collision frequency for oxygen molecules in the gas phase, we estimate the flux of oxygen molecules hitting the particle surface to be $\sim 1 \frac{mol}{cm^2 s}$. *Thus the outward flux of aluminum though the shell is considerably faster than the reaction rate with the surface. As a result the surface will become Al rich and some evaporation will take place.* In a prior work [26], we have found some conditions experimentally, in which an Al-NP oxidation results in a hollow product particle consistent with the above analysis. During the period when the temperature is held constant the peak of the flux plot shifts inwards as the core shrinks and finally reaches nearly zero net flux – consistent with the electric field results discussed earlier. The important point here is that a strong electric field is induced at the core-shell interface due to the positively charged core and the negatively charged shell. This electric field, in turn, causes migration of ions finally forming a homogeneous sub-oxide of Al. The idea that the flux of the ions is governed by the induced electric field is also strongly supported by the transport of oxygen anions. Comparing the region between 8 – 10 nm at 150 ps, we see an outward flux of oxygen anions, which is consistent with an inward electric field. Subsequently, with the core-shell interface moving inwards, at 700 ps, a radially outward electric field in the region 2 – 5 nm drives the oxygen anions inwards. The induced electric field thus drives the original core-shell particle towards a more uniform particle through migration of ions in the particle.

The formation of hollow particles was also seen in this work as a transient state as a gap between the core and the shell regions of the particle and can be attributed to the higher outward diffusion of Al ions compared to the inward diffusion of the shell ions. For example, at 300 ps, in the region between radii 4 nm and 5 nm, the outward flux of $\sim$ 27 $\frac{mol}{cm^2 s}$ of core Al cations is almost double that of the inward flux $\sim$ 14 $\frac{mol}{cm^2 s}$ of the shell O anions. This difference in fluxes leads to a transient hollow structure, prominently visible in Figure 12. The 'gap' between the core and the shell vanishes with transition towards the more homogeneous particle.
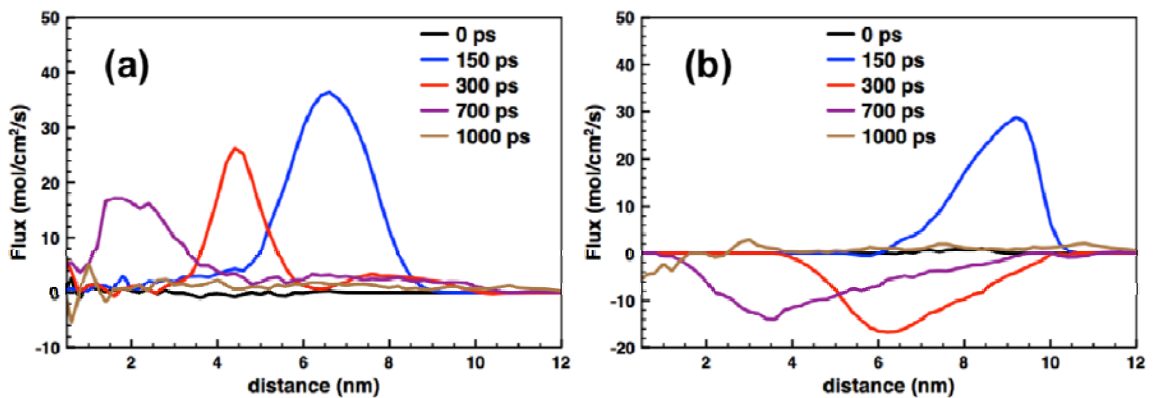


**Figure 11: Flux across the oxide coated Al particle - of (a) core Al and (b) shell O - at various times. A positive flux is radially outward.**

### Characteristic Times: Sintering Vs Reaction

179

The snapshots of the sintering simulation of the larger 16 nm particles are presented in Figure 12. In these simulations, the final temperature was fixed at 2000K. Similar behavior (inter-diffusion followed by fusion) is expected as long the final temperature is greater than the melting point of the aluminum (core). As discussed earlier, the particle size dependence of burning time for Al and B particles was seen to decrease with diminishing particle size into the nanometer range (Figure 2). The diffusion and kinetic limited burning theories generally apply to single particles or droplets. Nanoparticles, on the other hand typically exist as aggregates (for commercially available nanoparticles, the specified size is the average of the primary sizes in the aggregates). The important question here is what is the characteristic time scale for sintering relative to reaction. The sintering timescale is important since this would determine the effective particle size undergoing combustion. If the timescale for sintering is faster or at least comparable to the reaction timescale (combustion of the bulk of the nanoparticles), the burning time would then correspond to that of particles with larger characteristic length scales.

Reaction times are strongly dependent on the particular combustion system and configuration. Using a combustion cell, the pressure rise time for Al based thermites was seen to be of the order of 10 $\mu s$ [27]. Al nanoparticle combustion behind reflected shock waves in a shock tube at elevated pressures and temperatures yielded a reaction time of 50 – 500 $\mu s$ [28]. For the purpose of comparison, we take 10 $\mu s$ as the characteristic reaction timescale as the most conservative case.

The sintering time, is a sum of two components – time to heat the particles from the ambient temperature to the final temperature, and the fusion time. Since the coated particles are in the liquid state, the fusion takes place through viscous flow and the characteristic fusion time can be computed using Frenkel law [29] as

$$\tau_F = \frac{\eta d_p}{\sigma} \tag{2}$$

where $\eta$ is the temperature-dependent viscosity, $d_p$ is the particle diameter and $\sigma$ is the surface tension. If surface tension at these length scales can be assumed to be size-independent, the ratio of the fusion times of two different sized particles would be equal to the ratio of their diameters. Since our calculations show that two 8 nm particles completely fuse in ≈ 0.7 ns, we can, by scaling arguments, estimate the fusion time for two 50 nm particles to be ≈ 5 ns. Real aggregates have more than two primary particles, which can be accounted for by using Hawa & Zachariah's [30] power law modification to Frenkel's law. For N primaries of equivalent size in an aggregate of fractal dimension $D_f$, the fusion time is given by

$$\tau = \frac{\eta d_p}{\sigma} (N - 1)^{0.68 D_f} \tag{3}$$

Transmission Electron Microscope (TEM) images show that the fractal dimension of vapor grown aggregates is typically ≈ 1.8. So even for an aggregate consisting of 100 nanoparticles with average primary size of 50 nm, the total fusion time, calculated using

Equation 3, would be ≈ 50 ns. In our simulations, for computational efficiency, the heating rate was considered to be much larger than the speculated rate of $10^8$ K/s. According to the experimental heating rate, the time to heat the particles from 500 K to 2000 K would be ≈ 15 μs. This heating time, being several orders of magnitude larger than the fusion time, is thus the effective sintering time.

Thus the *sintering time is competitive with the reaction time. i.e. Al-NPs should sinter into larger structures before a significant amount of combustion can take place.* Depending on the number of primaries in an aggregate, the equivalent sphere may not be nano-sized and as such, there may not be an advantage in using (aggregated) nanoparticles under some critical size as energetic materials, since the main advantage of the nanoparticles, the high surface area to volume ratio, is negated.
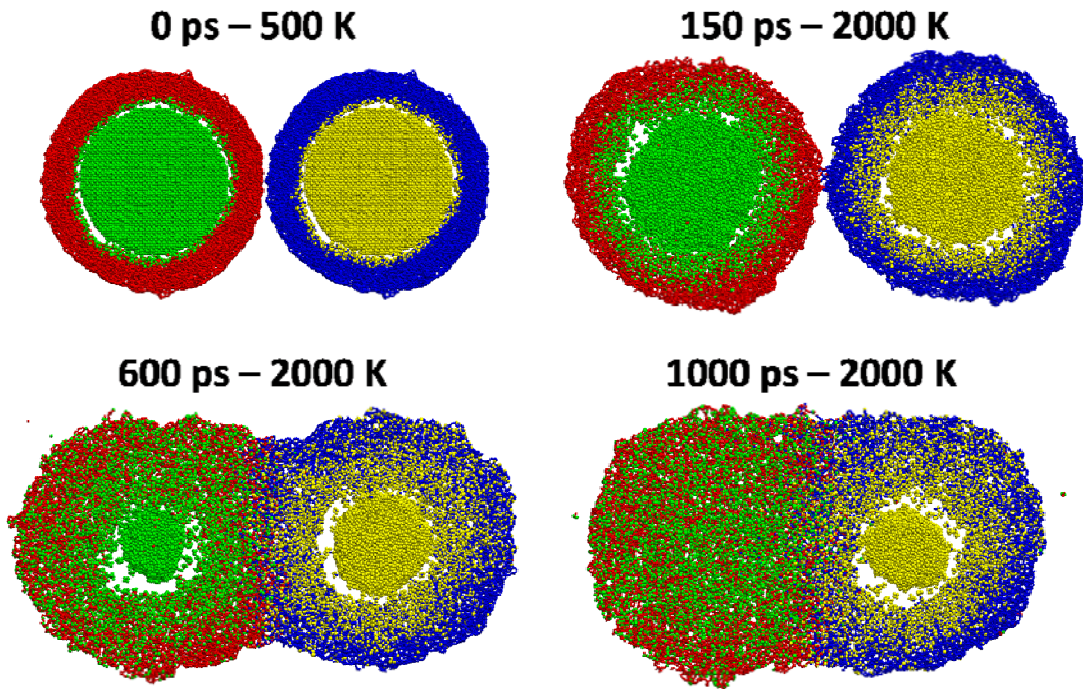


**Figure 12: Sintering simulation snapshots of the 16 nm oxide coated Al particles.**

## Conclusion

Reactive Molecular Dynamics simulations were carried out to study if the lower power dependence on particle size for burning nanoscale materials, was caused by particle sintering. Rapid heating of aluminum core/oxide shell particles found that as the core melts, the core Al atoms diffuse radically outward into the oxide shell, driven by an induced built-in electric field.

With the diffusion of core Al cations into the shell, the shell, which is now a sub-oxide of aluminum, melts at temperatures considerably lower than the melting point of

the oxide. Forces of surface tension then drive fusion of two such liquid particles. As a result, for aggregates of nanoparticles, sintering into larger structures can occur on the same time scale as combustion. This qualitatively may explain why the burning times do not get significantly shorter for very small particles.

# References

1. M. Trunov; M. Schoenitz; E. Dreizin, Combustion Theory and Modelling 10 (4) (2006) 603-623 DOI 10.1080/13647830600578506.

2. V. Levitas; B. Asay; S. Son; M. Pantoya, Applied Physics Letters   (2006) - ARTN 071909

DOI 10.1063/1.2335362.

3. S. Chowdhury; K. Sullivan; N. Piekiel; L. Zhou; M. Zachariah, Journal of Physical Chemistry C   (2010) 9191-9195 DOI 10.1021/jp906613p.

4. G. Young; K. Sullivan; M. Zachariah; K. Yu, Combustion and Flame 156 (2) (2009) 322-333 DOI 10.1016/j.combustflame.2008.10.007.

5. A. Macek; J. M. Semple, Combust. Sci. Technol. 1  (1969) 181-191

6. A. Maček, Symposium (International) on Combustion 14 (1) (1973) 1401-1411 10.1016/s0082-0784(73)80125-0.

7. S. C. Li; F. A. Williams, Ignition and Combustion of Boron Particles   (1993) 248-271

8. C. Yeh; K. Kuo, Progress in Energy and Combustion Science 22 (6) (1996) 511-541

9. T. Bazyn; H. Krier; N. Glumac, Proceedings of the Combustion Institute 31 (2007) 2021-2028 10.1016/j.proci.2006.07.161|10.1016/j.proci.2006.07.161.

10. R. Yetter; G. Risha; S. Son, Proceedings of the Combustion Institute 32  (2009) 1819-1838 10.1016/j.proci.2008.08.013|10.1016/j.proci.2008.08.013.

11. Y. Huang; G. Risha; V. Yang; R. Yetter, Proceedings of the Combustion Institute 31  (2007) 2001-2009 DOI 10.1016/j.proci.2006.08.103.

12. V. Levitas, Combustion and Flame 156 (2) (2009) 543-546 DOI 10.1016/j.combustflame.2008.11.006.

13. K. T. Sullivan; W.-A. Chiou; R. Fiore; M. R. Zachariah, Applied Physics Letters 97 (13) (2010) 133104

14. S. Chung; E. Guliants; C. Bunker; P. Jelliss; S. Buckner, Journal of Physics and Chemistry of Solids 72 (6) (2011) 719-724 DOI 10.1016/j.jpcs.2011.02.021.

15. A. van Duin; S. Dasgupta; F. Lorant; W. Goddard, Journal of Physical Chemistry a   (2001) 9396-9409 DOI 10.1021/jp004368u.

16. Q. Zhang; T. Cagin; A. van Duin; W. Goddard; Y. Qi; L. Hector, Physical Review B 69 (4) (2004) - ARTN 045423

DOI 10.1103/PhysRevB.69.045423.

17. S. Plimpton, Journal of Computational Physics 117 (1) (1995) 1-19

18. P. Puri; V. Yang, Journal of Nanoparticle Research 12 (8) (2010) 2989-3002 DOI 10.1007/s11051-010-9889-2.

19. S. M. Thompson; K. E. Gubbins; J. P. R. B. Walton; R. A. R. Chantry; J. S. Rowlinson, Journal of Chemical Physics 81 (1) (1984) 530-542

20. B. Henz; T. Hawa; M. Zachariah, Journal of Applied Physics   (2010) - ARTN 024901

DOI 10.1063/1.3247579.

21. C. Wagner, Z. **Phys. Chem. B**   (1933)

22. N. CABRERA; N. MOTT, Reports on Progress in Physics   (1948) 163-184

23. V. Zhdanov; B. Kasemo, Chemical Physics Letters   (2008) 285-288 DOI 10.1016/j.cplett.2008.01.006.

24. A. Ermoline; E. Dreizin, Chemical Physics Letters 505 (1-3) (2011) 47-50 DOI 10.1016/j.cplett.2011.02.022.

25. Handbook of Electrochemistry, Elsevier, Amsterdam, 2007, p.^pp.

26. A. Rai; K. Park; L. Zhou; M. Zachariah, Combustion Theory and Modelling 10 (5) (2006) 843-859 DOI 10.1080/13647830600800686.

27. K. Sullivan; M. Zachariah, Journal of Propulsion and Power 26 (3) (2010) 467-472 DOI 10.2514/1.45834.

28. T. Bazyn; H. Krier; N. Glumac, Combustion and Flame 145 (4) (2006) 703-713 DOI 10.1016/j.combustflame.2005.12.017.

29. S. K. Friedlander, Smoke, Dust and Haze. Fundamentals of Aerosol Dynamics, Oxford University Press, 2000, p.^pp.

30. T. Hawa; M. Zachariah, Journal of Aerosol Science 38 (8) (2007) 793-806 DOI 10.1016/j.jaerosci.2007.05.008.

## DEPARTMENT OF DEFENSE

DEFENSE THREAT REDUCTION
AGENCY
8725 JOHN J. KINGMAN ROAD
STOP 6201
FORT BELVOIR ,VA 22060
     ATTN: S. PEIRIS

DEFENSE TECHNICAL
INFORMATION CENTER
8725 JOHN J. KINGMAN ROAD,
SUITE 0944
FT. BELVOIR, VA  22060-6201
     ATTN: DTIC/OCA

## DEPARTMENT OF DEFENSE CONTRACTORS

EXELIS, INC.
1680 TEXAS STREET, SE
KIRTLAND AFB, NM  87117-5669
     ATTN: DTRIAC

DEPARTMENT OF MECHANICAL
ENGINEERING
UNIVERSITY OF MARYLAND
2181 GLENN L. MARTIN HALL,
BUILDING 088
COLLEGE PARK, MD  20742
     ATTN: M. R. ZACHARIAH